Numerical Modeling of Electrochemical and Mechanical Intercalations in All Solid-State Lithium-ion Batteries

by

Reza Behrou

M.Sc., Civil Engineering, University of Colorado Boulder, 2014

A thesis submitted to the

Faculty of the Graduate School of the

University of Colorado in partial fulfillment

of the requirements for the degree of

Doctor of Philosophy

Department of Civil, Environmental and Architectural Engineering

2016

This thesis entitled:
Numerical Modeling of Electrochemical and Mechanical Intercalations in All Solid-State Lithium-ion Batteries
written by Reza Behrou
has been approved for the Department of Civil, Environmental and Architectural Engineering

Prof. Kurt Maute

Prof. Richard Regueiro

Date

The final copy of this thesis has been examined by the signatories, and we find that both the content and the form meet acceptable presentation standards of scholarly work in the above mentioned discipline.

Behrou, Reza (Ph.D., Civil Engineering)

Numerical Modeling of Electrochemical and Mechanical Intercalations in All Solid-State Lithium-ion Batteries

Thesis directed by Prof. Kurt Maute

The rapid development of new technologies in recent decades has caused an ever increasing demand for energy storage devices that are lightweight, durable, and maintain high life-cycle expectancies. Lithium-ion batteries have emerged as a universal solution due to their exceptional energy storage and high power delivery. Lithium-ion batteries based on organic electrolytes suffer from safety concerns; specifically flammability, low temperature thresholds, and coupled electrochemical-mechanical degradation. From a design perspective, introducing a new type of lithium-ion battery with enhanced storage capacity, safe and reliable performance is the most ongoing challenge in battery research communities.

This research focuses on the numerical modeling of electrochemical and mechanical interactions in all solid-state lithium-ion batteries. In particular, we present physical and numerical modeling frameworks to model and understand the electrochemical and mechanical performance of all solid-state lithium-ion batteries under the influence of some electrochemical and mechanical degradation phenomena. To this end, we developed finite element modeling frameworks based on multi-scale and full resolution modeling methods. These models facilitate detailed understandings and comprehensive studies of the behavior of lithium-ion batteries under the evolution of degradation phenomena. While our model is not limited to any particular battery system and failure mechanism, we focus on the evaluation of the electrochemical performance of both thin and bulk solid-state lithium-ion batteries, stress-diffusion-damage coupling effects in the electrode active materials and interfacial debonding effects in the battery cell. The involved coupled physical phenomena includes mechanical deformation, diffusion-migration processes, stress-diffusion-damage coupling, electrochemical surface reactions, and cohesive zone model. To provide a predictive nu-

merical tool for optimizing the performance of battery cell, our finite element model is augmented with a parameter identification method. The parameter identification method provides unique opportunities for parametric study and identifying key design parameters in the life-time performance of all solid-state lithium-ion batteries.

The characteristics of the research are explored by presenting comprehensive numerical examples. The presented numerical examples illustrate the performance of the battery cell under the influence of different physical phenomena. We verified and calibrated the accuracy and stability of the developed framework by numerical and experimental examples. The parameter identification method is applied for parametric study and error minimization in the battery. The results revealed the great influence of material properties and geometric configuration on the electrochemical performance of the battery cell. The influence of damage evolution on the mechanical and electrochemical performance of the battery is explored by numerical examples. The results showed that diffusion-damage coupling has significant influences on the life-time performance of the battery cell. The results of cohesive zone modeling revealed the main contribution of the interface properties on the separation and the debonding phenomena at the interface of multi-phase material.

Acknowledgements

I would like to express my deepest appreciation to my Ph.D advisor, Professor Kurt Maute. It has been an honor and a joy to be his Ph.D student. His deep knowledge, experiences, encouragement, and patience help me to build up my knowledge, experiences and confidence in myself during the tough pursuit of Ph.D degree. I am deeply grateful for the excellent role model he has provided as a successful scholar and professor.

Besides my advisor, I would like to thank the rest of my committee members for their contribution of time, academic advice and guidance.

I would also like to thank Professor Sehee Lee for his genuine help.

Many thanks to my friends who have been supportive and make my life colorful.

Finally, funding for this research was provided by National Science Foundation. The support of the National Science Foundation under grant CMMI-1231048 is gratefully acknowledged.

Contents

Chapter

Tables

Table

Figures

Figure

Chapter 1

Introduction

1.1 Background

The rapid development of new technologies in recent decades has required energy storage devices to become lightweight, rechargeable, and portable. With demand growing in industrial applications, such as electric vehicles, wireless communication, and renewable energy, substantial improvement has been made to energy storage technologies; although, the enhancements have emphasized a multitude of remaining problems.

Lithium-ion batteries (LIBs) have emerged as a universal solution due to exceptional energy storage and high power delivery [123]. They feature high energy density, low self-discharging, relatively high thermal stability, and cycling performance. A traditional lithium-ion battery cell composed of a current collector, a negative electrode (anode), a separator, a positive electrode (cathode), and another current collector as shown in Figure 1.1. The material and structure of electrodes and the separator are varied widely; usually lithium metal oxide based materials for the cathode, graphite based materials for the anode, and semi-permeable membranes for the separator. The entire battery cell is immersed in the electrolyte, which is usually lithium salt with organic solvent. During the discharge process, electrons flow from the anode layer over an external circuit and reach to the cathode layer. While lithium ions migrate through the electrolyte via diffusion-migration and reach the cathode particles. The reverse of this action happens during the charge process.

In spite of all technological successes, LIBs are still experiencing numerous critical reliability

and safety issues. Most of these issues are related to the electrochemical, mechanical, and thermal phenomena and their interactions, which affect the life-cycle performance and reliability of these batteries. These phenomena diminish the storage capacity and increase the self-discharging rate during normal operation of the battery. In the past two decades, many of the LIBs safety and reliability issues have been addressed both experimentally and numerically, and improvements have been made to enhance the life-time performance and reliability of these batteries. During recent decade many of these potential safety concerns related to the capacity fade, such as the side reaction and formation of Solid Electrolyte Interface (SEI) [6, 37, 85, 111, 126], thermal abuse [8], aging [23, 119, 144, 146], and fracture of electrode materials [80, 93] have been addressed and studied widely to understand the main issues of capacity loss. For more information regarding the review of safety concerns in LIBs the reader is referred to [1].

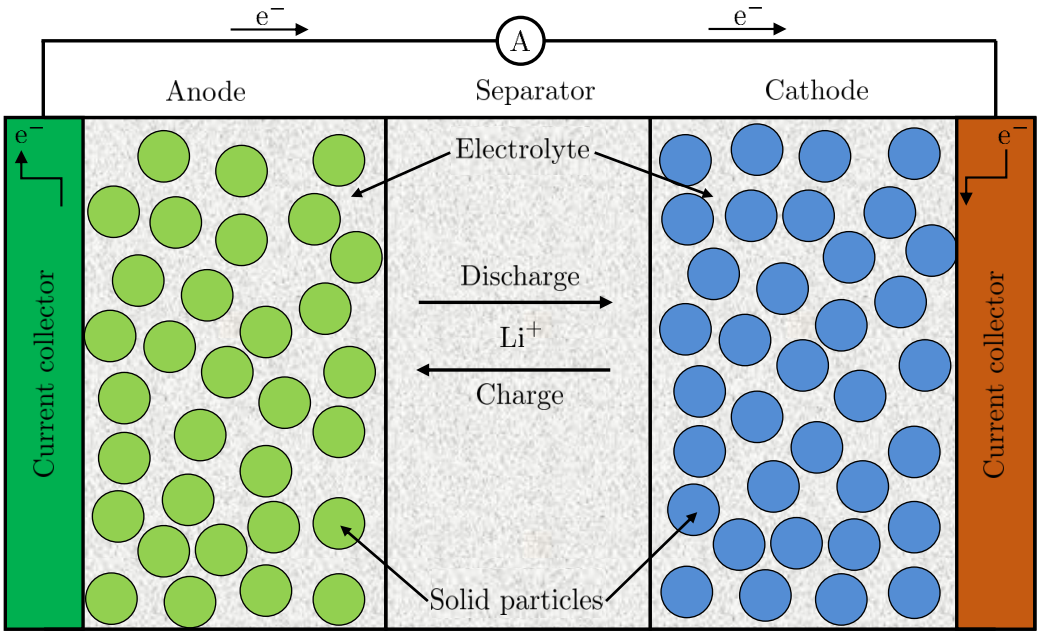

Figure 1.1: Schematic of lithium-ion battery cell.

The most important physical phenomena related to capacity fade and electrochemical-mechanical degradation in the LIB are illustrated in Figure 1.2 and described in detail in Section 1.3. These phenomena evolve upon charge-discharge cycles, and the evolution of these phenomena results in ca-

pacity fade and reduction in the life-time performance of the battery. During cyclic charge-discharge process deintercaltion/intercalation of lithium-ion cause shrinking/swelling in the electrode active materials. Upon a few first charge-discharge cycles formation of the SEI consumes lithium, see Figure 1.2, case a. The diffusion induced stresses cause evolution of micro-cracks or extension of pre-existing cracks on the surface of the electrode, see case b. These phenomena lead to the growth of SEI on the newly exposed electrode surface, see case c. The repeated cyclic charge-discharge process results in growth of the pre-existing crack and decomposition of the electrode materials, see case d. The interfacial debonding happens when the interface loses its electrochemical-mechanical functionality and a poor mechanical connection is established at the electrode/electrolyte interface, see case e. This phenomenon results in reduction in the surface reaction, and eventually capacity fade in the battery. Inside of the electrode material the cyclic process of shrinking/swelling causes the evolution of damage in the particle, see case f. The damage evolution leads to the reduction in the strength of materials and electrochemical performance (specifically diffusivity of the electrode) of the battery. This research focuses on the influence of some of these degradation phenomena on the life-time performance of Solid-State Lithium-Ion Batteries (SSLIBs).

1.2 Motivation

LIBs based on organic liquid state electrolytes suffer from safety concerns, specifically flammability and low temperature thresholds. The replacement of these electrolytes with a reliable and non-flammable electrolytes improves the safety and reliability of battery systems. From a design perspective, introducing a new type of LIB displaying improved enhanced storage capacity, safe and reliable performance, whilst diminishing cost are the most ongoing challenges in the battery community [62]. LIBs based on inorganic solid-state electrolytes have emerged as a promising candidate for the new generation of the battery. Most of the experimental studies in this field are focused toward finding suitable electrolyte materials for the new generation of LIBs. The lack of sophisticated numerical modeling frameworks for LIBs based on solid-state electrolytes motivated us to focus on building a numerical modeling framework to simulate, evaluate and predict the

coupled multi-physical responses in all SSLIBs.

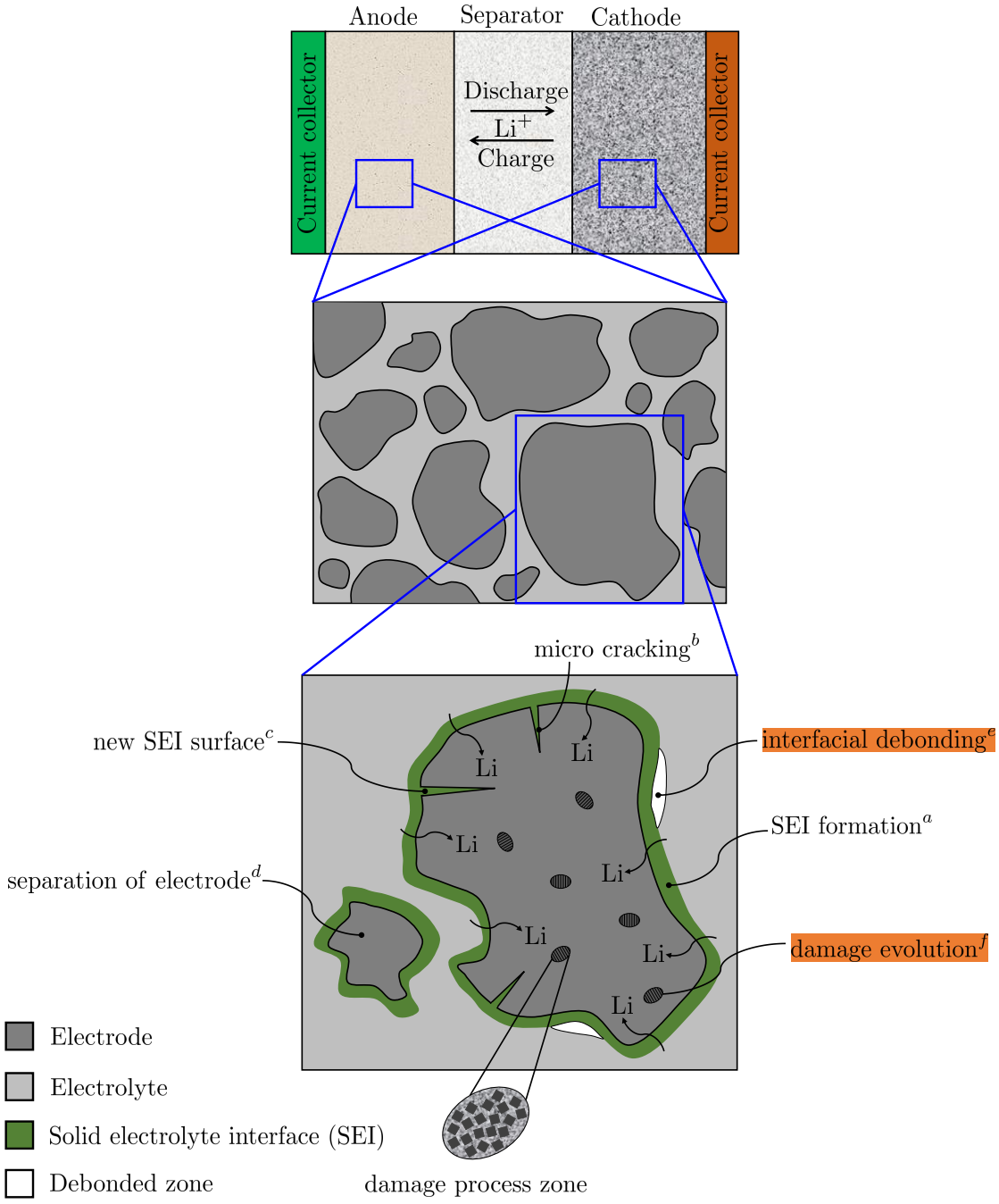

Figure 1.2: Electrochemical and mechanical degradation phenomena in the LIB during charge-discharge cycles. The highlighted phenomena are studied in this thesis.

1.3 Background on numerical modeling of LIBs

1.3.1 Models based on the liquid state electrolyte

Numerical modeling, in conjuncture with experimental observations, has proven to be a useful tool in recent decades for identifying the next generation of electrode and electrolyte materials as well as the optimizing of designs [25, 153, 154]. The primary and fundamental mathematical model for LIBs was developed over 20 years ago to describe the electrochemical phenomena in the electrode by employing porous electrode [101] and concentration solution theories [43, 44]. The porous electrode theory treats the electrode as a homogeneous porous structure at the macro-scale without resolving the detail of the exact geometric at the micro-scale. Most of electrolyte solutions in LIBs exhibit concentrated solution behavior as a non-ideal solution. The non-ideal solution assumes non-constant transport properties [90]. Recently, most of the developed numerical models for LIBs adopted the general modeling framework of [43, 44] for the conventional liquid state electrolyte. Comparisons with experimental results indicate that the model is capable of capturing transport processes and electrochemical reactions, for example see [20, 43, 44, 61, 106, 127].

Multi-scale and multi-physics models have received great attention during the past decade. These models describe the electrochemical, mechanical, and thermal intercalations between different physical phenomena at different length scales. Several detailed multi-scale modeling of LIBs with electro-mechanical effects that describes the behavior of micro-structure at different length scales presented in the past few years, for example see [52, 58, 120, 121, 122]. In most of these models computational homogenization techniques have been employed to describe the multi-physics phenomena in the micro-structure of the battery cell. In few of these models, the operation of lithium-ion batteries at two different physical domains is governed by electrochemistry and charge transport, for example see [74]. In comprehensive multi-scale models, the model accounts for the electrochemical, thermal and mechanical interactions at different length scale [58, 77, 147]. For more information and general overview about the recent development in the multi-scale modeling of LIBs the reader is referred to [52].

Battery intercalation compounds are experiencing shrinking and swelling of the electrodes during charge and discharge processes. During discharge process lithium ions deintercalate out of the anode electrode, then migrate through the electrolyte via diffusion-migration and eventually intercalate into the cathode active particles. The reverse of this action happens during the charge process. The repeated discharge-charge cycling process results in accumulation/loss of the strain energy in the particles that can lead into initiation of micro-cracks, and fracture in active particles. The cyclic degradation phenomena result in reduction in the electrical conductivity [124], initiation of micro-cracks and formation of the SEI layer in the newly exposed surface [42, 156], and fracture caused loss of active materials and the total stored energy of the system [93, 169].

Mechanical failure due to degradation of the electrode active materials have been identified as one of the most important factors in life-time performance of LIBs [4, 93, 169]. Stress generation due to intercalation phenomena has been identified as the main source of mechanical failures. The first intercalation induced stress model was developed by [112]; the results of stress analysis showed that the stress distribution generated by the intercalation process is highly dependent on the diffusion process derived from the surface concentration. Stress-diffusion coupling model has been employed in the most of numerical models to describe the intercalation induced stress in the electrode active particles, for example see [22, 30, 41, 115]. The results of stress-diffusion coupling showed that stress enhances the diffusion and swelling, for example see [163, 164]. The effects of mechanical stress on the electrochemical properties of both electrode and electrolyte have been investigated in few studies. For example, the study by [55] showed that there are significant influences of mechanical stress on the chemical potential of the electrode, however, these effects are negligible in the chemical potential of the solid-state electrolyte. The influences of hydrostatic, surface, and interface stresses have been studied in several numerical models [29, 31, 66, 87]; the results of these studies revealed the significant contribution of stress in the electrochemical performance of the electrode particle. Moreover, the effects of electrode geometry and topology on the stress distribution and capacity of the electrodes have been studied widely, for example see [48, 163, 164]. It is found that the geometry of the electrode has a substantial influence on the stress distribution as well as capacity

of the electrode. For example, the electrode with higher surface area relaxes the stress and increases the capacity [48]. Moreover, the study by [40] showed that stress generation in solid particles during lithium insertion decreases as particle radii decrease. However, with decreasing the particle size the surface stress begin to dominate the stress states. The results also show that hollow particles experience lower stress than the solid one [40]. In few numerical models, the effects of phase transformation in cathode active particles have been included in the coupled stress-diffusion model, for example see [107]; the results showed that the generated stress due to the phase transition is larger than the one due to the concentration gradient.

Stress generation and fracture caused by mechanical stresses in the electrode active particle are another main source of capacity fade in LIBs. Upon charge-discharge cycles, the diffusion induced stresses cause initiation of micro-cracks or growth of pre-existing cracks on the electrode surface. This leads to the growth of the SEI on the newly exposed surfaces, consumption of lithium due to formation of new SEI, and eventually capacity fade in the battery [42]. Capacity fade due to fracture and micro-cracks in the electrode active particles has been studied by few research groups. For example, modeling of fracture in a single spherical particle of cathode material showed that fractures in electrode particles are more probable at the rate of high power application and the probability of fracture increases with particle size [32, 33]. The surface of the particle can fracture at the end of lithium de-insertion process while core failure occurs at the beginning of insertion. Another study by [143] revealed that the electrode particle under fatigue-stress cycling tends to show the maximum tensile and shear stresses in the transition period from charging to discharging and viceversa. This study also demonstrated the importance of quick charge and slow discharge for the mechanical stability, it is shown that a long slow charge followed by a rapid discharge results in a greater tensile stress at the surface and higher strain-energy density relative to faster charges followed by slow discharges. The effects of fast charging and particle size on crack propagation have been studied by [166], the study showed that no pre-existing cracks can advance if the maximum energy release rate is smaller than the fracture energy. The results showed that this is a good indicator to calculate the critical particle size and optimal discharge rate prior to the fracture. It

was also shown that for the elasto-plastic behavior of the active particle (anode), soft material with small particle size have a better fracture strength [167].

Irreversible lithium loss due to formation of the SEI is another important source of capacity fade during life-time performance of the battery. Upon charging and discharging, the growth of the SEI or the formation of the SEI on newly exposed surfaces results in consumption of lithium at the electrode surfaces and capacity fade in the battery [42]. The study of capacity fade due to formation of the SEI has received great attention during recent years. The experimental-numerical study by [42] show that formation of the SEI at the surface of the electrode consumes lithium during the first few charge-discharge cycles, upon charging-discharging the pre-existing SEI grows gradually along with the formation of the SEI upon newly cracked surfaces. These mechanisms result in consumption of lithium and irreversible capacity loss in the battery. The operating conditions of the LIB have been proved to play an important role in the formation of the SEI [155, 160, 168]. For examples, it is found that there is significant influence of the operating temperature on the formation and growth of the SEI; low operating temperature effectively reduces the capacity loss process in the battery [155]. For more information and a general overview about the mechanism and formation of the SEI the reader is referred to [28]. Side reactions in LIBs result in number of substantial changes in the battery and lead to capacity loss. These reactions cause electrolyte decomposition and active materials dissolution [7], or, at the interface between the electrode and electrolyte, the unstable and lithiated electrode interacts with the organic solvents which results in irreversible loss of lithium [23]. For more information about an overview of the capacity fade due to side reaction the reader is referred to [7].

Most of organic liquid state electrolytes suffer from thermal abuse due to highly energetic materials and flammable electrolyte [2]. During normal operation of the battery, if the cell temperature exceeds the critical temperature gas and degradation reactions will initiate which result in thermal runaway. The temperature variation during the battery operation not only causes the thermal stress in the LIB but also significantly affects the mechanical and transport properties of the battery [36, 82]. For a critical review of the thermal issues in the LIB the reader is referred to

[8]. Understanding heat generation during normal operation of the battery is a necessary step in assessing the thermal stress of the battery. In addition to mechanical contributions, thermal effects have received considerable attention during the last decade. Few numerical frameworks have been developed to incorporate the heat generation and thermal abuse effects in lithium-ion batteries, for example see [18, 65, 76, 114, 132, 149]. These frameworks are useful for estimating cell thermal characteristics, reliable predictions of cell temperature, and heat generation rate required for the design and thermal management of battery systems. In lithium-ion batteries the heat generation comes from irreversible resistance heating, reversible entropy heating, the heat of mixing and heat of phase change. The irreversible resistance heating includes joule heating and the dissipated energy at the surface of particle [13]. The reversible entropy heating is related to the change of the Gibbs function of the cell contents. During electrochemical reactions, the composition of individual species in each phase departs from their initial composition and hence the total entropy of the cell varies. The heat of mixing represents the heat associated with the generation or relaxation of concentration profile. It was found that for a battery well designed to mitigate concentration overpotential, the heat of mixing was negligible [132].

1.3.2 Models based on solid-state electrolyte

SSLIBs are one of the most promising candidates for the next generation of batteries. Replacement of the liquid electrolyte with a solid conductor allows for high energy density, high thermal stability, excellent cycling performance, and a non-flammable system [113]. Substantial research efforts have been directed towards finding suitable solid electrolytes with high ionic conductivity and high electrochemical stability, for example see [51, 78, 103, 113, 130]. However, improving SSLIBs technology and introducing a high performance generation of these batteries requires profound understanding of the electrochemical, mechanical, and thermal processes involved. From mathematical modeling point of view, constructing a robust numerical model describing all electrochemical, mechanical, and thermal interactions in the solid-state battery is an ongoing challenge. For more information on numerical modeling concepts of SSLIBs the reader is referred to

[103].

The vast majorities of mathematical modeling of SSLIBs have been conducted toward modeling and investigation on thin-film configurations. These batteries are prepared by vacuum deposition techniques with length scales on the nano-meter level [102]. The main advantage of all solid-state thin-film batteries is that the size of the battery can be made smaller; where the capacity and ionic conductivity can be increased, depending on the type of solid-state electrolyte. The first solid-state battery model used Poissons equation to determine the potential in the solid electrolyte [12]. The results revealed that the electroneutrality condition is maintained throughout the electrolyte layer. Successively, a one-dimensional mathematical model was presented for thin-film SSLIBs [38]. In this model, an ionization reaction of immobile to mobile ions (lithium ions) and negative charges (vacancies) are considered to model the transport of ions in the solid-state electrolyte. The numerical input parameters were calibrated in order to fit numerical charge/discharge curves to the experimental results at different discharge rates. Another one-dimensional model for a thin-film micro-battery was presented at a similar time [50]. This model accounts for the diffusion-migration of lithium ions throughout the solid electrolyte, migration of electrons in the positive electrode, and reaction kinetics at the electrode/electrolyte interface. By employing experimental techniques to determine the electrochemical, mechanical, and material properties of the system, the model accurately predicted the charge/discharge response of the battery at different temperatures.

LIBs modeling and behaviors prediction requires a broad understanding of the coupled multi-physical phenomena in the battery. In addition to experimental studies, numerical modeling of the coupled multi-physics phenomena and understanding the electrochemical-mechanical interactions in SSLIBs have significant impacts on identifying the life-cycle performance and reliability of the new generation of batteries. In spite of all research efforts, to the best of our knowledge, no comprehensive numerical model has been developed yet to study the coupled electrochemical-mechanical intercalations in bulk SSLIBs. This is the first work that presents a comprehensive study for numerical simulation of coupled multi-physical responses in all SSLIBs. In particular, this research focuses on identify SSLIBs degradation phenomena and developing a finite element framework to

model, evaluate and predict the responses of all SSLIBs under the influence of these degradation phenomena.

1.4 Objectives

The main goal of this research is to present a comprehensive modeling framework for numerical simulation and evaluation of the coupled multi-physical responses in all SSLIBs. In particular, we aim to study and understand the influence of some mechanical and electrochemical degradation phenomena on life-time performance of SSLIBs. To the best of our knowledge, this is the first comprehensive numerical model for bulk SSLIBs that addresses the electrochemical-mechanical coupling effects. The developed numerical modeling framework provides unique opportunities for comprehensive studies and facilitates detailed understandings of the behavior of SSLIBs under the influence of degradation phenomena. The characteristics of our numerical modeling framework are described in Section 1.5. In spite of complexity in the physical modeling of degradation phenomena described in Section 1.1, in this research we focus on studying and physical model of:

(1) The electrochemical phenomena in both thin and bulk SSLIBs,

(2) The influence of damage evolution on the mechanical and electrochemical performance of the SSLIB,

(3) The effects of interfacial debonding on the electrochemical performance of the battery.

(4) The effects of material and geometric parameters on the electrochemical performance of the battery. In particular, what is the influence of uncertainty in material and geometric properties on the electrochemical performance of the battery?

The geometric configuration and structure of electrode layers in the LIB is highly complex. This complexity often arises due to random size and distribution of active particles in the electrode domain, see Figure 1.2. Numerical modeling and optimizing of this complex structure with finite element method need a robust computation and re-meshing techniques. The eXtended Finite

Element Method (XFEM) appears as an alternative promising solution for the numerical modeling of multi-phase structures with complex geometric configuration. In this research we adopt the XFEM to predict the structural response.

1.5 Approaches

In this section we wish to provide a detailed description of our numerical modeling approach. The main aspects of our approach for modeling of all SSLIBs are shown in Figure 1.3. Our finite element model accounts for the electrochemical and mechanical interactions in both thin and bulk SSLIBs. The involved coupled physical phenomena includes mechanical deformation, diffusion-migration processes, stress-diffusion coupling, damage-diffusion coupling, interfacial debonding and cohesive zone model, and electrochemical surface reactions. To provide a predictive numerical tool for optimizing the performance of SSLIBs, a Parameter Identification Method (PIM) is augmented into our finite element model. The PIM allows us to perform parametric study and identifying key design parameters in life-time performance of SSLIBs. The characteristics of our research approach are described as follows:

(1) Develop a full resolution model based on finite element and extended finite element methods for both thin-film and bulk SSLIBs. The model accounts for the transport processes, electric fields, and mechanical deformation in the entire battery cell. The XFEM model is developed for numerical modeling and topology optimization of electrode material with complex geometric configuration.

(2) Augment the full resolution model with non-local damage process in the electrode particle. This process accounts for mechanical and electrochemical coupling effects and capacity fade in the battery. In particular, we coupled the damage properties with the diffusivity of the electrode materials.

(3) Develop and augment a cohesive zone model that accounts for interfacial delamination and debonding in the structural configuration of the SSLIB model.

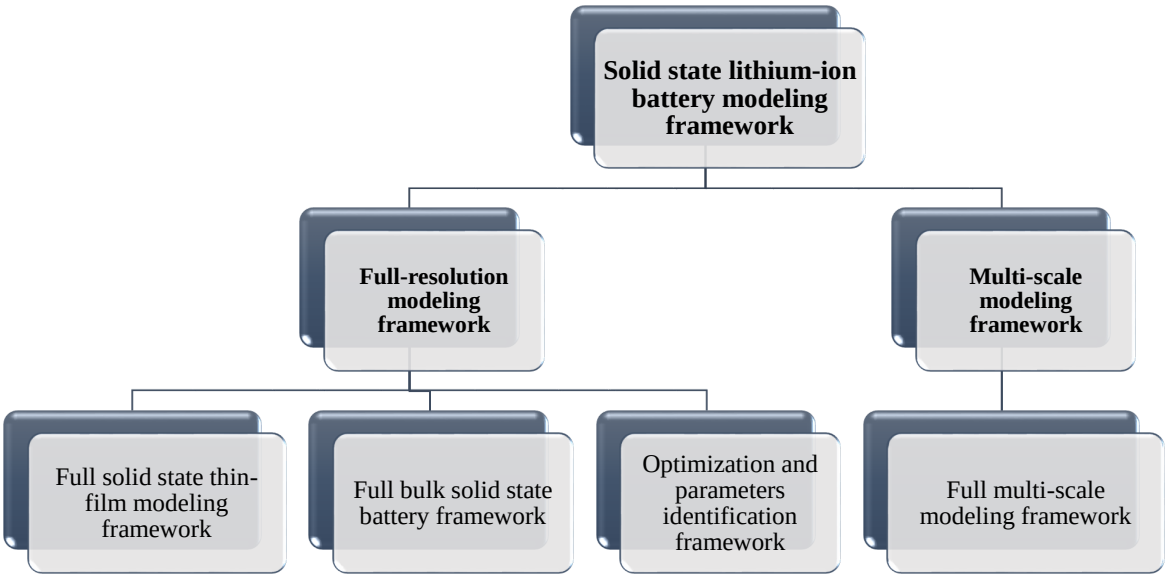

Figure 1.3: The main flowchart of research approaches.

(4) Develop comprehensive verification and calibration benchmark examples to examine different aspects of the full resolution modeling framework. The developed numerical examples evaluate different physical responses at both thin-film and bulk SSLIB models.

(5) Develop an augmented parameter identification and design optimization framework in both finite element and XFEM models.

(6) Develop a multi-scale modeling framework for SSLIBs.

The remainder of this thesis is organized as follows: in Chapter 2, we outline the formulation of coupled multi-physical responses in the entire battery cell. In Chapter 3, we discuss the numerical modeling and implementation of the SSLIB model. The PIM and design optimization method are described in Chapter 4. In Chapter 5, we study the main characteristics of the proposed framework with comprehensive numerical examples. Insight gained from this research and numerical studies are summarized in Chapter 6. Areas for future research are summarized in Chapter 7.

Chapter 2

Physical Modeling

2.1 Balance principles

This section is devoted to derive a general form of balance principles as ingredients for governing equations in the LIB modeling. In particular, this section discusses the basic balance equations and thermodynamics inequalities as integral balance conditions for the LIB applications. The latter will be used as a fundamental ingredient for dissipation phenomenon in the LIB damage model. In this section we aim to derive the mass, momentum, and energy balances for LIBs applications.

2.1.1 Balance of mass

For every continuum body, the mass is defined as the amount of material contained in the body that is invariant during a motion. For coupled deformation-diffusion problem it is assumed that no mass production occurs due to the electrochemical reaction. One may separate the balance of mass for the solid skeleton and chemical species. The total mass of a continuum body, Ω, for solid skeleton is defined by:

$$m = \int_{\Omega} \rho dv, \tag{2.1}$$

where ρ is the partial mass density, the balance of mass implies that:

$$\frac{Dm}{Dt} = \int_{\Omega} \gamma dv, \tag{2.2}$$

where γ is the mass supply.

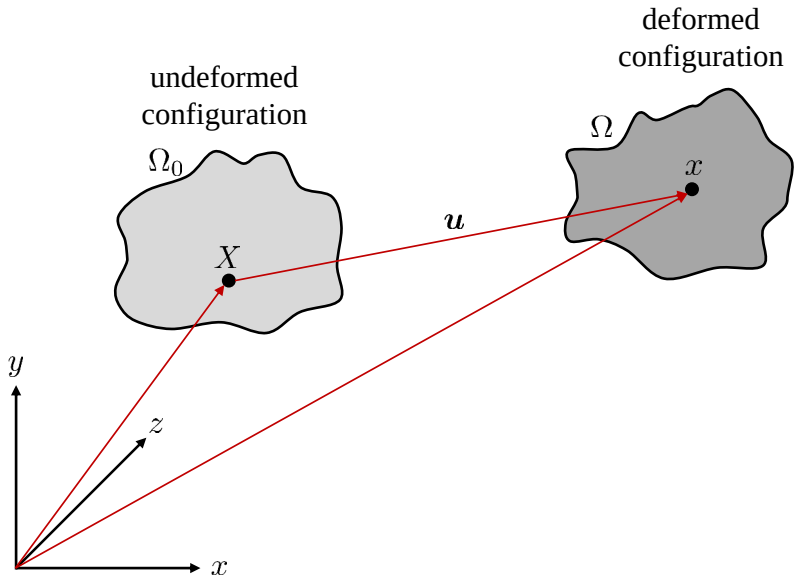

Figure 2.1: Kinematic relationship for a point in the undeformed and deformed configuration.

By equating Equations (2.1) and (2.2), localizing the integral to point wises, and assuming zero mass supply, $\gamma = 0$, the balance of mass for the solid skeleton is given as follows:

$$\frac{D\rho}{Dt} = \frac{\partial \rho}{\partial t} = 0. \tag{2.3}$$

For the electrochemical-mechanical coupling we consider the transport of lithium-ions during electrochemical reactions. The general form of the balance of mass for multiple species is defined as [67]:

$$\frac{D}{Dt}\int_{\Omega} \rho c_i dv = -\int_{\Gamma} \mathbf{J}_i \cdot \boldsymbol{n} ds + \int_{\Omega} h_i dv, \tag{2.4}$$

where ρc_i represents the species density, c_i is the concentration, $\mathbf{J}_i$ is the vectorial species flux, $\boldsymbol{n}$ is the outgoing normal vector, and h_i is the scalar species supply. By applying product rule on the left hand side of Equation (2.4):

$$\int_{\Omega} \left[c_i \frac{D\rho}{Dt} + \rho \frac{Dc_i}{Dt} \right] dv = -\int_{\Gamma} \mathbf{J}_i \cdot \mathbf{n} ds + \int_{\Omega} h_i dv. \tag{2.5}$$

Finally, by localizing the integrating, using the results of balance of mass for the solid skeleton, and applying the Divergence Theorem (DT) on the right hand side of Equation (2.5) the balance

of mass for species i is defined by:

$$\rho \frac{Dc_i}{Dt} = \rho \frac{\partial c_i}{\partial t} = -\nabla \cdot \mathbf{J}_i + h_i. \tag{2.6}$$

2.1.2 Balance of linear momentum

For a continuum body, Ω, with a set of material points, the total linear momentum, $\boldsymbol{L}(t)$, for a given motion $\boldsymbol{x} = \boldsymbol{x}(\boldsymbol{x}, t)$, partial mass density $\rho = \rho(\boldsymbol{x}, t)$ and spatial velocity field $\boldsymbol{v} = \boldsymbol{v}(\boldsymbol{x}, t)$ is defined as [69]:

$$\boldsymbol{L}(t) = \int_{\Omega} \rho(\boldsymbol{x}, t) \boldsymbol{v}(\boldsymbol{x}, t) dv. \tag{2.7}$$

The material time derivative of linear momentum for an arbitrary region in the continuum body results in the balance of linear momentum defined as follows:

$$\frac{D\boldsymbol{L}(t)}{Dt} = \int_{\Omega} \rho(\boldsymbol{x}, t) \boldsymbol{b} dv + \int_{\Gamma} \bar{\boldsymbol{t}} ds, \tag{2.8}$$

where $\boldsymbol{b}$ is the body force vector per unit mass, $\bar{\boldsymbol{t}}$ is the traction vector acting on boundary, Γ. By applying material time derivative on Equation (2.7) we obtain:

$$\frac{D\boldsymbol{L}}{Dt} = \int_{\Omega} \left[\frac{D\rho}{Dt} \boldsymbol{v} + \rho \frac{D\boldsymbol{v}}{Dt} \right] dv. \tag{2.9}$$

In addition, by applying the DT on the second term in Equation (2.8) the surface integral is converted to volume integral as follows:

$$\int_{\Gamma} \bar{\boldsymbol{t}} ds = \int_{\Gamma} \boldsymbol{\sigma} \cdot \boldsymbol{n} ds = \int_{\Omega} \nabla \cdot \boldsymbol{\sigma} dv, \tag{2.10}$$

where $\boldsymbol{\sigma}$ is the Cauchy stress tensor. Combining the left and right hand sides of the balance of linear momentum gives:

$$\int_{\Omega} \left[\rho \boldsymbol{b} + \nabla \cdot \boldsymbol{\sigma} \right] dv = \int_{\Omega} \rho \frac{D\boldsymbol{v}}{Dt} dv. \tag{2.11}$$

Finally, by localizing the integral the balance of linear momentum can be written as:

$$\nabla \cdot \boldsymbol{\sigma} + \rho \boldsymbol{b} = \rho \boldsymbol{a}. \tag{2.12}$$

2.1.3 Balance of energy (first law of thermodynamics)

The balance of energy in presence of species transport is defined as follows [67]:

$$\frac{DE_{\text{total}}}{Dt} = P_{\text{input}} + Q_{\text{input}} + I_{\text{input}}, \tag{2.13}$$

with

$$E_{\text{total}} = \int_{\Omega} \left(\frac{1}{2} \rho \boldsymbol{v} \cdot \boldsymbol{v} + \rho e \right) dv, \tag{2.14}$$

$$P_{\text{input}} = \int_{\Omega} \rho \boldsymbol{v} \cdot \boldsymbol{b} dv + \int_{\Gamma} \boldsymbol{v} \cdot \bar{\boldsymbol{t}} ds, \tag{2.15}$$

$$Q_{\text{input}} = \int_{\Omega} \left(-\nabla \cdot \boldsymbol{q} + \rho r \right) dv, \tag{2.16}$$

$$I_{\text{input}} = \sum_{i} \left(- \int_{\Gamma} \mu_i \ \mathbf{J}_i \cdot \boldsymbol{n} ds + \int_{\Omega} \mu_i h_i dv \right), \tag{2.17}$$

where E_{total} is the total internal energy, e is the internal energy per unit mass, P_{input} is the mechanical power input due to external forces, Q_{input} is the heat input rate, $\boldsymbol{q}$ is the heat flux vector, r is the heat input rate per unit mass, I_{input} is the energy flow due to the transport of all species, and μ_i is the chemical potential for specie i, respectively. By applying the material time derivative on the total internal energy, E_{total}, we get:

$$\begin{aligned} \frac{DE_{\text{total}}}{Dt} &= \int_{\Omega} \frac{D}{Dt} \left(\frac{1}{2} \rho \boldsymbol{v} \cdot \boldsymbol{v} + \rho e \right) dv \\ &= \int_{\Omega} \left[\frac{D\rho}{Dt} \left(\frac{1}{2} \boldsymbol{v} \cdot \boldsymbol{v} \right) + (\rho \cdot \boldsymbol{v}) \frac{D\boldsymbol{v}}{Dt} \right] dv + \int_{\Omega} \left[\frac{D\rho}{Dt} e + \rho \frac{De}{Dt} \right] dv. \end{aligned} \tag{2.18}$$

Using the relationship for the balance of mass (2.3), the material time derivative of the total internal energy is simplified as follows:

$$\frac{DE_{\text{total}}}{Dt} = \int_{\Omega} \left[\rho \boldsymbol{v} \cdot \boldsymbol{a} + \rho \frac{De}{Dt} \right] dv. \tag{2.19}$$

Moreover, one can apply the DT on the second term in the mechanical power input as follows:

$$\begin{aligned} \int_{\Gamma} \boldsymbol{v} \cdot \bar{\boldsymbol{t}} ds &= \int_{\Gamma} \boldsymbol{v} \cdot (\boldsymbol{\sigma} \cdot \boldsymbol{n}) ds \\ &= \int_{\Omega} \nabla \cdot (\boldsymbol{v} : \boldsymbol{\sigma}) dv = \int_{\Omega} (\boldsymbol{\sigma} : \dot{\boldsymbol{\varepsilon}} + \boldsymbol{v} \cdot \nabla \cdot \boldsymbol{\sigma}) dv, \end{aligned} \tag{2.20}$$

where $\dot{\boldsymbol{\varepsilon}}$ is the infinitesimal strain rate, by substituting the divergence of stress from the balance of linear momentum, the mechanical power is simplified as:

$$\begin{aligned} P_{\text{input}} &= \int_{\Omega} \cancel{\boldsymbol{v}\cdot\rho\boldsymbol{b}}dv + \int_{\Omega}(\boldsymbol{\sigma}:\dot{\boldsymbol{\varepsilon}} + \rho\boldsymbol{v}\cdot\boldsymbol{a} - \cancel{\boldsymbol{v}\cdot\rho\boldsymbol{b}})dv \\ &= \int_{\Omega}(\boldsymbol{\sigma}:\dot{\boldsymbol{\varepsilon}} + \rho\boldsymbol{v}\cdot\boldsymbol{a})dv. \end{aligned} \tag{2.21}$$

In the energy flow due to the transport of all species, one can apply the DT on the first term as follows:

$$\int_{\Gamma}\mu_i\ \mathbf{J}_i\cdot\boldsymbol{n}ds = \int_{\Omega}\nabla\cdot(\mu_i\cdot\mathbf{J}_i)dv = \int_{\Omega}(\mathbf{J}_i\cdot\nabla\mu_i + \mu_i\nabla\cdot\mathbf{J}_i)dv. \tag{2.22}$$

Finally, by substituting Equation (2.22) into (2.17) and using the balance of mass for the species (Equation 2.6), one can get the energy flow due to the transport of all species as follows:

$$\begin{aligned} I_{\text{input}} &= \sum_i\left(-\int_{\Omega}(\mathbf{J}_i\cdot\nabla\mu_i - \mu_i\cdot\nabla\cdot\mathbf{J}_i)dv + \int_{\Omega}\mu_i h_i dv\right) \\ &= \sum_i\left(\int_{\Omega}(\mu_i(-\nabla\cdot\mathbf{J}_i + h_i) - \mathbf{J}_i\cdot\nabla\mu_i)dv\right) \\ &= \sum_i\left(\int_{\Omega}\left(\rho\mu_i\frac{Dc_i}{Dt} - \mathbf{J}_i\cdot\nabla\mu_i\right)dv\right). \end{aligned} \tag{2.23}$$

Substituting above equations into the balance of energy equation results in:

$$\begin{aligned} &\int_{\Omega}\left[\cancel{\rho\boldsymbol{v}\cdot\boldsymbol{a}} + \rho\frac{De}{Dt}\right]dv \\ &= \int_{\Omega}(\boldsymbol{\sigma}:\dot{\boldsymbol{\varepsilon}} + \cancel{\rho\boldsymbol{v}\cdot\boldsymbol{a}})dv + \int_{\Omega}(-\nabla\cdot\boldsymbol{q} + \rho r)\,dv \\ &\quad + \sum_i\left(\int_{\Omega}\left(\rho\mu_i\frac{Dc_i}{Dt} - \mathbf{J}_i\cdot\nabla\mu_i\right)dv\right). \end{aligned} \tag{2.24}$$

By localizing the integral, the balance of energy is written as:

$$\rho\frac{De}{Dt} - \boldsymbol{\sigma}:\dot{\boldsymbol{\varepsilon}} + \nabla\cdot\boldsymbol{q} - \rho r - \sum_i\left(\rho\mu_i\frac{Dc_i}{Dt} - \mathbf{J}_i\cdot\nabla\mu_i\right) = 0. \tag{2.25}$$

2.1.4 Principle of entropy inequality (second law of thermodynamics)

The second law of thermodynamics is defined as:

$$\Gamma(t) \geq 0, \tag{2.26}$$

which states that the total production of entropy per unit time is non-negative, more specifically $\Gamma(t)$ is the total production of entropy per unit time, defined as:

$$\Gamma(t) = \frac{D}{Dt}\mathcal{S}(t) - \mathcal{Q}(t) \geq 0, \tag{2.27}$$

with

$$\mathcal{S}(t) = \int_{\Omega} \rho\eta dv, \tag{2.28}$$

$$\mathcal{Q}(t) = \int_{\Omega} \frac{1}{T}\rho r dv - \int_{\Gamma} \frac{1}{T}\boldsymbol{q}\cdot\boldsymbol{n} ds, \tag{2.29}$$

where $\mathcal{S}$ is the internal entropy, η is the entropy per unit mass, $\mathcal{Q}$ is the rate of entropy input, and T is the temperature field, respectively. The material time derivative of the internal entropy is defined as:

$$\frac{D\mathcal{S}}{Dt} = \int_{\Omega} \frac{D}{Dt}(\rho\eta)dv = \int_{\Omega} \left(\eta\frac{D\rho}{Dt} + \rho\frac{D\eta}{Dt}\right) dv. \tag{2.30}$$

Using Equation (2.3), the material time derivative of internal entropy is written as:

$$\frac{D\mathcal{S}}{Dt} = \int_{\Omega} \rho\frac{D\eta}{Dt}dv. \tag{2.31}$$

Moreover, by applying the DT on the second term in the rate of entropy input:

$$\begin{aligned} \int_{\Gamma} \frac{1}{T}\boldsymbol{q}\cdot\boldsymbol{n} ds &= \int_{\Omega} \frac{\partial}{\partial \boldsymbol{x}} \left(\frac{1}{T}\boldsymbol{q}\right) dv \\ &= \int_{\Omega} \left(-\frac{1}{T^2}\nabla T\cdot\boldsymbol{q} + \frac{1}{T}\nabla\cdot\boldsymbol{q}\right) dv. \end{aligned} \tag{2.32}$$

The rate of entropy input, therefore, is written as:

$$\mathcal{Q}(t) = \int_{\Omega} \frac{1}{T}\left(\rho r + \frac{1}{T}\nabla T\cdot\boldsymbol{q} - \nabla\cdot\boldsymbol{q}\right) dv. \tag{2.33}$$

From the balance of energy (Equation 2.25):

$$\rho r - \nabla\cdot\boldsymbol{q} = \rho\frac{De}{Dt} - \boldsymbol{\sigma}\colon\dot{\boldsymbol{\varepsilon}} - \sum_i \left(\rho\mu_i\frac{Dc_i}{Dt} - \mathbf{J}_i\cdot\nabla\mu_i\right). \tag{2.34}$$

Then we can get:

$$\mathcal{Q}(t) = \int_{\Omega} \frac{1}{T} \left(\rho \frac{De}{Dt} - \boldsymbol{\sigma} : \dot{\boldsymbol{\varepsilon}} - \sum_i \left(\rho \mu_i \frac{Dc_i}{Dt} - \mathbf{J}_i \cdot \nabla \mu_i \right) + \frac{1}{T} \nabla T \cdot \boldsymbol{q} \right) dv. \tag{2.35}$$

By substituting Equations (2.31) and (2.35) into (2.27) and by localizing the integral:

$$\rho \frac{D\eta}{Dt} - \frac{1}{T} \left(\rho \frac{De}{Dt} - \boldsymbol{\sigma} : \dot{\boldsymbol{\varepsilon}} - \sum_i \left(\rho \mu_i \frac{Dc_i}{Dt} - \mathbf{J}_i \cdot \nabla \mu_i \right) + \frac{1}{T} \nabla T \cdot \boldsymbol{q} \right) \geq 0. \tag{2.36}$$

Finally, by multiplying Equation (2.36) by T, the second law of thermodynamics can be written as:

$$\rho T \frac{D\eta}{Dt} - \rho \frac{De}{Dt} + \boldsymbol{\sigma} : \dot{\boldsymbol{\varepsilon}} + \sum_i \left(\rho \mu_i \frac{Dc_i}{Dt} - \mathbf{J}_i \cdot \nabla \mu_i \right) - \frac{1}{T} \nabla T \cdot \boldsymbol{q} \geq 0. \tag{2.37}$$

2.1.5 Clausius-Duhem inequality

Consider the Helmholtz free energy per unit mass:

$$\psi = e - T\eta. \tag{2.38}$$

By taking the material time derivative of Equation (2.38), using the first law of thermodynamics and substituting the results into the second law of thermodynamics one can end up with the Clausius-Duhem inequality. The material time derivative of the Helmholtz free energy per unit mass is written as:

$$\frac{D\psi}{Dt} = \frac{De}{Dt} - \eta \frac{DT}{Dt} - T \frac{D\eta}{Dt}. \tag{2.39}$$

By multiplying both sides with partial mass density ρ and rearranging:

$$\rho T \frac{D\eta}{Dt} - \rho \frac{De}{Dt} = -\rho \frac{D\psi}{Dt} - \rho \eta \frac{DT}{Dt}. \tag{2.40}$$

And finally by substituting Equation (2.40) into the second law of thermodynamics, the Clausius-Duhem inequality is defined as:

$$-\rho \frac{D\psi}{Dt} - \rho \eta \frac{DT}{Dt} + \boldsymbol{\sigma} : \dot{\boldsymbol{\varepsilon}} + \sum_i \left(\rho \mu_i \frac{Dc_i}{Dt} - \mathbf{J}_i \cdot \nabla \mu_i \right) - \frac{1}{T} \nabla T \cdot \boldsymbol{q} \geq 0. \tag{2.41}$$

We assume that the Helmholtz free energy per unit mass is a function of deformation, temperature, and concentration as $\psi(\boldsymbol{\varepsilon}, T, c_i)$. By applying the chain rule on the Helmholtz free energy:

$$\frac{D\psi}{Dt} = \frac{\partial \psi}{\partial \boldsymbol{\varepsilon}} : \dot{\boldsymbol{\varepsilon}} + \frac{\partial \psi}{\partial c_i} \cdot \dot{c}_i + \frac{\partial \psi}{\partial T} \cdot \dot{T}. \tag{2.42}$$

By substituting Equation (2.42) into (2.41) the Clausius-Duhem inequality is rewritten as follows:

$$\begin{aligned} \left(\boldsymbol{\sigma} - \rho \frac{\partial \psi}{\partial \boldsymbol{\varepsilon}}\right) : \dot{\boldsymbol{\varepsilon}} - \left(\rho \frac{\partial \psi}{\partial T} + \rho \eta\right) \cdot \dot{T} + \left(\sum_i \rho \mu_i \cdot \dot{c}_i - \rho \frac{\partial \psi}{\partial c_i} \cdot \dot{c}_i\right) \\ - \sum_i \mathbf{J}_i \cdot \nabla \mu_i - \frac{1}{T} \nabla T \cdot \boldsymbol{q} \geq 0. \end{aligned} \tag{2.43}$$

One can apply the Coleman and Noll argument [35] for the independent processes $\dot{\boldsymbol{\varepsilon}}$, $\dot{T}$, and $\dot{c}_i$, then for Equation (2.43) and the second law of thermodynamics to be satisfied, the following constitutive equations must hold:

$$\begin{aligned} \boldsymbol{\sigma} &= \rho \frac{\partial \psi}{\partial \boldsymbol{\varepsilon}}, \\ \eta &= -\frac{\partial \psi}{\partial T}, \\ \mu_i &= \frac{\partial \psi}{\partial c_i}. \end{aligned} \tag{2.44}$$

Therefore, the reduced energy dissipation inequalities become:

$$\begin{aligned} \sum_i \mathbf{J}_i \cdot \nabla \mu_i \geq 0, \\ \frac{1}{T} \nabla T \cdot \boldsymbol{q} \geq 0. \end{aligned} \tag{2.45}$$

where the dissipation inequality of Equation (2.43) is strongly requires satisfaction of inequalities in Equation (2.45).

2.2 SSLIBs full resolution model

The proposed full resolution model, based on dilute solution theory [100], predicts the electrochemical and mechanical phenomena in a half-cell model including the cathode and solid electrolyte layers. The whole electrochemical and mechanical process involves three main physical phenomena including species/ion transport, mechanical deformation, and electrochemical reactions. For the transport of species/ion three different phenomena are considered: the transport of ions through the electrolyte, the transport of species and electrons through the electrode particles. The transport of species and ion are treated as a diffusive process and it is assumed that the motion of the electrons is much faster than the diffusion of species, therefore the electrons movement is modeled with electrostatics. It is also assumed that the electrochemical reactions only occur at the interface of electrode and electrolyte. Although there are significant impacts of side reactions, formation of the SEI, diffusion induced micro-cracks, heat generation and electrolyte decomposition on battery performance and validity of the numerical model, we neglected the influences of these phenomenal in our numerical model, see Chapter 1. For an isothermal condition it is assumed that the mechanical response to the swelling is much faster than the diffusion process so the body is assumed to always be in a state of mechanical equilibrium. In our full-resolution model, the cathode layer can be represented by the pure solid material or solid material with voids either empty or filled with the electrolyte. The influence of the lithium metal anode on the electrochemical processes is replaced via representative boundary conditions. In the following sections the electrochemical and mechanical phenomena in the electrolyte, electrode, and interface are described in detail.

2.2.1 Electrolyte

The diffusive transport model in an electrolytic solution is described in terms of transport of charged species via diffusion-migration, electric currents, and electroneutrality condition. Unlike the concentrated liquid phase electrolyte, in the solid phase electrolyte the dilute solution theory is employed which considers the diffusion of charged species instead of simple diffusion [100]. The

most fundamental definitions of electrochemical processes in the solid phase electrolyte are described here. The electrochemical potential of an ionic species (the required energy for reversible transfer of charged species between two phases [83, 100]) is defined as:

$$\mu_{c_i} = \mu_{c_{i_0}} + RT\ln(c_i) + z_i F\phi_i - \Omega_i \sigma_h, \tag{2.46}$$

where $\mu_{c_{i_0}}$ is the initial electrochemical potential, R is the universal gas constant, T is the temperature, c_i is the concentration, z_i is the valence number (number of transferred electrons per ion), F is the Faraday's constant, ϕ_i is the electric potential of species i, Ω_i is the partial molar volume, and σ_h is the mechanical hydrostatic stress, respectively. For the diffusive transport model, the convection due to fluid-like motion of electrolyte is neglected. The flux density of each charged species which represents the migration of charged species in an electric field and diffusion caused by concentration gradient is defined by:

$$\mathbf{J}_i = -\frac{c_i D_i}{RT}\nabla\mu_{c_i}, \tag{2.47}$$

where D_i is the diffusion coefficient of species i. In addition, the electroneutrality condition implies that:

$$\sum_i z_i c_i = 0. \tag{2.48}$$

We assume the solution is composed of one kind of cation and one kind of anion [100] and is represented by c_+ as the cation and c_- as the anion concentration, respectively. The concentration of the electrolyte is then defined by:

$$\frac{c_+}{\nu_+} = \frac{c_-}{\nu_-} = c_l, \tag{2.49}$$

where ν_+ and ν_- are the numbers of cations and anions produced by dissociation of one molecule of electrolyte, respectively [100]. Moreover, the current density, $\mathbf{i}_i$, in an electrolytic solution due to the migration of charged species is defined by:

$$\mathbf{i}_i = F\sum_k^n z_k \mathbf{J}_k. \tag{2.50}$$

Based on these fundamental definitions the balance laws for the solid phase electrolyte is described in the following sections.

2.2.1.1 Balance of mass

The electrochemical transport of the cations and anions is governed by the balance of mass (2.6):

$$\frac{\partial c_i}{\partial t} + \nabla \cdot \mathbf{J}_i - h_i = 0, \tag{2.51}$$

where h_i is defined as the rate of volumetric production of the species via chemical reaction [100]. With the assumption of constant diffusion coefficients, the balance of mass for the cation and anion is expressed as:

$$\frac{\partial c_l}{\partial t} - D_+ \nabla^2 c_l - \frac{z_+ D_+}{RT} F \nabla \cdot (c_l \nabla \phi_l) - \frac{\Omega_l D_+}{RT} \nabla \cdot (c_l \nabla \sigma_h) - h_+ = 0, \tag{2.52}$$

$$\frac{\partial c_l}{\partial t} - D_- \nabla^2 c_l - \frac{z_- D_-}{RT} F \nabla \cdot (c_l \nabla \phi_l) - \frac{\Omega_l D_-}{RT} \nabla \cdot (c_l \nabla \sigma_h) - h_- = 0, \tag{2.53}$$

where c_l is the concentration, ϕ_l is the electric potential in the solid phase electrolyte, and Ω_l is the partial molar volume for the electrolyte, respectively. The electroneutrality condition allows the elimination of the electric potential field and the derivation of an effective material balance for the electrolyte. By combining the above equations, the effective balance of mass for the electrolyte is written as:

$$\frac{\partial c_l}{\partial t} + \nabla \cdot \mathbf{J}_l = h_r, \tag{2.54}$$

where h_r is the total chemical reaction production, and $\mathbf{J}_l$ is the electrolyte flux which accounts for stress-diffusion coupling as follows:

$$\mathbf{J}_l = D_{\text{eff}} \left(\nabla c_l - \frac{\Omega_l c_l}{RT} \nabla \sigma_h \right), \tag{2.55}$$

with the effective diffusion coefficient defined as [100]:

$$D_{\text{eff}} = \frac{2 z_- D_+ D_-}{z_+ D_+ - z_- D_-}, \tag{2.56}$$

and the hydrostatic stress:

$$\sigma_h = \frac{1}{3}(\sigma_{11} + \sigma_{22} + \sigma_{33}). \tag{2.57}$$

Following [38], the total chemical reaction production can be related to the ionic generation and the inverse recombination reactions described by the Arrhenius law. Therefore, the overall rate of the charge carrier generation and the net rate of the inverse reaction is considered in the electrolyte balance of mass in the following setting:

$$h_r = k_d \left(c_{l_{max}} - c_l\right) - k_r c_l^2, \qquad k_d = k_r c_{l_{max}} \frac{\xi_{c_l}^2}{1 - \xi_{c_l}}, \tag{2.58}$$

where $c_{l_{max}}$ is the maximum electrolyte concentration, k_d is the dissociation rate constant in the electrolyte, k_r is the Li-ion recombination reaction rate, and ξ_{c_l} is the fraction of free Li ions in the equilibrium.

2.2.1.2 Balance of charge

The conservation of charge states that the total current is conserved throughout the cell [43]:

$$\mathbf{i}_l + \mathbf{i}_s = \mathbf{I}_{\text{ext}}, \tag{2.59}$$

where $\mathbf{i}_l$ is the current density in the electrolyte, $\mathbf{i}_s$ is the current density in the electrode, and $\mathbf{I}_{\text{ext}}$ is the applied external current, respectively. For a constant discharge, taking the divergence of Equation (2.59) gives the relation between the ionic and electronic current densities. The balance of charge for the electrolyte is defined as:

$$\nabla \cdot \mathbf{i}_l = 0. \tag{2.60}$$

The current density in the electrolyte is evaluated by substituting the flux density of cation and anion into Equation (2.50) and summation over solution. Therefore, the current density in the electrolyte is given by:

$$\mathbf{i}_l = -F \left(z_+ D_+ + z_- D_-\right) \nabla c_l - z_+ \frac{F^2}{RT} \left(z_+ D_+ - z_- D_-\right) c_l \nabla \phi_l. \tag{2.61}$$

2.2.1.3 Balance of linear momentum

To account for the mechanical-diffusion coupling in the electrolyte the mechanical stress is coupled with the electrochemical model through the concentration induced swelling strain. For the

electrolyte the balance of linear momentum in absence of inertia term is given by:

$$\nabla \cdot \boldsymbol{\sigma}_l + \boldsymbol{b}_l = \mathbf{0}, \tag{2.62}$$

with the following linear constitutive and kinematic relationships [164]:

$$\boldsymbol{\sigma}_l = \mathbb{C}_l : (\boldsymbol{\varepsilon}_l - \frac{1}{3}\Omega_l \Delta c_l \boldsymbol{I}), \tag{2.63}$$

$$\boldsymbol{\varepsilon}_l = \frac{1}{2}(\nabla \boldsymbol{u} + \nabla \boldsymbol{u}^T), \tag{2.64}$$

where $\boldsymbol{\sigma}_l$ is the mechanical stress for the electrolyte, $\mathbb{C}_l$ is the electrolyte elasticity tensor, $\boldsymbol{\varepsilon}_l$ is the mechanical strain in the electrolyte, and $\boldsymbol{I}$ is the second order identity tensor, respectively.

2.2.2 Electrode

The electrochemical performance of active materials is described by the balance of mass that accounts for the diffusion of lithium ions, and the conservation of charge that accounts for the migration of electrons in the active materials. The governing equations for these phenomena are described here.

2.2.2.1 Balance of mass

Similar to the balance of mass for the electrolyte, the balance of mass for the electrode which accounts for the diffusion of Li^+ within the active materials is governed by:

$$\frac{\partial c_s}{\partial t} + \nabla \cdot \mathbf{J}_s = 0, \tag{2.65}$$

with the flux, $\mathbf{J}_s$, that accounts for the stress-diffusion coupling as follows:

$$\mathbf{J}_s = -D_s \left(\nabla c_s - \frac{\Omega_s c_s}{RT} \nabla \sigma_h \right), \tag{2.66}$$

where D_s is the diffusion coefficient of the electrode, c_s is the concentration of the electrode, Ω_s is the partial molar volume for the electrode, and σ_h is the hydrostatic stress defined by Equation (2.57).

2.2.2.2 Balance of charge

Similar to the balance of charge for the electrolyte, the current flowing in the electrode is governed by the Ohm's law [43]:

$$\nabla \cdot \mathbf{i}_s = 0, \tag{2.67}$$

with the current density in the electrode defined as follows:

$$\mathbf{i}_s = -\lambda_s \nabla \phi_s, \tag{2.68}$$

where λ_s is the electronic conductivity and ϕ_s is the electric potential in the electrode, respectively.

2.2.2.3 Balance of linear momentum

For the electrode particle the balance of linear momentum can be described by:

$$\nabla \cdot \boldsymbol{\sigma}_s + \boldsymbol{b}_s = \mathbf{0}, \tag{2.69}$$

with the constitutive and kinematic relationships defined as [164]:

$$\boldsymbol{\sigma}_s = \mathbb{C}_s : (\boldsymbol{\varepsilon}_s - \frac{1}{3}\Omega_s \Delta c_s \boldsymbol{I}), \tag{2.70}$$

$$\boldsymbol{\varepsilon}_s = \frac{1}{2}(\nabla \boldsymbol{u} + \nabla \boldsymbol{u}^T), \tag{2.71}$$

where $\boldsymbol{\sigma}_s$ is the mechanical stress for the electrode, $\mathbb{C}_s$ is the electrode elasticity tensor, and $\boldsymbol{\varepsilon}_s$ is the mechanical strain in the electrode, respectively.

2.2.3 Surface kinetics

The electrochemical reaction kinetics at the surface of particle is governed by the Butler-Volmer (BV) model which is commonly used in numerical modeling of lithium-ion batteries. For the electrochemical surface reaction:

$$j_{bv}(c_l, c_s, \phi_l, \phi_s) - F j_s = 0, \tag{2.72}$$

where j_{bv} is the BV equation for the given interface and j_s is surface flux. The BV equation is a model specific properties and different formulation is provided for different models.

2.3 SSLIBs multi-scale model

The multi-scale modeling approach developed here accounts for 3D modeling of all solid-state lithium-ion batteries. Our multi-scale modeling framework has originally been developed for liquid state electrolyte by [58] that is extended to account for the solid-state electrolyte [121]. The model, based on porous electrode and dilute solution theory, describes different physical phenomena at different length scales. This includes the interaction of different physical phenomena such as electrochemical, mechanical, and thermal processes at macro, meso, and micro scales. The main characteristics of our multi-sale model for SSLIBs are explored here.

2.3.1 Macro-scale model

At the macro-scale the electrochemical, mechanical, and thermal intercalations in the entire battery cell are characterized through transport of Li-ion via diffusion-migration, electric potential in both solid-state electrolyte and active particles, thermal transport, and macroscopic mechanical deformation. Following Equations (2.52) and (2.53), the electroneutrality condition allows the elimination of the electric potential field and the derivation of an effective material balance for the electrolyte. By solving Equation 2.50 for the electric potential field and substitution of the result into the balance of mass for the cation or anion, the effective balance of mass for the electrolyte is described as follows:

$$\bar{\varepsilon}_l \frac{\partial c_l}{\partial t} + \nabla \cdot \mathbf{J}_l + \frac{1}{z_+ F} \nabla \cdot \left(t_+^0 \cdot \mathbf{i}_l \right) - h_+ = 0, \tag{2.73}$$

where $\bar{\varepsilon}_l$ is the electrolyte volume fraction, and t_+^0 is the transference number defined as follows:

$$t_+^0 = \frac{z_+ D_+}{z_+ D_+ - z_- D_-}. \tag{2.74}$$

Unlike full resolution model, the effective diffusion coefficient needs to be modified to account for the electrolyte volume fraction. The effective diffusion coefficient for the multi-scale model is defined as follows:

$$D_{\text{eff}} = \bar{\varepsilon}_l \frac{2 z_- D_+ D_-}{z_+ D_+ - z_- D_-}. \tag{2.75}$$

Assumption that only the cation reacts at the electrode [100] means that the cation reaction rate can be related to the divergence of the electric current in the electrolyte via Faraday's law. This can be performed by multiplication of Equation 2.51 by $z_i F$ and summation over the number of species, the result implies that:

$$h_+ = \frac{1}{z_+ F} \nabla \cdot \mathbf{i}_l. \tag{2.76}$$

In multi-scale modeling the rate of volumetric production of the cation is related to the macro-scale effective pore-wall flux, j_{eff}, in the following setting:

$$h_+ = j_{\text{eff}}, \tag{2.77}$$

where the macro-scale effective pore-wall flux is related to the micro-scale pore-wall flux, j_s, the electrolyte volume fraction, $\bar{\varepsilon}_l$, the void volume fraction, $\bar{\varepsilon}_v$, and the electrode particle radius, R_s, as follows:

$$j_{\text{eff}} = \frac{3(1 - \bar{\varepsilon}_l - \bar{\varepsilon}_v)}{R_s} j_s. \tag{2.78}$$

By replacing the above mentioned relationships in the effective balance of mass for the electrolyte, one can write the balance of mass for the electrolyte as follows:

$$\bar{\varepsilon}_l \frac{\partial c_l}{\partial t} + \nabla \cdot \mathbf{J}_l + \frac{1}{z_+ F} \nabla t_+^0 \cdot \mathbf{i}_l - (1 - t_+^0) j_{\text{eff}} = 0. \tag{2.79}$$

Considering the effective pore-wall flux at the electrode/electrolyte interface, the currents flowing through the electrode and electrolyte are governed by the modified Ohm's law in the following settings:

$$\nabla \cdot \mathbf{i}_l - F j_{\text{eff}} = 0, \tag{2.80}$$

$$\nabla \cdot \mathbf{i}_s + F j_{\text{eff}} = 0, \tag{2.81}$$

where $\mathbf{i}_l$ and $\mathbf{i}_s$ are defined as Equations (2.61) and (2.68), respectively. To account for the electrochemical-mechanical coupling phenomena at macro-scale, the mechanical model is coupled

with the electrochemical model through homogenization method. In this model the balance of linear momentum is defined as follows:

$$\nabla \cdot \boldsymbol{\sigma}^M + \boldsymbol{b} = 0, \tag{2.82}$$

with the following linear constitutive and kinematic relationships:

$$\boldsymbol{\sigma}^M = \mathbb{C}_{\text{eff}} \colon (\boldsymbol{\varepsilon}^M - \boldsymbol{\varepsilon}^{\text{ch}}), \tag{2.83}$$

$$\boldsymbol{\varepsilon}^M = \frac{1}{2}(\nabla \boldsymbol{u} + \nabla \boldsymbol{u}^T), \tag{2.84}$$

where $\mathbb{C}_{\text{eff}}$ is the effective elasticity tensor, and $\boldsymbol{\varepsilon}^{\text{ch}}$ is the electrochemical eigenstrain tensor. The Mori-Tanaka (M-T) approach is used to compute an effective elasticity tensor and overall chemical eigenstrains of the aggregate as well as average stresses in the particles due to diffusion and mechanical loads [58, 96]. Based on this approach the effective elasticity tensor is given by:

$$\mathbb{C}_{\text{eff}} = \mathbb{C}_s + (1 - \bar{\varepsilon}_l)(\mathbb{C}_s - \mathbb{C}_l) \colon \mathbb{A}_s, \tag{2.85}$$

with

$$\mathbb{A}_s = \mathbb{A}_D \colon \left[\bar{\varepsilon}_l \boldsymbol{I} + (1 - \bar{\varepsilon}_l)\mathbb{A}_D\right]^{-1}, \tag{2.86}$$

$$\mathbb{A}_D = \left[\boldsymbol{I} + \mathbb{S} \colon \mathbb{C}_l^{-1} \colon (\mathbb{C}_s - \mathbb{C}_l)\right]^{-1}, \tag{2.87}$$

where $\mathbb{S}$ is the Eshelby's tensor. The Eshelby's tensor is a function of particle aspect ratio and the Poisson's ratio of the electrolyte phase. The detailed derivations of effective elasticity and Eshelby tensors can be found in Appendix B.

The thermal diffusion with Joule heating is described by:

$$\rho c_p \frac{\partial T}{\partial t} + \nabla \cdot (-\kappa \nabla T) - \mathbb{I} \cdot \mathbf{E} = 0, \tag{2.88}$$

where ρ is the partial mass density, c_p is the specific heat capacity, κ is the thermal conductivity, $\mathbb{I}$ is the current density, and $\mathbf{E}$ is the electric potential in the electrode and electrolyte phases. The

Joule heating $\mathbb{I} \cdot \mathbf{E}$ is defined as:

$$\mathbb{I} \cdot \mathbf{E} = \mathbf{i}_s \cdot \mathbf{E}_s + \bar{\varepsilon}_l \cdot \mathbf{i}_l \cdot \mathbf{E}_l, \tag{2.89}$$

with

$$\begin{aligned} \mathbf{E}_s &= -\nabla \phi_s, \\ \mathbf{E}_l &= -\nabla \phi_l. \end{aligned} \tag{2.90}$$

2.3.2 Micro-scale model

Similar to the full resolution model, the balance of mass for the micro-scale which accounts for the diffusion of Li^+ within the particles is governed by Equation (2.65). The balance of linear momentum for the micro-scale in the absence of body force is governed by Equation (2.69).

2.4 Electrode damage model

Fracture, micro-cracks, and damage have been identified as one of the most import sources of capacity fade and electrochemical degradation in the LIBs [42, 156, 93, 169]. Damage evolution in the electrode active materials is accompanied by the cyclic process of diffusion induced intercalation during normal operation of the battery. The damage evolution happens when the stress in the electrode active materials exceeds the strength of the material. Diffusion induced mechanical stress and reduction in the strength of material affect the electrochemical properties of the battery during normal life-time performance [26, 48]. The influence of diffusion induced stress, crack, and fracture on the life-time performance of the battery have been studied widely in the literature. Recently, a stochastic simulation approach is used by [9, 26, 27] to study the evolution of diffusion induced damage in electrode active particles. The model used random lattice spring mechanism to estimate microcracks initiation and damage accumulation in the electrode active particles assuming brittle fracture behavior. The lattice spring model displays stiffness in both axial and transverse shear directions. The model relates the formation of micro-cracks to degradation of the strength of active materials and reduction in the diffusivity of the electrode active particles. While the contribution of hydrostatic stress on the diffusion process was neglected in their model, the results revealed a great contribution of damage on capacity fading in LIBs. In addition, the model showed that the influence of crack on the surface concentration at the peripheral region is significantly greater than those located at the center of particle. The evolution of cracks during charge-discharge cycles exposes new surface for the SEI, this process consumes lithium that leads to capacity fade in the battery [42]. The results of damage model showed the influence of electrode particle size and discharge rate on damage effects [26, 27]. It was concluded that larger particle or higher discharge rate result in more capacity fade due to formation of lager zone of influence in the damage model. The purpose of this section is to study the influence of damage evolution on the electrochemical performance of SSLIBs. In particular, the influence of stress-diffusion coupling and deformation induced due to swelling on damage initiation and evolution in the electrode active particles are investigated. For

this purpose, we augmented the damage evolution model into our SSLIB full resolution model. The main characteristics of the damage evolution model are explored in this section.

For the damaged electrode materials, the total free energy of a system describes the coupled electrochemical-mechanical behavior of the damaged elastic materials. For an isothermal condition the total stored strain energy is defined in terms of the total strain, diffusion induced swelling and damage parameter as follows:

$$\psi(\boldsymbol{\varepsilon}_s, c_s, D) = (1 - D)\psi^0(\boldsymbol{\varepsilon}_s, c_s), \tag{2.91}$$

where ψ is the total free energy function per unit volume. The factor $(1 - D)$ is known as the damage reduction factor where the scalar $D \in [0, 1]$ is the damage parameter that describes the isotropic degradation of brittle materials. When $D = 0$ the material is undamaged while the value $D = 1$ is an upper limit such that the material is completely damaged and failure occurs. In the above equation, ψ^0 denotes a initial elastic stored free energy function of the undamaged material. In particular, for the electrode materials with linear elastic behavior and coupled with diffusion induced swelling the initial elastic stored free energy function is defined as follows:

$$\psi^0(\boldsymbol{\varepsilon}_s, c_s) = \frac{1}{2}\boldsymbol{\varepsilon}_s \colon \mathbb{C}_s \colon \boldsymbol{\varepsilon}_s - K\Omega_s \Delta c_s \boldsymbol{\varepsilon}_s \colon \boldsymbol{I}, \tag{2.92}$$

where K is the bulk modulus, and Δc_s is the concentration difference in the electrode phase. It is assumed that the total damage accumulation is based on stress softening of the material [69]. By employing the second law of thermodynamics and the Clausius-Duhem inequality derived in section 2.1, one can postulate the following inequality:

$$\begin{aligned} \mathcal{D}_{\text{int}} = \left(\boldsymbol{\sigma}_s - \frac{\partial \psi}{\partial \boldsymbol{\varepsilon}_s}\right) : \dot{\boldsymbol{\varepsilon}}_s + \left(\mu_s - \frac{\partial \psi}{\partial c_s}\right) \cdot \dot{c}_s \\ -\frac{\partial \psi}{\partial D} \cdot \dot{D} - \mathbf{J}_s \cdot \nabla \mu_s - \frac{1}{T} \nabla T \cdot \boldsymbol{q} \geq 0, \end{aligned} \tag{2.93}$$

where the damage related dissipation is a non-negative internal dissipation inequality. This inequality must hold true for any strain increment

$$\mathcal{D}_{\text{int}} = f\dot{D} \geq 0, \tag{2.94}$$

where f denotes as the thermodynamic force related to loading-unloading condition which governs the damage evolution. It turns out that f is identical to the stored strain energy function of the undamaged material, ψ^0. This inequality equation expresses the fact that damage is a dissipative process. In order to define a constitutive equation for the elastic materials with an isotropic damage including softening effects, the evolution equation for the damage parameter, D, should be determined. The inequality equation (2.93) yields the following elastic constitutive equation:

$$\boldsymbol{\sigma}_s = (1 - D)\boldsymbol{\sigma}_s^0(\boldsymbol{\varepsilon}_s, c_s), \tag{2.95}$$

where

$$\boldsymbol{\sigma}_s^0(\boldsymbol{\varepsilon}_s, c_s) = \mathbb{C}_s : \boldsymbol{\varepsilon}_s - K\Omega_s \Delta c_s \boldsymbol{I}. \tag{2.96}$$

2.4.1 Non-local damage formulation

In the damage mechanics modeling, the scalar damage parameter, D, is related to damage evolution law by:

$$D = \bar{g}(\kappa), \tag{2.97}$$

where $\bar{g}$ is the damage evolution function and κ is an internal variable that corresponds to the maximum level of equivalent strain ever reached in the previous history of the material. The internal inequality dissipation, known as the loading-unloading condition, implies that:

$$f(\boldsymbol{\varepsilon}, \kappa) = \boldsymbol{\varepsilon}_{\text{eq}}(\boldsymbol{\varepsilon}) - \kappa \leq 0, \qquad \dot{\kappa} \geq 0, \qquad f(\boldsymbol{\varepsilon}, \kappa)\dot{\kappa} = 0, \tag{2.98}$$

where $\boldsymbol{\varepsilon}_{\text{eq}}$ is a scalar measure of the strain level called the equivalent strain. The specific expression for the equivalent strain can be related to the shape of affected domain in the strain space. For example the equivalent strain can be related to the norm of strain energy or as a function of principle strains [92]. In this study the equivalent strain is defined as a function of the scaled norm of strain energy as follows:

$$\boldsymbol{\varepsilon}_{\text{eq}}(\boldsymbol{\varepsilon}) = \sqrt{\frac{\boldsymbol{\varepsilon} : \mathbb{C} : \boldsymbol{\varepsilon}}{E}}. \tag{2.99}$$

The scaling of the norm of strain energy by Young's modulus is considered to transform the energy into a strain-like quantity. In many loading cases the damage in materials dominates by tension than compression. The particular expression for the equivalent strain is defined such that the influence of tension is emphasized. For example, one can define the equivalent strain as a function of principle strain ([92]) as follows:

$$\boldsymbol{\varepsilon}_{\mathrm{eq}}(\boldsymbol{\varepsilon}) = \sqrt{\langle \boldsymbol{\varepsilon}_{11} \rangle^2 + \langle \boldsymbol{\varepsilon}_{22} \rangle^2 + \langle \boldsymbol{\varepsilon}_{33} \rangle^2}, \tag{2.100}$$

where the brackets $\langle \boldsymbol{\varepsilon} \rangle$ is defined as the positive part operator, such that:

$$\langle \boldsymbol{\varepsilon} \rangle = \begin{cases} \boldsymbol{\varepsilon} & \text{if } \boldsymbol{\varepsilon} > 0 \\ 0 & \text{if } \boldsymbol{\varepsilon} \leq 0 \end{cases}. \tag{2.101}$$

A suitable approach for the damage evolution law is to consider a non-local damage formulation which is associated with well-posed boundary value problem. The formulation smooths the damage variable computed from the local equivalent strain. To this end, the local equivalent strain ($\boldsymbol{\varepsilon}_{\mathrm{eq}}$) in the loading-unloading conditions (2.98) is replace with the weighted non-local strain in the following setting:

$$\bar{\boldsymbol{\varepsilon}}_{\mathrm{eq}} - \kappa \leq 0, \qquad \dot{\kappa} \geq 0, \qquad (\bar{\boldsymbol{\varepsilon}}_{\mathrm{eq}} - \kappa)\dot{\kappa} = 0. \tag{2.102}$$

An implicit gradient damage formulation [116] can be used to compute the weighted non-local equivalent strain. Following the approach proposed by [116], the non-local equivalent strain variable is indirectly defined as the solution of a Helmholtz-type differential equation:

$$\bar{\boldsymbol{\varepsilon}}_{\mathrm{eq}} - c\nabla^2 \bar{\boldsymbol{\varepsilon}}_{\mathrm{eq}} = \boldsymbol{\varepsilon}_{\mathrm{eq}}, \tag{2.103}$$

where the gradient enhanced parameter, c, is of the dimension length squared and control the smoothness of the damage. In particular, c is proportional to the length scale parameter (characteristic length). The length scale parameter is related to material properties, fracture energy, and aggregate size which needs to be determined experimentally [11]. Considering $\bar{\boldsymbol{\varepsilon}}_{\mathrm{eq}}$ as an independent variable that simplifies the formulation and enables a straightforward and continuous finite

element interpolation. The only major issue in the Helmholtz-type equation is the requirement of the additional boundary condition that needs to be satisfied. Following by [116], the most simple case for the additional boundary condition is that:

$$\nabla \bar{\boldsymbol{\varepsilon}}_{\text{eq}} \cdot \boldsymbol{n} = 0. \tag{2.104}$$

The evolution of damage then can be described by the damage evolution function, $\bar{g}(\kappa)$, which is defined in different forms of evolution law as a function of damage internal variable, κ. The simplest form of the evolution function can be expressed as a function of internal variable as follows [116]:

$$D = \bar{g}(\kappa) = 1 - \frac{\kappa_0}{\kappa}, \tag{2.105}$$

where κ_0 is the initial damage threshold. Following Equation (2.95), the rate form of tangent constitutive equation for damaged and undamaged electrode material is defined by:

$$\dot{\boldsymbol{\sigma}}_s = \begin{cases} (1-D)(\mathbb{C}_s : \dot{\boldsymbol{\varepsilon}}_s - K\Omega_s \boldsymbol{I} : \dot{c}_s) - \frac{\partial \bar{g}(\kappa)}{\partial \kappa} \boldsymbol{\sigma}_s^0 : \dot{\bar{\boldsymbol{\varepsilon}}}_{\text{eq}} & \text{if } \bar{\boldsymbol{\varepsilon}}_{\text{eq}} > \kappa \\ (1-D)(\mathbb{C}_s : \dot{\boldsymbol{\varepsilon}}_s - K\Omega_s \boldsymbol{I} : \dot{c}_s) & \text{if } \bar{\boldsymbol{\varepsilon}}_{\text{eq}} \leq \kappa \end{cases}, \tag{2.106}$$

The derivative of the damage evolution law (2.105) with respect to scalar history parameter, κ, is defined as:

$$\frac{\partial \bar{g}(\kappa)}{\partial \kappa} = \frac{\kappa_0}{\kappa^2}. \tag{2.107}$$

The update procedure for the non-local damage evolution with stress-diffusion coupling is expressed in the Algorithm 1.

In order to trigger the influence of damage evolution on the transport properties, discharge behavior, and electrochemical performance of the battery, the electrode diffusion coefficient, D_s, can be described as a function of the damage parameter, D, [26, 27]. The diffusion induced stresses cause the evolution of damage in the electrode active materials. With increasing the influence of the damage the diffusivity of the electrode is decreased. The reduction in the diffusivity of the electrode contribute to the capacity loss in the battery. To this end, the evolution of the damage is described by an exponential law such that the damage parameter, D, is expressed as

an exponential function of the damage internal variable, κ, as shown in Figure 2.2. Moreover, the electrode diffusion coefficient, D_s, is described as an exponential function of the damage internal variable, κ, as follows:

$$\begin{aligned} D &= 1 - \exp\left(-\beta \frac{k}{k_0}\right), \\ \tilde{D}_s &= \exp\left(-\beta \frac{k}{k_0}\right), \end{aligned} \tag{2.108}$$

where D is the damage evolution parameter, β is the damage sharpness and slope controlling parameter, κ_0 is the initial damage threshold, and $\tilde{D}_s$ is the nondimensional diffusion coefficient in the electrode phase.

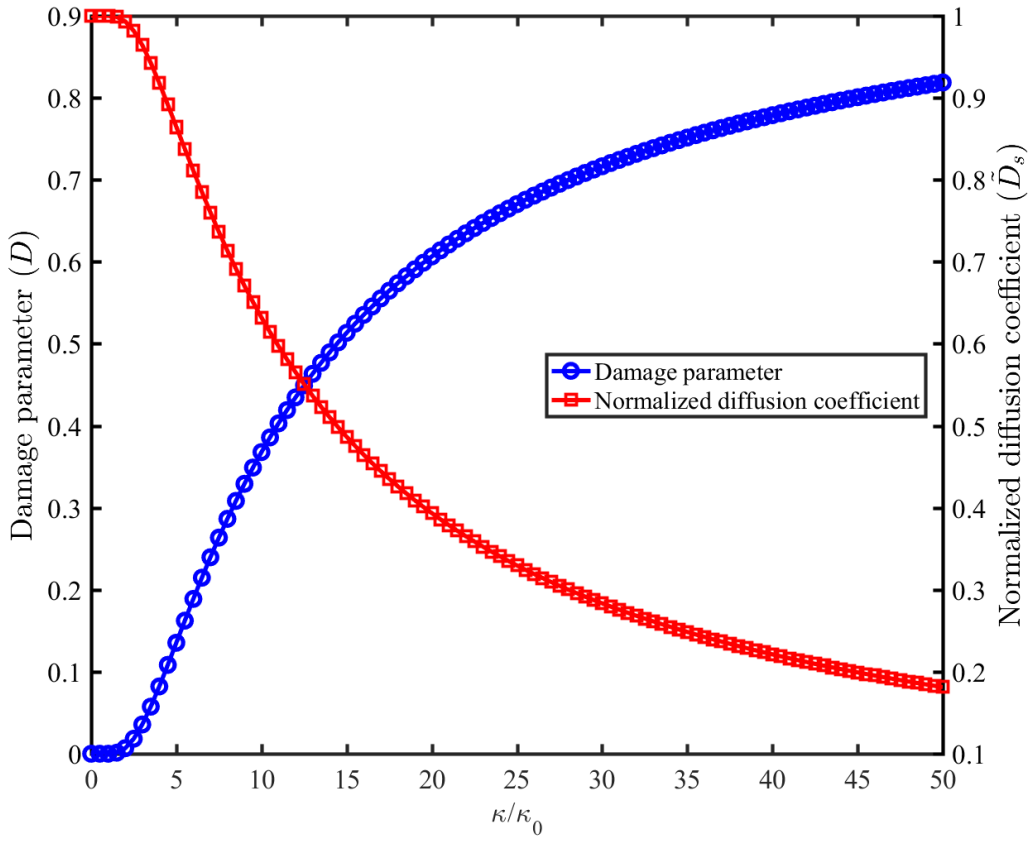

Figure 2.2: The evolution of damage parameter and electrode diffusion coefficient with damage internal variable.

2.5 Cohesive zone model in LIBs

The performance of engineering structures composed of multi-phase materials is often dominated by mechanical interface phenomena such as frictionless and frictional contacts. These phenomena can be observed in many engineering applications; such as: crack propagation, sliding contact, and metal forming operation. From design perspective, the performance of structures can be influenced by interface conditions and the influence of these phenomena need to be considered carefully in the design specially for the extreme loading condition. The frictional contact or adhesion represent a progressive nonlinear behavior along the interface. This phenomenon which relates the separation along the interface to the traction is called cohesive zone model. The cohesive zone model has received widespread interest among scientific communities during past three decades. It describes the material failure and interfacial debonding in engineering structures. It was initially introduced by Dugdale [45] to analyze the damage evolution and material failure around the crack tip. The model describes the existing cohesive forces along the interface as a function of interfacial separation. During the separation the traction along the interface grows up to the maximum value and then falls to zero and vanishes. Over the past three decades, numerical modeling of structural problems with cohesive zone models have received considerable attentions. The most primary and fundamental continuum mechanics model with an interface phenomenon was introduced by Needleman [99]. The model described the evolution of the interface phenomenon from an initial debonding through a perfect separation. The interface phenomenon was introduced through an energy based constitutive equation which describes a mechanical relation between traction and separation along the interface. The traction increases with growing interfacial separation, reaches the maximum value, then drops to zero, and eventually vanishes such that complete decohesion occurs. Considering the cohesive zone model led to a nonlinear mechanical problem, which acts at the interface to prevent either interpenetration or separation of bodies. The constitutive relation between traction and separation can be described by exponential, bilinear, and polynomial forms of cohesive zone laws [24, 136, 137, 157]. The standard bilinear cohesive zone model has

received much attention among the scientific communities, being used for simulation of interfacial debonding, matrix cracking, delamination of fiber reinforced composites [49, 84], and failure in functionally graded materials [165]. The normal and tangential traction can be represented as a function of both normal and tangential separation (coupled) or only one of them (uncoupled). This functionality is a useful tool to represent the behavior of materials at different fracture modes [139]. Both coupled and uncoupled cohesive zone models have been extensively studied in literature. For example, the cohesive zone model was used to study the fracture phenomenon in concrete and rock [10, 47, 109, 128, 117], to simulate the propagation of matrix cracks in thin composite plates subjected to low velocity impact [57]. For more information about review of cohesive zone models, the reader is referred to [108].

The cohesive zone model has received considerable attentions in the numerical modeling of lithium-ion batteries. In most cases it is considered to model fracture and fatigue induced delamination in the electrode particle during insertion of lithium [63, 19, 21, 81]. The influence of Interfacial debounding due to lithium intercalation induced stress in capacity fade of lithium-ion batteries studied extensively by [104]. Mechanical properties of the current collector have shown great influence on delamination behavior at the electrode/current collector interface [105]. We studied the influence of cohesive zone model on the electrochemical performance of SSLIBs. The main characteristics of the cohesive zone model in our LIB framework are explored in this section. The mechanical responses at the interface between electrolyte, $\bar{\Omega}^l$, and electrode, $\bar{\Omega}^s$, considering contact relations pertinent to the interface phenomena are illustrated in Figure 2.3. Here we introduce superscript p to represent either of phases electrolyte and electrode. Surface quantities $\boldsymbol{T}^p$, $\boldsymbol{n}^p$, and $\boldsymbol{t}^p$ are the traction, normal vector, and tangential vector for phase p, respectively. We define $\boldsymbol{u}^{ls}$ as the displacement jump across the interface. The mechanical response at the interface depends on the traction and relative displacement across the interface. For any given point on the

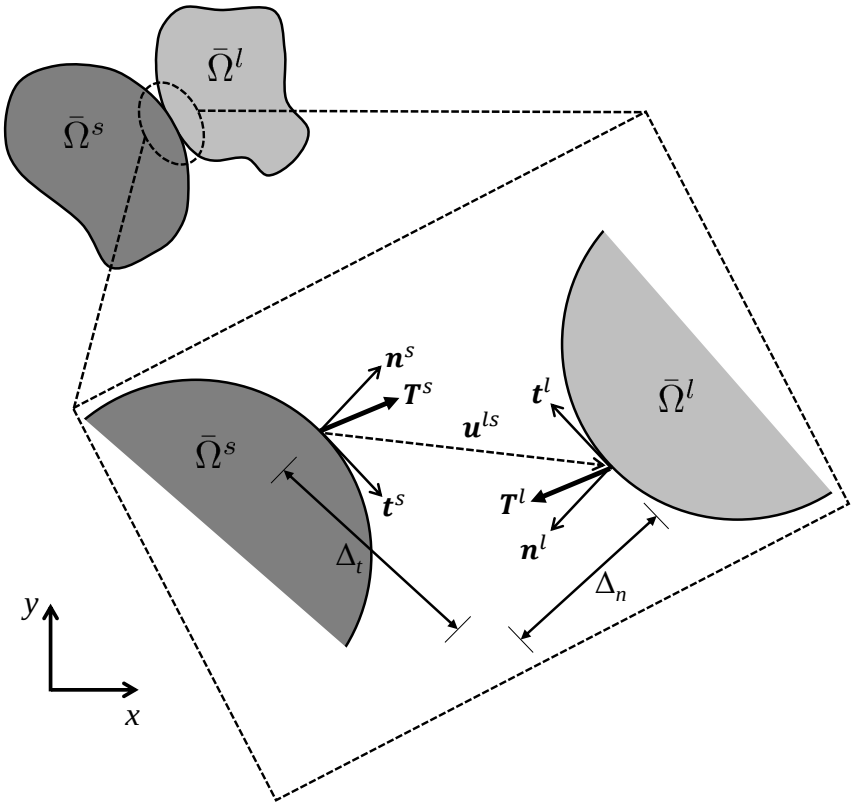

Figure 2.3: Schematic of two bodies in contact with cohesive interface.

interface, the normal and tangential traction and separations are defined as:

$$\begin{aligned} \Delta_n = \boldsymbol{u}^{ls} \cdot \boldsymbol{n}^s, \qquad \Delta_t = \boldsymbol{u}^{ls} \cdot \boldsymbol{t}^s, \qquad \boldsymbol{n}^s = -\boldsymbol{n}^l, \qquad \boldsymbol{t}^s = -\boldsymbol{t}^l \ , \\ \tilde{T}_n = \boldsymbol{T}^s \cdot \boldsymbol{n}^s = -\boldsymbol{T}^l \cdot \boldsymbol{n}^s, \qquad \tilde{T}_t = \boldsymbol{T}^s \cdot \boldsymbol{t}^s = -\boldsymbol{T}^l \cdot \boldsymbol{t}^s \ , \end{aligned} \tag{2.109}$$

where Δ_n is the normal separation, Δ_t is the tangential separation, $\tilde{T}_n$ is the magnitude of normal traction, and $\tilde{T}_t$ is the magnitude of tangential traction. The relationship between surface traction and relative displacement are illustrated in Figure 2.4. The variables δ_{c}^n, δ_{c}^t, δ_{f}^n, and δ_{f}^t represent the critical normal separation, the critical tangential separation, the normal separation at which the normal traction vanishes, and the tangential separation at which the tangential traction vanishes, respectively. In our uncoupled bilinear cohesive zone law three distinct regions are defined. The bonded zone refers to the linear elastic region where $\Delta_n \leq \delta_{\mathrm{c}}^n$ and $\Delta_t \leq \delta_{\mathrm{c}}^t$. The reduced zone is defined as the region where $\delta_{\mathrm{c}}^n \leq \Delta_n \leq \delta_{\mathrm{f}}^n$ and $\delta_{\mathrm{c}}^t \leq \Delta_t \leq \delta_{\mathrm{f}}^t$. Finally, the debonded zone refers to

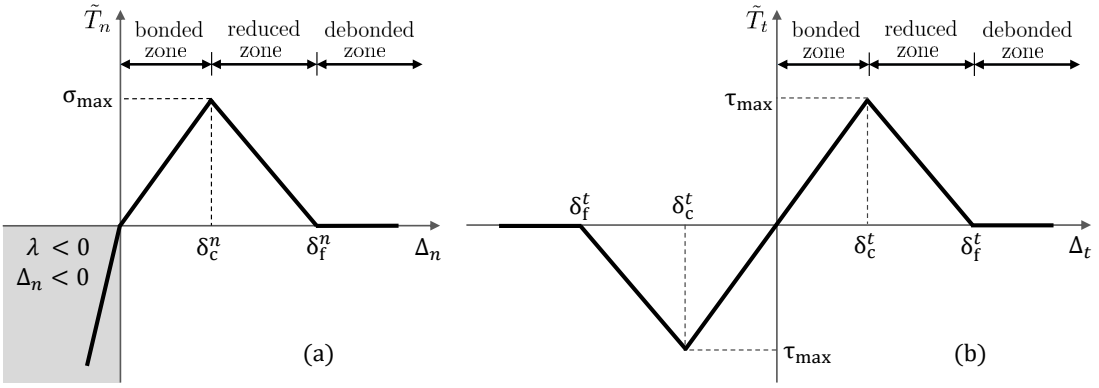

Figure 2.4: Uncoupled bilinear cohesive zone law, (a) normal response, (b) tangential response.

the region in which cohesion has vanished, i.e. $\Delta_n \geq \delta_{\mathrm{f}}^n$ and $\Delta_t \geq \delta_{\mathrm{f}}^t$.

Departing from the frequently used penalty method to prevent surface penetration, the compressive region depicted in the lower left quadrant of Figure 2.4(a) is handled separately by a stabilized Lagrange formulation. This mitigates ill-conditioning and accuracy issues that can arise with the use of penalty methods. During separation, the magnitude of normal and shear traction at the interface increases linearly to a prescribed maximum value, then falls to zero when separation has surpassed the cohesion limit. The governing equations for bilinear cohesion are defined as follows:

$$\tilde{T}_n(\Delta_n, \lambda) = \begin{cases} \lambda & \text{if } \lambda \leq 0 \\ \frac{\sigma_{\max}}{\delta_{\mathrm{c}}^n} \Delta_n & \text{if } 0 \leq \Delta_n \leq \delta_{\mathrm{c}}^n \\ \frac{\sigma_{\max}(\delta_{\mathrm{f}}^n - \Delta_n)}{\delta_{\mathrm{f}}^n - \delta_{\mathrm{c}}^n} & \text{if } \delta_{\mathrm{c}}^n < \Delta_n \leq \delta_{\mathrm{f}}^n \\ 0 & \text{if } \Delta_n > \delta_{\mathrm{f}}^n \end{cases}, \tag{2.110}$$

and

$$\tilde{T}_t(\Delta_t) = \begin{cases} \frac{\tau_{\max}}{\delta_{\mathrm{c}}^t} \Delta_t & \text{if } -\delta_{\mathrm{c}}^t \leq \Delta_t \leq \delta_{\mathrm{c}}^t \\ \frac{\tau_{\max}(\delta_{\mathrm{f}}^t - \Delta_t)}{\delta_{\mathrm{f}}^t - \delta_{\mathrm{c}}^t} & \text{if } \delta_{\mathrm{c}}^t < \Delta_t \leq \delta_{\mathrm{f}}^t \\ -\frac{\tau_{\max}(\delta_{\mathrm{f}}^t - \Delta_t)}{\delta_{\mathrm{f}}^t - \delta_{\mathrm{c}}^t} & \text{if } -\delta_{\mathrm{f}}^t \leq \Delta_t < -\delta_{\mathrm{c}}^t \\ 0 & \text{if } |\Delta_t| > \delta_{\mathrm{f}}^t \end{cases}, \tag{2.111}$$

where $\sigma_{\max}$ is the value of normal traction at the critical normal separation, δ_{c}^{n}; $\tau_{\max}$ is the tangential traction at the critical tangential separation, δ_{c}^{t}; λ is the Lagrange multiplier associated with the non-penetration condition. The constraint equation associated with the stabilized Lagrange multiplier is evaluated as follows:

$$\lambda - \bar{\boldsymbol{T}} \cdot \boldsymbol{n}^{s} - \gamma \Delta_{n} = 0 \ , \tag{2.112}$$

with

$$\bar{\boldsymbol{T}} = \bar{\boldsymbol{\sigma}} \cdot \boldsymbol{n}^{s}, \qquad \bar{\boldsymbol{\sigma}} = \omega^{s} \boldsymbol{\sigma}_{s} + \omega^{l} \boldsymbol{\sigma}_{l} \ , \tag{2.113}$$

where γ is a penalty factor. The penalty factor discourages penetration during the early stages of convergence but becomes insignificant as equilibrium is achieved and the relative normal separation goes to zero, i.e. $\Delta_{n} \approx 0$. The weighting factors, ω^{p}, are such that $\omega^{s} + \omega^{l} = 1$; in this work we assume that $\omega^{s} = \omega^{l} = 0.5$. The stabilized Lagrange multiplier for the contact non-penetration condition described in Equation (2.112) is approximated as being element-wise constant. The Lagrange multipliers are condensed out locally to determine the structural response.

Chapter 3

Numerical Modeling

3.1 Non-dimensionalization

In most of LIB cells the distance between two current collectors is significantly smaller than the in-plane dimensions of the cell. In order to obtain a well-posed numerical problem in two or three dimensions, a non-dimensionalization approach is considered. In this section, a variable denoted by $(\tilde{\bullet})$ indicates a non-dimensional variable. The non-dimensional degrees of freedom and differential operators are defined as follows:

$$\begin{aligned} \tilde{\boldsymbol{u}} = \frac{\boldsymbol{u}}{L_{\text{ref}}}, \quad \tilde{t} = \frac{D_{\text{ref}}}{L_{\text{ref}}^2} t, \quad \tilde{c}_l = \frac{c_l}{c_{l_{\text{ref}}}}, \quad \tilde{c}_s = \frac{c_s}{c_{s_{\text{ref}}}}, \\ \tilde{\phi}_l = \frac{\phi_l}{\phi_{\text{ref}}}, \quad \tilde{\phi}_s = \frac{\phi_s}{\phi_{\text{ref}}}, \quad \tilde{E} = \frac{E}{E_{\text{ref}}}, \quad \tilde{\nabla} = L_{\text{ref}} \nabla, \end{aligned} \tag{3.1}$$

where L_{ref} is the reference length, D_{ref} is the reference diffusion coefficient, $c_{l_{\text{ref}}}$ is the electrolyte reference concentration, $c_{s_{\text{ref}}}$ is the electrode reference concentration, ϕ_{ref} is the reference electric potential, and E_{ref} is the reference Young's modulus. This leads to the following non-dimensional system of equations. The diffusion of the electrolyte, the electric potential, and the balance of linear momentum in the electrolyte are described as follows:

$$\gamma \frac{\partial \tilde{c}_l}{\partial \tilde{t}} + \tilde{\nabla} . \tilde{\mathbf{J}}_l - \tilde{h}_r = 0, \tag{3.2}$$

$$\tilde{\nabla} \cdot \tilde{\mathbf{i}}_l = 0, \tag{3.3}$$

$$\tilde{\nabla} \cdot \tilde{\boldsymbol{\sigma}}_l + \tilde{\boldsymbol{b}}_l = \mathbf{0}, \tag{3.4}$$

where

$$\gamma = \frac{c_{l_{\text{ref}}}}{c_{s_{\text{ref}}}}, \qquad \tilde{\boldsymbol{\sigma}}_l = \frac{\boldsymbol{\sigma}_l}{E_{\text{ref}}}, \qquad \tilde{\boldsymbol{b}}_l = \frac{L_{\text{ref}}}{E_{\text{ref}}}\boldsymbol{b}_l, \tag{3.5}$$

$$\tilde{\mathbf{J}}_l = \frac{2z_-\tilde{D}_+\tilde{D}_-}{z_+\tilde{D}_+ - z_-\tilde{D}_-}\left(\tilde{\nabla}\tilde{c}_l - \frac{E_{\text{ref}}}{c_{l_{\text{ref}}}}\frac{\tilde{\Omega}_l\tilde{c}_l}{RT}\tilde{\nabla}\tilde{\sigma}_h\right), \quad \tilde{D}_{+/-} = \frac{c_{l_{\text{ref}}}}{c_{s_{\text{ref}}}D_{\text{ref}}}D_{+/-}, \tag{3.6}$$

$$\tilde{h}_r = \tilde{k}_d\left(\tilde{c}_{l_{max}} - \tilde{c}_l\right) - \tilde{k}_r\tilde{c}_l^2, \tag{3.7}$$

$$\tilde{k}_r = \frac{L_{\text{ref}}^2 c_{l_{\text{ref}}}}{D_{\text{ref}}}k_r, \qquad \tilde{k}_d = \tilde{k}_r\tilde{c}_{l_{max}}\frac{\xi_{c_l}^2}{1-\xi_{c_l}}, \tag{3.8}$$

$$\tilde{\mathbf{i}}_l = -(z_+\tilde{D}_+ + z_-\tilde{D}_-)\tilde{\nabla}\tilde{c}_l - z_+\tilde{c}_l(z_+\tilde{D}_+ - z_-\tilde{D}_-)\tilde{\nabla}\tilde{\phi}_l. \tag{3.9}$$

In a similar manner, the diffusion of electrode, the electric potential, and the balance of linear momentum in the electrode are described as follows:

$$\frac{\partial\tilde{c}_s}{\partial\tilde{t}} + \tilde{\nabla}.\tilde{\mathbf{J}}_s = 0, \tag{3.10}$$

$$\tilde{\nabla}\cdot\tilde{\mathbf{i}}_s = 0, \tag{3.11}$$

$$\tilde{\nabla}\cdot\tilde{\boldsymbol{\sigma}}_s + \tilde{\boldsymbol{b}}_s = \mathbf{0}, \tag{3.12}$$

where

$$\tilde{\mathbf{J}}_s = -\tilde{D}_s\left(\tilde{\nabla}\tilde{c}_s - \frac{E_{\text{ref}}}{c_{s_{\text{ref}}}}\frac{\tilde{\Omega}_s\tilde{c}_s}{RT}\tilde{\nabla}\tilde{\sigma}_h\right), \qquad \tilde{D}_s = \frac{D_s}{D_{\text{ref}}}, \tag{3.13}$$

$$\tilde{\mathbf{i}}_s = -\tilde{\lambda}\tilde{\nabla}\tilde{\phi}_s, \qquad \tilde{\lambda} = \frac{\phi_{\text{ref}}}{D_{\text{ref}}c_{s_{\text{ref}}}F}\lambda, \tag{3.14}$$

$$\tilde{\boldsymbol{\sigma}}_s = \frac{\boldsymbol{\sigma}_s}{E_{\text{ref}}}, \qquad \tilde{\boldsymbol{b}}_s = \frac{L_{\text{ref}}}{E_{\text{ref}}} \boldsymbol{b}_s, \tag{3.15}$$

The detailed derivations of non-dimensionalization are presented in Appendix D.

3.2 Finite element analysis

3.2.1 Strong and weak forms

In this section, the weak form based upon the strong form of the governing equations for the full resolution model is presented. The standard Galerkin's finite element method is adopted to seek approximate solutions for the weak form of governing equations. The displacement, $\boldsymbol{u}$, the electrolyte concentration, c_l, the electric potential in the electrolyte, ϕ_l, the electrode concentration, c_s, the electric potential in the electrode, ϕ_s, the hydrostatic stress, σ_h, and the non-local equivalent strain, $\bar{\boldsymbol{\varepsilon}}_{\text{eq}}$, are selected as independent state variables, see Figure 3.1. The governing equations used in this section are presented in Chapter 2.

Find $\boldsymbol{u}(\boldsymbol{x},t) \in \mathscr{L}^u$, $c_l(\boldsymbol{x},t) \in \mathscr{L}^{c_l}$, $\phi_l(\boldsymbol{x},t) \in \mathscr{L}^{\phi_l}$, $c_s(\boldsymbol{x},t) \in \mathscr{L}^{c_s}$, $\phi_s(\boldsymbol{x},t) \in \mathscr{L}^{\phi_s}$, $\sigma_h(\boldsymbol{x},t) \in \mathscr{L}^{\sigma_h}$, $\bar{\boldsymbol{\varepsilon}}_{\text{eq}}(\boldsymbol{x},t) \in \mathscr{L}^{\bar{\boldsymbol{\varepsilon}}_{\text{eq}}}$ such that:

For the electrolyte phase:

$$
\begin{cases}
\dfrac{\partial c_l}{\partial t} + \nabla \cdot \mathbf{J}_l - h_r = 0 & \in \bar{\Omega}^l \\
\mathbf{J}_l \cdot \boldsymbol{n}_{bv}^{la} = -\dfrac{D_-}{F(D_+ + D_-)} j_{bv}^{la} & \in \Gamma_{bv}^{la} \\
\mathbf{J}_l \cdot \boldsymbol{n}_{bv}^{lc} = -\dfrac{D_-}{F(D_+ + D_-)} j_{bv}^{lc} & \in \Gamma_{bv}^{lc} \\
\nabla \cdot \mathbf{i}_l = 0 & \in \bar{\Omega}^l \\
\mathbf{i}_l \cdot \boldsymbol{n}_I^{la} = -j_{bv}^{la} & \in \Gamma_{bv}^{la} \\
\mathbf{i}_l \cdot \boldsymbol{n}_I^{lc} = -j_{bv}^{lc} & \in \Gamma_{bv}^{lc} \\
\nabla \cdot \boldsymbol{\sigma}_l + \boldsymbol{b}_l = \mathbf{0} & \in \bar{\Omega}^l \\
\boldsymbol{u} = \bar{\boldsymbol{u}}_l & \in \Gamma_u^{la} \\
\boldsymbol{\sigma}_l \cdot \boldsymbol{n}_t^l = \bar{\boldsymbol{t}}_l & \in \Gamma_t^{la} \\
\sigma_h - \dfrac{1}{3}\text{tr}(\boldsymbol{\sigma}_l) = 0 & \in \bar{\Omega}^l
\end{cases}, \tag{3.16}
$$

and for the electrode phase:

$$
\begin{cases}
\dfrac{\partial c_s}{\partial t} + \nabla \cdot \mathbf{J}_s = 0 & \in \bar{\Omega}^s \\
\mathbf{J}_s \cdot \boldsymbol{n}_{bv}^{lc} = \dfrac{1}{F} j_{bv}^{lc} & \in \Gamma_{bv}^{lc} \\
\nabla \cdot \mathbf{i}_s = 0 & \in \bar{\Omega}^s \\
\mathbf{i}_s \cdot \boldsymbol{n}_I^{cc} = \mathbf{I}_{\text{ext}} & \in \Gamma_I^{cc} \\
\mathbf{i}_s \cdot \boldsymbol{n}_{bv}^{lc} = j_{bv}^{lc} & \in \Gamma_{bv}^{lc} \\
\nabla \cdot \boldsymbol{\sigma}_s + \boldsymbol{b}_s = \mathbf{0} & \in \bar{\Omega}^s \\
\boldsymbol{u} = \bar{\boldsymbol{u}}_s & \in \Gamma_u^{cc} \\
\boldsymbol{\sigma}_s \cdot \boldsymbol{n}_t^s = \bar{\boldsymbol{t}}_s & \in \Gamma_t^{cc} \\
\sigma_h - \dfrac{1}{3}\text{tr}(\boldsymbol{\sigma}_s) = 0 & \in \bar{\Omega}^s \\
\bar{\boldsymbol{\varepsilon}}_{\text{eq}} - c\nabla^2 \bar{\boldsymbol{\varepsilon}}_{\text{eq}} - \boldsymbol{\varepsilon}_{\text{eq}} = 0 & \in \bar{\Omega}^s
\end{cases}, \tag{3.17}
$$

where $\mathscr{L}^u$, $\mathscr{L}^{c_l}$, $\mathscr{L}^{\phi_l}$, $\mathscr{L}^{c_s}$, $\mathscr{L}^{\phi_s}$, $\mathscr{L}^{\sigma_h}$, $\mathscr{L}^{\bar{\boldsymbol{\varepsilon}}_{\text{eq}}}$ are the trial solution spaces defined as follows:

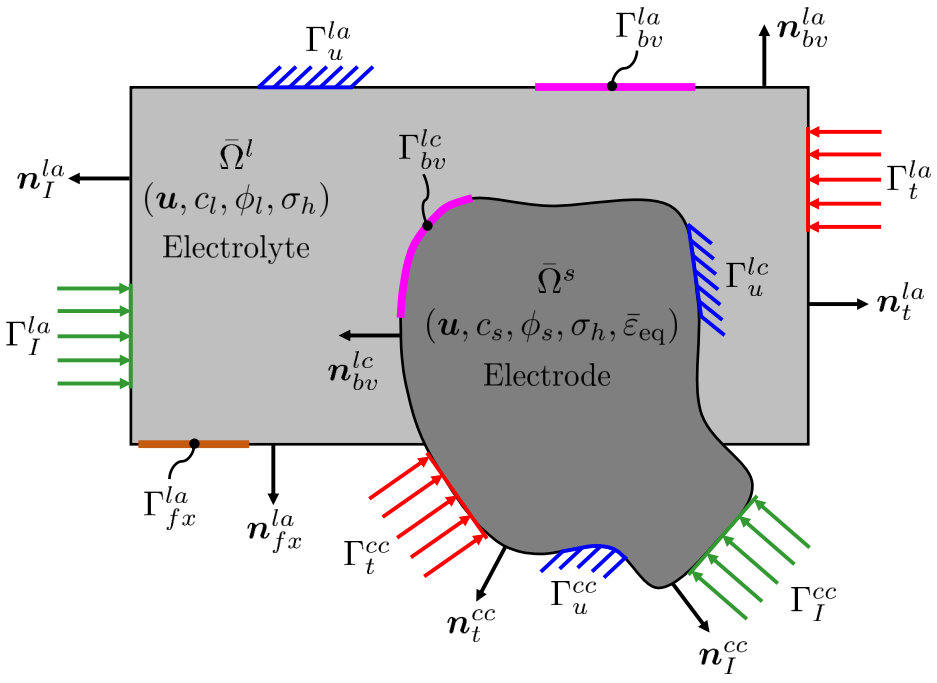

Figure 3.1: Schematic of two-phase solid-state lithium-ion battery with boundary conditions.

$$
\begin{aligned}
\mathscr{L}^{u} &= \left\{u_i \colon \bar{\Omega}^p \times [0,T] \mapsto \mathbb{R}^n, u_i \in H^1, u_i(t) = \bar{u}_i(t) \text{ on } \Gamma_u^p, u_i(\boldsymbol{x},0) = u_{i_0}(\boldsymbol{x})\right\}, \\
\mathscr{L}^{c_p} &= \left\{c_p \colon \bar{\Omega}^p \times [0,T] \mapsto \mathbb{R}^n, c_p \in H^1, c_p(\boldsymbol{x},0) = c_{p_0}(\boldsymbol{x})\right\}, \\
\mathscr{L}^{\phi_p} &= \left\{\phi_p \colon \bar{\Omega}^p \times [0,T] \mapsto \mathbb{R}^n, \phi_p \in H^1, \phi_p(\boldsymbol{x},0) = \phi_{p_0}(\boldsymbol{x})\right\}, \\
\mathscr{L}^{\sigma_h} &= \left\{\sigma_h \colon \bar{\Omega}^p \times [0,T] \mapsto \mathbb{R}^n, \sigma_h \in H^1, \sigma_h(\boldsymbol{x},0) = \sigma_{h_0}(\boldsymbol{x})\right\}, \\
\mathscr{L}^{\bar{\boldsymbol{\varepsilon}}_{\mathrm{eq}}} &= \left\{\bar{\boldsymbol{\varepsilon}}_{\mathrm{eq}} \colon \bar{\Omega}^p \times [0,T] \mapsto \mathbb{R}^n, \bar{\boldsymbol{\varepsilon}}_{\mathrm{eq}} \in H^1, \bar{\boldsymbol{\varepsilon}}_{\mathrm{eq}}(\boldsymbol{x},0) = \bar{\boldsymbol{\varepsilon}}_{\mathrm{eq}_0}(\boldsymbol{x})\right\},
\end{aligned}
\tag{3.18}
$$

where $\boldsymbol{x}$ is the vector of coordinates, $\bar{\Omega}^p$ is the volume occupied by phase p, which represents either electrolyte, l, or electrode, s, and Γ^p is the boundary of the phase p; Γ_{bv}^{la} is the BV boundary at the anode/electrolyte interface, Γ_I^{la} is the applied external current boundary at the anode/electrolyte interface, Γ_u^{la} is the boundary at anode/electrolyte interface where the displacement is prescribed, Γ_t^{la} is the boundary at anode/electrolyte interface where the traction is prescribed, Γ_{fx}^{la} is the flux boundary at anode/electrolyte interface. In addition, Γ_{bv}^{lc} is the BV boundary at the cathode/electrolyte interface, Γ_u^{lc} is the prescribed displacement boundary at cathode/electrolyte interface, Γ_t^{cc} is the traction boundary at cathode/current collectors interface, Γ_u^{cc} is the prescribed displacement boundary at cathode/current collector interface, and Γ_I^{cc} is the applied external current boundary at the cathode/current collector interface. In the above mentioned solution spaces, u_{i_0} is the initial displacement vector, c_{p_0} is the initial concentration, ϕ_{p_0} is the initial electric potential, and σ_{h_0} is the initial hydrostatic stress, $\bar{\boldsymbol{\varepsilon}}_{\mathrm{eq}_0}$ is the initial non-local equivalent strain in phase p. $\mathbb{R}^n$ is the linear space and H^1 is the first Sobolev space [71].

In order to define the variational or the weak form of the strong form of the governing equations, proper weighting functions of independent state variables need to be defined as follows:

$$
\begin{aligned}
\boldsymbol{w}_u(\boldsymbol{x},t) &= \delta\boldsymbol{u}(\boldsymbol{x},t),\\
w_{c_l}(\boldsymbol{x},t) &= \delta c_l(\boldsymbol{x},t),\\
w_{\phi_l}(\boldsymbol{x},t) &= \delta\phi_l(\boldsymbol{x},t),\\
w_{c_s}(\boldsymbol{x},t) &= \delta c_s(\boldsymbol{x},t),\\
w_{\phi_s}(\boldsymbol{x},t) &= \delta\phi_s(\boldsymbol{x},t),\\
w_{\sigma_h}(\boldsymbol{x},t) &= \delta\sigma_h(\boldsymbol{x},t),\\
w_{\bar{\boldsymbol{\varepsilon}}_{\mathrm{eq}}}(\boldsymbol{x},t) &= \delta\bar{\boldsymbol{\varepsilon}}_{\mathrm{eq}}(\boldsymbol{x},t),
\end{aligned}
\tag{3.19}
$$

where $\boldsymbol{w}_u \in \mathscr{V}^u$, $w_{c_l} \in \mathscr{V}^{c_l}$, $w_{\phi_l} \in \mathscr{V}^{\phi_l}$, $w_{c_s} \in \mathscr{V}^{c_s}$, $w_{\phi_s} \in \mathscr{V}^{\phi_s}$, $w_{\sigma_h} \in \mathscr{V}^{\sigma_h}$, $w_{\bar{\boldsymbol{\varepsilon}}_{\mathrm{eq}}} \in \mathscr{V}^{\bar{\boldsymbol{\varepsilon}}_{\mathrm{eq}}}$ such that:

$$
\begin{aligned}
\mathscr{V}^u &= \left\{ w_i^u \colon \bar{\Omega}^p \times [0,T] \mapsto \mathbb{R}^n, w_i^u \in H^1, w_i^u = 0 \text{ on } \Gamma_u^p \right\},\\
\mathscr{V}^{c_l} &= \left\{ w_{c_l} \colon \bar{\Omega}^l \times [0,T] \mapsto \mathbb{R}^n, w_{c_l} \in H^1 \right\},\\
\mathscr{V}^{\phi_l} &= \left\{ w_{\phi_l} \colon \bar{\Omega}^l \times [0,T] \mapsto \mathbb{R}^n, w_{\phi_l} \in H^1 \right\},\\
\mathscr{V}^{c_s} &= \left\{ w_{c_s} \colon \bar{\Omega}^s \times [0,T] \mapsto \mathbb{R}^n, w_{c_s} \in H^1 \right\},\\
\mathscr{V}^{\phi_s} &= \left\{ w_{\phi_s} \colon \bar{\Omega}^s \times [0,T] \mapsto \mathbb{R}^n, w_{\phi_s} \in H^1 \right\},\\
\mathscr{V}^{\sigma_h} &= \left\{ w_{\sigma_h} \colon \bar{\Omega}^p \times [0,T] \mapsto \mathbb{R}^n, w_{\sigma_h} \in H^1 \right\},\\
\mathscr{V}^{\bar{\boldsymbol{\varepsilon}}_{\mathrm{eq}}} &= \left\{ w_{\bar{\boldsymbol{\varepsilon}}_{\mathrm{eq}}} \colon \bar{\Omega}^p \times [0,T] \mapsto \mathbb{R}^n, w_{\bar{\boldsymbol{\varepsilon}}_{\mathrm{eq}}} \in H^1 \right\},
\end{aligned}
\tag{3.20}
$$

The weak form of the diffusion and migration of Li^+ in the electrolyte is described by:

$$
\begin{aligned}
\mathbf{R}_{c_l} \colon & \int_{\bar{\Omega}^l} w_{c_l} \left(\frac{\partial c_l}{\partial t} + \nabla . \mathbf{J}_l - h_r \right) dv\\
= & \int_{\bar{\Omega}^l} w_{c_l} \frac{\partial c_l}{\partial t} dv + \int_{\bar{\Omega}^l} w_{c_l} \nabla \cdot \mathbf{J}_l dv - \int_{\bar{\Omega}^l} w_{c_l} \cdot h_r dv = 0.
\end{aligned}
\tag{3.21}
$$

The chain rule and the DT imply that:

$$
\begin{aligned}
\int_{\bar{\Omega}^l} w_{c_l} \nabla \cdot \mathbf{J}_l dv &= \int_{\bar{\Omega}^l} \nabla \cdot (w_{c_l} \mathbf{J}_l) dv - \int_{\bar{\Omega}^l} \nabla w_{c_l} \cdot \mathbf{J}_l dv\\
&= \int_{\Gamma^l} w_{c_l} \mathbf{J}_l \cdot \boldsymbol{n}^l ds - \int_{\bar{\Omega}^l} \nabla w_{c_l} \cdot \mathbf{J}_l dv.
\end{aligned}
\tag{3.22}
$$

Substituting Equation (3.22) into (3.21) results in:

$$
\mathbf{R}_{c_l} \colon \int_{\bar{\Omega}^l} w_{c_l} \frac{\partial c_l}{\partial t} dv - \int_{\bar{\Omega}^l} \nabla w_{c_l} \cdot \mathbf{J}_l dv - \int_{\bar{\Omega}^l} w_{c_l} \cdot h_r dv + \int_{\Gamma^l} w_{c_l} \mathbf{J}_l \cdot \boldsymbol{n}^l ds = 0. \tag{3.23}
$$

Similar to the balance of mass for the electrolyte, the weak form of the diffusion of Li^+ in the electrode active materials is described by:

$$\mathbf{R}_{c_s}: \int_{\bar{\Omega}^s} w_{c_s} \frac{\partial c_s}{\partial t} dv - \int_{\bar{\Omega}^s} \nabla w_{c_s} \cdot \mathbf{J}_s dv + \int_{\Gamma^s} w_{c_s} \mathbf{J}_s \cdot \boldsymbol{n}^s ds = 0. \tag{3.24}$$

The electrolyte electric potential is governed by the Ohm's law and the weak form is given by:

$$\mathbf{R}_{\phi_l}: \int_{\bar{\Omega}^l} w_{\phi_l} \nabla \cdot \mathbf{i}_l dv = 0. \tag{3.25}$$

Applying the chain rule and the DT give:

$$\begin{aligned} \int_{\bar{\Omega}^l} w_{\phi_l} \nabla \cdot \mathbf{i}_l dv &= \int_{\bar{\Omega}^l} \nabla \cdot (w_{\phi_l} \mathbf{i}_l) dv - \int_{\bar{\Omega}^l} \nabla w_{\phi_l} \cdot \mathbf{i}_l dv \\ &= \int_{\Gamma^l} w_{\phi_l} \mathbf{i}_l \cdot \boldsymbol{n}^l ds - \int_{\bar{\Omega}^l} \nabla w_{\phi_l} \cdot \mathbf{i}_l dv. \end{aligned} \tag{3.26}$$

Finally, Equation (3.25) is rewritten as follows:

$$\mathbf{R}_{\phi_l}: -\int_{\bar{\Omega}^l} \nabla w_{\phi_l} \cdot \mathbf{i}_l dv + \int_{\Gamma^l} w_{\phi_l} \mathbf{i}_l \cdot \boldsymbol{n}^l ds = 0, \tag{3.27}$$

and the weak form of the electrode electric potential, governed by the Ohm's law, is defined in the similar fashion as follows:

$$\mathbf{R}_{\phi_s}: -\int_{\bar{\Omega}^s} \nabla w_{\phi_s} \cdot \mathbf{i}_s dv + \int_{\Gamma^s} w_{\phi_s} \mathbf{i}_s \cdot \boldsymbol{n}^s ds = 0. \tag{3.28}$$

The weak form for the balance of linear momentum in the electrolyte is defined by:

$$\mathbf{R}_u: \int_{\bar{\Omega}^l} \boldsymbol{w}_u (\nabla \cdot \boldsymbol{\sigma}_l + \boldsymbol{b}_l) dv = 0. \tag{3.29}$$

By applying the chain rule and the DT:

$$\begin{aligned} \int_{\bar{\Omega}^l} \boldsymbol{w}_u \nabla \cdot \boldsymbol{\sigma}_l dv &= \int_{\bar{\Omega}^l} \nabla \cdot (\boldsymbol{w}_u \boldsymbol{\sigma}_l) dv - \int_{\bar{\Omega}^l} \nabla \boldsymbol{w}_u \cdot \boldsymbol{\sigma}_l dv \\ &= \int_{\Gamma^l} \boldsymbol{w}_u \boldsymbol{\sigma}_l \cdot \boldsymbol{n}^l ds - \int_{\bar{\Omega}^l} \nabla \boldsymbol{w}_u \cdot \boldsymbol{\sigma}_l dv. \end{aligned} \tag{3.30}$$

Finally, Equation (3.29) is rewritten as follows:

$$\mathbf{R}_u: \int_{\bar{\Omega}^l} \nabla \boldsymbol{w}_u \cdot \boldsymbol{\sigma}_l dv - \int_{\bar{\Omega}^l} \boldsymbol{w}_u \cdot \boldsymbol{b}_l dv - \int_{\Gamma^l} \boldsymbol{w}_u \boldsymbol{\sigma}_l \cdot \boldsymbol{n}^l ds = 0, \tag{3.31}$$

and in the electrode:

$$\mathbf{R}_u : \int_{\bar{\Omega}^s} \nabla \boldsymbol{w}_u \cdot \boldsymbol{\sigma}_s dv - \int_{\bar{\Omega}^s} \boldsymbol{w}_u \cdot \boldsymbol{b}_s dv - \int_{\Gamma^s} \boldsymbol{w}_u \boldsymbol{\sigma}_s \cdot \boldsymbol{n}^s ds = 0. \tag{3.32}$$

The weak form of the hydrostatic stress in the electrolyte is described by:

$$\begin{aligned} \mathbf{R}_{\sigma_h} : & \int_{\bar{\Omega}^l} w_{\sigma_h} \left(\sigma_h - \frac{1}{3} \mathrm{tr}(\boldsymbol{\sigma}_l) \right) dv \\ = & \int_{\bar{\Omega}^l} w_{\sigma_h} \sigma_h dv - \int_{\bar{\Omega}^l} \frac{1}{3} w_{\sigma_h} \mathrm{tr}(\boldsymbol{\sigma}_l) dv = 0, \end{aligned} \tag{3.33}$$

Similarly, the weak form of the hydrostatic stress in the electrode is described by:

$$\begin{aligned} \mathbf{R}_{\sigma_h} : & \int_{\bar{\Omega}^s} w_{\sigma_h} \left(\sigma_h - \frac{1}{3} \mathrm{tr}(\boldsymbol{\sigma}_s) \right) dv \\ = & \int_{\bar{\Omega}^s} w_{\sigma_h} \sigma_h dv - \int_{\bar{\Omega}^s} \frac{1}{3} w_{\sigma_h} \mathrm{tr}(\boldsymbol{\sigma}_s) dv = 0. \end{aligned} \tag{3.34}$$

Finally the weak form of the Helmholtz-type differential equation for the non-local damage evolution is defined as:

$$\mathbf{R}_{\bar{\boldsymbol{\varepsilon}}_{\mathrm{eq}}} : \int_{\bar{\Omega}^s} w_{\bar{\boldsymbol{\varepsilon}}_{\mathrm{eq}}} (\bar{\boldsymbol{\varepsilon}}_{\mathrm{eq}} - c \nabla^2 \bar{\boldsymbol{\varepsilon}}_{\mathrm{eq}} - \boldsymbol{\varepsilon}_{\mathrm{eq}}) dv = 0. \tag{3.35}$$

By applying the chain rule and the DT:

$$\begin{aligned} \int_{\bar{\Omega}^s} w_{\bar{\boldsymbol{\varepsilon}}_{\mathrm{eq}}} \cdot c \nabla^2 \bar{\boldsymbol{\varepsilon}}_{\mathrm{eq}} dv = & \int_{\bar{\Omega}^s} \nabla (w_{\bar{\boldsymbol{\varepsilon}}_{\mathrm{eq}}} \cdot c \nabla \bar{\boldsymbol{\varepsilon}}_{\mathrm{eq}}) dv - \int_{\bar{\Omega}^s} \nabla w_{\bar{\boldsymbol{\varepsilon}}_{\mathrm{eq}}} \cdot c \nabla \bar{\boldsymbol{\varepsilon}}_{\mathrm{eq}} dv \\ & \int_{\Gamma^s} w_{\bar{\boldsymbol{\varepsilon}}_{\mathrm{eq}}} \cdot c \nabla \bar{\boldsymbol{\varepsilon}}_{\mathrm{eq}} \cdot \boldsymbol{n}^s ds - \int_{\bar{\Omega}^s} \nabla w_{\bar{\boldsymbol{\varepsilon}}_{\mathrm{eq}}} \cdot c \nabla \bar{\boldsymbol{\varepsilon}}_{\mathrm{eq}} dv \\ & = - \int_{\bar{\Omega}^s} \nabla w_{\bar{\boldsymbol{\varepsilon}}_{\mathrm{eq}}} \cdot c \nabla \bar{\boldsymbol{\varepsilon}}_{\mathrm{eq}} dv. \end{aligned} \tag{3.36}$$

Therefore

$$\mathbf{R}_{\bar{\boldsymbol{\varepsilon}}_{\mathrm{eq}}} : \int_{\bar{\Omega}^s} w_{\bar{\boldsymbol{\varepsilon}}_{\mathrm{eq}}} \cdot \bar{\boldsymbol{\varepsilon}}_{\mathrm{eq}} + \int_{\bar{\Omega}^s} \nabla w_{\bar{\boldsymbol{\varepsilon}}_{\mathrm{eq}}} \cdot c \nabla \bar{\boldsymbol{\varepsilon}}_{\mathrm{eq}} dv - \int_{\bar{\Omega}^s} w_{\bar{\boldsymbol{\varepsilon}}_{\mathrm{eq}}} \cdot \boldsymbol{\varepsilon}_{\mathrm{eq}} dv = 0. \tag{3.37}$$

The derivatives of the residual equations with respect to independent state variables are presented in the Appendix A.

3.2.2 Finite element formulation

For the finite element simulation we adopt the standard Galerkin's method for the approximation of solutions in the weak form of governing equations. To this end, let's introduce $\mathscr{L}^h$ and

$\mathscr{V}^h$ for the finite dimensional approximation associated with the discretization of the domain $\bar{\Omega}$ which is parameterized by the characteristic length scale h. The domain $\bar{\Omega}^h$ is discretized into the domain $\bar{\Omega}^e$, $1 \leq e \leq n_{el}$, where n_{el} is the number of elements in the domain. The solutions are approximated by using mixed elements such that higher order element (i.e. quad-8 or hex-20) is used for the quadratic interpolation of displacement solutions and linear interpolation is used for the approximation of concentrations, electric potentials, hydrostatic stress, and non-local strain fields. Using interpolation functions, we write $\boldsymbol{u}^h$, $\boldsymbol{w}_u^h$, c_l^h, $w_{c_l}^h$, ϕ_l^h, $w_{\phi_l}^h$, c_s^h, $w_{c_s}^h$, ϕ_s^h, $w_{\phi_s}^h$, σ_h^h, $w_{\sigma_h}^h$, $\bar{\boldsymbol{\varepsilon}}_{\text{eq}}^h$, $w_{\bar{\boldsymbol{\varepsilon}}_{\text{eq}}}^h$ in natural coordinates as follows:

Displacement $\boldsymbol{u}$:

$$\boldsymbol{u}^h(\boldsymbol{\xi}, t) = \sum_{a=1}^{n_{nd}^q} N_a^{e,u}(\boldsymbol{\xi}) \hat{u}_a^e(t) = \boldsymbol{N}^{e,u} \cdot \hat{\boldsymbol{u}}^e, \tag{3.38}$$

$$\boldsymbol{w}_u^h(\boldsymbol{\xi}) = \sum_{a=1}^{n_{nd}^q} N_a^{e,u}(\boldsymbol{\xi}) (\hat{w}_u^e)_a = \boldsymbol{N}^{e,u} \cdot \hat{\boldsymbol{w}}_u^e, \tag{3.39}$$

$$\nabla \boldsymbol{w}_u^h(\boldsymbol{\xi}) = \sum_{a=1}^{n_{nd}^q} B_a^{e,u}(\boldsymbol{\xi}) (\hat{w}_u^e)_a = \boldsymbol{B}^{e,u} \cdot \hat{\boldsymbol{w}}_u^e, \tag{3.40}$$

where, $\hat{u}_a^e$ is the nodal displacements, $N_a^{e,u}$ is the associated shape functions, $B_a^{e,u}$ is the spatial derivative of the shape functions for element e, and n_{nd}^q is the number of nodes in the quadratic interpolation. The components of the vector $\hat{\boldsymbol{w}}_u^e$ correspond to the nodal values of the weighting function $\boldsymbol{w}_u^h$.

Concentration at phase $p \in [l, s]$, c_p:

$$c_p^h(\boldsymbol{\xi}, t) = \sum_{a=1}^{n_{nd}^l} N_a^{e,c_p}(\boldsymbol{\xi}) (\hat{c}_p^e)_a(t) = \boldsymbol{N}^{e,c_p} \cdot \hat{\boldsymbol{c}}_p^e, \tag{3.41}$$

$$w_{c_p}^h(\boldsymbol{\xi}) = \sum_{a=1}^{n_{nd}^l} N_a^{e,c_p}(\boldsymbol{\xi}) (\hat{w}_{c_p}^e)_a = \boldsymbol{N}^{e,c_p} \cdot \hat{\boldsymbol{w}}_{c_p}^e, \tag{3.42}$$

$$\nabla w_{c_p}^h(\boldsymbol{\xi}) = \sum_{a=1}^{n_{nd}^l} B_a^{e,c_p}(\boldsymbol{\xi})(\hat{w}_{c_p}^e)_a = \boldsymbol{B}^{e,c_p} \cdot \hat{\boldsymbol{w}}_{c_p}^e, \tag{3.43}$$

where, $(\hat{c}_p^e)_a$ is the nodal concentrations, N_a^{e,c_p} is the associated shape functions, B_a^{e,c_p} is the spatial derivatives of shape functions for element e at phase p, and n_{nd}^l is the number of nodes in the linear interpolation. The components of the vector $\hat{\boldsymbol{w}}_{c_p}^e$ correspond to the nodal values of the weighting function $w_{c_p}^h$.

Electric potential at phase p, ϕ_p:

$$\phi_p^h(\boldsymbol{\xi}, t) = \sum_{a=1}^{n_{nd}^l} N_a^{e,\phi_p}(\boldsymbol{\xi})(\hat{\phi}_p^e)_a(t) = \boldsymbol{N}^{e,\phi_p} \cdot \hat{\boldsymbol{\phi}}_p^e, \tag{3.44}$$

$$w_{\phi_p}^h(\boldsymbol{\xi}) = \sum_{a=1}^{n_{nd}^l} N_a^{e,\phi_p}(\boldsymbol{\xi})(\hat{w}_{\phi_p}^e)_a = \boldsymbol{N}^{e,\phi_p} \cdot \hat{\boldsymbol{w}}_{\phi_p}^e, \tag{3.45}$$

$$\nabla w_{\phi_p}^h(\boldsymbol{\xi}) = \sum_{a=1}^{n_{nd}^l} B_a^{e,\phi_p}(\boldsymbol{\xi})(\hat{w}_{\phi_p}^e)_a = \boldsymbol{B}^{e,\phi_p} \cdot \hat{\boldsymbol{w}}_{\phi_p}^e, \tag{3.46}$$

where, $(\hat{\phi}_p^e)_a$ is the nodal electric potential, N_a^{e,ϕ_p} is the associated shape functions, and B_a^{e,ϕ_p} is the spatial derivative of shape functions for element e at phase p. The components of the vector $\hat{\boldsymbol{w}}_{\phi_p}^e$ correspond to the nodal values of the weighting function $w_{\phi_p}^h$.

Hydrostatic stress, σ_h:

$$\sigma_h^h(\boldsymbol{\xi}, t) = \sum_{a=1}^{n_{nd}^l} N_a^{e,\sigma_h}(\boldsymbol{\xi})(\hat{\sigma}_h^e)_a(t) = \boldsymbol{N}^{e,\sigma_h} \cdot \hat{\boldsymbol{\sigma}}_h^e, \tag{3.47}$$

$$w_{\sigma_h}^h(\boldsymbol{\xi}) = \sum_{a=1}^{n_{nd}^l} N_a^{e,\sigma_h}(\boldsymbol{\xi})(\hat{w}_{\sigma_h}^e)_a = \boldsymbol{N}^{e,\sigma_h} \cdot \hat{\boldsymbol{w}}_{\sigma_h}^e, \tag{3.48}$$

where, $(\hat{\sigma}_h^e)_a$ is the nodal hydrostatic stress and N_a^{e,σ_h} is the associated shape functions for element e. The components of the vector $\hat{\boldsymbol{w}}_{\sigma_h}^e$ correspond to the nodal values of the weighting function $w_{\sigma_h}^h$.

Non-local equivalent strain, $\bar{\boldsymbol{\varepsilon}}_{\text{eq}}$:

$$\bar{\boldsymbol{\varepsilon}}^h_{\text{eq}}(\boldsymbol{\xi},t)=\sum_{a=1}^{n^l_{nd}} N_a^{e,\bar{\boldsymbol{\varepsilon}}_{\text{eq}}}(\boldsymbol{\xi})(\hat{\bar{\boldsymbol{\varepsilon}}}^e_{\text{eq}})_a(t)=\boldsymbol{N}^{e,\bar{\boldsymbol{\varepsilon}}_{\text{eq}}}\cdot\hat{\boldsymbol{\phi}}^e_p, \tag{3.49}$$

$$w^h_{\bar{\boldsymbol{\varepsilon}}_{\text{eq}}}(\boldsymbol{\xi})=\sum_{a=1}^{n^l_{nd}} N_a^{e,\bar{\boldsymbol{\varepsilon}}_{\text{eq}}}(\boldsymbol{\xi})(\hat{w}^e_{\bar{\boldsymbol{\varepsilon}}_{\text{eq}}})_a=\boldsymbol{N}^{e,\bar{\boldsymbol{\varepsilon}}_{\text{eq}}}\cdot\hat{\boldsymbol{w}}^e_{\bar{\boldsymbol{\varepsilon}}_{\text{eq}}}, \tag{3.50}$$

$$\nabla w^h_{\bar{\boldsymbol{\varepsilon}}_{\text{eq}}}(\boldsymbol{\xi})=\sum_{a=1}^{n^l_{nd}} B_a^{e,\bar{\boldsymbol{\varepsilon}}_{\text{eq}}}(\boldsymbol{\xi})(\hat{w}^e_{\bar{\boldsymbol{\varepsilon}}_{\text{eq}}})_a=\boldsymbol{B}^{e,\bar{\boldsymbol{\varepsilon}}_{\text{eq}}}\cdot\hat{\boldsymbol{w}}^e_{\bar{\boldsymbol{\varepsilon}}_{\text{eq}}}, \tag{3.51}$$

where, $(\hat{\bar{\boldsymbol{\varepsilon}}}^e_{\text{eq}})_a$ is the nodal non-local equivalent strain, $N_a^{e,\bar{\boldsymbol{\varepsilon}}_{\text{eq}}}$ is the associated shape functions, and $B_a^{e,\bar{\boldsymbol{\varepsilon}}_{\text{eq}}}$ is the spatial derivative of shape functions for element e. The components of the vector $\hat{\boldsymbol{w}}^e_{\bar{\boldsymbol{\varepsilon}}_{\text{eq}}}$ correspond to the nodal values of the weighting function $w^h_{\bar{\boldsymbol{\varepsilon}}_{\text{eq}}}$.

Considering all of these expressions, the update algorithm for the damage evolution is given be the following algorithm:

3.2.3 Time integration

We discretize our equations in time by the implicit backward Euler scheme [56]. For an ordinary differential equation using the implicit backward Euler scheme implies that:

$$\frac{d\boldsymbol{u}}{dt}=f(\boldsymbol{u},t)\Rightarrow\boldsymbol{u}(t_{n+1})=\boldsymbol{u}(t_n)+\Delta t\cdot f(\boldsymbol{u}(t_{n+1}),t_{n+1}). \tag{3.52}$$

Integrating the deferential equation from t_n to $t_{n+1}=t_n+\Delta t$ yields:

$$\begin{aligned}\int_{t_n}^{t_{n+1}}\frac{d\boldsymbol{u}}{dt}dt&=\int_{t_n}^{t_{n+1}}f(\boldsymbol{u},t)dt\\ \Rightarrow\boldsymbol{u}(t_{n+1})-\boldsymbol{u}(t_n)&=\int_{t_n}^{t_{n+1}}f(\boldsymbol{u},t)dt.\end{aligned} \tag{3.53}$$

The approximation of the right hand side integral gives:

$$\boldsymbol{u}(t_{n+1})=\boldsymbol{u}(t_n)+\Delta t\cdot f(\boldsymbol{u}(t_{n+1}),t_{n+1}). \tag{3.54}$$

Algorithm 1: Algorithm for non-local damage evolution and updating precedure.

Input: $\hat{\boldsymbol{u}}^{n+1}$, $\hat{\boldsymbol{c}}_s^{n+1}$, $\hat{\bar{\boldsymbol{\varepsilon}}}_{\text{eq}}^{n+1}$,$\kappa^n$

if $\bar{\varepsilon}_{\text{eq}}^{n+1} \leq \kappa^n$ **(no damage evolution occurs) then**

- 1) $\kappa^{n+1} = \kappa^n$
- 2) $D^{n+1} = D^n = \bar{g}(\kappa^n)$
- 3) $\boldsymbol{\sigma}_s^{n+1} = (1 - D^{n+1})(\boldsymbol{\sigma}_s^0)^{n+1}$,
  $(\boldsymbol{\sigma}_s^0)^{n+1} = \mathbb{C}_s \boldsymbol{B}^u \hat{\boldsymbol{u}}^{n+1} - K\Omega_s \boldsymbol{N}^{c_s}(\hat{\boldsymbol{c}}_s^{n+1} - \hat{\boldsymbol{c}}_s^0)\boldsymbol{I}$
- 4) $\frac{\partial \boldsymbol{\sigma}_s^{n+1}}{\partial \hat{\boldsymbol{u}}^{n+1}} = (1 - D^{n+1})\mathbb{C}_s \boldsymbol{B}^u$
- 5) $\frac{\partial \boldsymbol{\sigma}_s^{n+1}}{\partial \hat{c}_s^{n+1}} = -(1 - D^{n+1})K\Omega_s \boldsymbol{N}^{c_s}\boldsymbol{I}$
- 6) $\frac{\partial \boldsymbol{\sigma}^{n+1}}{\partial \hat{\bar{\boldsymbol{\varepsilon}}}_{\text{eq}}^{n+1}} = \boldsymbol{0}$

else

- 1) $\kappa^{n+1} = \bar{\boldsymbol{\varepsilon}}_{\text{eq}}^{n+1}$
- 2) $D^{n+1} = \bar{g}(\kappa^{n+1})$
- 3) $\boldsymbol{\sigma}_s^{n+1} = (1 - D^{n+1})(\boldsymbol{\sigma}_s^0)^{n+1}$,
  $(\boldsymbol{\sigma}_s^0)^{n+1} = \mathbb{C}_s \boldsymbol{B}^u \hat{\boldsymbol{u}}^{n+1} - K\Omega_s \boldsymbol{N}^{c_s}(\hat{\boldsymbol{c}}_s^{n+1} - \hat{\boldsymbol{c}}_s^0)\boldsymbol{I}$
- 4) $\frac{\partial \boldsymbol{\sigma}_s^{n+1}}{\partial \hat{\boldsymbol{u}}^{n+1}} = (1 - D^{n+1})\mathbb{C}_s \boldsymbol{B}^u$
- 5) $\frac{\partial \boldsymbol{\sigma}_s^{n+1}}{\partial \hat{c}_s^{n+1}} = -(1 - D^{n+1})K\Omega_s \boldsymbol{N}^{c_s}\boldsymbol{I}$
- 6) $\frac{\partial \boldsymbol{\sigma}^{n+1}}{\partial \hat{\bar{\boldsymbol{\varepsilon}}}_{\text{eq}}^{n+1}} = -\frac{\partial \bar{g}(\kappa^{n+1})}{\partial \kappa^{n+1}}(\boldsymbol{\sigma}^0)^{n+1}\boldsymbol{N}^{\bar{\boldsymbol{\varepsilon}}_{\text{eq}}}$

Unlike the explicit backward Euler scheme which is conditionally stable and needs to satisfy certain conditions, this approximation results in an unconditionally stable method. The resulting discretized governing equations are written in the following compact form:

$$\begin{aligned} \mathbf{R}_{\text{dyn}}^{n+1} &= \frac{1}{\Delta t}\mathbf{M}^{n+1}\left(\hat{\mathbf{x}}^{n+1} - \hat{\mathbf{x}}^n\right) + \mathbf{R}^{n+1}(\hat{\mathbf{x}}^{n+1}) = \mathbf{0} \\ \mathbf{J}_{\text{dyn}}^{n+1} &= \frac{1}{\Delta t}\mathbf{M}^{n+1} + \mathbf{J}^{n+1}(\hat{\mathbf{x}}^{n+1}), \end{aligned} \tag{3.55}$$

where $\mathbf{R}_{\text{dyn}}^{n+1}$ represents the residual of all governing equations, $\mathbf{M}^{n+1}$ is the capacitance matrix, $\hat{\mathbf{x}}^{n+1}$ and $\hat{\mathbf{x}}^n$ are the vector of all variables at current and previous time steps, respectively, $\mathbf{R}^{n+1}$ is vector of the residual equations, $\mathbf{J}_{\text{dyn}}^{n+1}$ is the derivative of all residual equations, and $\mathbf{J}^{n+1}$ is the Jacobian of the corresponding residual equation. Newton's method is used to solve the nonlinear

equations using analytically derived Jacobians.

3.3 eXtended Finite Element Method

During recent decades, numerical methods have been developed and emerged as appropriate tools to predict the response of engineering structures composed of multi-phase materials. With advancement in science and technology, the demand for analyzing and modeling of interface phenomena and crack in complex multi-phase structures has become a challenging task. Consequently the development of appropriate numerical tools and more efficient algorithms considering computational costs and accuracy of the solutions is quite essential. Mesh based numerical methods is one of the most important challenges in computational mechanics. Mesh updating and re-meshing for multi-phase structural systems are the main issues in these techniques and in most cases cause a high computational cost for large and complex structures.

The Level Set Method (LSM) is a promising approach for defining the geometry of the interface in multi-phase materials. In the LSM, the boundary between materials is explicitly defined by an iso-contour of the Level Set Function (LSF), ϕ, at a particular value; commonly $\phi = 0$ at the interface. The interface geometry between two distinct material phases can be described by explicit or implicit LSM. Unlike an implicit LSM, which typically solves the Hamilton-Jacobi equation (e.g. [3]), explicit LSMs define the discretized level set field as explicit functions of the nodal variables [89, 110, 150]. For more information and a review of recent developments of LSMs, the reader is referred to [141]. For geometries defined through the LSM, the mechanical model can be constructed by either a body fitted mesh, an Ersatz material approach, or immersed boundary techniques. Numerical simulation of multi-phase structural systems with interface phenomena may be carried out through different approaches, such as: the boundary element formulation [161], the element free Galerkin method [14], and the finite element formulation [158]. In standard finite element methods, a common approach is to introduce an interface element between volume elements. Remeshing may or may not be necessary depending on the magnitude of surface geometry changes in the mechanical deformation [15, 64, 72, 133]. The eXtended Finite Element Method (XFEM) has been developed to model arbitrary discontinuities in the finite element model without remeshing. Initially developed

for modeling materials with brittle and ductile fractures [94], the XFEM leverages the partition of unity concept with appropriate enrichment functions to accurately resolve solution fields along the interface [94, 95]. The XFEM is well-suited for evaluating the response of a structure whose geometry is described by a LSF. The combination of the XFEM-LSM is a promising approach for defining the geometry of the interface and approximating the solution field along the interface. The XFEM retains the sharp definition of surface geometry afforded by the LSM and provides a reliable mechanical response throughout the evolution of the design domain. The reader is referred to [53] and [75] for an introduction and general overview of the XFEM. To retain a sharp definition of the interface, we adopt the XFEM for predicting the structural response. The particular framework for integrating the explicit LSM and the generalized formulation of the XFEM used in this study are described in detail in [91] and [145].

For problems involving multi-phase materials and interface phenomena, the solution field at material boundaries are strongly discontinuous. Therefore, a Heaviside enrichment strategy is used exclusively for this work. For more information regarding different enrichment strategies, the reader is referred to [54]. The solution field, u_i, throughout the design domain is defined as follows:

$$u_i(\mathbf{x}) = \sum_{m=1}^{M} \left(H(-\phi(\mathbf{x})) \sum_{k=1}^{N_e} N_k(\mathbf{x})\ \delta_{mp}^{A,k}\ u_{i,k}^{A,m} + H(\phi(\mathbf{x})) \sum_{k=1}^{N_e} N_k(\mathbf{x})\ \delta_{mq}^{B,k}\ u_{i,k}^{B,m} \right) , \tag{3.56}$$

where the Heaviside step function is:

$$H(\phi) = \begin{cases} 1 & \text{if } \phi > 0, \\ 0 & \text{if } \phi \leq 0\ . \end{cases} \tag{3.57}$$

The shape functions are denoted as $N_i(\mathbf{x})$, M is the number of enrichment levels, N_e is the number of elemental node, $u_{i,k}^{p,m}$ is the degree of freedom of enrichment level m at node k corresponding to the solution u_i in phase p, and δ is the Kronecker delta. The Heaviside function turns on/off the interpolation functions associated with each material. For each material, multiple enrichment functions may be necessary to interpolate the solution to multiple, disconnected regions to prevent

fictitious coupling or load transferring. The Kronecker delta, $\delta_{mq}^{p,k}$, applies the active enrichment level q for node k such that the solution fields at point $\mathbf{x}$ are interpolated by only one set of degrees of freedom defined at node k, satisfying the partition of unity principle. To maintain the continuity of the solution field across the elemental boundaries, an appropriate enrichment level is chosen. The approach used in this study is adapted from [91], for more description the reader is referred to [91, 131, 134]. The XFEM allows the integration of the weak form of governing equations in an intersected element by decomposing into triangles (2D) and tetrahedrons (3D) while in non-intersected elements the solution fields are approximated by the standard finite element interpolation.

3.3.1 XFEM interface contribution - coupled cohesive zone model and stabilized Lagrange multiplier

The main contributions of the cohesive zone model in LIB were explored in Section 2.5. In this section the XFEM implementation of the coupled cohesive zone model and stabilized Lagrange multiplier for LIBs application are described in detail. In the XFEM formulation and for an intersected element, the boundary term in the weak form of governing equations is applied as the XFEM interface contribution. In this section the XFEM interface contribution associated with cohesive zone model and stabilized Lagrange multiplier considering coupling between electrochemical-mechanical phenomena are explored. The residual equation at the interface derived from the balance of linear momentum is defined as follows:

$$\mathbf{R}_u^{\Gamma^{ls}} = \int_{\Gamma^{ls}} (\boldsymbol{w}_u)_i t_i ds, \tag{3.58}$$

where $(\boldsymbol{w}_u)_i$ is the test function and t_i is the global interfacial traction which is described as a function of local traction in the following setting:

$$t_i(u_k) = R_{ji}\tilde{T}_j(\Delta_k, \lambda_k), \tag{3.59}$$

where R_{ji} is the rotation matrix and $\tilde{T}_j$ is total local traction which is a function of local interfacial separation, local Lagrange multiplier, and electrochemical concentration. The total local traction

is decomposed into the following components:

$$\tilde{T}_j(\Delta_k, \lambda_k) = \bar{T}_j(\Delta_k) + \hat{T}_j(\lambda_k), \tag{3.60}$$

where $\bar{T}_j$ is the separation associated component of the total local traction and $\hat{T}_j$ is the stabilized Lagrange multiplier associated component of the total local traction. The interfacial separation is a function of displacement jump across the interface which is defined as follows:

$$\Delta_i = R_{ip} u_p, \tag{3.61}$$

where Δ_i is the interfacial separation in local coordinate, R_{ip} is the rotation matrix and u_p is the displacement jump across the interface in global coordinate. The displacement jump is defined as follows:

$$u_p = \bar{N}_{pq} \bar{\hat{u}}_q = N^l_{pq} \hat{u}^l_q - N^s_{pq} \hat{u}^s_q, \tag{3.62}$$

where N^p_{pq} is the shape function and $\hat{u}^p_q$ is the nodal displacement for phase p, respectively. The local cohesive traction in normal and tangential directions is defined as:

$$\bar{T}_n(\Delta_n) = \begin{cases} 0 & \text{if } \Delta_n < 0 \\ \frac{\sigma_{\max}}{\delta^n_{\mathrm{c}}} \Delta_{\mathrm{n}} & \text{if } 0 \le \Delta_n \le \delta^n_{\mathrm{c}} \\ \frac{\sigma_{\max}(\delta^n_{\mathrm{f}} - \Delta_n)}{\delta^n_{\mathrm{f}} - \delta^n_{\mathrm{c}}} & \text{if } \delta^n_{\mathrm{c}} < \Delta_n \le \delta^n_{\mathrm{f}} \\ 0 & \text{if } \Delta_n > \delta^n_{\mathrm{f}} \end{cases}, \tag{3.63}$$

$$\bar{T}_t(\Delta_t) = \begin{cases} \frac{\tau_{\max}}{\delta^t_{\mathrm{c}}} \Delta_{\mathrm{t}} & \text{if } -\delta^t_{\mathrm{c}} \le \Delta_t \le \delta^t_{\mathrm{c}} \\ \frac{\tau_{\max}(\delta^t_{\mathrm{f}} - \Delta_t)}{\delta^t_{\mathrm{f}} - \delta^t_{\mathrm{c}}} & \text{if } \delta^t_{\mathrm{c}} < \Delta_t \le \delta^t_{\mathrm{f}} \\ -\frac{\tau_{\max}(\delta^t_{\mathrm{f}} - \Delta_t)}{\delta^t_{\mathrm{f}} - \delta^t_{\mathrm{c}}} & \text{if } -\delta^t_{\mathrm{f}} \le \Delta_t < -\delta^t_{\mathrm{c}} \\ 0 & \text{if } |\Delta_t| > \delta^t_{\mathrm{f}} \end{cases}, \tag{3.64}$$

and the contribution from the stabilize Lagrange multiplier during penetration is described as follows:

$$\hat{T}_n(\lambda_n) = \begin{cases} \lambda_n & \text{if } \lambda_n \le 0 \\ 0 & \text{if } \lambda_n > 0 \end{cases}, \tag{3.65}$$

$$\hat{T}_t(\lambda_t) = \begin{cases} \lambda_t & \text{if } \lambda_n \leq 0 \\ \\ 0 & \text{if } \lambda_n > 0 \end{cases}, \tag{3.66}$$

where λ_n and λ_t are the normal and tangential components of the stabilized Lagrange multiplier in the local coordinate. The stabilized Lagrange multiplier in the local coordinate is related to the global component as follows:

$$\lambda_m = R_{mi}\tilde{\lambda}_i, \tag{3.67}$$

where the stabilized Lagrange multiplier in the global coordinate is defined as follows:

$$\tilde{\lambda}_i = K_{ik}^{-1} f_k, \tag{3.68}$$

where

$$K_{ik} = \mu \int_{\Gamma^{ls}} \delta_{ik} ds,, \tag{3.69}$$

$$f_k = \mu \int_{\Gamma^{ls}} \bar{P}^{n+1} \cdot n_k ds + \gamma\mu \int_{\Gamma^{ls}} \tilde{g} \cdot n_k ds, \tag{3.70}$$

with

$$\begin{aligned} \bar{P}^{n+1} &= \bar{\sigma}_{ij}^{n+1} n_i n_j \\ \tilde{g} &= ((u_l)_i - (u_s)_i) n_i, \end{aligned} \tag{3.71}$$

where μ is the stabilized Lagrange multiplier test function and γ is the penalty factor. The derivatives of global traction with respect to displacement and concentration at phase p are described as follows:

$$\begin{aligned} \frac{\partial t_i}{\partial \hat{u}_k^p} &= R_{ji} \frac{\partial \tilde{T}_j}{\partial \Delta_m} \frac{\partial \Delta_m}{\partial \hat{u}_k^p} + R_{ji} \frac{\partial \tilde{T}_j}{\partial \lambda_m} \frac{\partial \lambda_m}{\partial \hat{u}_k^p}, \\ \frac{\partial t_i}{\partial \hat{c}_k^p} &= R_{ji} \frac{\partial \tilde{T}_j}{\partial \Delta_m} \cancelto{0}{\frac{\partial \Delta_m}{\partial \hat{c}_k^p}} + R_{ji} \frac{\partial \tilde{T}_j}{\partial \lambda_m} \frac{\partial \lambda_m}{\partial \hat{c}_k^p}, \end{aligned} \tag{3.72}$$

The local separation is a function of displacement jump across the interface, by using Equations (3.60) and (3.61) the total derivatives of the global traction with respect to displacement and

concentration at phase p are described as:

$$\begin{aligned}\frac{\partial t_i}{\partial \hat{u}_k^p} &= R_{ji}\frac{\partial \bar{T}_j}{\partial \Delta_m}\frac{\partial \Delta_m}{\partial u_p}\frac{\partial u_p}{\partial \hat{u}_k^p} + R_{ji}\frac{\partial \hat{T}_j}{\partial \lambda_m}\frac{\partial \lambda_m}{\partial \tilde{\lambda}_p}\frac{\partial \tilde{\lambda}_p}{\partial \hat{u}_k^p}, \\ &= R_{ji}\frac{\partial \bar{T}_j}{\partial \Delta_m}R_{mp}\frac{\partial u_p}{\partial \hat{u}_k^p} + R_{ji}\delta_{jm}R_{mp}\frac{\partial \tilde{\lambda}_p}{\partial \hat{u}_k^p},\end{aligned} \tag{3.73}$$

$$\frac{\partial t_i}{\partial \hat{c}_k^p} = R_{ji}\frac{\partial \hat{T}_j}{\partial \lambda_m}\frac{\partial \lambda_m}{\partial \tilde{\lambda}_p}\frac{\partial \tilde{\lambda}_p}{\partial \hat{c}_k^p} = R_{ji}\delta_{jm}R_{mp}\frac{\partial \tilde{\lambda}_p}{\partial \hat{c}_k^p}. \tag{3.74}$$

The derivatives of local traction with respect to local separations are described as follows:

$$\frac{\partial \bar{T}_n}{\partial \Delta_n} = \begin{cases} 0 & \text{if } \Delta_n < 0 \\ \frac{\sigma_{\max}}{\delta_{\mathrm{c}}^n} & \text{if } 0 \le \Delta_n \le \delta_{\mathrm{c}}^n \\ -\frac{\sigma_{\max}}{\delta_{\mathrm{f}}^n - \delta_{\mathrm{c}}^n} & \text{if } \delta_{\mathrm{c}}^n < \Delta_n \le \delta_{\mathrm{f}}^n \\ 0 & \text{if } \Delta_n > \delta_{\mathrm{f}}^n \end{cases}, \tag{3.75}$$

$$\frac{\partial \bar{T}_t}{\partial \Delta_t} = \begin{cases} \frac{\tau_{\max}}{\delta_{\mathrm{c}}^t} & \text{if } -\delta_{\mathrm{c}}^t \le \Delta_t \le \delta_{\mathrm{c}}^t \\ -\frac{\tau_{\max}}{\delta_{\mathrm{f}}^t - \delta_{\mathrm{c}}^t} & \text{if } \delta_{\mathrm{c}}^t < \Delta_t \le \delta_{\mathrm{f}}^t \\ \frac{\tau_{\max}}{\delta_{\mathrm{f}}^t - \delta_{\mathrm{c}}^t} & \text{if } -\delta_{\mathrm{f}}^t \le \Delta_t < -\delta_{\mathrm{c}}^t \\ 0 & \text{if } |\Delta_t| > \delta_{\mathrm{f}}^t \end{cases}, \tag{3.76}$$

and

$$\frac{\partial \hat{T}_n}{\partial \lambda_n} = \begin{cases} 1 & \text{if } \lambda_n \le 0 \\ 0 & \text{if } \lambda_n > 0 \end{cases}, \tag{3.77}$$

$$\frac{\partial \hat{T}_t}{\partial \lambda_t} = \begin{cases} 1 & \text{if } \lambda_n \le 0 \\ 0 & \text{if } \lambda_n > 0 \end{cases}. \tag{3.78}$$

Following Equations (3.58), (3.59), and (3.60), the residual equation can be decomposed into the contribution from local separation and the stabilized Lagrange multiplier:

$$\mathbf{R}_u^{\Gamma^{ls}} = \int_{\Gamma^{ls}} (\boldsymbol{w}_u)_i R_{ji} \bar{T}_j ds + \int_{\Gamma^{ls}} (\boldsymbol{w}_u)_i R_{ji} \hat{T}_j ds. \tag{3.79}$$

Since the rotation matrix and stabilized Lagrange multiplier are constant parameters for the entire integral, one can rewrite Equation (3.79) in the following setting:

$$\mathbf{R}_u^{\Gamma^{ls}} = \int_{\Gamma^{ls}} (\boldsymbol{w}_u)_i \bar{T}_j ds R_{ji} + \int_{\Gamma^{ls}} (\boldsymbol{w}_u)_i ds R_{ji} \hat{T}_j. \tag{3.80}$$

The derivatives of interface residual with respect to the solutions are written as follows:

$$\frac{\partial \mathbf{R}_u^{\Gamma^{ls}}}{\partial \hat{u}_k^p} = \int_{\Gamma^{ls}} (\boldsymbol{w}_u)_i \frac{\partial \bar{T}_j}{\partial \Delta_m} \frac{\partial u_p}{\partial \hat{u}_k^p} ds R_{ji} R_{mp} + \int_{\Gamma^{ls}} (\boldsymbol{w}_u)_i ds R_{ji} \delta_{jm} R_{mp} \frac{\partial \tilde{\lambda}_p}{\partial \hat{u}_k^p}, \tag{3.81}$$

$$\frac{\partial \mathbf{R}_u^{\Gamma^{ls}}}{\partial \hat{c}_k^p} = \int_{\Gamma^{ls}} (\boldsymbol{w}_u)_i ds R_{ji} \delta_{jm} R_{mp} \frac{\partial \tilde{\lambda}_p}{\partial \hat{c}_k^p}. \tag{3.82}$$

The derivatives of the stabilized Lagrange multiplier with respect to the nodal solutions are provided in Appendix C.

3.3.2 XFEM interface contribution - Nitsche's method for stress-diffusion coupling problems

Unlike cohesive zone model, the continuity of the mechanical displacement at the electrode/electrolyte interface is enforced using Nitsche formulation. However, the electrochemical reaction kinetic in enforced by using the BV formulation. For the mechanical portion, the residual equation using Nitsche formulation is described in the following variational setting:

$$\mathbf{R}_u^{\Gamma^{ls}} = -\int_{\Gamma^{ls}} [\delta \boldsymbol{u}] \cdot \{\boldsymbol{\sigma} \cdot \boldsymbol{n}\} \, ds \mp \int_{\Gamma^{ls}} \{\delta(\boldsymbol{\sigma} \cdot \boldsymbol{n})\} \cdot [\boldsymbol{u}] ds + \gamma \int_{\Gamma^{ls}} [\delta \boldsymbol{u}] \cdot [\boldsymbol{u}] ds, \tag{3.83}$$

where $\{\boldsymbol{\sigma} \cdot \boldsymbol{n}\}$ represents an averaged interface traction, $[\boldsymbol{u}]$ is displacement jump across the interface, $\boldsymbol{\sigma}$ is the Cauchy stress, $\boldsymbol{n}$ is the outward pointing surface normal, and γ is the penalty factor. For stress-diffusion coupling problem the Cauchy stress for phase p is described as follows:

$$\boldsymbol{\sigma}_p = \mathbb{C}_p \colon (\boldsymbol{\varepsilon}_p - \frac{1}{3} \Omega_p \Delta c_p \boldsymbol{I}). \tag{3.84}$$

In finite element context the discretized form of Equation (3.83) is written as:

$$\mathbf{R}_u^{\Gamma^{ls}} = (\hat{\boldsymbol{w}}_u^e)^T \Bigg[\underbrace{-\int_{\Gamma^{ls}} (\bar{\boldsymbol{N}}^{e,u})^T \cdot \{\boldsymbol{\sigma}\cdot\boldsymbol{n}\}\, ds}_{{}^1\mathbf{R}_u^{\Gamma_{ls}}} \mp \underbrace{\int_{\Gamma^{ls}} \left\{ \frac{\partial(\boldsymbol{\sigma}\cdot\boldsymbol{n})}{\partial(\boldsymbol{u}^e)^{n+1}} \right\} \cdot [\boldsymbol{u}] ds}_{{}^2\mathbf{R}_u^{\Gamma_{ls}}} + \gamma \underbrace{\int_{\Gamma^{ls}} (\bar{\boldsymbol{N}}^{e,u})^T \cdot [\boldsymbol{u}] ds}_{{}^3\mathbf{R}_u^{\Gamma_{ls}}} \Bigg] \mp (\hat{w}_{c_p}^e)^T \Bigg[\underbrace{\int_{\Gamma^{ls}} \left\{ \frac{\partial(\boldsymbol{\sigma}\cdot\boldsymbol{n})}{\partial(\hat{\boldsymbol{c}}_p^e)^{n+1}} \right\} \cdot [\boldsymbol{u}] ds}_{{}^4\mathbf{R}_u^{\Gamma_{ls}}} \Bigg]. \tag{3.85}$$

Due to complexity, the residual equation is decomposed into four portions and the contribution of each portion will describe separately.

Let's focus on ${}^1\mathbf{R}_u^{\Gamma_{ls}}$:

$${}^1\mathbf{R}_u^{\Gamma_{ls}} = -\int_{\Gamma^{ls}} (\bar{\boldsymbol{N}}^{e,u})^T \cdot \{\boldsymbol{\sigma}\cdot\boldsymbol{n}\}\, ds = -\int_{\Gamma^{ls}} \Big((\boldsymbol{N}_l^{e,u})^T - (\boldsymbol{N}_s^{e,u})^T \Big) \Big(\omega^l \boldsymbol{\sigma}_l \cdot \boldsymbol{n}_{bv}^{lc} + \omega^s \boldsymbol{\sigma}_s \cdot \boldsymbol{n}_{bv}^{lc} \Big) ds, \tag{3.86}$$

where $(\bar{\boldsymbol{N}}^{e,u})^T$ is the jump in shape function between two phases, ω^p is the weight factor for the stress contribution in phase p, and $\boldsymbol{n}_{bv}^{ls}$ is the outgoing normal vector. This residual contribution is decomposed into the residual contributions from the electrode and electrolyte phases in the following setting:

$$\begin{aligned} {}^1\mathbf{R}_{u_l}^{\Gamma_{ls}} &= -\int_{\Gamma^{ls}} (\boldsymbol{N}_l^{e,u})^T \cdot \Big(\omega^l \boldsymbol{\sigma}_l \cdot \boldsymbol{n}_{bv}^{lc} + \omega^s \boldsymbol{\sigma}_s \cdot \boldsymbol{n}_{bv}^{lc} \Big) ds, \\ {}^1\mathbf{R}_{u_s}^{\Gamma_{ls}} &= +\int_{\Gamma^{ls}} (\boldsymbol{N}_s^{e,u})^T \cdot \Big(\omega^l \boldsymbol{\sigma}_l \cdot \boldsymbol{n}_{bv}^{lc} + \omega^s \boldsymbol{\sigma}_s \cdot \boldsymbol{n}_{bv}^{lc} \Big) ds. \end{aligned} \tag{3.87}$$

The derivatives of each component with respect to independent state variables (i.e. $(\hat{\boldsymbol{u}}_l^e)^{n+1}$, $(\hat{\boldsymbol{u}}_s^e)^{n+1}$, $(\hat{\boldsymbol{c}}_l^e)^{n+1}$, and $(\hat{\boldsymbol{c}}_s^e)^{n+1}$) in each phase is described as follows:

$$\begin{aligned} \frac{\partial {}^1\mathbf{R}_{u_l}^{\Gamma_{ls}}}{\partial(\hat{\boldsymbol{u}}_l^e)^{n+1}} &= -\int_{\Gamma^{ls}} (\boldsymbol{N}_l^{e,u})^T \cdot \frac{\partial\big(\omega^l \boldsymbol{\sigma}_l \cdot \boldsymbol{n}_{bv}^{lc}\big)}{\partial(\hat{\boldsymbol{u}}_l^e)^{n+1}} ds, \\ \frac{\partial {}^1\mathbf{R}_{u_l}^{\Gamma_{ls}}}{\partial(\hat{\boldsymbol{u}}_s^e)^{n+1}} &= -\int_{\Gamma^{ls}} (\boldsymbol{N}_l^{e,u})^T \cdot \frac{\partial\big(\omega^s \boldsymbol{\sigma}_s \cdot \boldsymbol{n}_{bv}^{lc}\big)}{\partial(\hat{\boldsymbol{u}}_s^e)^{n+1}} ds, \\ \frac{\partial {}^1\mathbf{R}_{u_s}^{\Gamma_{ls}}}{\partial(\hat{\boldsymbol{u}}_l^e)^{n+1}} &= \int_{\Gamma^{ls}} (\boldsymbol{N}_s^{e,u})^T \cdot \frac{\partial\big(\omega^l \boldsymbol{\sigma}_l \cdot \boldsymbol{n}_{bv}^{lc}\big)}{\partial(\hat{\boldsymbol{u}}_l^e)^{n+1}} ds, \\ \frac{\partial {}^1\mathbf{R}_{u_s}^{\Gamma_{ls}}}{\partial(\hat{\boldsymbol{u}}_s^e)^{n+1}} &= \int_{\Gamma^{ls}} (\boldsymbol{N}_s^{e,u})^T \cdot \frac{\partial\big(\omega^s \boldsymbol{\sigma}_s \cdot \boldsymbol{n}_{bv}^{lc}\big)}{\partial(\hat{\boldsymbol{u}}_s^e)^{n+1}} ds. \end{aligned} \tag{3.88}$$

Since the stress is a function of both displacement and concentration at both phases, the derivatives of the residuals in both phases with respect to electrode and electrolyte concentrations are non-zero, therefore the derivatives of residuals with respect to electrode and electrolyte concentrations are described as follows:

$$\begin{aligned}
\frac{\partial^1 \mathbf{R}_{u_l}^{\Gamma_{ls}}}{\partial(\hat{\boldsymbol{c}}_l^e)^{n+1}} &= -\int_{\Gamma^{ls}} (\boldsymbol{N}_l^{e,u})^T \cdot \frac{\partial\big(\omega^l \boldsymbol{\sigma}_l \cdot \boldsymbol{n}_{bv}^{lc}\big)}{\partial(\hat{\boldsymbol{c}}_l^e)^{n+1}} ds, \\
\frac{\partial^1 \mathbf{R}_{u_l}^{\Gamma_{ls}}}{\partial(\hat{\boldsymbol{c}}_s^e)^{n+1}} &= -\int_{\Gamma^{ls}} (\boldsymbol{N}_l^{e,u})^T \cdot \frac{\partial\big(\omega^s \boldsymbol{\sigma}_s \cdot \boldsymbol{n}_{bv}^{lc}\big)}{\partial(\hat{\boldsymbol{c}}_s^e)^{n+1}} ds, \\
\frac{\partial^1 \mathbf{R}_{u_s}^{\Gamma_{ls}}}{\partial(\hat{\boldsymbol{c}}_l^e)^{n+1}} &= \int_{\Gamma^{ls}} (\boldsymbol{N}_s^{e,u})^T \cdot \frac{\partial\big(\omega^l \boldsymbol{\sigma}_l \cdot \boldsymbol{n}_{bv}^{lc}\big)}{\partial(\hat{\boldsymbol{c}}_l^e)^{n+1}} ds, \\
\frac{\partial^1 \mathbf{R}_{u_s}^{\Gamma_{ls}}}{\partial(\hat{\boldsymbol{c}}_s^e)^{n+1}} &= \int_{\Gamma^{ls}} (\boldsymbol{N}_s^{e,u})^T \cdot \frac{\partial\big(\omega^s \boldsymbol{\sigma}_s \cdot \boldsymbol{n}_{bv}^{lc}\big)}{\partial(\hat{\boldsymbol{c}}_s^e)^{n+1}} ds.
\end{aligned} \tag{3.89}$$

For the second component of the total residual, ${}^2\mathbf{R}_u^{\Gamma_{ls}}$:

$$\begin{aligned}
{}^2\mathbf{R}_u^{\Gamma_{ls}} &= \mp \int_{\Gamma^{ls}} \left\{ \frac{\partial(\boldsymbol{\sigma} \cdot \boldsymbol{n})}{\partial(\hat{\boldsymbol{u}}^e)^{n+1}} \right\} \cdot [\boldsymbol{u}] ds \\
= \mp \int_{\Gamma^{ls}} \left(\frac{\partial(\omega^l \boldsymbol{\sigma}_l \cdot \boldsymbol{n}_{bv}^{lc})}{\partial(\hat{\boldsymbol{u}}_l^e)^{n+1}} + \frac{\partial(\omega^s \boldsymbol{\sigma}_s \cdot \boldsymbol{n}_{bv}^{lc})}{\partial(\hat{\boldsymbol{u}}_s^e)^{n+1}} \right) &\cdot \Big(\boldsymbol{N}_l^{e,u}(\hat{\boldsymbol{u}}_l^e)^{n+1} - \boldsymbol{N}_s^{e,u}(\hat{\boldsymbol{u}}_s^e)^{n+1} \Big) ds.
\end{aligned} \tag{3.90}$$

In a similar manner, one can decompose this residual into the contribution from electrode and electrolyte phases:

$$\begin{aligned}
{}^2\mathbf{R}_{u_l}^{\Gamma_{ls}} &= \mp \int_{\Gamma^{ls}} \left(\frac{\partial(\omega^l \boldsymbol{\sigma}_l \cdot \boldsymbol{n}_{bv}^{lc})}{\partial(\hat{\boldsymbol{u}}_l^e)^{n+1}} \right) \cdot \Big(\boldsymbol{N}_l^{e,u}(\hat{\boldsymbol{u}}_l^e)^{n+1} - \boldsymbol{N}_s^{e,u}(\hat{\boldsymbol{u}}_s^e)^{n+1} \Big) ds \\
{}^2\mathbf{R}_{u_s}^{\Gamma_{ls}} &= \mp \int_{\Gamma^{ls}} \left(\frac{\partial(\omega^s \boldsymbol{\sigma}_s \cdot \boldsymbol{n}_{bv}^{lc})}{\partial(\hat{\boldsymbol{u}}_s^e)^{n+1}} \right) \cdot \Big(\boldsymbol{N}_l^{e,u}(\hat{\boldsymbol{u}}_l^e)^{n+1} - \boldsymbol{N}_s^{e,u}(\hat{\boldsymbol{u}}_s^e)^{n+1} \Big) ds.
\end{aligned} \tag{3.91}$$

The derivatives of residuals with respect to independent state variables in both phases are written as follows:

$$\begin{aligned}
\frac{\partial^2 \mathbf{R}_{u_l}^{\Gamma_{ls}}}{\partial(\hat{\boldsymbol{u}}_l^e)^{n+1}} &= \mp \int_{\Gamma^{ls}} \left(\frac{\partial(\omega^l \boldsymbol{\sigma}_l \cdot \boldsymbol{n}_{bv}^{lc})}{\partial(\hat{\boldsymbol{u}}_l^e)^{n+1}} \right) \cdot \boldsymbol{N}_l^{e,u} ds, \\
\frac{\partial^2 \mathbf{R}_{u_l}^{\Gamma_{ls}}}{\partial(\hat{\boldsymbol{u}}_s^e)^{n+1}} &= \pm \int_{\Gamma^{ls}} \left(\frac{\partial(\omega^l \boldsymbol{\sigma}_l \cdot \boldsymbol{n}_{bv}^{lc})}{\partial(\hat{\boldsymbol{u}}_l^e)^{n+1}} \right) \cdot \boldsymbol{N}_s^{e,u} ds, \\
\frac{\partial^2 \mathbf{R}_{u_s}^{\Gamma_{ls}}}{\partial(\hat{\boldsymbol{u}}_l^e)^{n+1}} &= \mp \int_{\Gamma^{ls}} \left(\frac{\partial(\omega^s \boldsymbol{\sigma}_s \cdot \boldsymbol{n}_{bv}^{lc})}{\partial(\hat{\boldsymbol{u}}_s^e)^{n+1}} \right) \cdot \boldsymbol{N}_l^{e,u} ds, \\
\frac{\partial^2 \mathbf{R}_{u_s}^{\Gamma_{ls}}}{\partial(\hat{\boldsymbol{u}}_s^e)^{n+1}} &= \pm \int_{\Gamma^{ls}} \left(\frac{\partial(\omega^s \boldsymbol{\sigma}_s \cdot \boldsymbol{n}_{bv}^{lc})}{\partial(\hat{\boldsymbol{u}}_s^e)^{n+1}} \right) \cdot \boldsymbol{N}_s^{e,u} ds.
\end{aligned} \tag{3.92}$$

For the third component, ${}^3\mathbf{R}_u^{\Gamma_{ls}}$:

$$\begin{aligned} {}^3\mathbf{R}_u^{\Gamma_{ls}} &= \gamma \int_{\Gamma^{ls}} (\bar{\boldsymbol{N}}^{e,u})^T \cdot [\boldsymbol{u}] ds \\ &= \gamma \int_{\Gamma^{ls}} \Big((\boldsymbol{N}_l^{e,u})^T - (\boldsymbol{N}_s^{e,u})^T \Big) \cdot \Big(\boldsymbol{N}_l^{e,u} (\hat{\boldsymbol{u}}_l^e)^{n+1} - \boldsymbol{N}_s^{e,u} (\hat{\boldsymbol{u}}_s^e)^{n+1} \Big) ds. \end{aligned} \tag{3.93}$$

The decomposed form of this residual is written as follows:

$$\begin{aligned} {}^3\mathbf{R}_{u_l}^{\Gamma_{ls}} &= +\gamma \int_{\Gamma^{ls}} (\boldsymbol{N}_l^{e,u})^T \cdot \Big(\boldsymbol{N}_l^{e,u} (\hat{\boldsymbol{u}}_l^e)^{n+1} - \boldsymbol{N}_s^{e,u} (\hat{\boldsymbol{u}}_s^e)^{n+1} \Big) ds, \\ {}^3\mathbf{R}_{u_s}^{\Gamma_{ls}} &= -\gamma \int_{\Gamma^{ls}} (\boldsymbol{N}_s^{e,u})^T \cdot \Big(\boldsymbol{N}_l^{e,u} (\hat{\boldsymbol{u}}_l^e)^{n+1} - \boldsymbol{N}_s^{e,u} (\hat{\boldsymbol{u}}_s^e)^{n+1} \Big) ds. \end{aligned} \tag{3.94}$$

And the derivatives:

$$\begin{aligned} \frac{\partial^3 \mathbf{R}_{u_l}^{\Gamma_{ls}}}{\partial (\hat{\boldsymbol{u}}_l^e)^{n+1}} &= +\gamma \int_{\Gamma^{ls}} (\boldsymbol{N}_l^{e,u})^T \cdot \boldsymbol{N}_l^{e,u} ds, \\ \frac{\partial^3 \mathbf{R}_{u_l}^{\Gamma_{ls}}}{\partial (\hat{\boldsymbol{u}}_s^e)^{n+1}} &= -\gamma \int_{\Gamma^{ls}} (\boldsymbol{N}_l^{e,u})^T \cdot \boldsymbol{N}_s^{e,u} ds, \\ \frac{\partial^3 \mathbf{R}_{u_s}^{\Gamma_{ls}}}{\partial (\hat{\boldsymbol{u}}_l^e)^{n+1}} &= -\gamma \int_{\Gamma^{ls}} (\boldsymbol{N}_s^{e,u})^T \cdot \boldsymbol{N}_l^{e,u} ds, \\ \frac{\partial^3 \mathbf{R}_{u_s}^{\Gamma_{ls}}}{\partial (\hat{\boldsymbol{u}}_s^e)^{n+1}} &= +\gamma \int_{\Gamma^{ls}} (\boldsymbol{N}_s^{e,u})^T \cdot \boldsymbol{N}_s^{e,u} ds. \end{aligned} \tag{3.95}$$

Finally, for the concentration driven contribution of the residual, ${}^4\mathbf{R}_u^{\Gamma_{ls}}$:

$$\begin{aligned} {}^4\mathbf{R}_u^{\Gamma_{ls}} &= \mp \int_{\Gamma^{ls}} \left\{ \frac{\partial (\boldsymbol{\sigma} \cdot \boldsymbol{n})}{\partial (\hat{\boldsymbol{c}}_p^e)^{n+1}} \right\} \cdot [\boldsymbol{u}] ds \\ &= \mp \int_{\Gamma^{ls}} \left(\frac{\partial (\omega^l \boldsymbol{\sigma}^l \cdot \boldsymbol{n}_{bv}^{lc})}{\partial (\hat{\boldsymbol{c}}_l^e)^{n+1}} + \frac{\partial (\omega^s \boldsymbol{\sigma}_s \cdot \boldsymbol{n}_{bv}^{lc})}{\partial (\hat{\boldsymbol{c}}_s^e)^{n+1}} \right) \cdot \Big(\boldsymbol{N}_l^{e,u} (\hat{\boldsymbol{u}}_l^e)^{n+1} - \boldsymbol{N}_s^{e,u} (\hat{\boldsymbol{u}}_s^e)^{n+1} \Big) ds \end{aligned} \tag{3.96}$$

The decomposed form of this residual is written as follows:

$$\begin{aligned} {}^4\mathbf{R}_{u_l}^{\Gamma_{ls}} &= \mp \int_{\Gamma^{ls}} \left(\frac{\partial (\omega^l \boldsymbol{\sigma}^l \cdot \boldsymbol{n}_{bv}^{lc})}{\partial (\hat{\boldsymbol{c}}_l^e)^{n+1}} \right) \cdot \Big(\boldsymbol{N}_l^{e,u} (\hat{\boldsymbol{u}}_l^e)^{n+1} - \boldsymbol{N}_s^{e,u} (\hat{\boldsymbol{u}}_s^e)^{n+1} \Big) ds, \\ {}^4\mathbf{R}_{u_s}^{\Gamma_{ls}} &= \mp \int_{\Gamma^{ls}} \left(\frac{\partial (\omega^s \boldsymbol{\sigma}_s \cdot \boldsymbol{n}_{bv}^{lc})}{\partial (\hat{\boldsymbol{c}}_s^e)^{n+1}} \right) \cdot \Big(\boldsymbol{N}_l^{e,u} (\hat{\boldsymbol{u}}_l^e)^{n+1} - \boldsymbol{N}_s^{e,u} (\hat{\boldsymbol{u}}_s^e)^{n+1} \Big) ds, \end{aligned} \tag{3.97}$$

and the derivatives with respect to independent state variables:

$$\begin{aligned} \frac{\partial^4 \mathbf{R}_{u_l}^{\Gamma_{ls}}}{\partial (\hat{\boldsymbol{u}}_l^e)^{n+1}} &= \mp \int_{\Gamma^{ls}} \left(\frac{\partial (\omega^l \boldsymbol{\sigma}_l \cdot \boldsymbol{n}_{bv}^{lc})}{\partial (\hat{\boldsymbol{c}}_l^e)^{n+1}} \right) \cdot \boldsymbol{N}_l^{e,u} ds, \\ \frac{\partial^4 \mathbf{R}_{u_l}^{\Gamma_{ls}}}{\partial (\hat{\boldsymbol{u}}_s^e)^{n+1}} &= \pm \int_{\Gamma^{ls}} \left(\frac{\partial (\omega^l \boldsymbol{\sigma}_l \cdot \boldsymbol{n}_{bv}^{lc})}{\partial (\hat{\boldsymbol{c}}_l^e)^{n+1}} \right) \cdot \boldsymbol{N}_s^{e,u} ds, \\ \frac{\partial^4 \mathbf{R}_{u_s}^{\Gamma_{ls}}}{\partial (\hat{\boldsymbol{u}}_l^e)^{n+1}} &= \mp \int_{\Gamma^{ls}} \left(\frac{\partial (\omega^s \boldsymbol{\sigma}_s \cdot \boldsymbol{n}_{bv}^{lc})}{\partial (\hat{\boldsymbol{c}}_s^e)^{n+1}} \right) \cdot \boldsymbol{N}_l^{e,u} ds, \\ \frac{\partial^4 \mathbf{R}_{u_s}^{\Gamma_{ls}}}{\partial (\hat{\boldsymbol{u}}_s^e)^{n+1}} &= \pm \int_{\Gamma^{ls}} \left(\frac{\partial (\omega^s \boldsymbol{\sigma}_s \cdot \boldsymbol{n}_{bv}^{lc})}{\partial (\hat{\boldsymbol{c}}_s^e)^{n+1}} \right) \cdot \boldsymbol{N}_s^{e,u} ds. \end{aligned} \tag{3.98}$$

Chapter 4

Parameter identification and Topology Optimization

4.1 Introduction

The numerical modeling of the LIB systems requires accurate battery models with many model and material parameters. The simulation aims to predict the performance of the battery for a specific set of parameters. However, insufficient and incorrect input parameters lead to incorrect results and discrepancy between numerical predictions and experimental observations. The high experimental expense caused by the measurement of large number of material parameters. This leads to an inefficient application for calibration of numerical models against experimental observations. Moreover, measurement of some material and model parameters in the battery cell requires specific tools and methods. Numerical techniques such as the stochastic analysis [68] and deterministic approach are used to reduce difficulties caused by the measurement of some material and model parameters. Unlike the stochastic analysis that uses sufficient measurements and samples, the deterministic approach allows performing analysis with insufficient measurements.

In the numerical modeling of the LIB, identifying important parameters governing the electrochemical performance of the battery needs robust numerical techniques. In this section we aim to get insight into the contribution of model and material parameters dominating the performance of the bulk SSLB. To this end, we introduced the PIM into our full resolution model. The PIM enables us to minimize the discrepancies and mismatch between numerical predictions and experimental observations using material and model parameters. The method employs the deterministic approach using the main features of the gradient based optimization. The gradient based and gra-

dient free are the most well-known optimization techniques. Unlike the gradient free method which is non-differentiable and has costly gradient evaluation procedures, the gradient based optimization is differentiable and a well-established approach. In the gradient based approach the optimization problem is defined as follows:

The objective:

$$\min_{\boldsymbol{s}} \qquad z(\boldsymbol{s}, \boldsymbol{u}(\boldsymbol{s}, t), t), \tag{4.1}$$

subject to inequality and equality constraints:

$$\begin{aligned} g_i(\boldsymbol{s}, \boldsymbol{u}(\boldsymbol{s}, t), t) \leq 0 \quad i = 1, 2, ..., N_g \\ h_j(\boldsymbol{s}, \boldsymbol{u}(\boldsymbol{s}, t), t) = 0 \quad j = 1, 2, ..., N_h, \end{aligned} \tag{4.2}$$

with

$$\boldsymbol{s} \in \boldsymbol{S} = \left\{ \mathbb{R}^{N_s} \mid s_j^L \leq s_j \leq s_j^U, j = 1, 2, ...N_s \right\}, \tag{4.3}$$

where $\boldsymbol{s}$ is the vector of design variables, $\boldsymbol{u}$ is the vector of independent state variables, and t is the time, g_i is the inequality constraint, and h_j is the equality constraint. The number of design variables is N_s; the lower and upper bounds on the design variable, s_j are denoted by s_j^L and s_j^U, respectively. In a class of gradient based optimization we seek to compute the gradient of a global scalar with respect to the design variables. To this end the following steps are needed:

1) Define a global scalar: the global scalar is an explicit and implicit function of the design variables. The general form of the global scalar over the volume is define as:

$$q(\boldsymbol{s}, \boldsymbol{u}(\boldsymbol{s}, t)) = \int_\Omega f_q(\boldsymbol{u}(\boldsymbol{s}, t)) dv \tag{4.4}$$

2) Define criteria: the criteria are physical quantities such as strain energy, displacement and stress measures, etc. The general form of a criterion over time is defined as:

$$Q(q(\boldsymbol{s}, \boldsymbol{u}(\boldsymbol{s}, t))) = \int_0^T f_Q(q(\boldsymbol{s}, \boldsymbol{u}(\boldsymbol{s}, t))) dt \tag{4.5}$$

3) Define the optimization quantities:

$$\begin{aligned} z(\boldsymbol{s}, \boldsymbol{u}(\boldsymbol{s}, t), t) &= z(Q), \\ g(\boldsymbol{s}, \boldsymbol{u}(\boldsymbol{s}, t), t) &= g(Q), \\ h(\boldsymbol{s}, \boldsymbol{u}(\boldsymbol{s}, t), t) &= h(Q). \end{aligned} \tag{4.6}$$

We seek to compute the gradient of optimization quantities:

$$\begin{aligned} \frac{dz}{d\boldsymbol{s}} &= \frac{dz}{dQ}\frac{dQ}{dq}\frac{dq}{d\boldsymbol{s}}, \\ \frac{dg}{d\boldsymbol{s}} &= \frac{dg}{dQ}\frac{dQ}{dq}\frac{dq}{d\boldsymbol{s}}, \\ \frac{dh}{d\boldsymbol{s}} &= \frac{dh}{dQ}\frac{dQ}{dq}\frac{dq}{d\boldsymbol{s}}. \end{aligned} \tag{4.7}$$

The converged residual equations a time step $n+1$ implies that:

$$\mathbf{R}^{n+1}(\boldsymbol{s}, \boldsymbol{u}^{n+1}(\boldsymbol{s}, t), t) = \mathbf{0}, \tag{4.8}$$

where $\boldsymbol{u}^{n+1}$ is the vector of all state variable solutions, and $\mathbf{R}^{n+1}$ is vector of residual equations at current time step. The derivative of the residual equations with respect to design variables is defined as:

$$\frac{d\mathbf{R}^{n+1}}{d\boldsymbol{s}} = \frac{\partial \mathbf{R}^{n+1}}{\partial \boldsymbol{s}} + \frac{\partial \mathbf{R}^{n+1}}{\partial \boldsymbol{u}^{n+1}}\frac{\partial \boldsymbol{u}^{n+1}}{\partial \boldsymbol{s}} = \mathbf{0}, \tag{4.9}$$

and the derivative of the global scalar with respect to design variables:

$$\frac{dq}{d\boldsymbol{s}} = \frac{\partial q}{\partial \boldsymbol{s}} + \frac{\partial q}{\partial \boldsymbol{u}^{n+1}}\frac{\partial \boldsymbol{u}^{n+1}}{\partial \boldsymbol{s}}. \tag{4.10}$$

By computing the partial derivative of state variables with respect to design variables from Equation (4.9) and replacing into Equation (4.10), the derivative of the global scalar with respect to design variables can be defined using the following methods:

a) Direct method:

$$\frac{dq}{ds_i} = \frac{\partial q}{\partial s_i} - \left(\frac{\partial q}{\partial s_j}\right)^T \gamma_{ij}, \tag{4.11}$$

where

$$\gamma_{ij} = \left(\frac{\partial R_i^{n+1}}{\partial u_k^{n+1}}\right)^{-1} \frac{\partial R_k^{n+1}}{\partial s_j} = \frac{\partial u_i^{n+1}}{\partial s_j}. \tag{4.12}$$

b) Adjoint method:

$$\frac{dq}{ds_i} = \frac{\partial q}{\partial s_i} - \lambda_j^T \frac{\partial R_i^{n+1}}{\partial s_j}, \tag{4.13}$$

where

$$\lambda_i = \left(\frac{\partial R_i^{n+1}}{\partial u_j^{n+1}}\right)^{-T} \frac{\partial q}{\partial u_j^{n+1}} = \frac{\partial R_i^{n+1}}{\partial q}. \tag{4.14}$$

Considering the computational costs of each method, we used the adjoint method for our purpose.

4.2 Parameter identification in LIBs

In this study, we utilize the capability of optimization techniques and defined the PIM that is integrated into our full resolution battery model. The objective in the parameters identification study is minimizing the discrepancies and mismatch between numerical solutions and experimental observations by varying the design variables. To this end, we used the discharge curve in the battery cell which is a representative solution for the global performance of the battery cell. The state variable in this case is the electrical potential in the electrode. As the state variable (i.e. electrode potential) at the measurement point is varying over the discharge time, a transient minimization problem needs to be solved. In this framework we use a gradient based nonlinear programming method namely Globally Convergent Method of Moving Asymptotes (GCMMA) to solve a nonlinear problem. This method requires the gradients of the objective function and constraints with respect to the design variables. Despite the complexity of coupled physical phenomena in the battery model we applied analytical sensitivities for the transient problem using adjoint sensitivity equation. For more information about design optimization of lithium-ion battery using adjoint method the reader is referred to [59, 60]. According to the parameter identification method defined in this study, for a

given discharge rate, the objective is defined by an integral of the discrepancy between the computed and target discharge curves over full discharge time. The minimization problem for each discharge rate is defined as:

$$\begin{aligned} \bar{Z}_i &= z_i(\boldsymbol{s}, \boldsymbol{u}(\boldsymbol{s}, t), t) \\ \boldsymbol{s} \in \boldsymbol{S} &= \left\{ \mathbb{R}^{N_s} \mid s_j^L \leq s_j \leq s_j^U, j = 1, 2, ...N_s \right\}, \end{aligned} \tag{4.15}$$

where z_i is decomposed into the explicit and implicit terms as follows:

$$z_i(\boldsymbol{s}, \boldsymbol{u}(\boldsymbol{s}, t), t) = \cancelto{0}{z_i(\boldsymbol{s})} + \omega \int_0^T \left(\phi_{s_{\text{num}}}(\boldsymbol{u}(\boldsymbol{s}, t), t) - \phi_{s_{\text{tar}}}(t)\right)^2 dt, \tag{4.16}$$

and ω is the objective function scaling factor, $\phi_{s_{\text{num}}}$ is the electrode potential at a given time for the numerical model and $\phi_{s_{\text{tar}}}$ is electrode potential at a given time for the target model (i.e. experimental model). Using mid-point integration rule, Equation (4.16) is approximated as follows:

$$z_i(\boldsymbol{s}, \boldsymbol{u}(\boldsymbol{s}, t), t) = \omega \sum_{j=1}^{N_T} \underbrace{\left(\bar{\phi}^j_{s_{\text{num}}}(\boldsymbol{u}(\boldsymbol{s}, t), t) - \bar{\phi}^j_{s_{\text{tar}}}(t)\right)^2 \Delta t_j}_{\tilde{z}^{(j)}}, \tag{4.17}$$

where

$$\bar{\phi}^j_{s_{\text{num}}}(\boldsymbol{u}(\boldsymbol{s}, t), t) = \frac{\phi^j_{s_{\text{num}}}(\boldsymbol{u}(\boldsymbol{s}, t), t) + \phi^{j-1}_{s_{\text{num}}}(\boldsymbol{u}(\boldsymbol{s}, t), t)}{2}, \quad \bar{\phi}^j_{s_{\text{tar}}}(t) = \frac{\phi^j_{s_{\text{tar}}}(t) + \phi^{j-1}_{s_{\text{tar}}}(t)}{2}, \tag{4.18}$$

and $\phi^j_{s_{\text{num}}}$ and $\phi^{j-1}_{s_{\text{num}}}$ are the electrode electrical potentials for the numerical model and $\phi^j_{s_{\text{tar}}}$ and $\phi^{j-1}_{s_{\text{tar}}}$ are the electrode electrical potentials for the experimental results at current and previous discharge times and Δt_j is the time step size in the transient analysis, see Figure 4.1 for more details. We applied this framework for the parameter identification study in both single-problem and multi-problem. In the case of multi-problem we discharge the battery cell in sequential forward analyses with different discharge rates. In our multi-problem which is computationally much more complex we solve multiple forward problems and transient sensitivity analyses at the same time for unique design variables. In the case of multi-problem the total objective value is defined as the sum of individual objective for each discharge rate:

$$\min_{\boldsymbol{s}} \qquad Z = \sum_{i=1}^{N_p} \bar{Z}_i, \tag{4.19}$$

where N_p is the number of discharge rates. The performance of the parameter identification framework is studied with numerical examples given in Section 5.

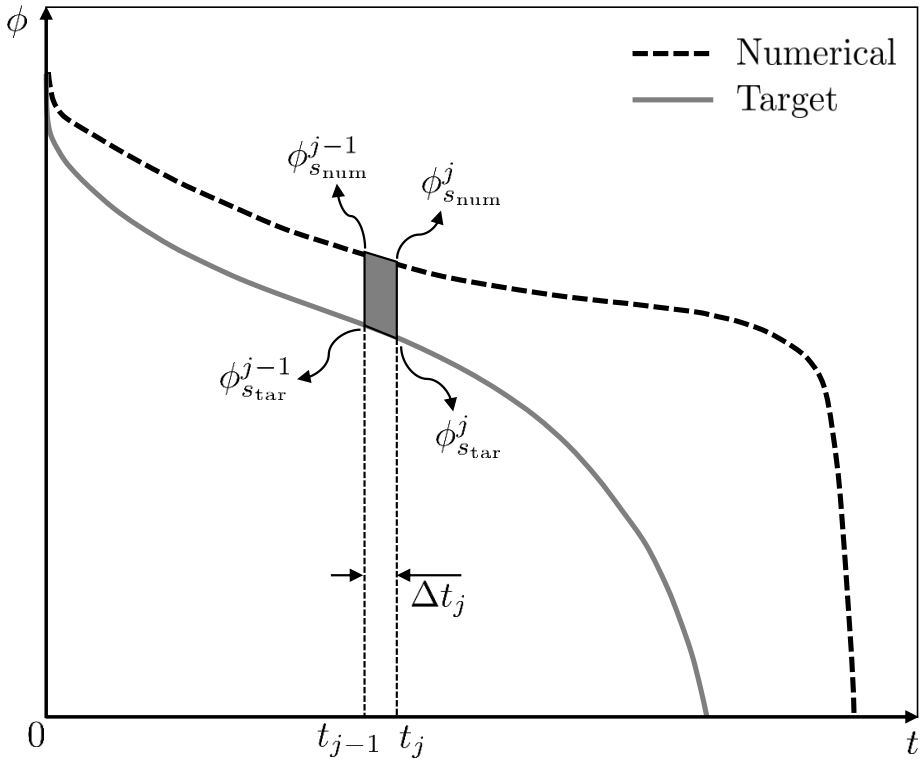

Figure 4.1: Schematic of objective evaluation in parameter identification problem.

The derivatives of objective function with respect to design variables are computed by the adjoint method. We adopt the discrete formulation for a transient problem of [34, 59]. The derivatives of the objective function with respect to design variables is divided into explicit and implicit terms:

$$\frac{d\bar{Z}_i}{ds_k} = \cancelto{0}{\frac{\partial z_i}{\partial s_k}} + \omega \sum_{j=1}^{N_T} \frac{\partial \tilde{z}^{(i)}}{\partial \boldsymbol{u}^{(j)}}^T \frac{\partial \boldsymbol{u}^{(j)}}{\partial s_k}, \tag{4.20}$$

where the explicit derivative with respect to design variables is zero. The implicit term is computed by the adjoint method as follows:

$$\omega \sum_{j=1}^{N_T} \frac{\partial \tilde{z}^{(i)}}{\partial \boldsymbol{u}^{(j)}}^T \frac{\partial \boldsymbol{u}^{(j)}}{\partial s_k} = \omega \sum_{j=1}^{N_T} \left(\lambda^{(j)}\right)^T \frac{\partial \left(\mathbf{R}^{(j)}\right)^{n+1}}{\partial s_k} \tag{4.21}$$

For more information about the sensitivity analysis for transient problems the reader is referred to [34, 59].

4.3 Topology optimization

Design optimization methods can be classified by the geometric changes that are allowable during the optimization process. Optimization methods in which geometry variation is restricted to affecting the shape of the material interface is known as shape optimization. Optimization methods in which geometry variation allows for changes in both shape and number of design components is known as topology optimization. To provide a high level of design freedom, a topology optimization framework is used in this research. Density methods, such as the Solid Isotropic Material with Penalization (SIMP) approach, are the most common method of describing the geometry in topology optimization. The SIMP approach was originally developed by [17, 118] and describes the geometry of a body by defining the material distribution in the design domain as a function of design variables. A fictitious porous material with density, $0 \leq \rho \leq 1$, defines a continuous transition between two or more materials. For more information and an overview of recent developments, the reader is referred to [16, 39, 125]. By representing topology as a continuous transition between materials, density methods effectively smear-out the interface geometry. This loss of precise interface geometry proves challenging when modeling design dependent surface loads.

The LSM, on the other hand, is a promising alternative approach for defining the geometry of the interface in topology optimization problems. In this study, we combine the LSM with the XFEM. Using the LSM, the geometry of the structure is defined by the LSF, $\phi(\mathbf{x})$, where $\mathbf{x}$ is the vector of spatial coordinates. For a two-phase problem, the LSF describes the spatial distribution of both phases as follows:

$$\begin{cases} \phi(\mathbf{x}) > 0 & \forall\ \mathbf{x} \in \Omega^A \\ \phi(\mathbf{x}) < 0 & \forall\ \mathbf{x} \in \Omega^B \\ \phi(\mathbf{x}) = 0 & \forall\ \mathbf{x} \in \Gamma^{AB} \end{cases}, \tag{4.22}$$

where Ω^A is the volume occupied by phase A, Ω^B is the volume occupied by phase B, and Γ^{AB} is the interface between two phases. The parameters of the discretized LSF are defined by explicit functions of the optimization variables. The level set field can be parameterized to describe any particular geometry such as circles or rectangles. The location and geometry of these primitives are defined by the optimization variables. This approach has proven to be effective in optimization studies of stress and strain energy minimization [142, 148]. Following to the approach of [79], to increase design freedom, the domain is discretized by finite elements and one optimization variable is associated with each finite element node, i.e. $N_s = N_n$, where N_n is the number of nodes. The level set value at the i^{th} node is defined by the following linear filter:

$$\phi_i = \left(\sum_{j=1}^{N_n} w_{ij} \right)^{-1} \sum_{j=1}^{N_n} w_{ij} s_j \ , \qquad \text{with} \qquad w_{ij} = max\left(0, (r - |\mathbf{x}_i - \mathbf{x}_j|)\right) \ , \tag{4.23}$$

where r is the filter radius, and $\mathbf{x}_j$ the position of the j^{th} node. The level set filter (4.23) enhances the convergence of the optimization process by widening the zone of influence of the optimization variables on the level set field [79]. The main features of the combined parameter identification and topology optimization are explored in numerical examples.

Chapter 5

Numerical Examples

In this chapter, we provide comprehensive numerical benchmark examples that are intended to test the functionality and demonstrate the performance of the developed numerical framework for all SSLIBs. The objective, characteristics, and results of each numerical examples are explored here.

5.1 Full resolution model - verification examples

5.1.1 Solid-state thin-film battery

The numerical study is described here to illustrate the accuracy, stability and convergence performance of the implemented finite element model for solid-state thin-film application. Thin-film lithium-ion batteries are typically developed for small scale application with low storage capacity. For this purpose, we consider a conventional all solid-state thin-film model, shown in Figure 5.1, consist of $LiCoO_2$, as a positive electrode, and Li_3PO_4, as a solid phase electrolyte. The model has originally been studied by [38], both experimentally and numerically, and COMSOL multiphysics for one-dimensional application that is extended for a three dimensional model. The developed 3D model provides unique opportunity to compare model predictions with experimental measurements as well as existing numerical models. To simplify the model, the influence of current collectors on the electrochemical processes is neglected and only half cell of thin-film is modeled. As mentioned in Section (2.2) the contribution from the lithium metal anode is considered through relevant boundary and interface conditions. The model configuration, material parameters, and boundary

conditions are listed in Tables 5.1 and 5.2, respectively.

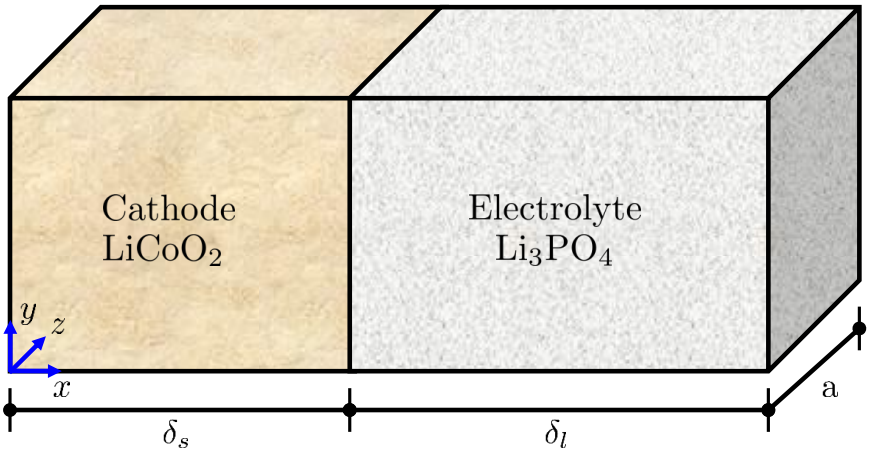

Figure 5.1: Schematic of all solid-state thin-film battery.

In this model the electrochemical interface reactions happen at both anode/electrolyte and cathode/electrolyte interfaces. Both reactions can be described by the BV expression [38]. On the negative electrode interface, lithium metal reacts with lithium-ions in the electrolyte. The BV expression which describes the reaction kinetic at this interface is given by:

$$j_{bv}^{la} = F k_A^s \left(\frac{c_l}{c_{l_{max}}}\right)^{\alpha_A} \left(\exp\left[\frac{\alpha_A F \eta}{RT}\right] - \exp\left[-\frac{(1-\alpha_A) F \eta}{RT}\right]\right), \tag{5.1}$$

with

$$\eta = \phi_s - \phi_l, \tag{5.2}$$

where k_A^s is the BV reaction rate constant at the anode/electrolyte interface and α_A is the anodic transfer coefficient. On the positive electrode interface the active materials react and the reaction which results in flux continuity at the interface can also be described by the BV expression as follows:

$$j_{bv}^{lc} = i_{0_C} \left(\exp\left[\frac{\alpha_C F}{RT}(\eta - U'(c_s))\right] - \exp\left[-\frac{(1-\alpha_C) F}{RT}(\eta - U'(c_s))\right]\right), \tag{5.3}$$

Table 5.1: Thin-film model parameters and material properties [38].

Description	Symbol	Value	Unit
electrolyte thickness	δ_l	1.50×10^{-6}	m
electrode thickness	δ_s	0.32×10^{-6}	m
in-plane length	a	1.0×10^{-2}	m
maximum Li concentration	$c_{s_{max}}$	23300	mol m^{-3}
minimum Li concentration	$c_{s_{min}}$	11650	mol m^{-3}
initial Li concentration	c_{s_0}	11766.5	mol m^{-3}
maximum Li^+ concentration	$c_{l_{max}}$	60100	mol m^{-3}
initial Li^+ concentration	c_{l_0}	10818	mol m^{-3}
electronic conductivity	λ_s	1.13	S m^{-1}
diffusion coefficient of Li^+	D_l^+	0.9×10^{-15}	m^2 s^{-1}
diffusion coefficient of n^-	D_l^-	5.1×10^{-15}	m^2 s^{-1}
diffusion coefficient of Li	D_s	1.76×10^{-15}	m^2 s^{-1}
BV reaction rate	k_A^s	1.0×10^{-2}	mol/$m^2 \cdot$ s
BV reaction rate	k_C^s	5.1×10^{-4}	mol/$m^2 \cdot$ s
anodic transfer coefficient	α_A	0.4	-
cathodic transfer coefficient	α_C	0.6	-
recombination coefficient	k_r	9.0×10^{-9}	$m^3mol^{-1}s^{-1}$
fraction of free Li	ξ_{c_l}	0.18	-
Faraday's constant	F	96485	C/mol
universal gas constant	R	8.3145	N.m/K.mol
reference temperature	T	298.15	K
electrode Young's modulus	E_s	7.0×10^4	MPa
electrolyte Young's modulus	E_l	10.34×10^4	MPa
electrode Poisson's ratio	ν_s	0.20	MPa
electrolyte Poisson's ratio	ν_l	0.26	MPa
electrode partial molar volume	Ω_s	3.852×10^{-7}	m^3mol^{-1}
electrolyte partial molar volume	Ω_l	0.0	m^3mol^{-1}
applied external current	$\mathbf{I}_{\text{ext}}$	var.	A/m^2

Table 5.2: Solid-state thin-film model boundary conditions [38].

Boundary condition	Symbol	$(\Gamma^{cc})^{\text{a}}$	$(\Gamma^{lc})^{\text{b}}$	$(\Gamma^{la})^{\text{c}}$
electrode flux	$\mathbf{J}_s \cdot \boldsymbol{n}$	0	$\frac{1}{F} j_{bv}^{lc}$	-
electrolyte flux	$\mathbf{J}_l \cdot \boldsymbol{n}$	-	$-\frac{D_-}{F(D_+ + D_-)} j_{bv}^{lc}$	$-\frac{D_-}{F(D_+ + D_-)} j_{bv}^{lc}$
electrode current	$\mathbf{i}_s \cdot \boldsymbol{n}$	$\mathbf{I}_{\text{ext}}$	j_{bv}^{lc}	-
electrolyte current	$\mathbf{i}_l \cdot \boldsymbol{n}$	-	$-j_{bv}^{lc}$	$-j_{bv}^{la}$

[a] Cathode-current collector interface

[b] Cathode-electrolyte interface

[c] Anode-electrolyte interface

where

$$i_{0_C} = F k_C^s \left(\frac{(c_{s_{max}} - c_s) c_l}{(c_{s_{max}} - c_{s_{min}}) c_{l_{max}}} \right)^{\alpha_C} \left(\frac{c_s - c_{s_{min}}}{c_{s_{max}} - c_{s_{min}}} \right)^{1-\alpha_C}, \tag{5.4}$$

and k_C^s is the BV reaction rate constant at the cathode/electrolyte interface, α_C is the cathodic transfer coefficient, and $U'(c_s)$ is the open circuit potential. For numerical verification, the model is discharged at different discharge rates; namely 1.6, 3.2, 6.4, 12.8, 25.6, and 51.2 C rates. The performance of the model is evaluated by comparing the discharge curves at different discharge rates with reference solutions [38]. The results are shown in Figure 5.2, the comparison demonstrates that there is excellent agreement between solutions. The comparison also reveals the performance, stability, and extensibility of full 3D solid-state battery model. To show the performance of the thin-film model the profile of concentration over total length of thin-film model at different discharge time is presented in Figure 5.3. The comparison of concentration profile at different discharge time step shows that initially the concentration profiles in both electrode and electrolyte are constant and the model is in equilibrium. However, as soon as the discharge current established, significant concentration gradients evolve in both electrode and electrolyte layers.

5.1.1.1 Mesh refinement study

In order to evaluate the influence of geometric configuration on the overall performance of the battery, a mesh refinement study has been performed. While the number of elements in the thickness direction remains constant as the one-dimensional reference model, the influence of in-plane discretization has been studied through variation of mesh size in in-plane directions. The study shows there is negligible sensitivity of solutions with mesh refinement and the response of the battery model can be captured with coarse mesh configuration. This study enables us to evaluate the performance of battery cell with a coarse mesh configuration and minimal computational cost. As an example the plot of mesh convergence study for a single discharge rate is shown in Figure 5.4. The results show that there is very negligible influence of mesh refinement on the performance of the thin-film model.

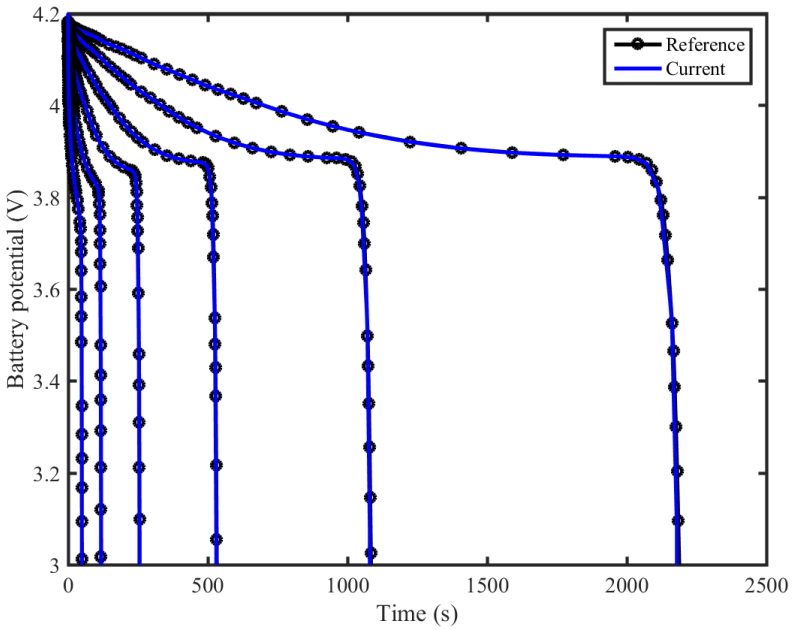

Figure 5.2: Comparison of discharge curves in all solid-state thin-film battery.

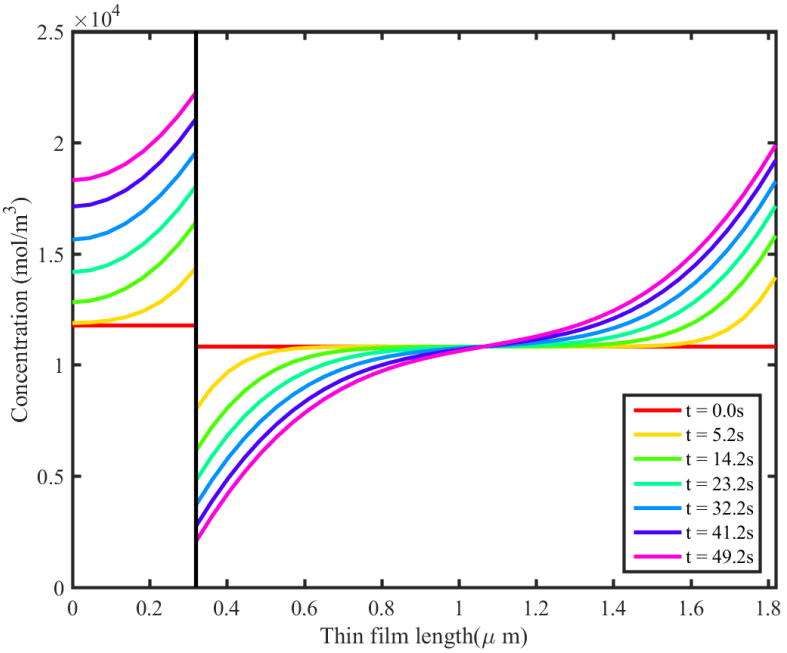

Figure 5.3: The evolution of concentration in time and space (discharge rate: 51.2C).

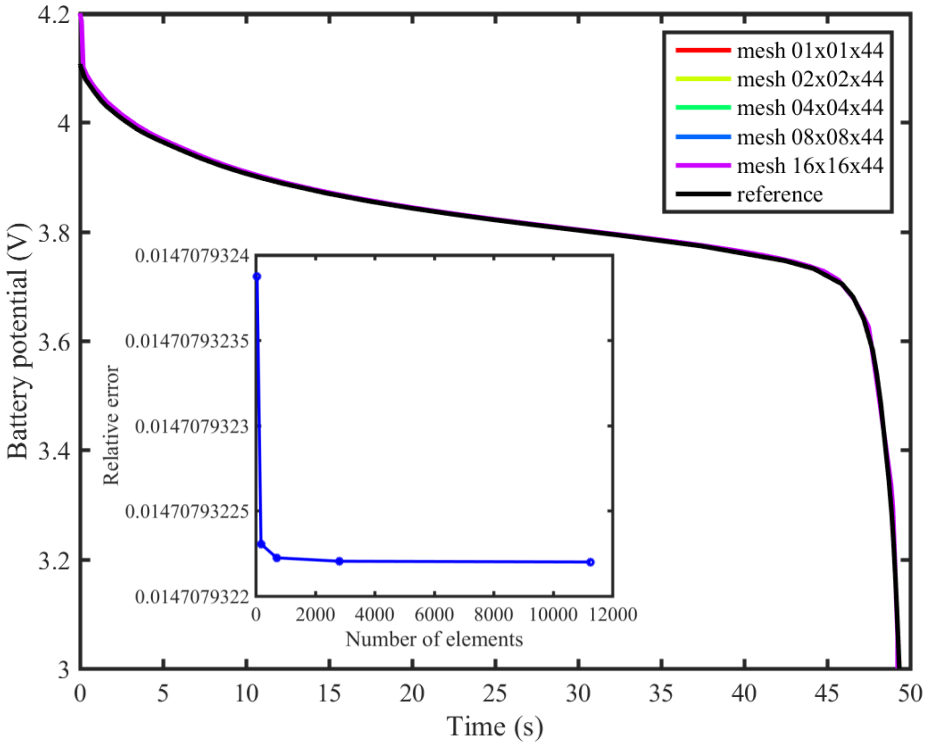

Figure 5.4: Study of the performance of thin-film model with mesh refinement (discharge rate: C-51.2). The relative error represents the error between numerical model and reference solution.

5.2 Full resolution model - calibration examples

5.2.1 Calibration of TiS_2 model

In this section we aim to evaluate the performance of the full-resolution model by comparing the numerical predictions with experimental observations for bulk SSLBs. As such, we chose a well known solid-state battery system using a sulfide glass electrolyte and TiS_2 electrode. The TiS_2 has been studied for many decades in liquid state, thin-film, and bulk SSLBs [152, 73, 135]. For numerical modeling, two different models are considered. The first model accounts for a dense bulk solid-state battery. The differences between this model and the thin-film solid-state model presented in Section 5.1.1 are thicknesses of the electrode and electrolyte which are greater than the thin-film model. In order to get more insights into the numerical response of the bulk solid-state batteries, a porous electrode model is developed based on the initial configuration of the dense bulk model. The objective of this model is to evaluate the performance of the numerical model when voids are introduced inside of the cathode layer and at the electrode/electrolyte interface.

5.2.1.1 Experimental Procedures

All experiments are conducted in a dry argon environment. The 77.5 $Li_2S - 22.5P_2S_5$ solid electrolyte (denoted as a77.5) is prepared by planetary ball-milling Li_2S (Alfa, 99.9%) and P_2S_5 (Sigma, 99%) in a 77.5 to 22.5 molar ratio for 20 hours in a 500 mL stainless steel jar. A reinforced cell die is used for all electrochemical tests. 150 mg of a77.5 is pressed at 75 MPa as a separator. Commercial TiS_2 (Alfa, 99%, 50μm) is pressed onto one side of the separator at 375 MPa. Lithium metal foil (Alfa) is pressed onto the other side of the separator as a counter electrode using 20 in-lb torque delivered by a torque wrench (California torque) to tighten the cell die. This is the same pressure used when operating the cells. Galvanostatic Intermittant Titration Technique (GITT) and cycling was performed using an Arbin BT2000 Battery Test Station. The GITT is performed by using a rate of C/20 for 1 hour followed by a 6 hour relaxation. An aerial current density of 0.054 $mAcm^{-2}$ corresponds to a rate of C/10. The operating voltage window was 3-1 V (vs.

Li^+/Li). All electrochemical tests are performed at 60°C unless otherwise noted; cells are allowed 3 hours of temperature acclimating before tests are performed. Thicknesses of separator and cathode were determined by using calipers during preparation. All experimental studies are conducted for charge/discharge process and at different discharge rates, the battery's performance is evaluated with charge/discharge curves.

5.2.1.2 Assumptions

In our numerical models, for simplicity, we neglected the mechanical contribution on the electrochemical performance of the battery. However, a number of assumptions must be made in order to reduce the computational intensity of the model.

- Effects of lithium anode: the effect of this on the electrochemical performance of the model is replaced with the BV equation described in Section 5.1.1.
- Charge transfer at the interface: it is assumed that no substantial charge transfer happens at the cathode/electrolyte interface.
- Effects of porosity: the effects of porosity in the electrode layer on the charge/discharge performance of the battery is considered through introducing porosity in the electrode layer and at the electrode/electrolyte interface.
- Anisotropic diffusion in electrode: the effects of anisotropic diffusion in the electrode is considered through the electrode diffusion coefficient profile described as a function of the State of Charge (SOC).
- Volume changes in the active material: the impact of volume changes in the active material on the electrochemical performance of the battery is neglected.

5.2.1.3 Bulk solid electrode model

This model accounts for full bulk solid electrode materials that has been used in the experimental setup. The 2D view of the geometric configuration and boundary conditions of this model are presented in Figure 5.5 and Table 5.2, respectively. The model geometry and material parameters are listed in Table 5.3. For numerical simulation, 3150 8-node brick elements. The cathode/electrolyte and anode/electrolyte interface contributions are modeled through Equations (5.1) and (5.3). The determined diffusion coefficient (D_s) as a function of state of charge ($SOC = c_s/c_{s_{max}}$), are used in the bulk solid electrode model. Figure 5.6 displays the experimentally derived diffusion coefficient within the TiS_2 by the GITT. The trend of increasing diffusion coefficient due to resistance in c-axis spreading from lithium intercalation is a well observed and modeled trend, for example see [140, 138].

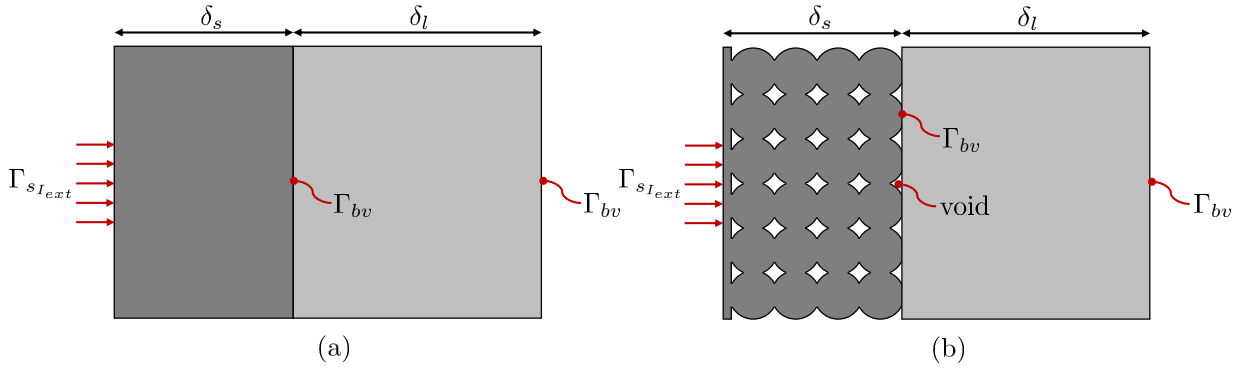

Figure 5.5: Schematic of solid electrode model, (a) dense bulk electrode (b) porous bulk electrode.

The model is discharged at different rates; namely C, C/2, C/5, C/10, C/20, and C/50. The results of numerical modeling presented in terms of variation of battery potential with discharge time are compared with experimental observations; as displayed in Figure 5.7. There is a remarkable agreement between numerical and experimental results at low discharge rates of C/20 and C/50. The exact capacity, overpotentials, and general discharge curve shapes are captured. However, at higher rates, discrepancies begin to arise. For all rates C through C/10, the model consistently predicts a greater discharge time (and thus greater capacity) than actually exhibited. This would

Table 5.3: $LiTiS_2$ model parameters and material properties.

Description	Symbol	Value	Unit
electrolyte thickness	δ_l	1.0×10^{-3}	m
electrode thickness bulk model	δ_s	7.0×10^{-6}	m
electrode thickness void model	δ_s	7.1×10^{-6}	m
surface area	A	1.3273×10^{-4}	m^2
maximum Li concentration	$c_{s_{max}}$	25995	mol m^{-3}
minimum Li concentration	$c_{s_{min}}$	1.0×10^{-6}	mol m^{-3}
initial Li concentration	c_{s_0}	1.0×10^{-5}	mol m^{-3}
maximum Li^+ concentration	$c_{l_{max}}$	28032	mol m^{-3}
initial Li^+ concentration	c_{l_0}	27751	mol m^{-3}
electronic conductivity	λ_s	10.0	S m^{-1}
diffusion coefficient of Li^+	D_l^+	1.0×10^{-12}	m^2 s^{-1}
diffusion coefficient of n^-	D_l^-	1.0×10^{-14}	m^2 s^{-1}
BV reaction rate	k_A^s	1.0×10^{-2}	$mol/m^2 \cdot s$
BV reaction rate	k_C^s	5.1×10^{-4}	$mol/m^2 \cdot s$
anodic transfer coefficient	α_A	0.4	-
cathodic transfer coefficient	α_C	0.6	-
recombination coefficient	k_r	9.0×10^{-9}	$m^3 mol^{-1} s^{-1}$
fraction of free Li	ξ_{c_l}	0.99	-
Faraday's constant	F	96485	C/mol
universal gas constant	R	8.3145	N.m/K.mol
reference temperature	T	333.0	K
applied current	$\mathbf{I}_{\text{ext}}$	var.	A/m^2

indicate the model may not predict the harsher conditions in the experimental battery. Additionally, the precise curve begins to deviate, more particularly at lower potentials the discrepancies are the largest. These discrepancies highlight the major differences between the thin-film and bulk models. In this bulk model, similar to the thin-film model the electrode is assumed completely dense. Therefore, it could capture rates as high as 51.2C with the thin-film model, yet begin to see discrepancy at C/10 for the bulk model. Therefore, transition to the bulk model need to be made to more accurately depict the true experimental setup.

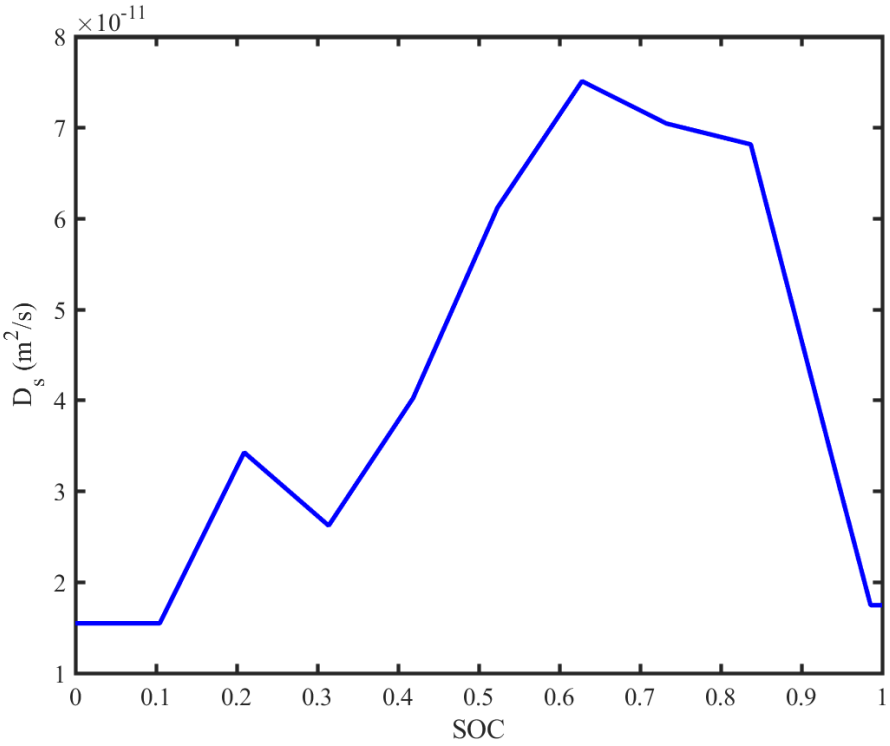

Figure 5.6: The profile of electrode diffusion coefficient as a function of state of charge.

5.2.1.4 Porous solid electrode model

In order to get more insight into the numerical and experimental performances of bulk SSLIBs, a porous solid electrode model is developed based on the initial framework of the bulk model. In particular, the objective of this model is to evaluate the performance of the numerical model when voids are introduced within the cathode and at the electrode/electrolyte interface. The 2D view of the model setup is shown in Figure 5.5. The porosity is assumed to be about 10%, it is also assumed that the electrolyte does not flow through porous media. For a solid battery, the introduction of voids is more akin to the real world conditions actually exhibited. The compaction of powders will also create an imperfect density profile (assuming not a completely ductile material). Changing the void space at the electrode/electrolyte interface provides an opportunity to look at the effect of defectual connections in diffusion paths of lithium ions.

The results of the computed discharge curves versus experimental results for porous model is

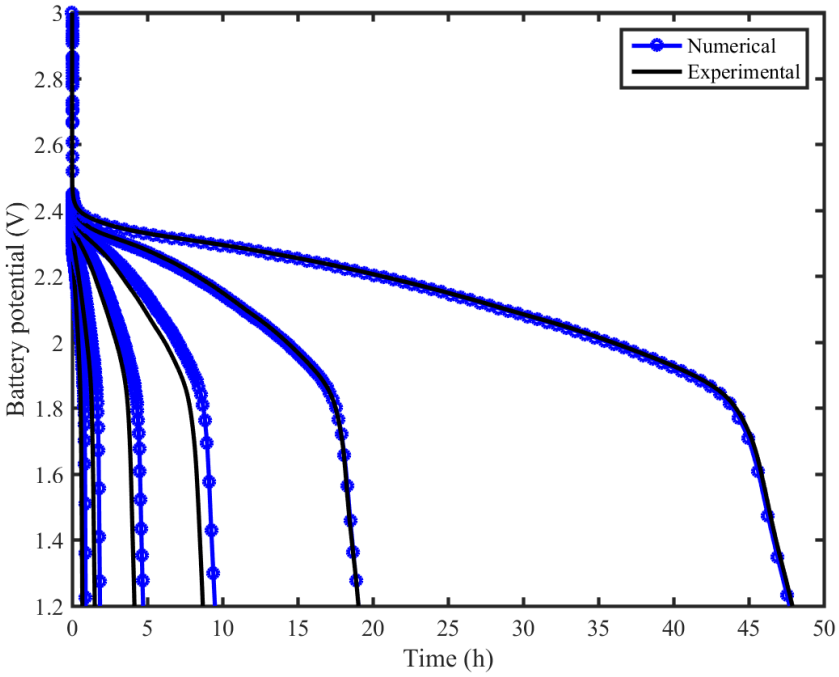

Figure 5.7: Comparison of discharge curves in all solid-state bulk cell.

shown in Figure 5.8. In this model, rates of C/50 and C/20 are excluded for clarity. Additionally these lower rates were adequately captured in the previous model and they present lower rates than commercially useful, they are not explored for the remainder of this work but did serve a valuable calibration role. The porous model provides less discrepancy for the high rate discharge than the bulk model. The model indicates that the presence of voids in the bulk SSLIBs is crucial, as shown in Figure 5.8.

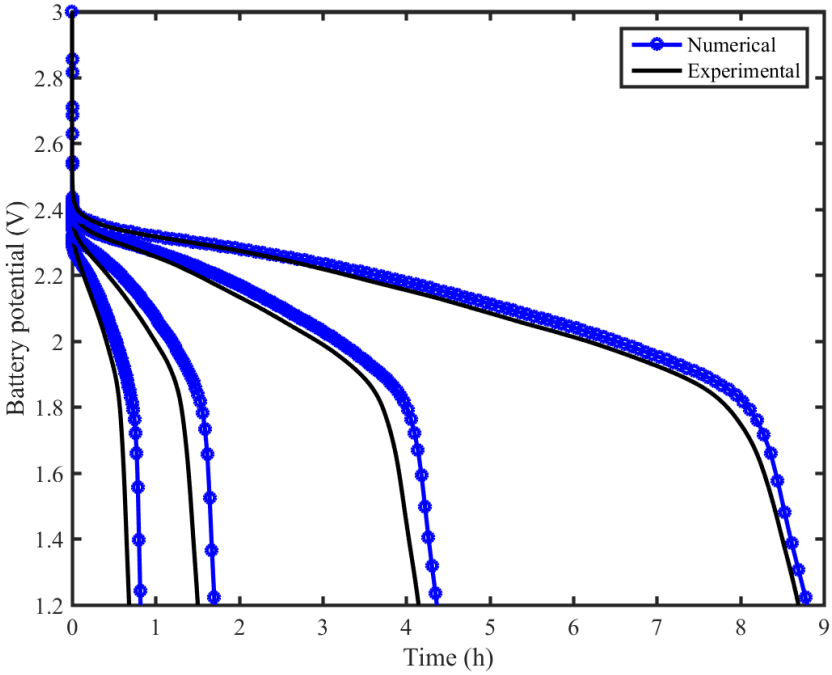

Figure 5.8: Comparison of discharge curves in all solid-state bulk cell with porous electrode.

5.2.2 Calibration of L333 model

The current commercially available cathode materials for SSLIBs suffer from life cycle performance and reliability during harsh operational condition. Lithium nickel-manganese-cobalt oxide Li, $LiNi_{1/3}Mn_{1/3}Co_{1/3}O_2$ (L333) have been studied extensively as a high performance cathode material for the SSLIB application. They represent high specific energy and relatively low cost [159]. The SSLIB based on these material represents as exceptional specific energy and life cycle performance. This battery fabricated for high performance solid-state batteries application [1] . The aim of this example is to explore the characteristics and performance of the SSLIB based on L333 cathode material and compare the numerical results with experimental observations.

The following assumptions must be made in order to reduce the computational intensity of the model.

- Effects of lithium anode; the effects of lithium metal on the electrochemical process are neglected in the numerical modeling.
- Mechanical effects; Due to configuration of experimental setup and for simplicity we neglected the contribution of mechanical deformation and stress-diffusion coupling.
- Effects of porosity: The numerical model is constructed based on porous electrode model and it is assumed that the electrolyte flow through the porous media.

The representative configuration of the L333 SSLIB model is shown in Figure 5.9. Each unit cell is composed of electrode and electrolyte phases, the interaction between two phases is represented through an interface model. The full numerical model is constructed from combination of multiple unit cells as shown in Figure 5.10. For numerical simulation purpose periodic boundary conditions are used in both x and y directions and only one unit cell is considered in those directions, while, multiple unit cells are used in z direction. The model is discretized with 15696 hexahedron elements and linear interpolation is used for solution fields. The model parameters and material properties are shown in Table 5.4.

[1] The experimental model developed by Prof. Se-Hee Lee and Dr. Jae Ha Woo.

Unlike thin-film and TiS_2 SSLIB models, the electrochemical interface reactions happens only at cathode/electrolyte interface. This reaction can be described by the BV expression as follows:

$$j_{bv}^{lc} = i_{0_C}\left(\exp\left[\frac{\alpha_C F}{RT}(\eta - U'(c_s))\right] - \exp\left[-\frac{(1-\alpha_C)F}{RT}(\eta - U'(c_s))\right]\right), \tag{5.5}$$

where

$$i_{0_C} = F k_C^s (c_s)^{\alpha_C} (c_l)^{\alpha_C} (c_{s_{max}})^{1-\alpha_C}, \tag{5.6}$$

and k_C^s is the BV reaction rate constant at the cathode/electrolyte interface, α_C is the cathodic transfer coefficient, and $U'(c_s)$ is the open circuit potential.

For numerical simulation the model is discharged with four different discharge rates, namely C/5, C/10, C/20, and C/50. The results are presented in terms of variation of cell potential over discharge time and are compared with experimental observations, as shown in Figure 5.11. There is a good agreement between numerical and experimental results at high discharge rates of C/5 and C/10. However, at lower discharge rate (C/20 and C/50) discrepancies begin to arise and the model predicts a lower discharge time (and thus lower capacity) than the experimental observations. The snapshots of the concentration distribution over the electrode layer for the C/5 and C/50 discharge rates are shown in Figures 5.12 and 5.13.

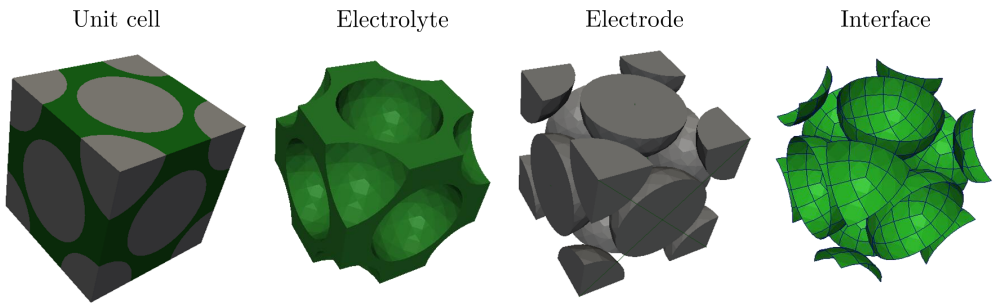

Figure 5.9: The schematic of the unit cell in L333 SSLIB model.

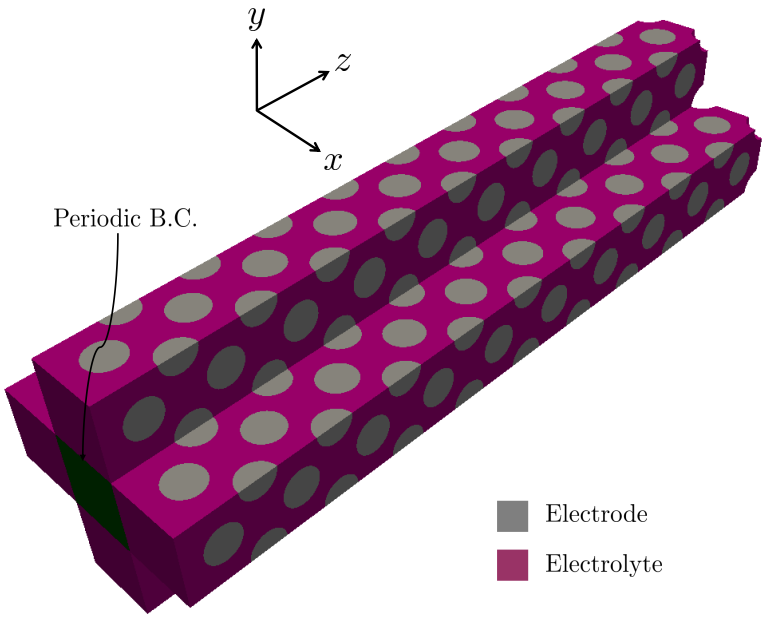

Figure 5.10: The schematic of full L333 SSLIB model composed from multiple unit cells.

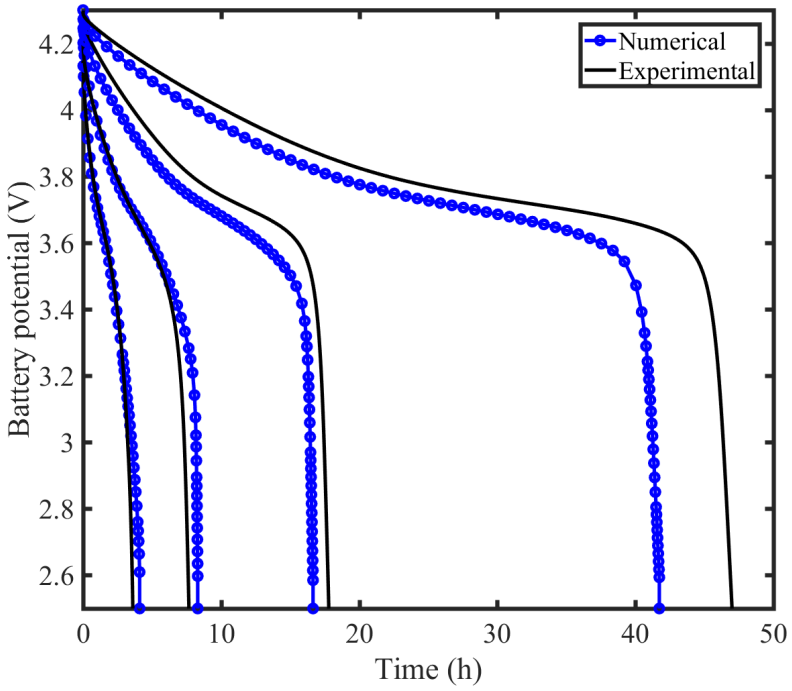

Figure 5.11: Numerical and experimental discharge curves for different discharge rates in the L333 model.

Table 5.4: The L333 model parameters and material properties.

Description	Symbol	Value	Unit
electrolyte thickness	δ_l	9.0×10^{-4}	m
electrode thickness	δ_s	1.0×10^{-4}	m
cross sectional area	a	1.3273×10^{-4}	m
maximum Li concentration	$c_{s_{max}}$	48263	mol m^{-3}
minimum Li concentration	$c_{s_{min}}$	22833	mol m^{-3}
initial Li concentration	c_{s_0}	22833	mol m^{-3}
maximum Li^+ concentration	$c_{l_{max}}$	34588	mol m^{-3}
initial Li^+ concentration	c_{l_0}	34242	mol m^{-3}
electronic conductivity	λ_s	3.6565×10^{-2}	S m^{-1}
diffusion coefficient of Li^+	D_l^+	1.8×10^{-12}	m^2 s^{-1}
diffusion coefficient of n^-	D_l^-	1.8182×10^{-14}	m^2 s^{-1}
diffusion coefficient of Li	D_s	6.3×10^{-14}	m^2 s^{-1}
BV reaction rate	k_A^s	0.0	$mol/m^2 \cdot s$
BV reaction rate	k_C^s	6.117219×10^{-14}	$mol/m^2 \cdot s$
anodic transfer coefficient	α_A	0.4	-
cathodic transfer coefficient	α_C	0.6	-
fraction of free Li	ξ_{c_l}	0.99	-
Faraday's constant	F	96485	C/mol
universal gas constant	R	8.3145	N.m/K.mol
reference temperature	T	303	K
electrode Young's modulus	E_s	1.6×10^5	MPa
electrolyte Young's modulus	E_l	3.719×10^4	MPa
electrode Poisson's ratio	ν_s	0.30	MPa
electrolyte Poisson's ratio	ν_l	0.296	MPa
electrode partial molar volume	Ω_s	4.2855×10^{-5}	$m^3 mol^{-1}$
electrolyte partial molar volume	Ω_l	0.0	$m^3 mol^{-1}$
applied external current	$\mathbf{I}_{\text{ext}}$	var.	A/m^2

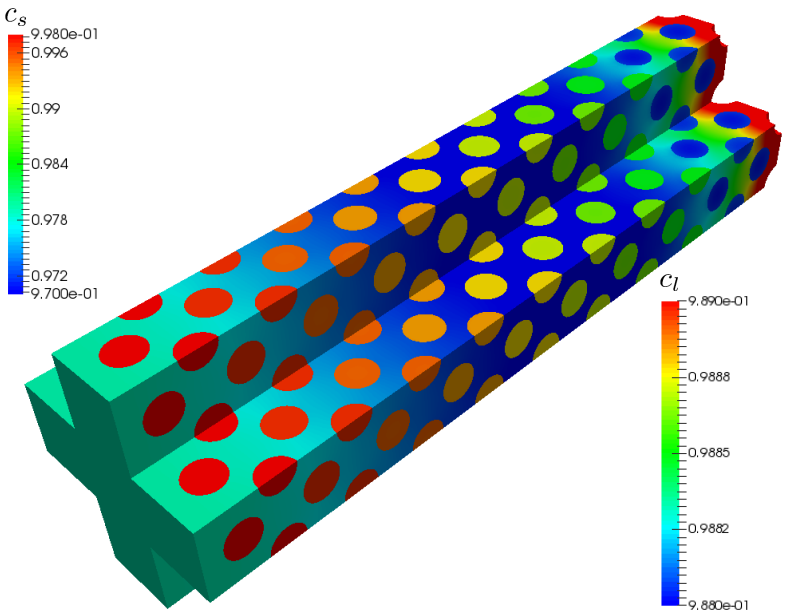

Figure 5.12: Electrode and electrolyte concentrations distribution in the L333 model, discharge rate: C/5.

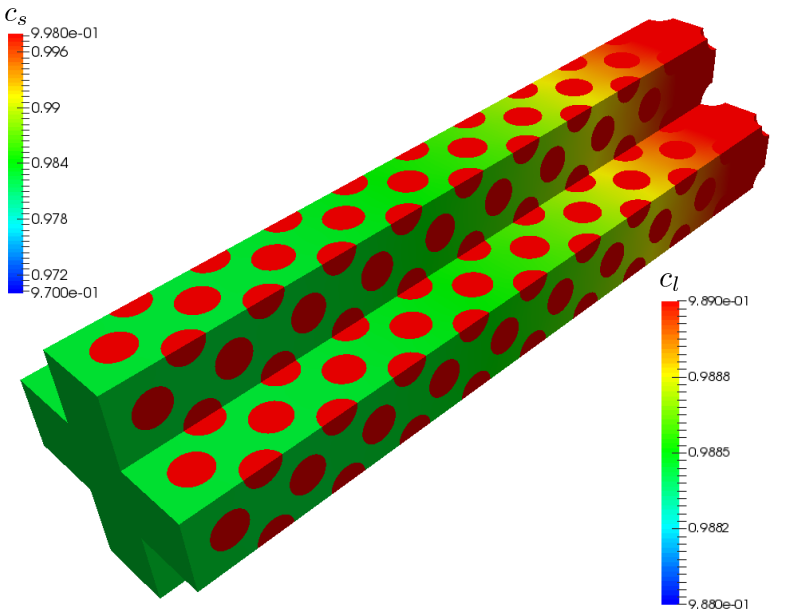

Figure 5.13: Electrode and electrolyte concentrations distribution in the L333 model, discharge rate: C/50.

5.3 Full resolution model - parameter identification

5.3.1 Verification example

In this section, we aim to test the functionality and robustness of the implemented parameter identification framework through a numerical example. To this end, the solid-state thin-film model presented in Section 5.1 has been selected. In order to verify the performance and robustness of the framework we artificially perturbed some material properties for the thin-film model, then we discharged the model simultaneously for all discharge rates used in Section 5.1. The material parameters are perturbed by about 10%. The perturbed material parameters are the electrode diffusion coefficient, D_s, the electrode maximum concentration, $c_{s_{max}}$, the electrode electronic conductivity, λ_s, the diffusion coefficient of Li^+, D_l^+, the diffusion coefficient of n^-, D_l^-, the electrolyte maximum concentration, $c_{l_{max}}$, the BV reaction rates, k_A^s and l_C^s.

The results of initial configuration in the solid-state thin-film battery model , with perturbed material properties, are shown in Figure 5.14. The results show that the perturbed material properties create large discrepancies between numerical and reference results. The comparison between Figures 5.2 and 5.14 reveals the influence of material properties in the SSLIB modeling. The evolution of the objective as well as initial and final views of discharge curves are shown in Figure 5.15. The results show the robustness of the parameter identification framework in capturing the performance of the battery with multiple discharge rates.

5.3.2 parameter identification of TiS_2 model

We wish to extend this framework to study the performance of dense and porous bulk SSLBs mentioned in Section 5.2.1. In these examples our design variables are the electrode and electrolyte material parameters mentioned in Section 5.3.1. The results show that the parameter identification decreases error from near 50% to under 10%. The initial and optimized material parameters for the dense electrode model are presented in Table 5.5. The initial and optimized discharge curves are shown in Figure 5.16. It is clear that there is not a large difference between initial and optimal

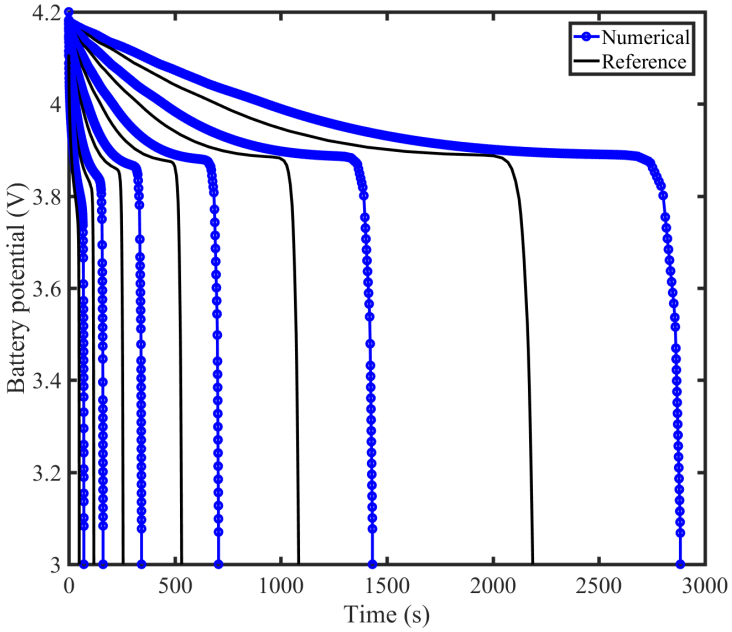

Figure 5.14: The dicharge profiles in the solid-state thin-film model after pertubing the material parameters.

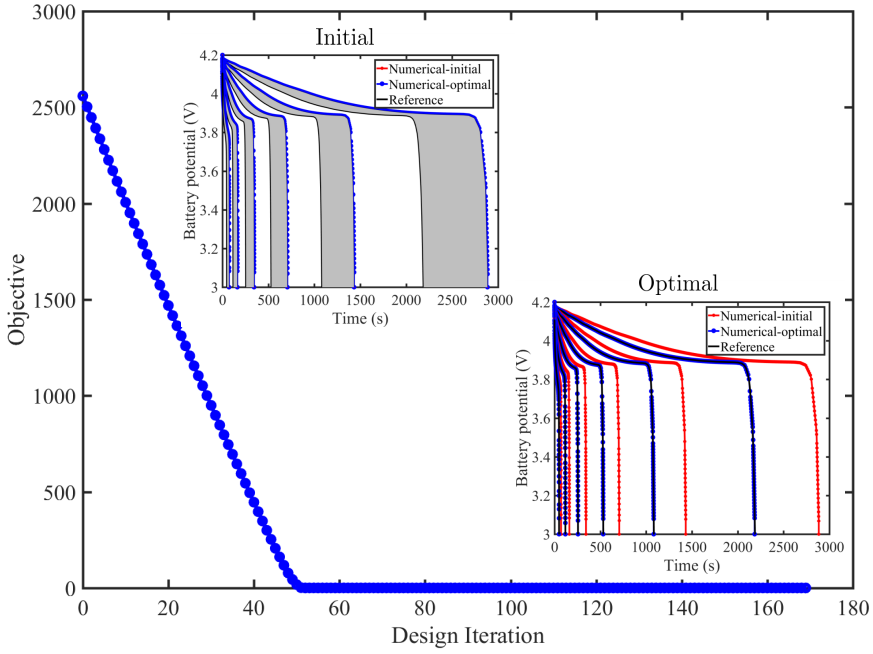

Figure 5.15: The evolution of the objective, initial and optimal design in the thin-film SSLIB.

values, indicating initial design variables were adequate and the model is not sensitive to many of those material parameters. Of all the possible optimized values, the value with the greatest impact is the diffusion coefficient in TiS_2. Interestingly, this is one of the few parameters experimentally derived and not taken from literature. However, there has been documentation on the inadequacies of GITT [151]; additionally a variety of diffusion values for TiS_2 have been reported varying over orders of magnitude [138]. parameter identification for the porous model is displayed in Figure 5.17.

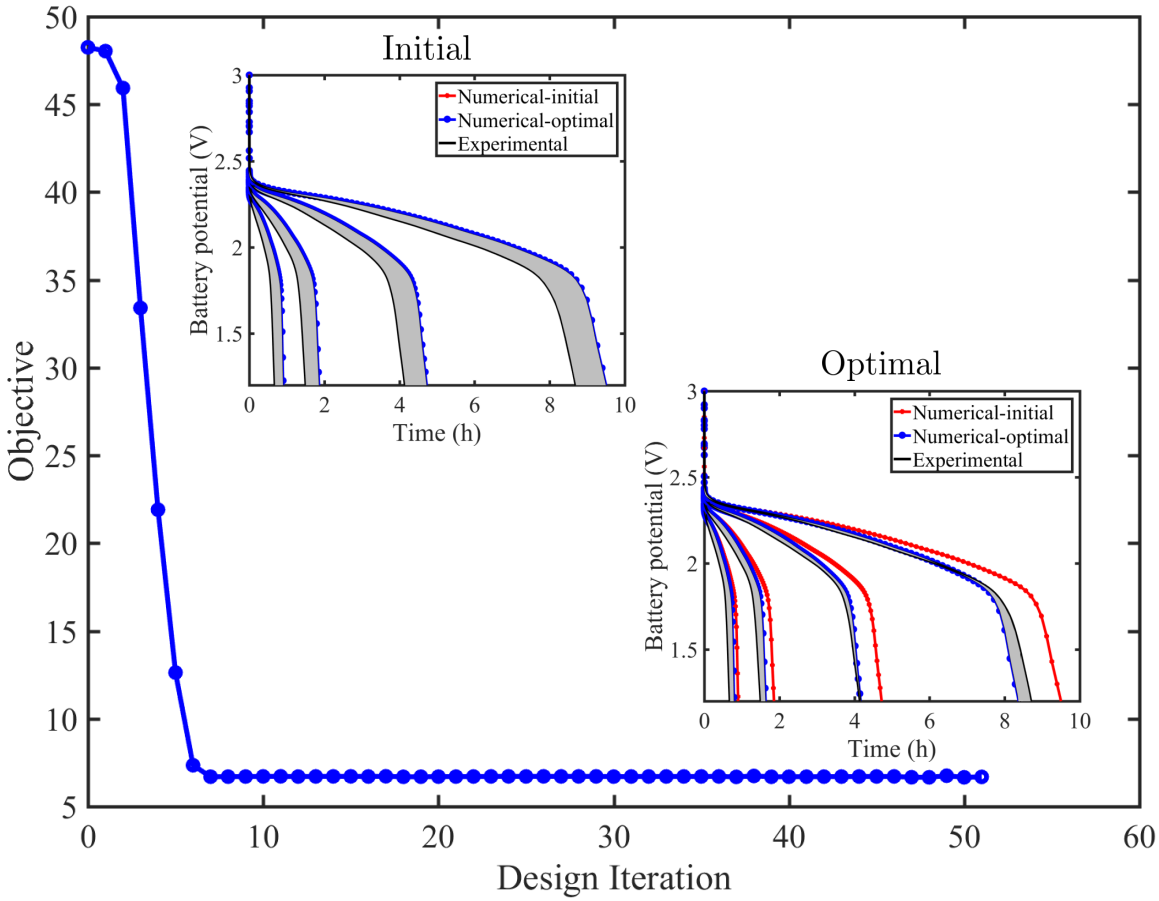

Figure 5.16: The evolution of the objective, initial and optimal design in the dense TiS_2 model (discharge rates: C, C/2, C/5, C/10).

Initial and optimized material parameters are displayed in Table 5.6. The porous model was already fit more accurately by the model than the dense model. Interestingly, parameter identification keeps the diffusion coefficient closer to experimentally derived values than the dense model, as the porous

Table 5.5: Initial and optimized values of material parameters in $LiTiS_2$ for the dense electrode model.

Description	Symbol	Unit	Initial	Optimized
diffusion coeff. of Li	D_s	m^2s^{-1}	10.0×10^{-14}	8.59×10^{-14}
electronic conductivity	λ_s	Sm^{-1}	10.0	9.99
diffusion coeff. of Li^+	D_l^+	m^2s^{-1}	10.0×10^{-13}	9.97×10^{-13}
diffusion coeff. of n^-	D_l^-	m^2s^{-1}	10.1×10^{-15}	10.1×10^{-15}
max. Li^+ concentration	$c_{l_{max}}$	$molm^{-3}$	28032	27951
BV reaction rate	k_C^s	mol/m^2s	5.10×10^{-4}	4.98×10^{-4}
BV reaction rate	k_A^s	mol/m^2s	10.0×10^{-3}	9.99×10^{-3}

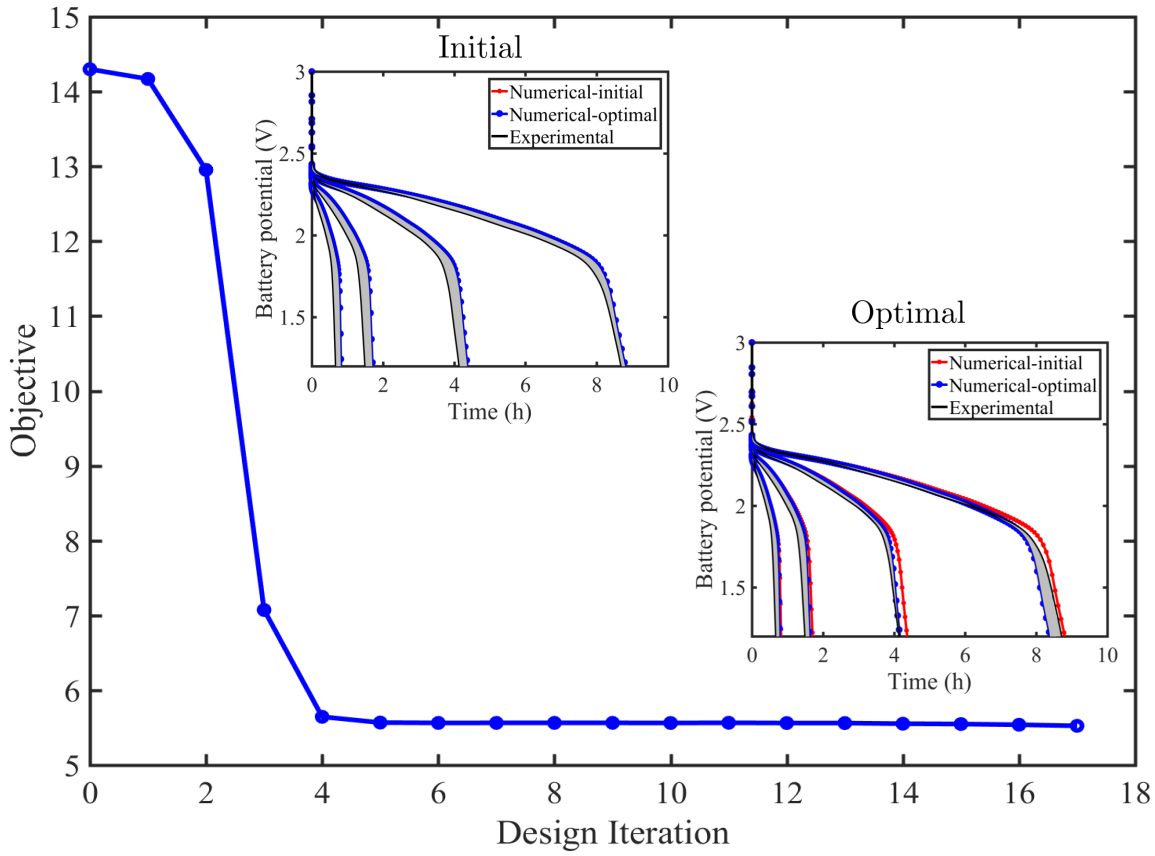

Figure 5.17: The evolution of the objective, initial and optimal design in the porous TiS_2 model (discharge rates: C, C/2, C/5, C/10).

model would be more in line with the GITT experiment performed. The largest parameter changed

in this case is the cathodic reaction rate. The cathodic reaction rate has never been measured for TiS_2 and is little regarded in literature. Therefore, it would be understandable that this value would change. Interestingly, both models converge to approximately the same solution in terms of overall discharge time. However, the dense model must lower the diffusion coefficient in the cathode further. This indicates that the diffusion within the cathode is especially important for bulk solid-state batteries as the system will always be porous so long as manufacturing methods such as sintering are not involved. Therefore, solid systems will hinge upon either achieving an extremely dense structure or increasing the diffusion with the active material. One way to deal with this requirement is adding solid electrolyte into the cathode and reducing the particle size of the active material to reduce the overall diffusion distances. This strategy has been successfully reported in the past [98, 162].

Table 5.6: Initial and optimized values of material parameters in $LiTiS_2$ for the porous electrode model.

Description	Symbol	Unit	Initial	Optimized
diffusion coeff. of Li	D_s	m^2s^{-1}	10.0×10^{-14}	9.53×10^{-14}
electronic conductivity	λ_s	Sm^{-1}	10.0	9.99
diffusion coeff. of Li^+	D_l^+	m^2s^{-1}	10.0×10^{-13}	9.99×10^{-13}
diffusion coeff. of n^-	D_l^-	m^2s^{-1}	10.1×10^{-15}	10.1×10^{-15}
max. Li^+ concentration	$c_{l_{max}}$	$molm^{-3}$	28032	27999
BV reaction rate	k_C^s	mol/m^2s	5.10×10^{-4}	4.62×10^{-4}
BV reaction rate	k_A^s	mol/m^2s	10.0×10^{-3}	9.92×10^{-3}

5.3.3 parameter identification of L333 model

Similar to the TiS_2 model we wish to study the performance of the L333 SSLIB model during changes in material properties. For this model we examine the performance of our parameter identification framework with single and multiple problem. In all cases the design variables are the electrode and electrolyte material properties. First we examined the behavior of the L333 model for a single discharge rate. In particular, we run a full parameter identification analysis for each

individual discharge rates. The initial and optimized design for each discharge rate are shown in Figures 5.18 - 5.21. The results show the capability of the parameter identification framework in minimizing the discrepancy between numerical and experimental solutions. The optimized design parameters are compared for all discharge rates as shown in Figures 5.22 and 5.23. The results show that for some design parameters (e.g. λ_s, $c_{l_{max}}$, D_l^+, D_l^-, k_C^s, and A_c) there is similar trend for all discharge rates, however, the optimized values are different between discharge rates.

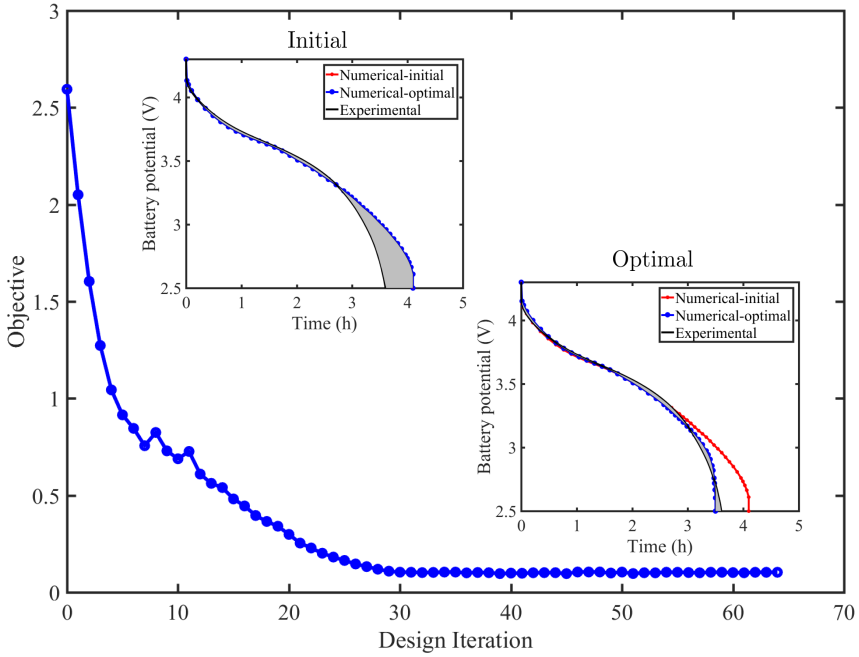

Figure 5.18: The evolution of the objective, initial and optimal design in the L333 model, C/5.

Next, we combine two upper (C/5 and C/10) and two lower (C/20 and C/50) discharge rates and perform parameter identification analysis for multiple problems. The evolution of the objective function as well as the initial and optimized designs are shown in Figures 5.24 and 5.25. The results show the significant decrease of the objective for upper discharge rates, however, small discrepancies can be observed for lower discharge rates. Finally, we combine all discharge rates and perform a parameter identification analysis for multiple problems considering all discharge rates. The evolution of the objective function as well as the initial and optimal designs are shown in

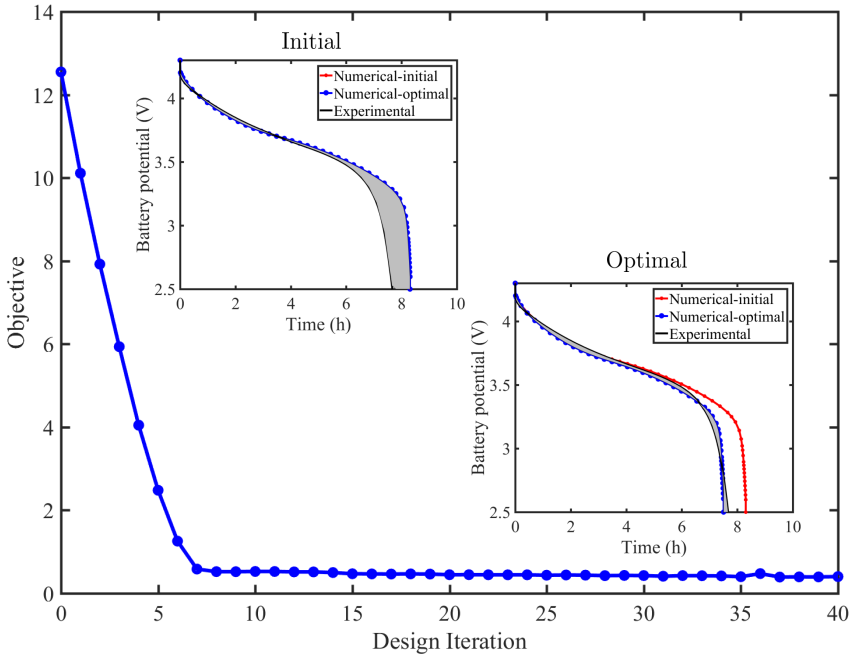

Figure 5.19: The evolution of the objective, initial and optimal design in the L333 model, C/10.

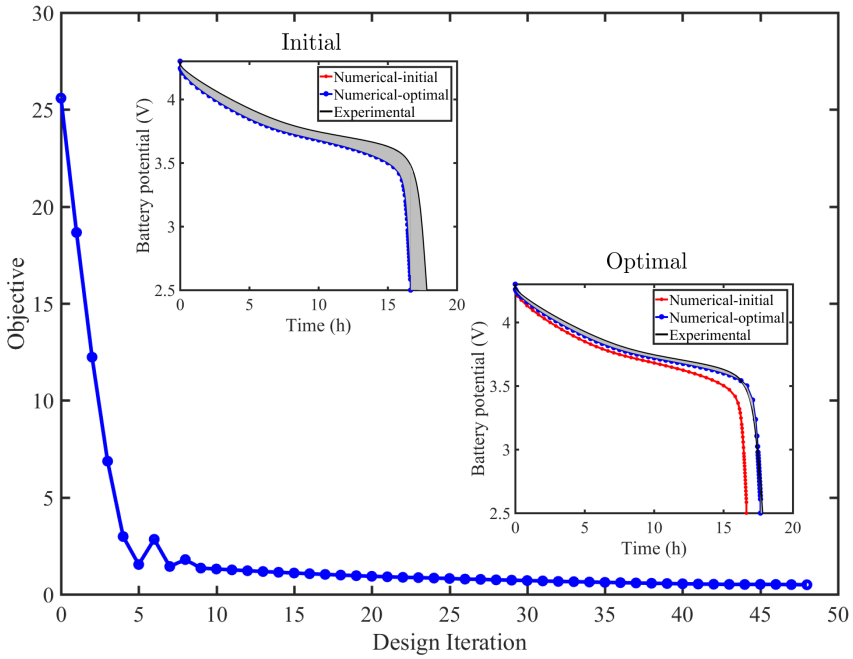

Figure 5.20: The evolution of the objective, initial and optimal design in the L333 model, C/20.

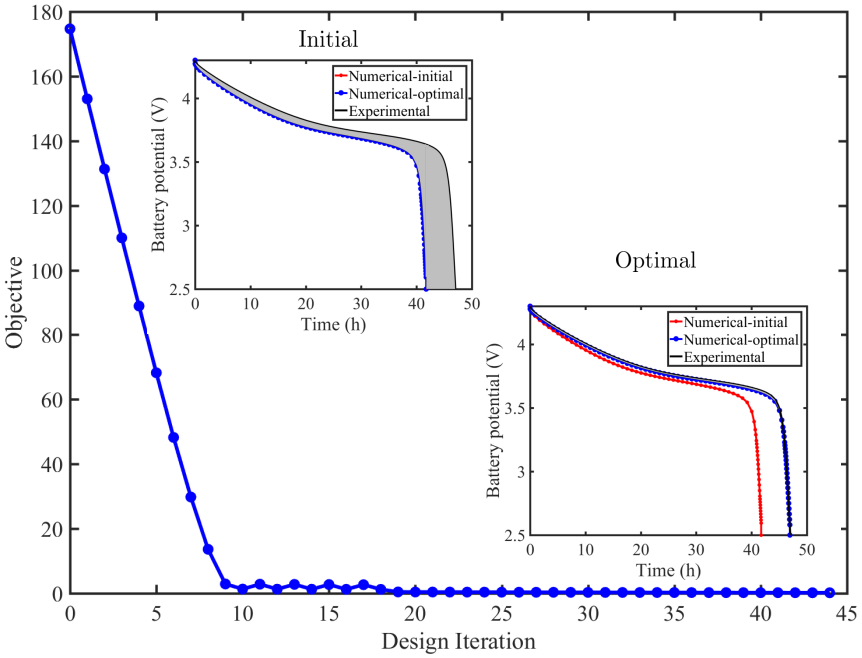

Figure 5.21: The evolution of the objective, initial and optimal design in the L333 model, C/50.

Figure 5.26. While there is a significant decrease in the objective value, but there is a considerable discrepancies between the optimized results and experimental observations, especially for lower discharge rates.

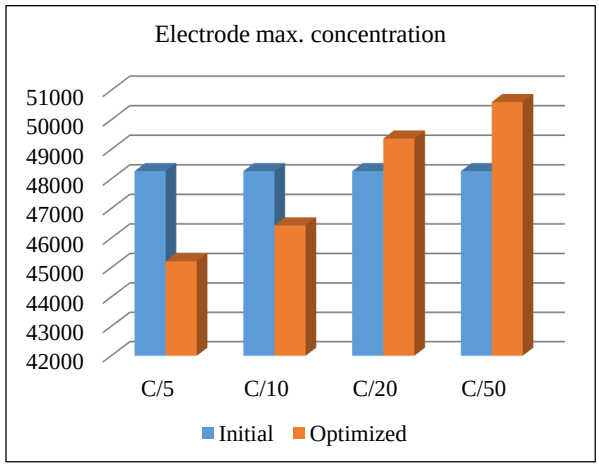

(a) $c_{s_{max}}$

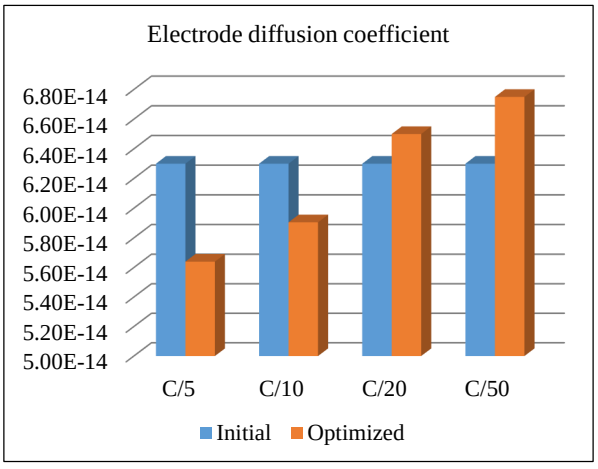

(b) D_s

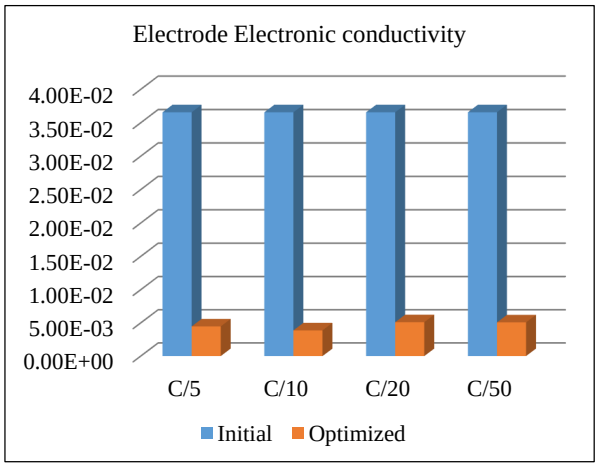

(c) λ_s

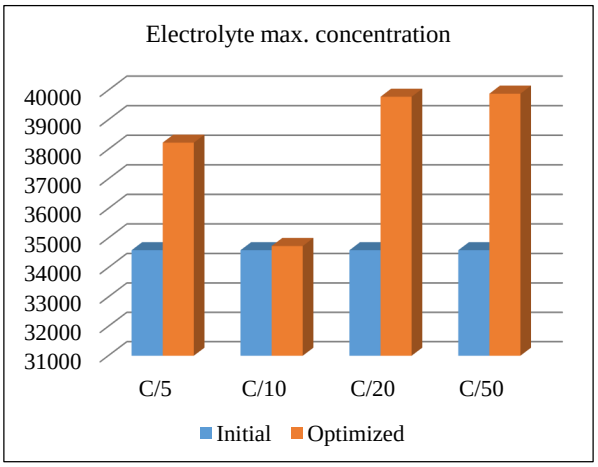

(d) $c_{l_{max}}$

Figure 5.22: Comparison of the initial and optimized values of material properties for a single parameter identification problem in L333 SSLIB model.

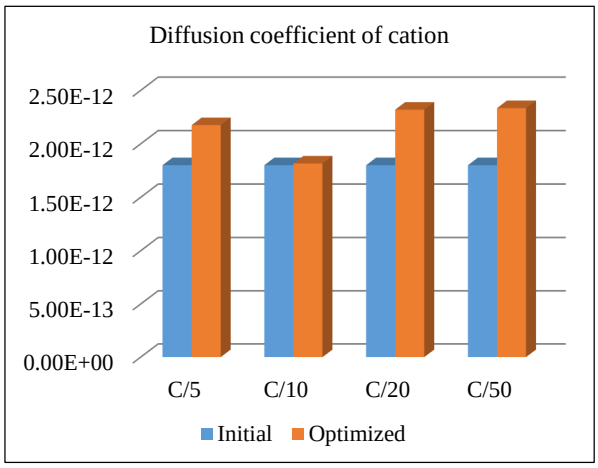

(a) D_l^+

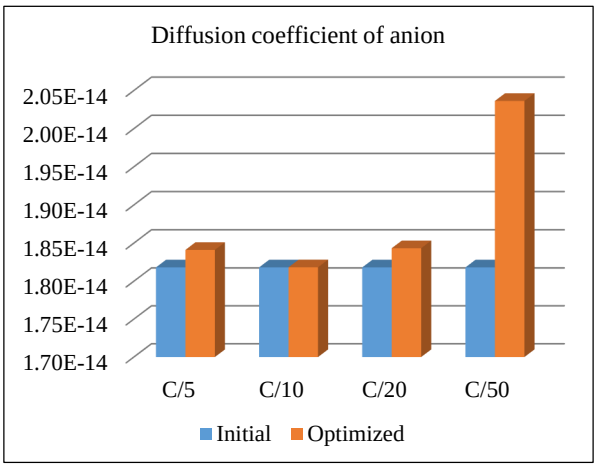

(b) D_l^-

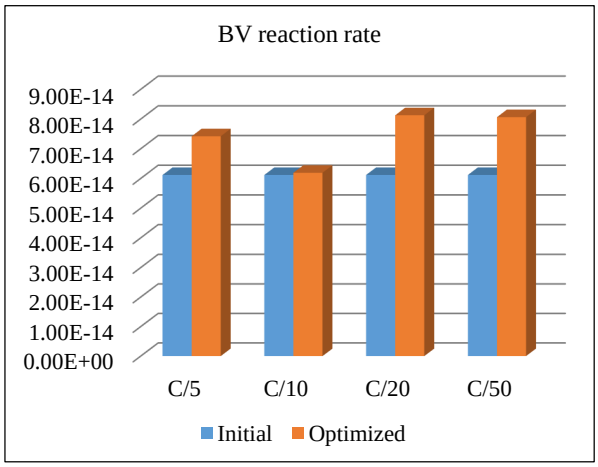

(c) k_C^s

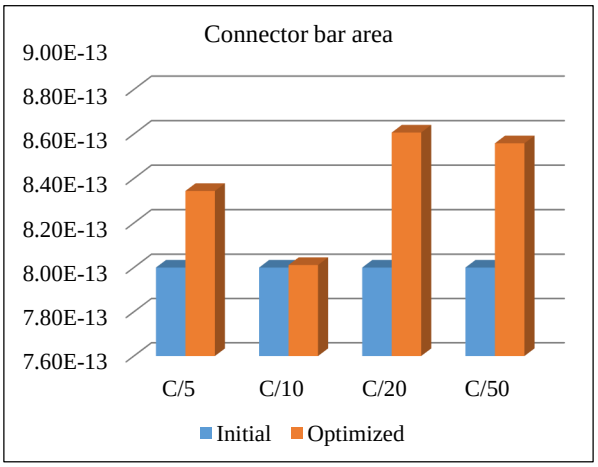

(d) A_c

Figure 5.23: Comparison of the initial and optimized values of material properties for a single parameter identification problem in L333 SSLIB model.

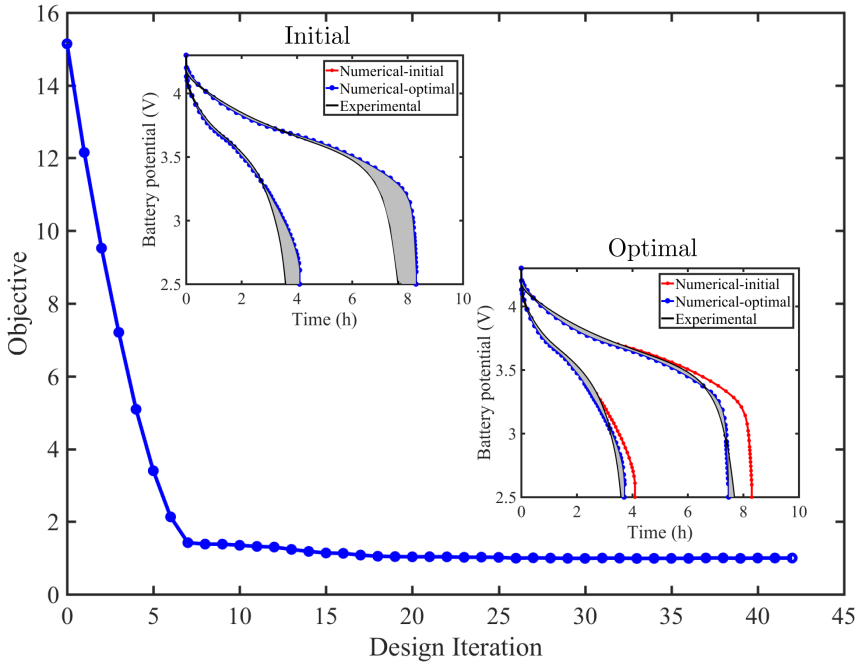

Figure 5.24: The evolution of the objective, initial and optimal design in the L333 model, C/5, C/10.

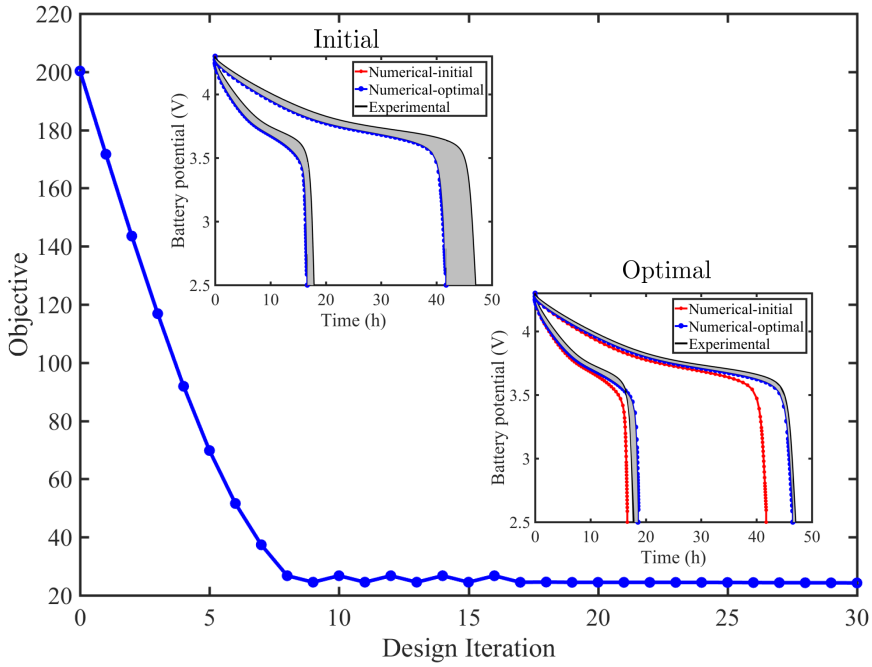

Figure 5.25: The evolution of the objective, initial and optimal design in the L333 model, C/20, C/50.

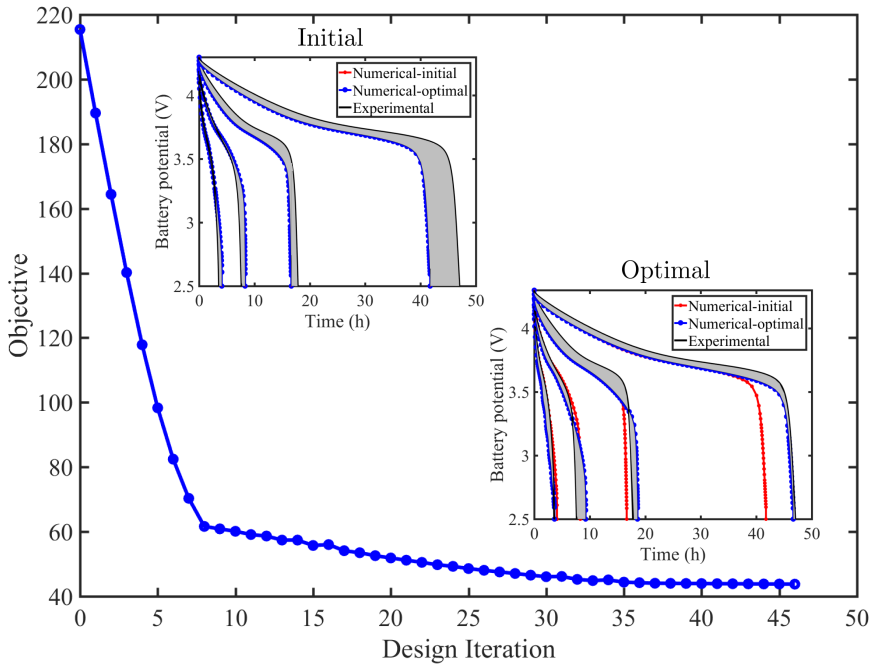

Figure 5.26: The evolution of the objective, initial and optimal design in the L333 model.

5.4 Numerical examples for Non-local damage model

In order to evaluate the performance of the non-local damage formulation, series of analytical and numerical examples are provided for structural problems. To this end, first an analytical example is described for a one-dimensional bar and the results are compared with numerical solutions. The influence of the structure geometric configuration on damage evolution and the zone of influence is studied by several numerical examples. In addition, the accuracy of solutions for different mesh configurations is studied by mesh refinement for a three-dimensional example. Finally, the effects of gradient parameter (c) on the width of damage influence zone are investigated for different gradient parameters.

5.4.1 Analytical solution for non-local damage model

An analytical example is provided to evaluate the performance of non-local damage formulation. This example has originally been developed by [116] for gradient enhanced damage model (non-local damage model) and utilized here to evaluate the performance of finite element model based on non-local damage formulation. To this end, a bar with length L and isotropic material properties is considered. The bar is subjected to a uniaxial and pure tensile loading by using prescribed displacement at both ends. While the material properties are considered uniform for the entire bar, the cross-sectional area, A, has been reduced by a factor (1 - α) for the length l. The purpose of the reduction in the cross-sectional area is to trigger localization of the deformation at the middle of the bar. The schematic of the described 3D beam with damage influence zone is shown in Figure 5.27.

In order to calculate the width of damage influence zone, w, and damage variable, an analytical solution is derived for the one-dimensional case [116]. For the one-dimensional case the equivalent local strain $\boldsymbol{\varepsilon}_{\text{eq}}$ is set to the axial strain $\boldsymbol{\varepsilon}$ for uniaxial condition, thus, the differentiation of Equation (2.103) can be written as:

$$\bar{\varepsilon}_{\text{eq}} - c\frac{d^2\bar{\varepsilon}_{\text{eq}}}{dx^2} = \boldsymbol{\varepsilon}. \tag{5.7}$$

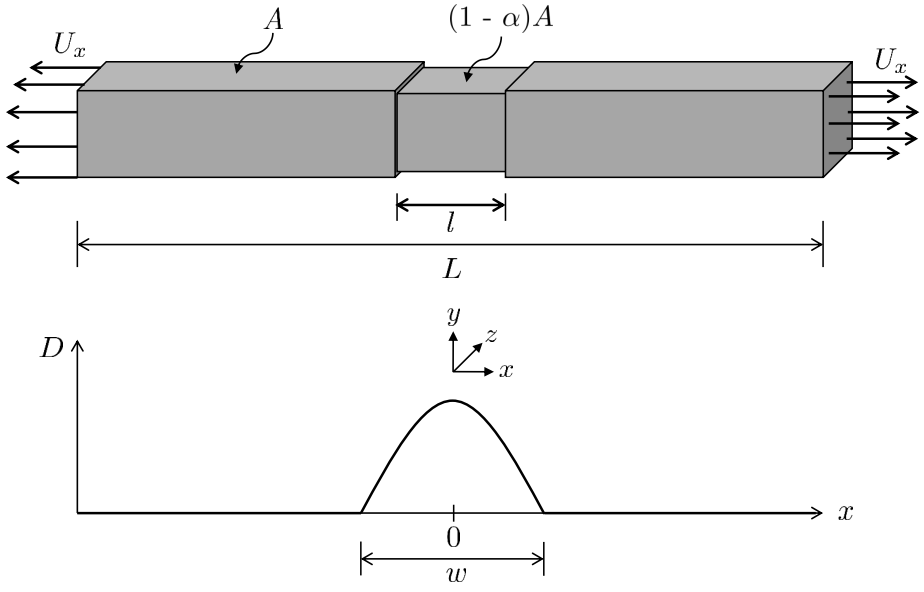

Figure 5.27: Schematic of 3D beam with damage influence zone for non-local damage model.

By employing the stress-strain relation

$$\sigma = (1 - D)E\boldsymbol{\varepsilon}, \tag{5.8}$$

where D is the damage variable. Substituting Equation (5.8) into (5.7) gives:

$$\bar{\varepsilon}_{\text{eq}} - c\frac{d^2\bar{\varepsilon}_{\text{eq}}}{dx^2} = \frac{\sigma}{(1 - D)E}. \tag{5.9}$$

The boundary condition for non-local strain implies that

$$\frac{d\bar{\varepsilon}_{\text{eq}}}{dx} = 0, \tag{5.10}$$

which should be imposed at the end of bar. The reduction in cross-sectional area in the beam implies that the actual stress in the weakened zone should be different compare to the other parts. Considering the symmetry condition, only one half of the bar is considered for the analytical derivation. On the interval $(\frac{1}{2}l, \frac{1}{2}L)$ one can define the stress as follows:

$$\sigma = (1 - \beta)E\kappa_i \qquad \text{with} \qquad \beta > 0, \tag{5.11}$$

where κ_i is the initial value of damage history parameter. In the weakened zone the length l is assumed to be smaller than the width of damage influence zone, w, the stress can be, therefore, is defined by

$$\sigma = (1+\gamma)E\kappa_i \qquad \text{with} \qquad \gamma > 0. \tag{5.12}$$

In the undamaged zone $(\frac{1}{2}w, \frac{1}{2}L)$ the damage variable $D = 0$, substituting $D = 0$ in the Equation (5.11) yields the linear form of differential equation

$$\bar{\varepsilon}_{\text{eq}} - c\frac{d^2\bar{\varepsilon}_{\text{eq}}}{dx^2} = (1-\beta)\kappa_i \tag{5.13}$$

Solving this linear differential equation results in the following solution

$$\bar{\varepsilon}_{\text{eq}}(x) = (1-\beta)\kappa_i + A_1 \exp\left(\frac{1}{\sqrt{c}}x\right) + A_2 \exp\left(-\frac{1}{\sqrt{c}}x\right) \qquad \text{for} \qquad \frac{1}{2}w < x \leq \frac{1}{2}L \tag{5.14}$$

where A_1 and A_2 are the integration constants. In the area where damage is increasing, the history parameter, κ, equals to the non-local strain, $\bar{\varepsilon}_{\text{eq}}$. Using this relationship and substituting damage evolution law (2.105) into Equation (5.9) the following differential equation for damage on interval $(0,\ \frac{1}{2}w)$ can be concluded

$$\left(1 - \frac{\sigma_{xx}}{E\kappa_i}\right)\bar{\varepsilon}_{\text{eq}} - c\frac{d^2\bar{\varepsilon}_{\text{eq}}}{dx^2} = 0 \tag{5.15}$$

By substituting the definition of stress for the weakened and unweakened zones two solutions for the differential equation (5.15) can be found as follow

$$\bar{\varepsilon}_{\text{eq}}(x) = B_1 \exp\left(\sqrt{\frac{\beta}{c}}x\right) + B_2 \exp\left(-\sqrt{\frac{\beta}{c}}x\right) \qquad \text{for} \quad \frac{1}{2}l < x \leq \frac{l}{2}w \tag{5.16}$$

$$\bar{\varepsilon}_{\text{eq}}(x) = C\cos\left(\sqrt{\frac{\gamma}{c}}x\right) \qquad \text{for} \quad 0 \leq x \leq \frac{l}{2}l \tag{5.17}$$

The integration constants, A_1, A_2, B_1, B_2, C, the stress factors β, γ, and the width of damage influence zone width, w, can be derived from boundary and continuity requirements. At $x = \frac{1}{2}l$ and $x = \frac{1}{2}w$, the continuity of the displacement field imposes the continuity of the non-local strain and its first derivative as follows

$$B_1 \exp\left(\frac{1}{2}l\sqrt{\frac{\beta}{c}}\right) + B_2 \exp\left(-\frac{1}{2}l\sqrt{\frac{\beta}{c}}\right) = C\cos\left(\frac{1}{2}l\sqrt{\frac{\gamma}{c}}\right) \qquad \text{at} \quad x = \frac{l}{2}l \tag{5.18}$$

$$\begin{aligned} B_1 \exp\left(\frac{1}{2}w\sqrt{\frac{\beta}{c}}\right) + B_2 \exp\left(-\frac{1}{2}w\sqrt{\frac{\beta}{c}}\right) \\ = (1-\beta)\kappa_i + A_1 \exp\left(\frac{1}{2}w\frac{1}{\sqrt{c}}\right) + A_2 \exp\left(-\frac{1}{2}w\frac{1}{\sqrt{c}}\right) \qquad \text{at} \quad x = \frac{l}{2}w \end{aligned} \tag{5.19}$$

and for the first derivative

$$\sqrt{\frac{\beta}{c}}B_1 \exp\left(\frac{1}{2}l\sqrt{\frac{\beta}{c}}\right) - \sqrt{\frac{\beta}{c}}B_2 \exp\left(-\frac{1}{2}l\sqrt{\frac{\beta}{c}}\right) = -C\sqrt{\frac{\gamma}{c}}\sin\left(\frac{1}{2}l\sqrt{\frac{\gamma}{c}}\right) \qquad \text{at} \quad x = \frac{l}{2}l \tag{5.20}$$

$$\begin{aligned} \sqrt{\frac{\beta}{c}}B_1 \exp\left(\frac{1}{2}w\sqrt{\frac{\beta}{c}}\right) - \sqrt{\frac{\beta}{c}}B_2 \exp\left(-\frac{1}{2}w\sqrt{\frac{\beta}{c}}\right) \\ \frac{1}{\sqrt{c}}A_1 \exp\left(\frac{1}{2}w\frac{1}{\sqrt{c}}\right) - \frac{1}{\sqrt{c}}A_2 \exp\left(-\frac{1}{2}w\frac{1}{\sqrt{c}}\right) \qquad \text{at} \quad x = \frac{l}{2}w \end{aligned} \tag{5.21}$$

Furthermore, at $x = \frac{1}{2}w$ the non-local strain must be equal to the initial value of the history parameter, κ_i,

$$\kappa_i = B_1 \exp\left(\frac{1}{2}w\sqrt{\frac{\beta}{c}}\right) + B_2 \exp\left(-\frac{1}{2}w\sqrt{\frac{\beta}{c}}\right) \qquad \text{at} \quad x = \frac{l}{2}w \tag{5.22}$$

and the discontinuity in the stress fields at $x = \frac{1}{2}l$ should be proportional with the surface reduction as follows:

$$\frac{(1-\beta)E\kappa_i}{(1+\gamma)E\kappa_i} = \frac{(1-\alpha)A}{A} \quad \Rightarrow \quad \frac{(1-\beta)}{(1+\gamma)} = \frac{(1-\alpha)}{1} \quad \Rightarrow \quad (1-\beta) = (1+\gamma)(1-\alpha) \tag{5.23}$$

At the end of the bar, the boundary condition, $\nabla\bar{\boldsymbol{\varepsilon}}_{\text{eq}} \cdot \hat{\mathbf{n}} = 0$, is applied in the following setting

$$\frac{1}{\sqrt{c}}A_1 \exp\left(\frac{1}{2}L\frac{1}{\sqrt{c}}\right) - \frac{1}{\sqrt{c}}A_2 \exp\left(-\frac{1}{2}L\frac{1}{\sqrt{c}}\right) = 0 \qquad \text{at} \quad x = \frac{l}{2}L \tag{5.24}$$

Finally, at the end of the bar a prescribed displacement, $\frac{1}{2}\Delta L$, is applied. This is related to the non-local strain by

$$\begin{aligned} \frac{1}{2}\Delta L = \int_0^{\frac{1}{2}L} \boldsymbol{\varepsilon}\, dx = \int_0^{\frac{1}{2}L} \left(\bar{\boldsymbol{\varepsilon}}_{\text{eq}} - c\frac{d^2\bar{\boldsymbol{\varepsilon}}_{\text{eq}}}{dx^2}\right) dx \\ = \int_0^{\frac{1}{2}L} \bar{\boldsymbol{\varepsilon}}_{\text{eq}}\, dx - c\frac{d\bar{\boldsymbol{\varepsilon}}_{\text{eq}}}{dx}\Big|_0^{\frac{1}{2}L} = \int_0^{\frac{1}{2}L} \bar{\boldsymbol{\varepsilon}}_{\text{eq}}\, dx = \int_0^{\frac{1}{2}l} \bar{\boldsymbol{\varepsilon}}_{\text{eq}}\, dx + \int_{\frac{1}{2}l}^{\frac{1}{2}w} \bar{\boldsymbol{\varepsilon}}_{\text{eq}}\, dx + \int_{\frac{1}{2}w}^{\frac{1}{2}L} \bar{\boldsymbol{\varepsilon}}_{\text{eq}}\, dx \end{aligned} \tag{5.25}$$

By substituting the non-local strains

$$\begin{aligned}\frac{1}{2}\Delta L = &\int_0^{\frac{1}{2}l} C\cos\left(\sqrt{\frac{\gamma}{c}}x\right)\ dx \\ &+\int_{\frac{1}{2}l}^{\frac{1}{2}w} B_1\exp\left(\sqrt{\frac{\beta}{c}}x\right)+B_2\exp\left(-\sqrt{\frac{\beta}{c}}x\right)\ dx \\ &+\int_{\frac{1}{2}w}^{\frac{1}{2}L}(1-\beta)\kappa_i+A_1\exp\left(\frac{1}{\sqrt{c}}x\right)+A_2\exp\left(-\frac{1}{\sqrt{c}}x\right)\ dx\end{aligned} \tag{5.26}$$

This condition can be simplified as follows

$$\begin{aligned}\frac{1}{2}\Delta L = &\frac{C\sin\left(\frac{1}{2}l\sqrt{\frac{\gamma}{c}}\right)}{\sqrt{\frac{\gamma}{c}}} \\ &+\frac{B_1\left(\exp\left(\frac{1}{2}w\sqrt{\frac{\beta}{c}}\right)-\exp\left(\frac{1}{2}l\sqrt{\frac{\beta}{c}}\right)\right)}{\sqrt{\frac{\beta}{c}}}+\frac{B_2\left(\exp\left(-\frac{1}{2}l\sqrt{\frac{\beta}{c}}\right)-\exp\left(-\frac{1}{2}w\sqrt{\frac{\beta}{c}}\right)\right)}{\sqrt{\frac{\beta}{c}}} \\ &+A_1\sqrt{c}\left(\exp\left(\frac{1}{2\sqrt{c}}L\right)-\exp\left(\frac{1}{2\sqrt{c}}w\right)\right)+A_2\sqrt{c}\left(\exp\left(-\frac{1}{2\sqrt{c}}w\right)-\exp\left(-\frac{1}{2\sqrt{c}}L\right)\right) \\ &+\frac{1}{2}(1-\beta)\kappa_i(L-w)\end{aligned} \tag{5.27}$$

In order to compute integration constants, stress factors, and the width of damage influence zone, Equations (5.18 - 5.27) can be solved numerically for particular values of geometry and material parameters. Then the strain and damage variable can be computed using the solution of non-local strain.

For the finite element simulation, the length $L = 100mm$ and the cross-sectional area $A = 10mm^2$ are assigned to the model. The length of the weakened zone is set to $l = 10mm$ and the cross-sectional reduction factor, α, is set to 0.1. Linear isotropic material with Young's modulus $E = 2000\ N/mm^2$ and Poisson's ration $\nu = 0.0$ is considered. In the numerical simulation the initial damage history parameter $\kappa_0 = 10^{-4}$ and the gradient parameter in Helmholtz equation is set to $c = 1mm^2$. The applied displacement is $U_x = 0.05mm$. For finite element simulation a one-dimensional model is considered, quadratic elements are used to predict the displacement field, while, linear interpolation is used to solve the Helmholtz equation for non-local damage variables. The results of finite element simulation are compared with analytical solutions for the damage variable and local strain. The distributions of the damage variable and local strain over the length

of the bar are shown in Figures 5.28 and 5.29. The results show that there is excellent agreement between analytical and numerical solutions. The results also reveal that there is high concentration of damage and strain in the weakened zone and extreme damage occurs in the weakened zone which is associated with localization of the local strain.

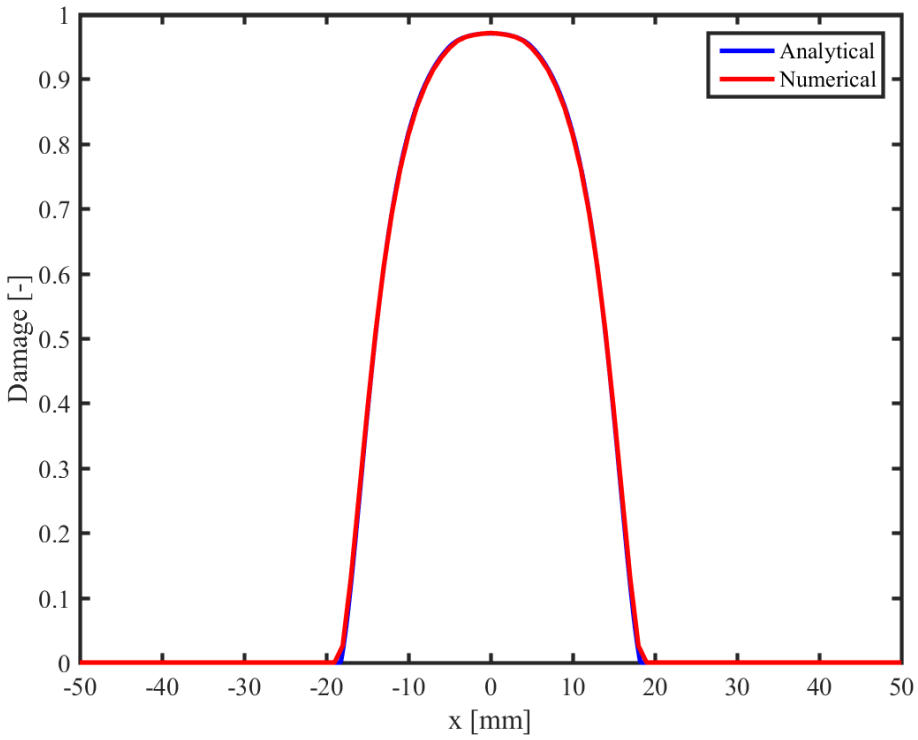

Figure 5.28: Plot of the distribution of damage variable in one-dimensional bar model.

5.4.2 Frustum beam model

To evaluate the performance of the non-local damage model in multi-dimensional cases a three-dimensional finite element example is provided. Two connected Frustum beam with total length L is considered, which is subjected to a uniaxial and pure tensile loading using prescribed displacement at both ends. The material properties are uniform for the entire bar, however, the cross-sectional area, A, is varying through the length by factor α, where α is the ratio between

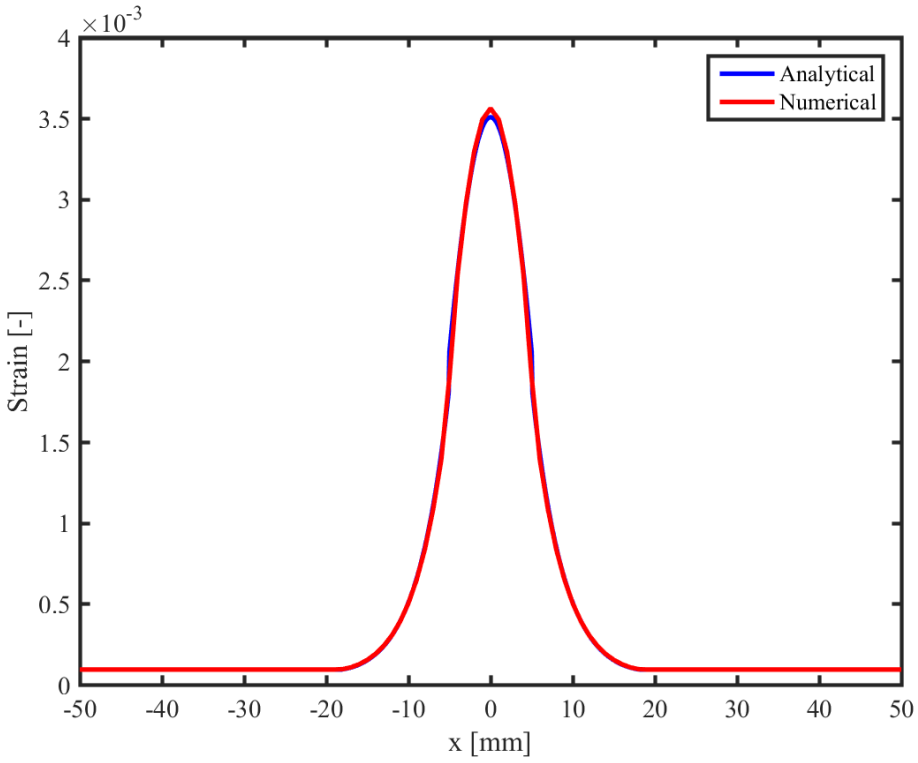

Figure 5.29: Plot of the distribution of local strain along the length of the bar.

the start and end cross sections. The schematic and 2D view of the beam is shown in Figure 5.30. For finite element simulation, the length $L = 20mm$ and the radius of sectional area $r = 2mm$ are assigned to the model. The cross section reduction factor, α, is set to $0.2 \leq \alpha \leq 1.0$. Linear isotropic material with Young's modulus $E = 20000\ N/mm^2$ and Poisson's ration $\nu = 0.0$ is considered. For the damage model, linear damage evolution law (2.105) with initial damage history parameter $\kappa_0 = 10^{-4}$ and the gradient parameter $c = 0.25mm^2$ is considered. The applied displacement is set to $U_x = 0.025mm$. Due to symmetry only one eighth of the model is considered, the quadratic interpolation with hexahedron element is used for displacement field, while, the linear interpolation with 8-node element is used for approximation of the non-local damage variables. The evolution of the non-local strain as a function of α is shown in Figure 5.31. The results show that with a increasing α the influence of the non-local strain is increased and eventually for $\alpha = 1.0$ a uniform

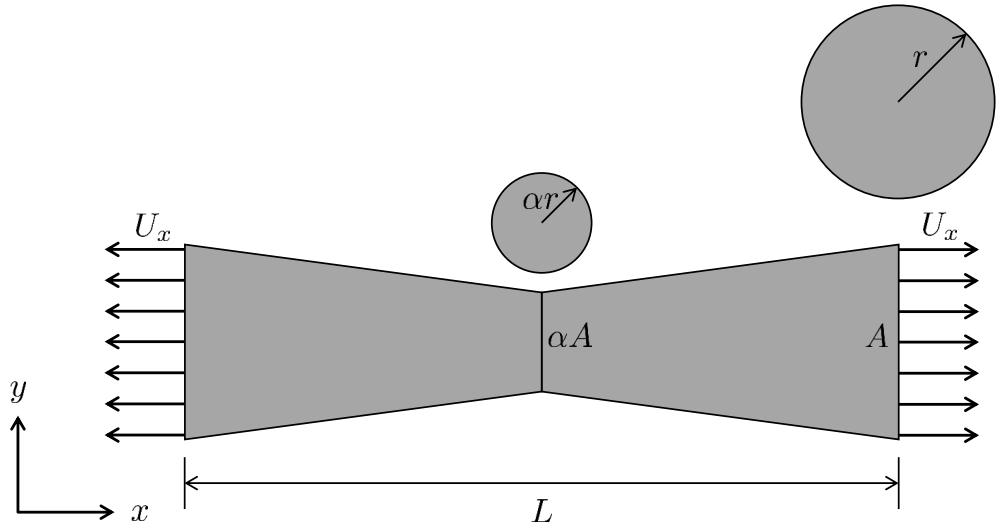

Figure 5.30: Schematic and 2D view of the Frustum beam.

non-local strain is observed. The zone of influence of the non-local strain along the length of the bar for different α is shown in Figure 5.32. As it can be seen for small values of α the localization of the strain can be observed, however, by increasing the α ratio the zone of influence is increased and the localization is decreased. The variation of the non-local damage along the length of bar for different α is shown in Fig. 5.33. It can be seen for a uniform cross section a uniform damage can be observed. Finally, the evolution of the local strain is shown in Figure 5.34. Compared to the non-local strain the localization effect can be seen in the local strain plot and higher value in the local strain plot can be observed for small α.

5.4.2.1 Mesh refinement

In order to evaluate the influence of geometric configuration on the overall performance of non-local damage model, a mesh refinement study has been performed. To this end, the Frustum beam model with different mesh configurations, i.e. $5 \times 5 \times 15$, $7 \times 7 \times 19$, $9 \times 9 \times 23$, $11 \times 11 \times 27$, is considered. The results of the mesh refinement study are presented in terms of variation of damage variable, local and non-local strains along the length of the beam, see Figures (5.35-5.37). The results show that there is a negligible sensitivity of damage evolution formulation with respect to

the size of element and an accurate solution can be captured even with coarse mesh configuration.

5.4.2.2 Influence of Helmholtz gradient parameter

In order to investigate the influence of the gradient parameter, c, in the Helmholtz equation, a series of simulations with different values of c have been performed. To this end, the Frustum beam model is considered and the simulation is performed with $c = 0.0625mm^2$, $c = 0.125mm^2$, $c = 0.25mm^2$, and $c = 0.5mm^2$. The results are presented in terms of variation of the damage variable, local and non-local strains along the length of the beam, see Figures (5.38-5.40). The results show that with increasing the c parameter the damage zone of influence is growing, while, localization effects can be observed for smaller c.

5.4.3 Double notched plates

In the other example, two symmetric and non-symmetric double notched plates with total length (L) and different locations for cylindrical hole are considered. The plates are subjected to uniaxial and pure tensile loading by using prescribed displacement at the ends. The schematic of the plates and boundary conditions are shown in Fig. 5.41. The material properties are uniform for the entire plate. Linear isotropic material with Young's modulus $E = 20000N/mm^2$ and Poisson's ration $\nu = 0.0$ is considered. The applied displacement is set to $U_y = 1.2mm$. The dimensions of the plates are set to $L = 10\ mm$, $t = 2\ mm$ and $r = 2\ mm$ that represent the length, the thickness and the radius of the hole, respectively. The distribution and profiles of of non-local strain are shown in Fig. 5.42 and 5.43. The localization of strain can be observed in both cases.

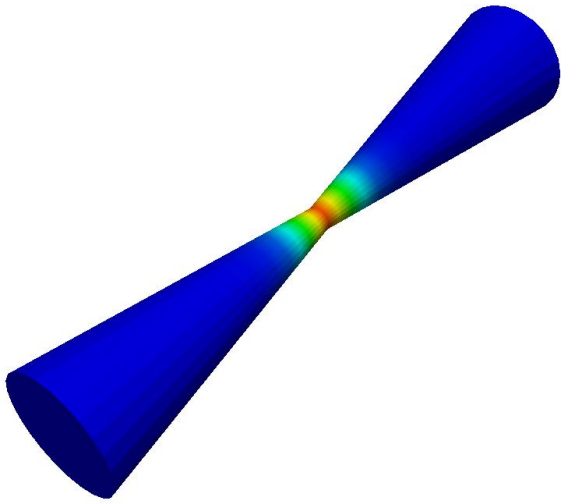

(a) Non-local strain distribution for $\alpha = 0.2$.

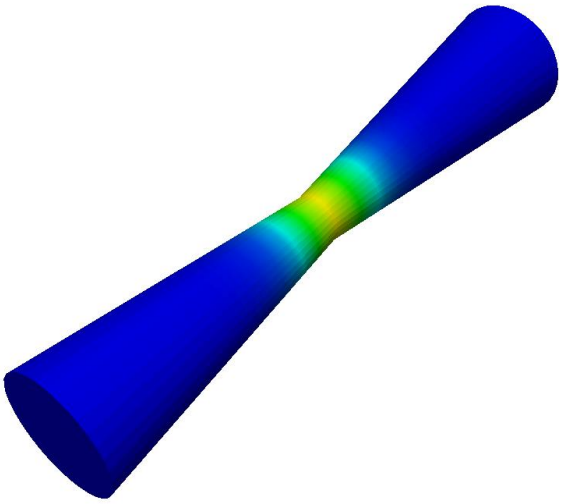

(b) Non-local strain distribution for $\alpha = 0.4$.

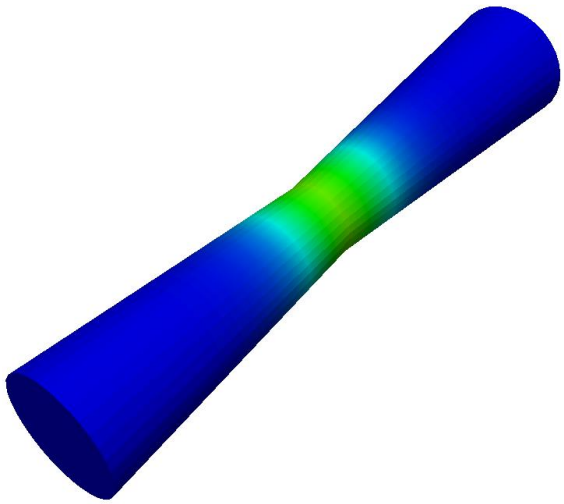

(c) Non-local strain distribution for $\alpha = 0.6$.

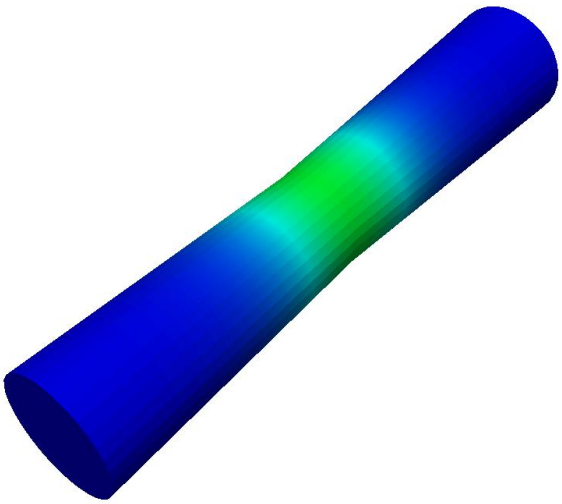

(d) Non-local strain distribution for $\alpha = 0.8$.

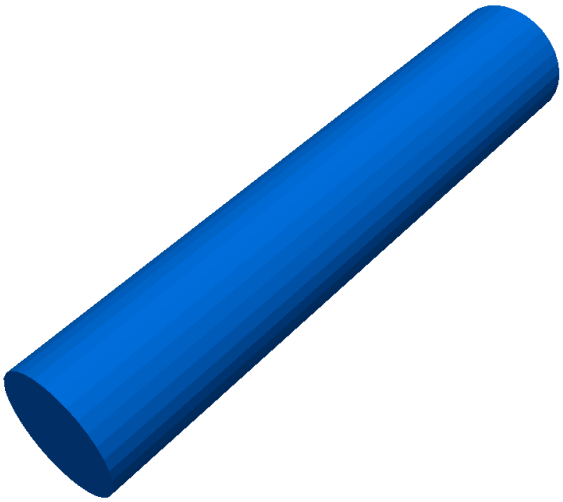

(e) Non-local strain distribution for $\alpha = 1.0$.

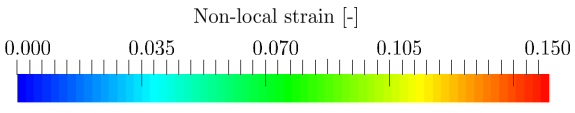

(f) Legend.

Figure 5.31: Evolution of non-local strain with α.

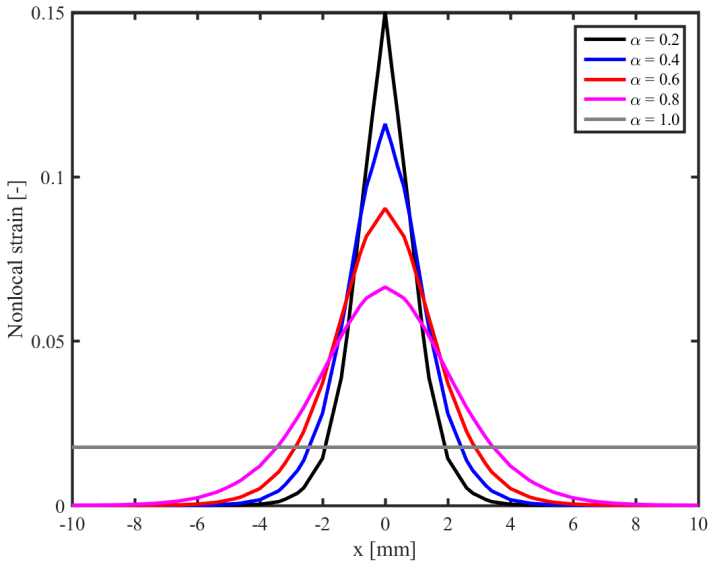

Figure 5.32: Variation of non-local strain along the length of Frustum for different α.

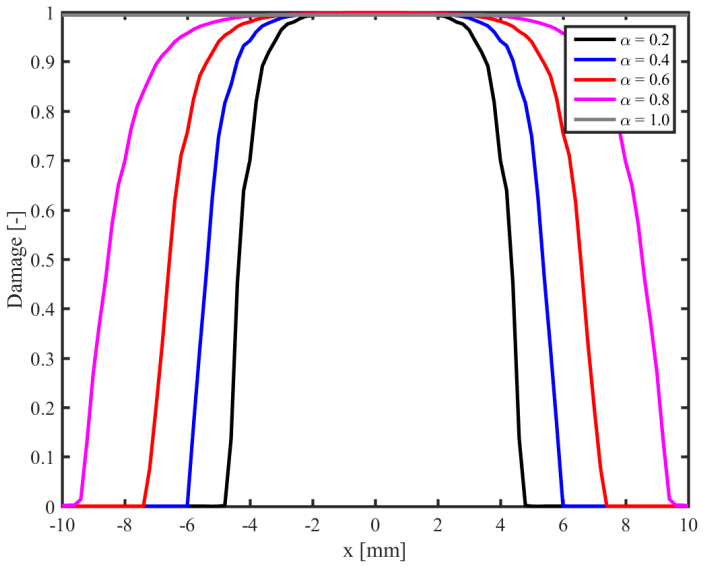

Figure 5.33: Variation of non-local damage along the length of Frustum for different α.

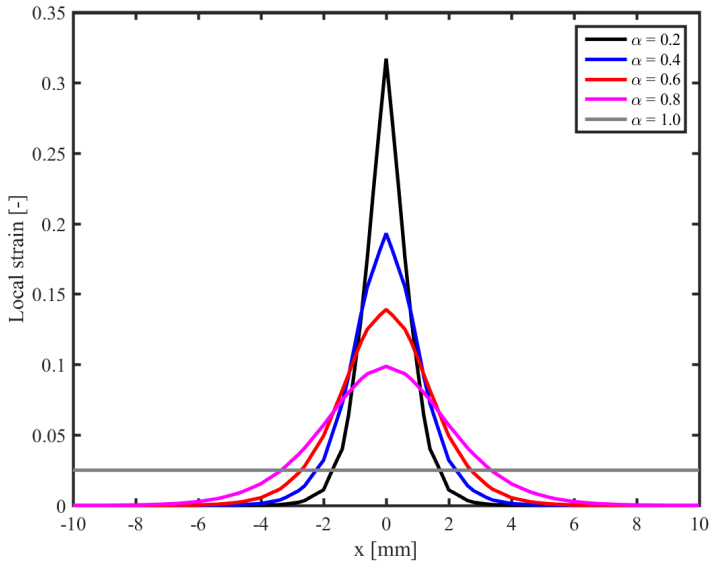

Figure 5.34: Variation of local strain along the length of Frustum for different α.

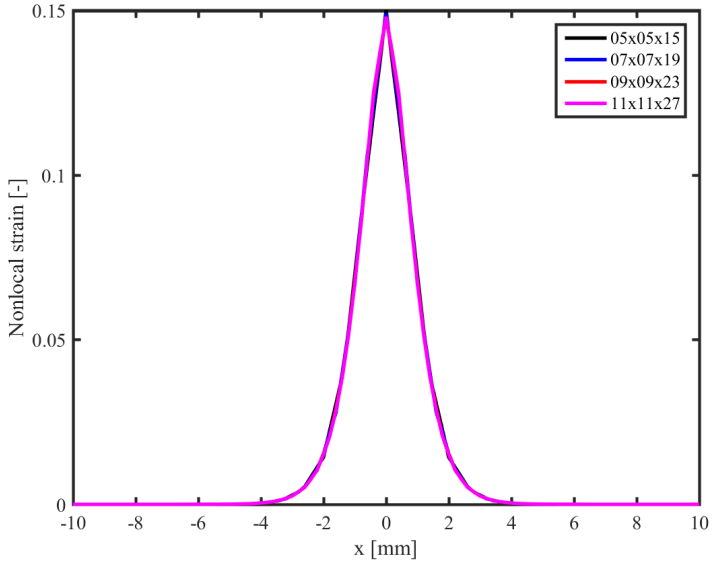

Figure 5.35: Variation of non-local strain along the length of Frustum for different mesh configurations.

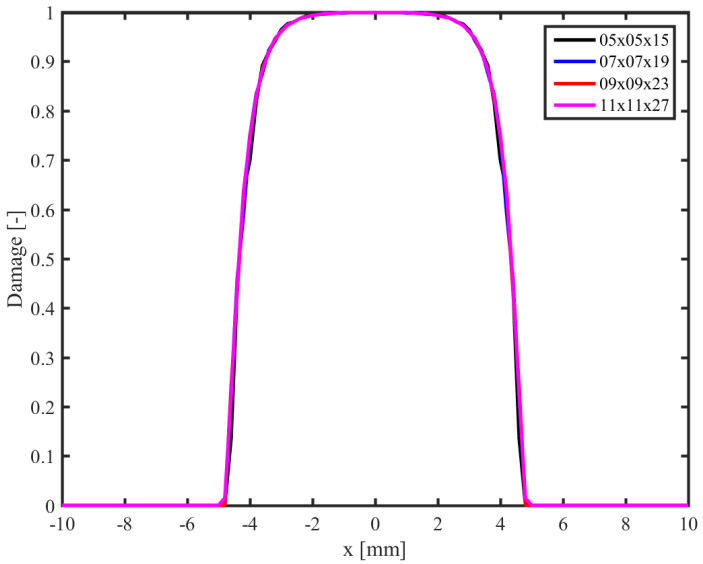

Figure 5.36: Variation of non-local damage along the length of Frustum for different mesh configurations.

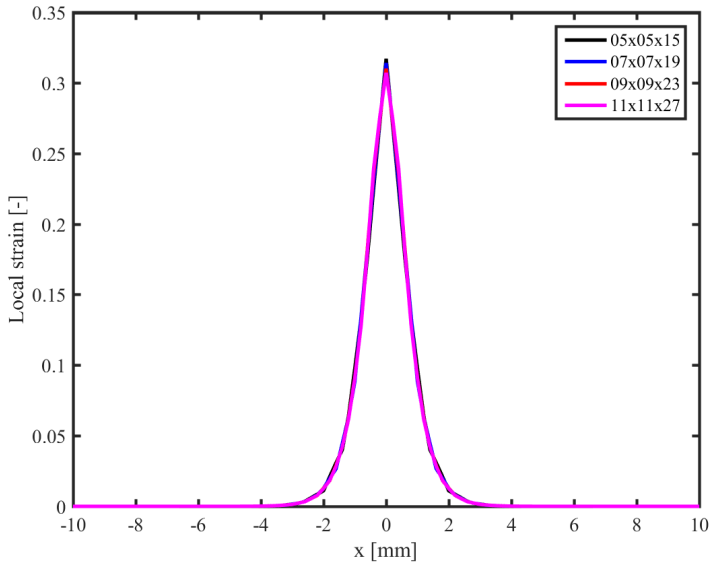

Figure 5.37: Variation of local strain along the length of Frustum for different mesh configurations.

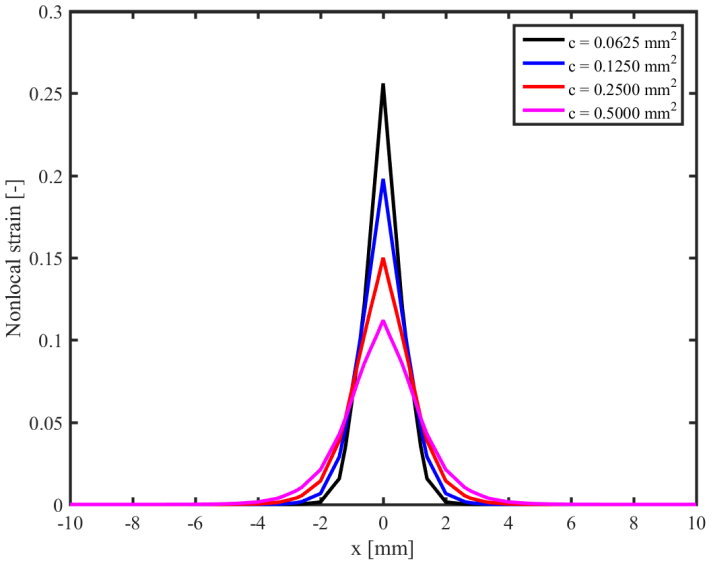

Figure 5.38: Variation of non-local strain along the length of Frustum for different Helmholtz gradient parameter (c).

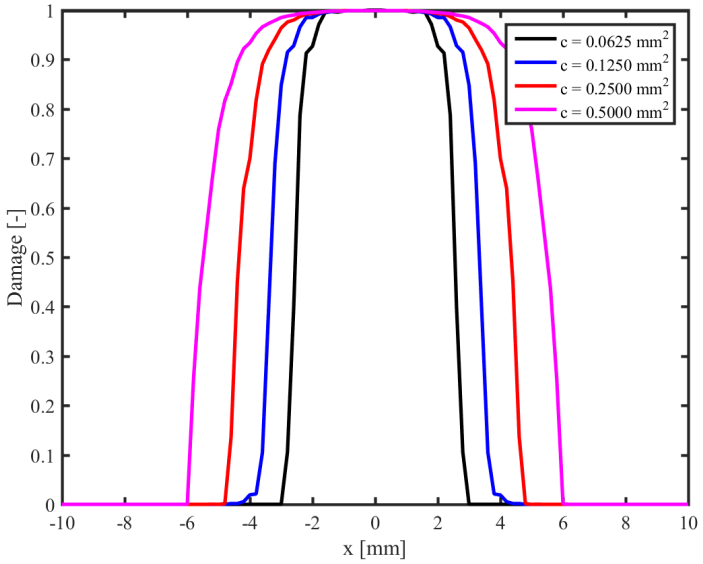

Figure 5.39: Variation of non-local damage along the length of Frustum for different Helmholtz gradient parameter (c).

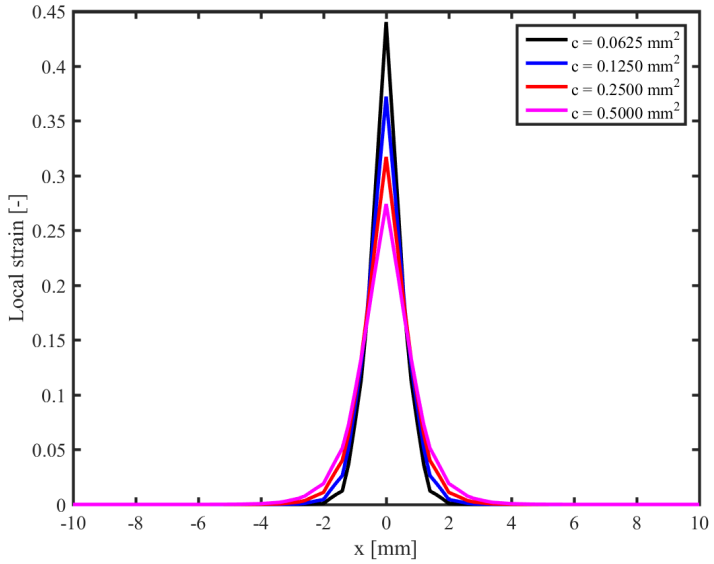

Figure 5.40: Variation of local strain along the length of Frustum for different Helmholtz gradient parameter (c).

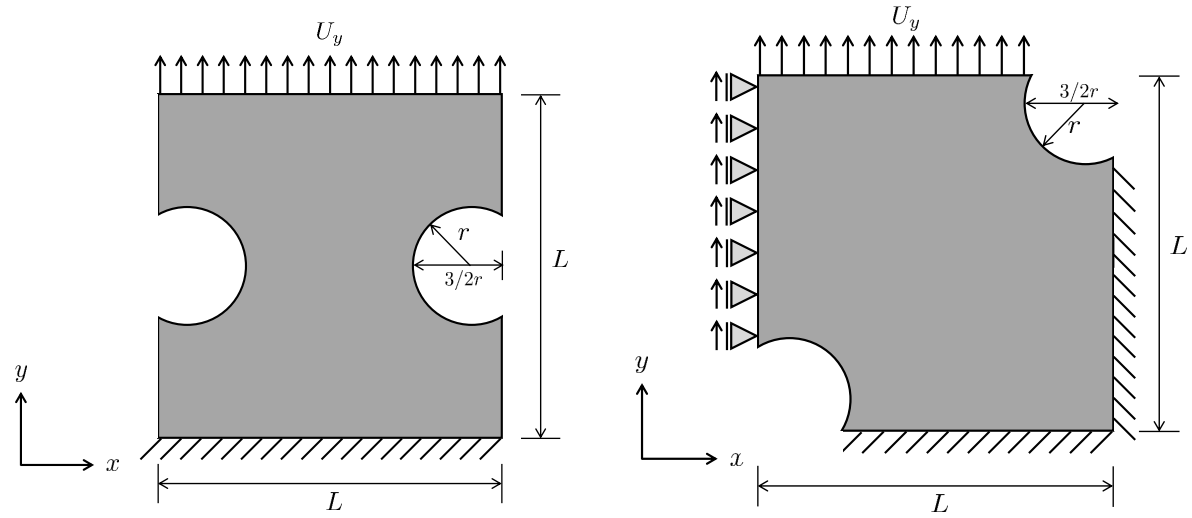

(a) Double notched plate with symmetric cylindrical holes(b) Double notched plate with non-symmetric cylindrical holes

Figure 5.41: Schematic of double notched plates

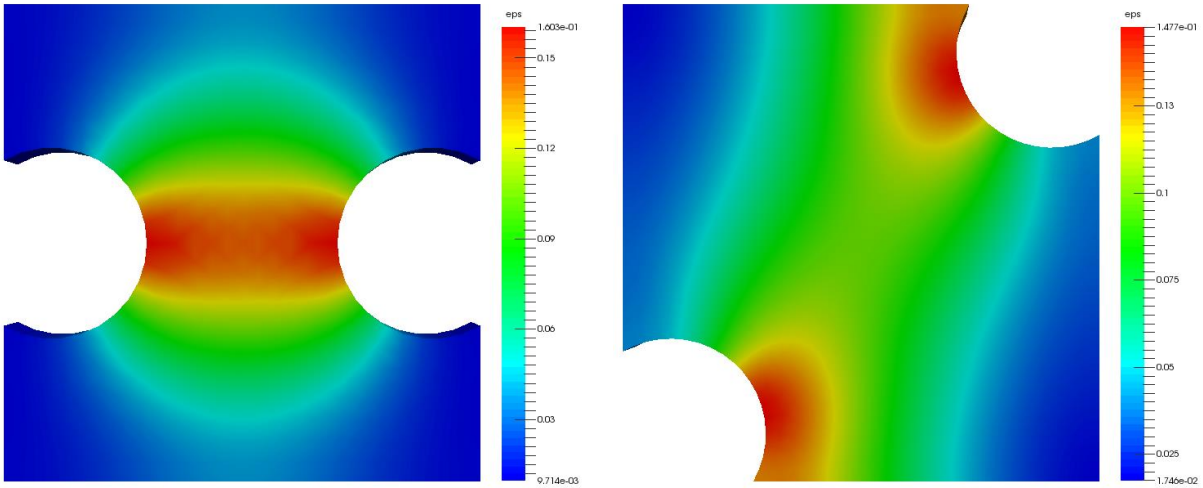

(a) Symmetric double notched plate (b) Non-symmetric double notched plate

Figure 5.42: The distribution of non-local strain in double notched plates

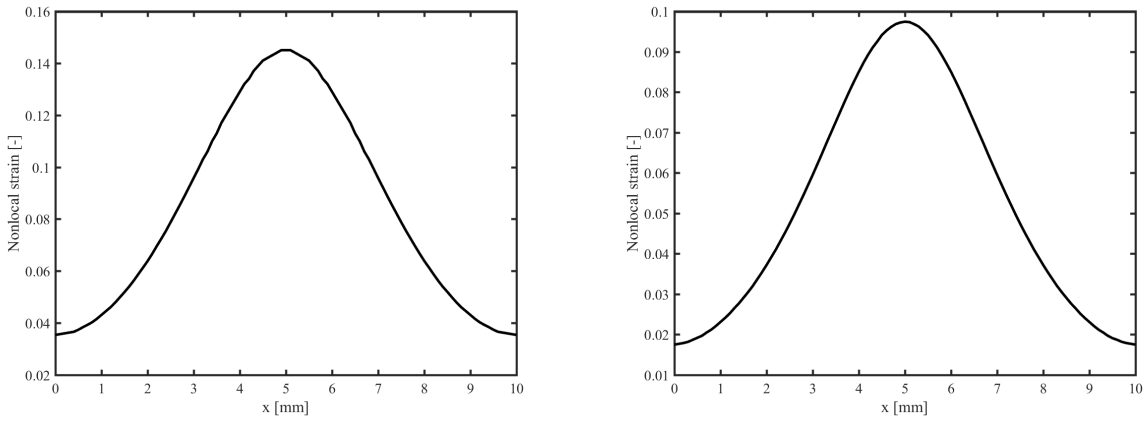

(a) Symmetric double notched plate (b) Non-symmetric double notched plate

Figure 5.43: The profile of non-local strain in double notched plates

5.5 Damage evolution in SSLIBs

In this section we aim to illustrate the performance of SSLIBs under damage evolution effects through 2D and 3D numerical examples. To this end, we perform parametric studies on the influence of damage mechanics on the electrochemical performance of SSLIBs. In particular, we study the influence of particle shape and cyclic charge-discharge process on the damage evolution and overall performance of SSLIBs through numerical examples. The impact of damage evolution on the discharge behavior and life-time performance of the battery is assessed by coupling the damage parameter with the diffusivity of the electrode particle. To study the performance of the SSLIB cell under damage evolution effects, the damage evolution mechanism is related to electrochemical properties of the battery. In particular, the electrode diffusion coefficient, D_s is described as a function of damage internal variable, κ. The influence of damage evolution on the diffusivity of the electrode has been studied by [26, 48] through stochastic modeling of damage evolution in LIBs. To this end, the evolution of the damage is described by an exponential law such that the damage parameter, D, is expressed as an exponential function of the damage internal variable, κ, as shown in Figure 2.2. The main features of damage evolution in the battery are explored here.

5.5.1 One-dimensional analytical expression for the non-local damage model

In this section we aim to present an analytical expression for the evolution of non-local damage model in LIBs and the influence of gradient parameter, c, on the non-local damage distribution. To illustrate the evolution of damage in the electrode active particle, lets consider a sphere of radius R_s, for a constant diffusion coefficient the balance of mass in the spherical coordinate system can be expressed as follows [30]:

$$\frac{\partial c_s}{\partial t} - \frac{D_s}{r^2}\frac{\partial}{\partial r}\left(r^2\frac{\partial c_s}{\partial r}\right) = 0, \tag{5.28}$$

for the galvanostatic operation (constant current) the following initial and boundary conditions hold:

$$\begin{aligned} c_s(r,0) &= c_{s_0}, \qquad \text{for} \qquad 0 \le r \le R_s \\ D_s \frac{\partial c_s(r,t)}{\partial r}\Big|_{r=0} &= 0, \qquad \text{for} \qquad t \ge 0 \\ D_s \frac{\partial c_s(r,t)}{\partial r}\Big|_{r=R_s} &= \frac{\mathbf{I}_{\text{ext}}}{F}, \qquad \text{for} \qquad t \ge 0. \end{aligned} \tag{5.29}$$

The analytic solution for the balance of mass (Equation (5.28)) is given by [30]:

$$c_s(r,t) = c_{s_0} + \frac{R_s \mathbf{I}_{\text{ext}}}{F D_s}\Big[3\tilde{t} + \frac{1}{2}\tilde{r}^2 - \frac{3}{10} - \frac{2}{\tilde{r}}\sum_{n=1}^{\infty}\Big(\frac{\sin(\lambda_n \tilde{r})}{\lambda_n^2 \sin(\lambda_n)}\exp(-\lambda_n^2 \tilde{t})\Big)\Big], \tag{5.30}$$

where $\lambda_n (n = 1, 2, 3, ...)$ are the positive roots of $\tan(\lambda_n) = \lambda_n$, $\tilde{r} = r/R_s$ is the non-dimensional length, and $\tilde{t} = D_s/R_s^2 t$ is the non-dimensional time, respectively. Considering the stress-diffusion coupling within the spherical particle, the radial and tangential stresses that satisfy the balance of linear momentum equation in the spherical coordinate system are given by [30]:

$$\begin{aligned} \sigma_r(r,t) &= \frac{2E_s\Omega_s}{9(1-\nu_s)}\Big[\bar{c}_s(R_s,t) - \bar{c}_s(r,t)\Big], \\ \sigma_\theta(r,t) &= \frac{E_s\Omega_s}{9(1-\nu_s)}\Big[2\bar{c}_s(R_s,t) + \bar{c}_s(r,t) - 3c_s(r,t)\Big], \end{aligned} \tag{5.31}$$

where

$$\begin{aligned} \bar{c}_s(r,t) = \frac{3}{r^3}\int_0^r r^2 c_s(r,t)dr = c_{s_0} + 3\left(\frac{R_s\mathbf{I}_{\text{ext}}}{FD_s}\right)\Bigg[\tilde{t} + \frac{1}{10}(\tilde{r}^2 - 1) \\ -\frac{2}{\tilde{r}^3}\sum_{n=1}^{\infty}\Big(\frac{\sin(\lambda_n\tilde{r}) - (\lambda_n\tilde{r})\cos(\lambda_n\tilde{r})}{\lambda_n^4\sin(\lambda_n)}\exp(-\lambda_n^2\tilde{t})\Big)\Bigg], \end{aligned} \tag{5.32}$$

$$\bar{c}_s(R_s,t) = c_{s_0} + 3\left(\frac{R_s\mathbf{I}_{\text{ext}}}{FD_s}\right)\tilde{t} = c_{s_0} + 3\left(\frac{\mathbf{I}_{\text{ext}}}{FR_s}\right)t. \tag{5.33}$$

Substituting Equations (5.32), (5.33), and (5.30) into Equation (5.31) results in the following expressions for the radial and tangential stresses:

$$\begin{aligned} \frac{\sigma_r(r,t)}{\Big[\big(E_s\Omega_s/(3(1-\nu_s))\big)\big(R_s\mathbf{I}_{\text{ext}}/(FD_s)\big)\Big]} \\ = \frac{1}{5}(1-\tilde{r}^2) + \frac{4}{\tilde{r}^3}\sum_{n=1}^{\infty}\Big(\frac{\sin(\lambda_n\tilde{r}) - (\lambda_n\tilde{r})\cos(\lambda_n\tilde{r})}{\lambda_n^4\sin(\lambda_n)}\exp(-\lambda_n^2\tilde{t})\Big) \\ = \tilde{\sigma}_r(\tilde{r},\tilde{t}), \end{aligned} \tag{5.34}$$

$$\begin{aligned}
&\frac{\sigma_\theta(r,t)}{\Big[\big(E_s\Omega_s/(3(1-\nu_s))\big)\big(R_s\mathbf{I}_{\text{ext}}/(FD_s)\big)\Big]} \\
&= \frac{1}{5}(1-2\tilde{r}^2) + 2\sum_{n=1}^{\infty}\frac{\exp(-\lambda_n^2\tilde{t})}{\lambda_n\sin(\lambda_n)} \\
&\times\left(\frac{\sin(\lambda_n\tilde{r})}{\lambda_n\tilde{r}} - \frac{\sin(\lambda_n\tilde{r}) - (\lambda_n\tilde{r})\cos(\lambda_n\tilde{r})}{\lambda_n^3\tilde{r}^3}\right) = \tilde{\sigma}_\theta(\tilde{r},\tilde{t}).
\end{aligned} \tag{5.35}$$

For the diffusion induced deformation the strain energy density can be calculated from the stresses, for the isotropically deform sphere the strain energy per unit volume is defined as [30]:

$$\psi(r) = \frac{\sigma_r^2(r) + 2\sigma_\theta^2(r) - 2\nu_s\sigma_\theta(r)\Big[2\sigma_r(r) + \sigma_\theta(r)\Big]}{2E_s}, \tag{5.36}$$

and the total stored elastic energy in the sphere can be calculated by integrating the strain energy density over the entire volume of the sphere:

$$\Psi(r) = 4\pi\int_0^{R_s}\psi(r)r^2dr. \tag{5.37}$$

Using Equation (5.34) and (5.35) the total non-dimensional stored elastic energy in the sphere can be defined as:

$$\begin{aligned}
&\frac{\Psi(r,t)}{2\pi R_s^3E_s\Big[\Omega_sR_s\mathbf{I}_{\text{ext}}/(3(1-\nu_s)FD_s)\Big]^2} \\
&= \int_0^1\Big[\tilde{\sigma}_r^2(\tilde{r},\tilde{t}) + 2\tilde{\sigma}_\theta^2(\tilde{r},\tilde{t}) - 2\nu_s\tilde{\sigma}_\theta(\tilde{r},\tilde{t})\Big(2\tilde{\sigma}_r(\tilde{r},\tilde{t}) + \tilde{\sigma}_\theta(\tilde{r},\tilde{t})\Big)\Big]\tilde{r}^2d\tilde{r} \\
&= \tilde{\Psi}(r,t).
\end{aligned} \tag{5.38}$$

Following the non-local damage equations defined by the Helmoltz-type equation, the non-dimensional form of the non-local damage can be expressed as follows:

$$\bar{\boldsymbol{\varepsilon}}_{\text{eq}}(\tilde{r},\tilde{t}) - \tilde{c}\frac{1}{\tilde{r}^2}\frac{\partial}{\partial\tilde{r}}\left(\tilde{r}^2\frac{\partial\bar{\boldsymbol{\varepsilon}}_{\text{eq}}(\tilde{r},\tilde{t})}{\partial\tilde{r}}\right) = \boldsymbol{\varepsilon}_{\text{eq}}(\tilde{r},\tilde{t}). \tag{5.39}$$

The simplified format of Equation (5.39) can be written as:

$$\bar{\boldsymbol{\varepsilon}}_{\text{eq}}(\tilde{r},\tilde{t}) - \tilde{c}\frac{2}{\tilde{r}}\frac{\partial\bar{\boldsymbol{\varepsilon}}_{\text{eq}}(\tilde{r},\tilde{t})}{\partial\tilde{r}} - \tilde{c}\frac{\partial^2\bar{\boldsymbol{\varepsilon}}_{\text{eq}}(\tilde{r},\tilde{t})}{\partial\tilde{r}^2} = \boldsymbol{\varepsilon}_{\text{eq}}(\tilde{r},\tilde{t}). \tag{5.40}$$

The equivalent local strain can be defined as a function of strain energy density:

$$\boldsymbol{\varepsilon}_{\text{eq}}(\tilde{r},\tilde{t}) = \sqrt{\tilde{\psi}(\tilde{r},\tilde{t})}, \tag{5.41}$$

where

$$\tilde{\psi}(\tilde{r},\tilde{t}) = \frac{\tilde{\sigma}_r^2(\tilde{r},\tilde{t}) + 2\tilde{\sigma}_\theta^2(\tilde{r},\tilde{t}) - 2\nu_s\tilde{\sigma}_\theta(\tilde{r},\tilde{t})\Big[2\tilde{\sigma}_r(\tilde{r},\tilde{t}) + \tilde{\sigma}_\theta(\tilde{r},\tilde{t})\Big]}{2} \tag{5.42}$$

By solving Equation (5.40) numerically, the non-local strain is expressed as a function of particle radius, $\tilde{r}$, non-dimensional gradient parameter, $\tilde{c}$, Poisson's ratio, and non-dimensional time, $\tilde{t}$. The residual form of the Helmholtz-type equation in the spherical coordinate can be written as:

$$\mathbf{R}_{\bar{\boldsymbol{\varepsilon}}_{\text{eq}}}: \int_{\bar{\Omega}^s} w_{\bar{\boldsymbol{\varepsilon}}_{\text{eq}}}\Big(\bar{\boldsymbol{\varepsilon}}_{\text{eq}} - \frac{2\tilde{c}}{\tilde{r}}\tilde{\nabla}_{\tilde{r}}\bar{\boldsymbol{\varepsilon}}_{\text{eq}} - \tilde{c}\tilde{\nabla}^2_{\tilde{r}}\bar{\boldsymbol{\varepsilon}}_{\text{eq}} - \boldsymbol{\varepsilon}_{\text{eq}}\Big)dv = 0. \tag{5.43}$$

$$\begin{aligned}\mathbf{R}_{\bar{\boldsymbol{\varepsilon}}_{\text{eq}}}: &\int_{\bar{\Omega}^s} w_{\bar{\boldsymbol{\varepsilon}}_{\text{eq}}}\cdot\bar{\boldsymbol{\varepsilon}}_{\text{eq}}dv - \int_{\bar{\Omega}^s}\frac{2\tilde{c}}{\tilde{r}}w_{\bar{\boldsymbol{\varepsilon}}_{\text{eq}}}\cdot\tilde{\nabla}_{\tilde{r}}\bar{\boldsymbol{\varepsilon}}_{\text{eq}}dv \\ +\int_{\bar{\Omega}^s}\tilde{c}\tilde{\nabla}_{\tilde{r}}w_{\bar{\boldsymbol{\varepsilon}}_{\text{eq}}}\cdot\tilde{\nabla}_{\tilde{r}}\bar{\boldsymbol{\varepsilon}}_{\text{eq}}dv &- \int_{\bar{\Omega}^s} w_{\bar{\boldsymbol{\varepsilon}}_{\text{eq}}}\cdot\boldsymbol{\varepsilon}_{\text{eq}}dv = 0\end{aligned} \tag{5.44}$$

The variation of the non-local strain over the particle radius and for different gradient parameter and Poisson's ratio are shown in Figures 5.44 - 5.46. The results show that for an increasing gradient parameter, the damage influence zone is increased and the model behave more ductile. The results also show that with an increasing the Poisson's ratio the influence of non-local strain decreases.

5.5.2 Effect of electrode particle shape - 2D

In this example we wish to examine the influences of particle shape and topology on the electrochemical performance of the battery cell through damage evolution in the electrode particle. In particular, the objective of this example is to evaluate the effect of electrode shape and topology on damage evolution and capacity fade in the battery. To this end, three different configurations based on the solid-state thin-film model presented in Section 5.1 are considered. While the volumes

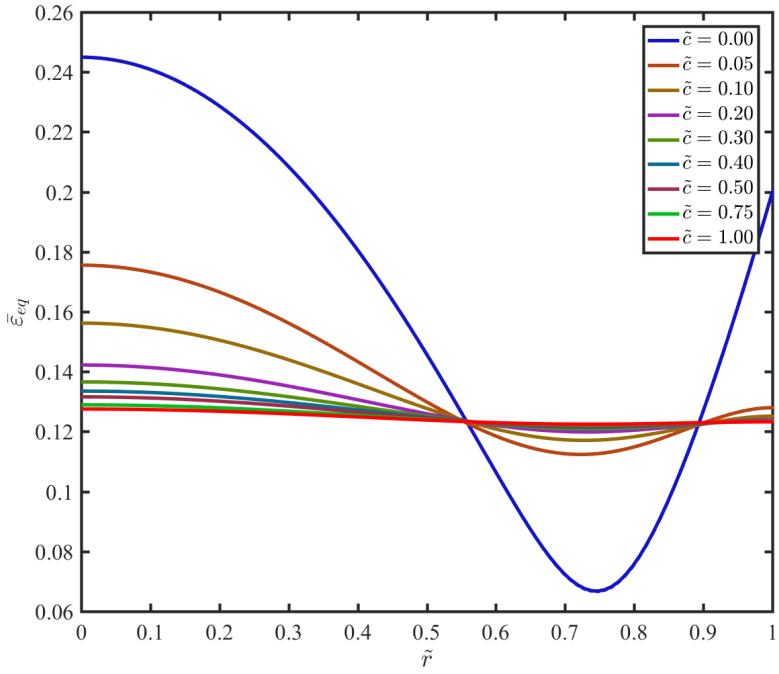

Figure 5.44: Variation of the non-local strain over the particle radius for different damage gradient parameter, $\tilde{c}$, for Poisson's ratio $\nu_s = 0.0$.

are the same in all configurations, the geometric shape of the electrode and electrolyte is changing by varying geometric parameters (i.e. major and minor radii). The schematic of the solid-state thin-film model with different configurations shape is shown in Figure 5.47. The volume of the electrode and the electrolyte are set to $V_s = 0.32\mu m^3$ and $V_l = 1.50\mu m^3$, respectively. The material and geometric properties are given in Table 5.1 and the damage parameters are given in Table 5.7. For numerical modeling, one-fourth of the design domain is discretized with 1076, 1104, and 1220 quadrilateral elements for cases $a/b = 1.0$, $a/b = 2.0$, and $a/b = 3.0$, respectively. To avoid stress oscillations, quadratic interpolation polynomials have been used for the displacement field, while linear interpolations have been used for concentrations, electric potentials, hydrostatic stress, and non-local strain fields. The forward analysis is solved with a 2D plane strain condition.

For the numerical simulation four different scenarios have been considered for each geometric configuration. In the first scenario, the model is discharged at C-rate of 51.2; without any mechanical contribution and stress-diffusion coupling effects. This scenario is called the nominal

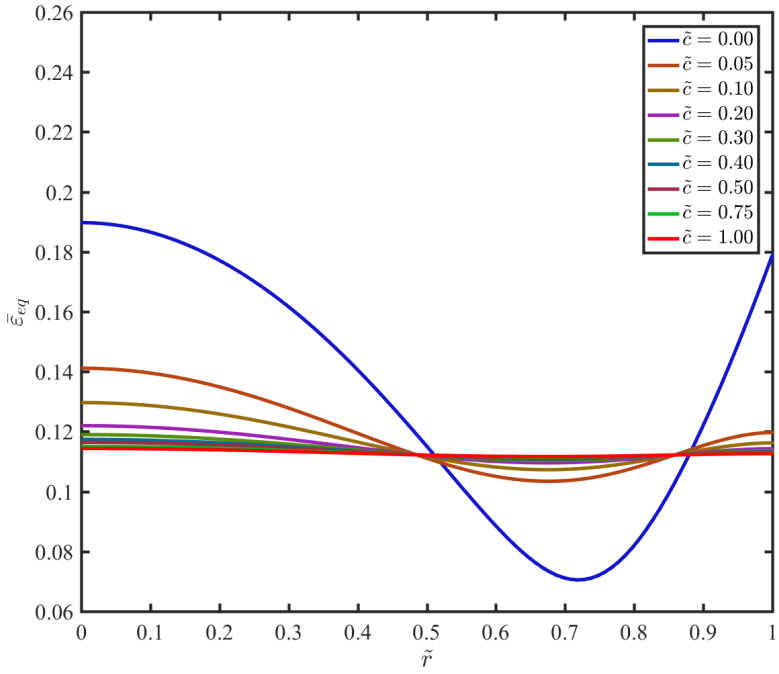

Figure 5.45: Variation of the non-local strain over the particle radius for different damage gradient parameter, $\tilde{c}$, for Poisson's ratio $\nu_s = 0.2$.

Table 5.7: Damage parameters in the SSLIB model.

Description	Symbol	Value	Unit
damage initiation threshold	κ_0	7.5×10^{-5}	-
damage sharpness parameter	β	10	-
damage gradient parameter	c	1.0×10^{-5}	m^2

analysis for the rest of this study. In the second scenario, the influence of mechanical deformation is considered through stress-diffusion coupling effects in the nominal analysis. The influence of the damage evolution on the mechanical performance of the battery is considered in the third scenario. Finally, the effects of damage evolution on the electrochemical performance of the battery model is assessed by considering damage-diffusion coupling. The results are presented in terms of variation of battery's parameters in time and space.

The variations of electrode and electrolyte concentrations at the end of discharge in both

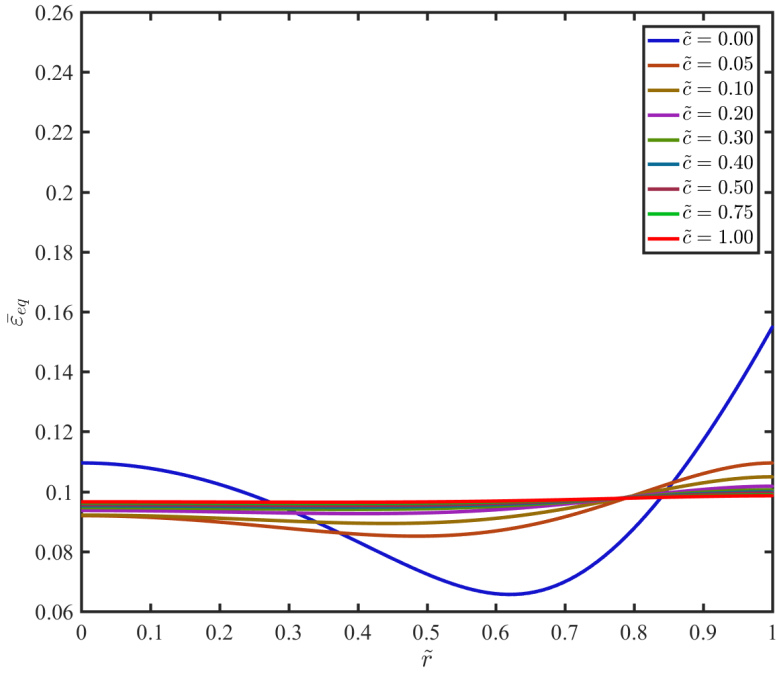

Figure 5.46: Variation of the non-local strain over the particle radius for different damage gradient parameter, $\tilde{c}$, for Poisson's ratio $\nu_s = 0.4$.

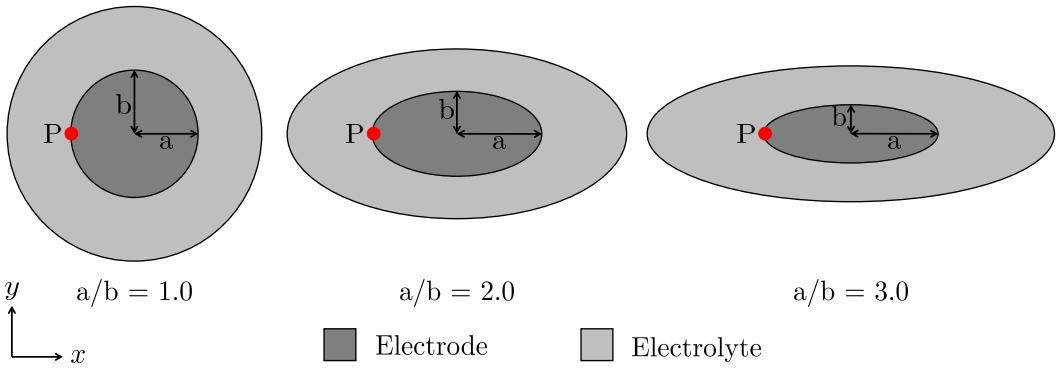

Figure 5.47: Schematic of the solid-state thin-film model with different configurations, P is the damage measurement point.

directions (i.e. x and y) and for different aspect ratios (ratio of a/b) are shown in Figures 5.48 and 5.49, respectively. The results show that there is a great influence of the electrode shape on the SSLIB performance. By increasing the aspect ratio, the electrode concentration is increased in both directions. This indicates that the capacity increases with an increasing aspect ratio,

these effects had been observed by [164] for the liquid state electrolyte. Moreover, comparison of the electrolyte concentration profiles shows that with an increasing aspect ratio the gradient of the electrolyte concentration decreases, this behavior is presented graphically in Figure 5.50. The results show that unlike the electrode layer, a uniform concentration can be observed in the electrolyte layer with higher aspect ratios, however, high concentration gradients are observed in the y direction. In addition, Figures 5.48, 5.49, and 5.50 indicate that for a damaged electrode particle, there is a substantial change in the electrode concentration profile. This change shows the significant influence of the damage evolution on the battery's capacity and overall performance. The evolution of damage parameter, D, and electrode diffusion coefficient, $\tilde{D}_s$, during a full discharge process is shown in Figure 5.51. Initially the damage doesn't have any contribution on the diffusion coefficient and electrochemical performance of the battery. After reaching the damage threshold, the damage evolves and eventually increases during the discharge process, while, the diffusion coefficient and consequently the capacity of the battery decrease. This influence is shown in Figure 5.52. Comparison of the discharge profile for different aspect ratio shows that increasing the aspect ratio results in increase in the capacity of the battery cell, while, the damage induced capacity fade is decreasing with increasing the aspect ratio. This indicates that the capacity fade and reduction in the electrochemical performance of the battery cell can be minimized by maximizing the particle aspect ratio.

The results of different type of mechanical stresses are presented in Figures 5.53 - 5.57. For all aspect ratios, the highest stress occurs at the interface due to the difference in material properties. The stress is uniform for the case a/b = 1.0 and the absolute value of stress is increasing with an increasing aspect ratio and discharge time.

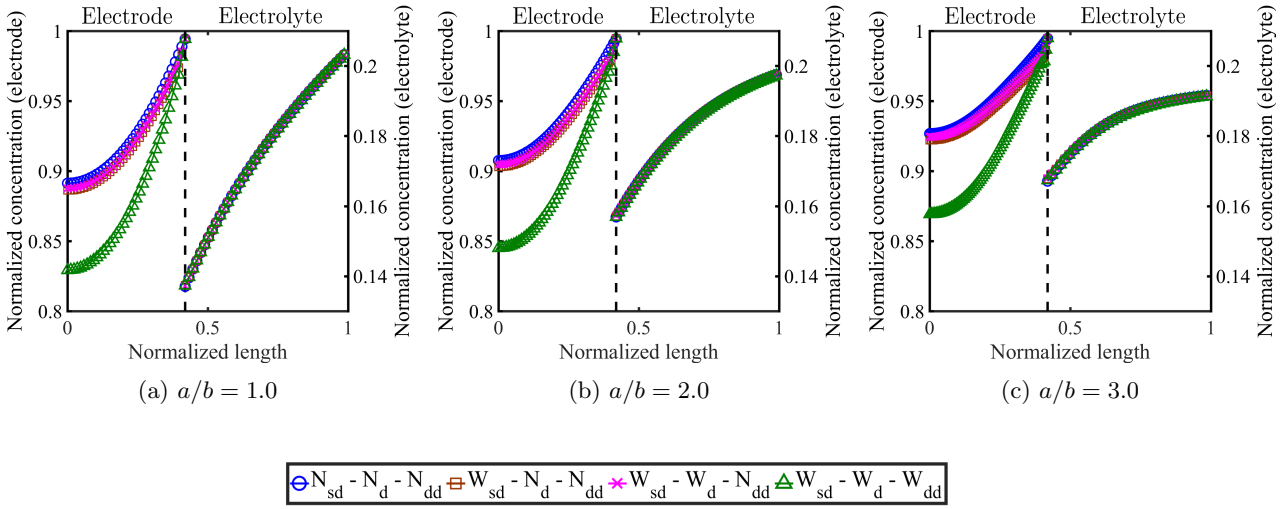

(a) $a/b = 1.0$ (b) $a/b = 2.0$ (c) $a/b = 3.0$

Figure 5.48: The normalized concentrations at the end of discharge along x direction and for different aspect ratio (N_{sd}: without stress-diffusion coupling, W_{sd}: with stress-diffusion coupling, N_d: without damage, W_d: with damage, N_{dd}: without damage-diffusion coupling, W_{sd}: with damage-diffusion coupling).

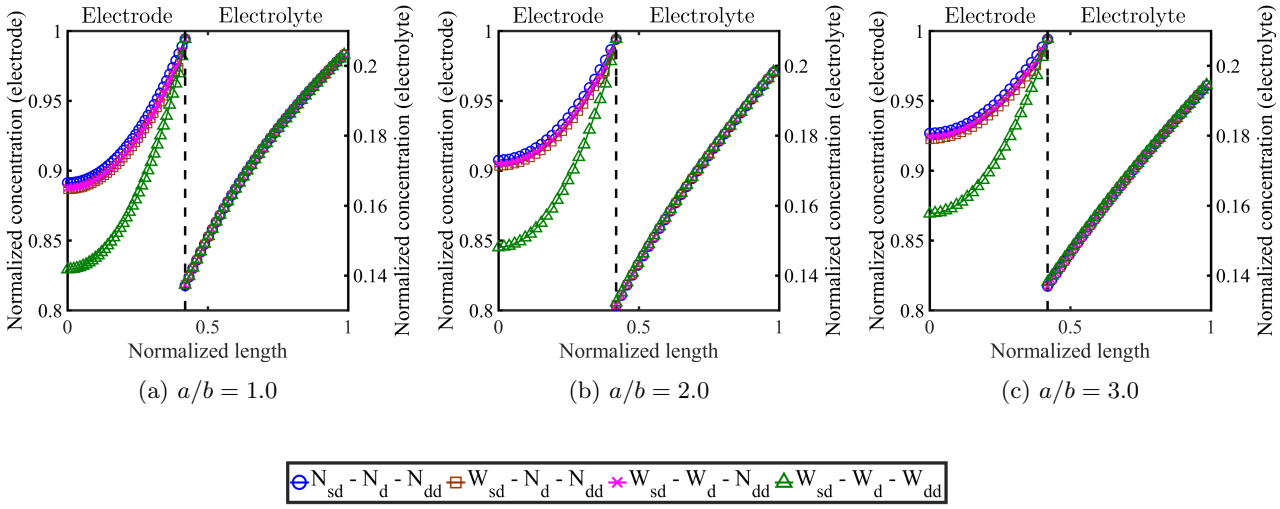

(a) $a/b = 1.0$ (b) $a/b = 2.0$ (c) $a/b = 3.0$

Figure 5.49: The normalized concentrations at the end of discharge along y direction and for different aspect ratio.

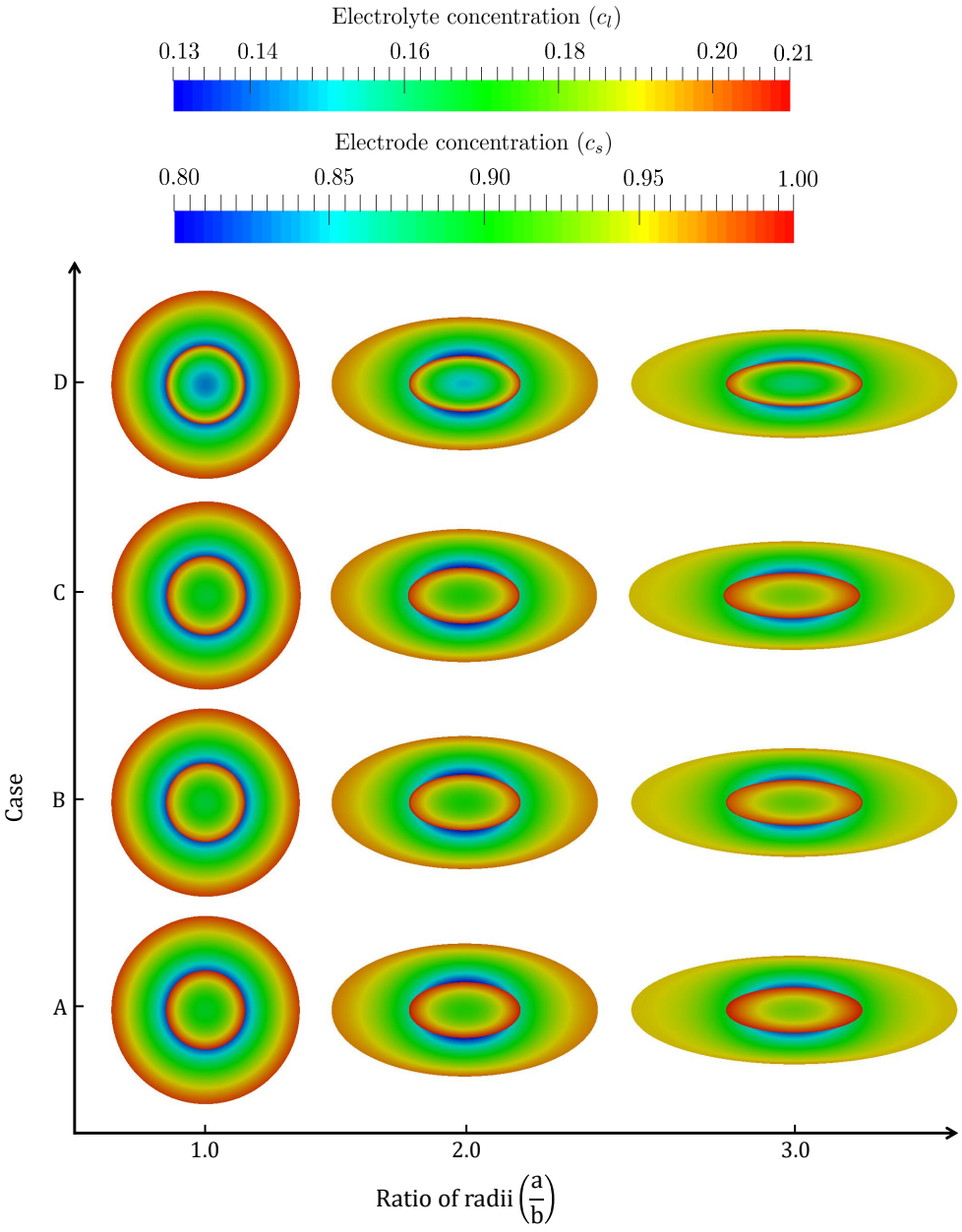

Figure 5.50: Variation of electrode and electrolyte concentrations at the end of discharge for C-rate: 51.2 (A: without stress-diffusion coupling, without damage, without damage-diffusion coupling, B: with stress-diffusion coupling, without damage, without damage-diffusion coupling, C: with stress-diffusion coupling, with damage, without damage-diffusion coupling, D: with stress-diffusion coupling, with damage, with damage-diffusion coupling).

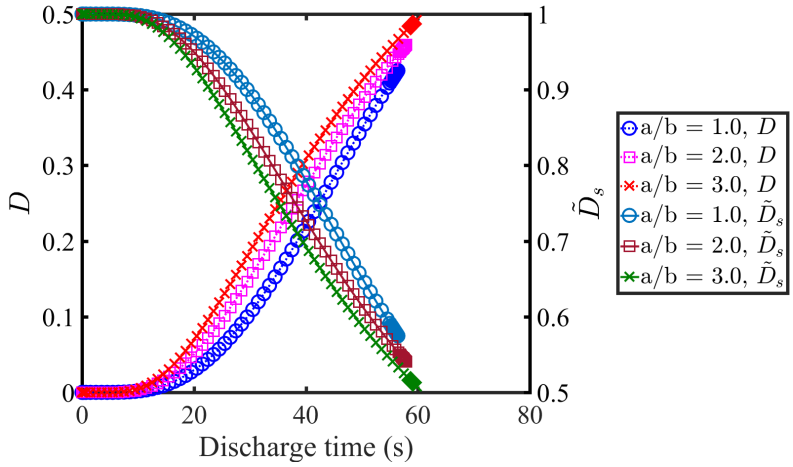

Figure 5.51: Evolution of damage and electrode diffusion coefficient during the battery discharge process.

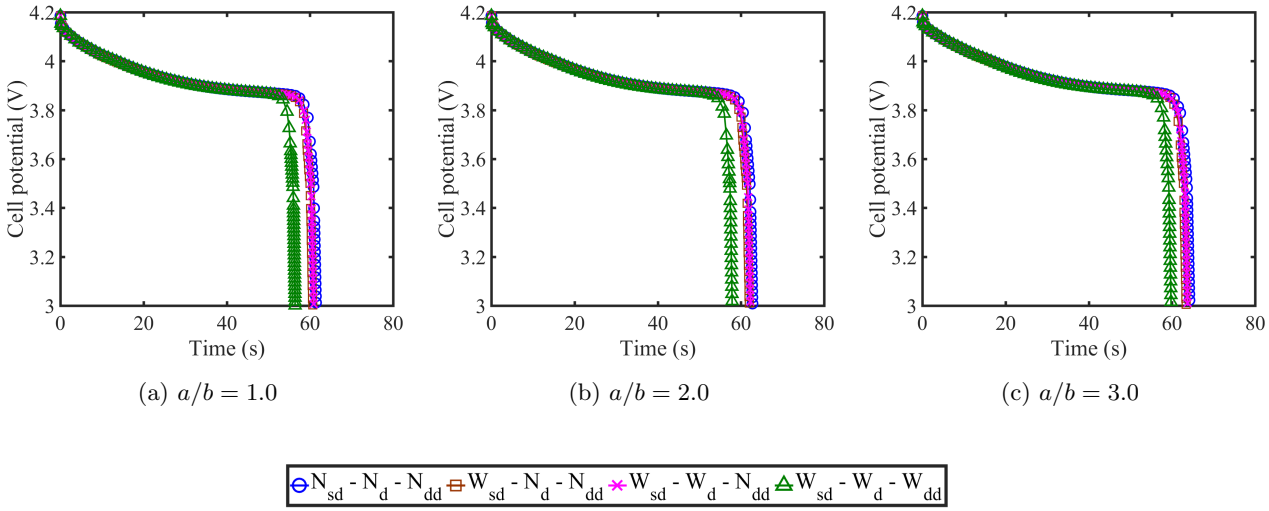

(a) $a/b = 1.0$ (b) $a/b = 2.0$ (c) $a/b = 3.0$

Figure 5.52: Variation of cell potential as a function of discharge time for different ratio of radii.

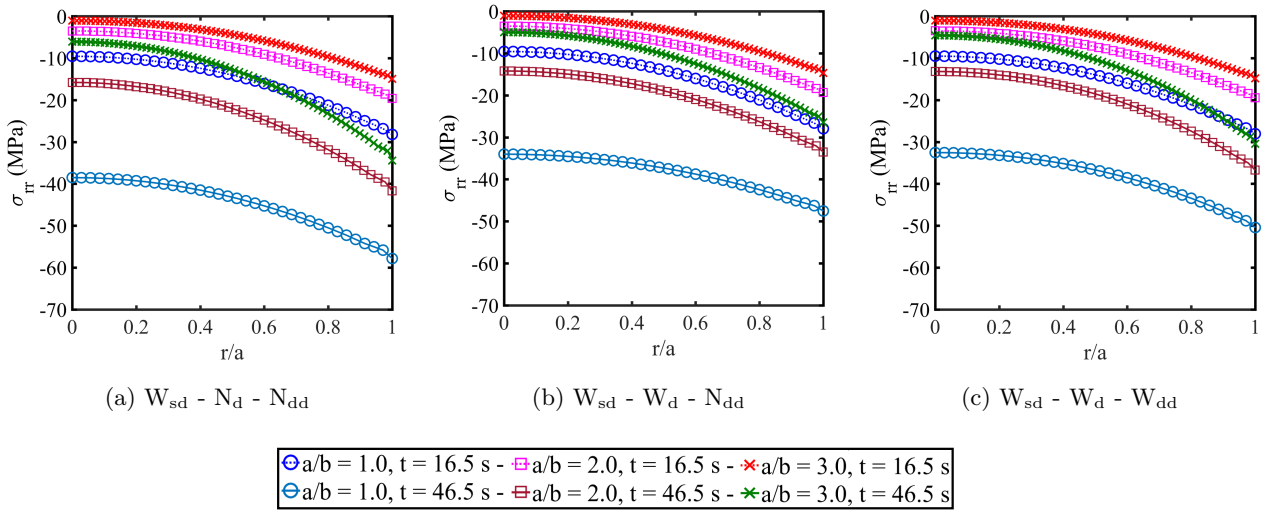

(a) W_{sd} - N_d - N_{dd} (b) W_{sd} - W_d - N_{dd} (c) W_{sd} - W_d - W_{dd}

Figure 5.53: Variation of radial stress for different discharge times, along x direction.

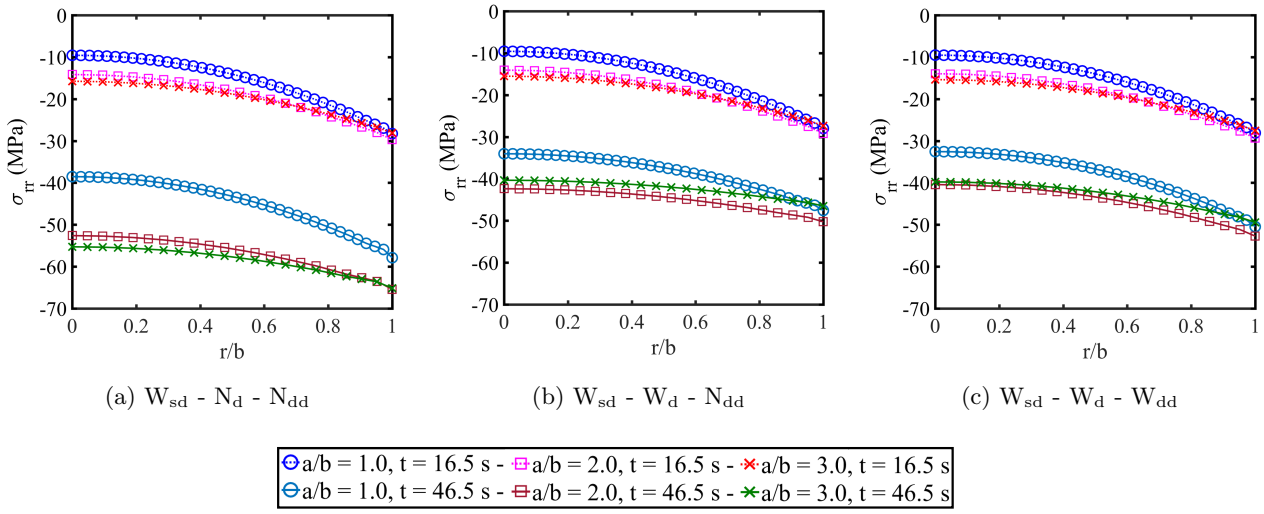

(a) W_{sd} - N_d - N_{dd} (b) W_{sd} - W_d - N_{dd} (c) W_{sd} - W_d - W_{dd}

Figure 5.54: Variation of radial stress for different discharge times, along y direction.

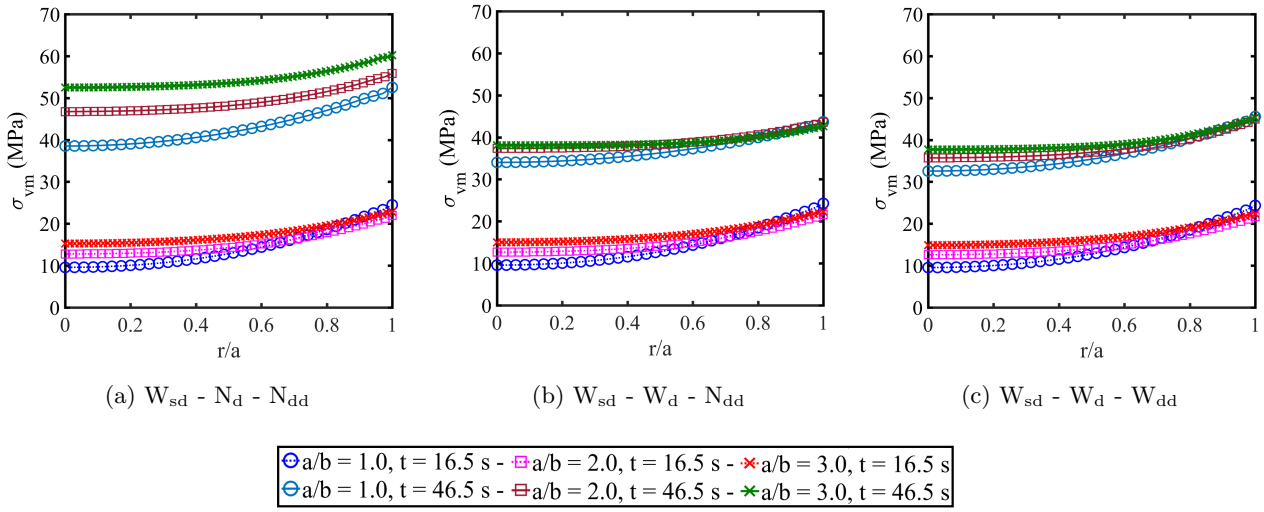

(a) W_{sd} - N_d - N_{dd} (b) W_{sd} - W_d - N_{dd} (c) W_{sd} - W_d - W_{dd}

Figure 5.55: Variation of von mises stress for different discharge times, along x direction.

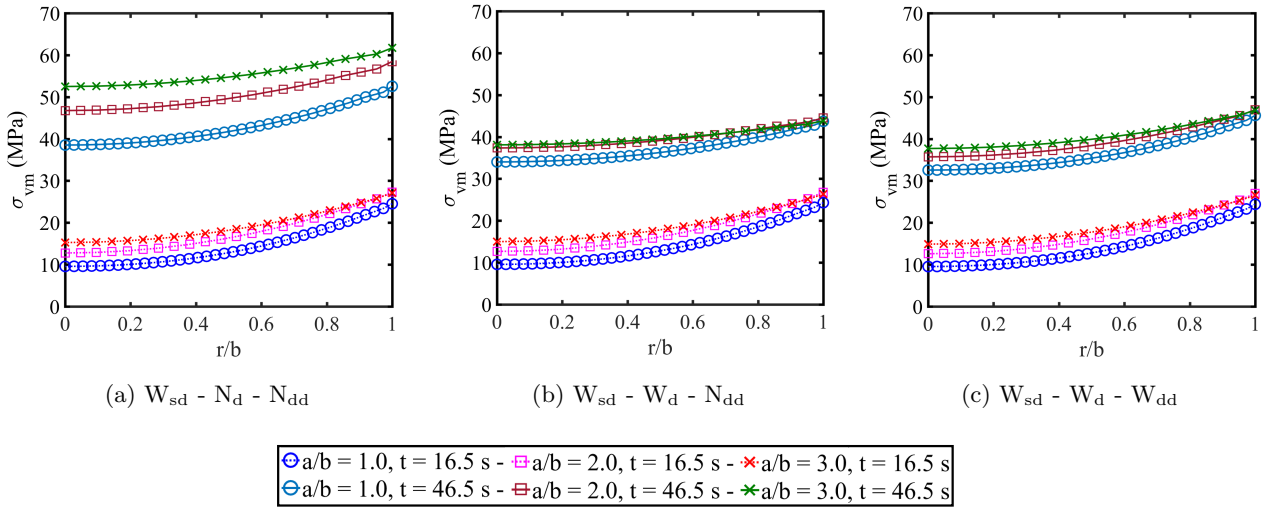

(a) W_{sd} - N_d - N_{dd} (b) W_{sd} - W_d - N_{dd} (c) W_{sd} - W_d - W_{dd}

Figure 5.56: Variation of von mises stress for different discharge times, along y direction.

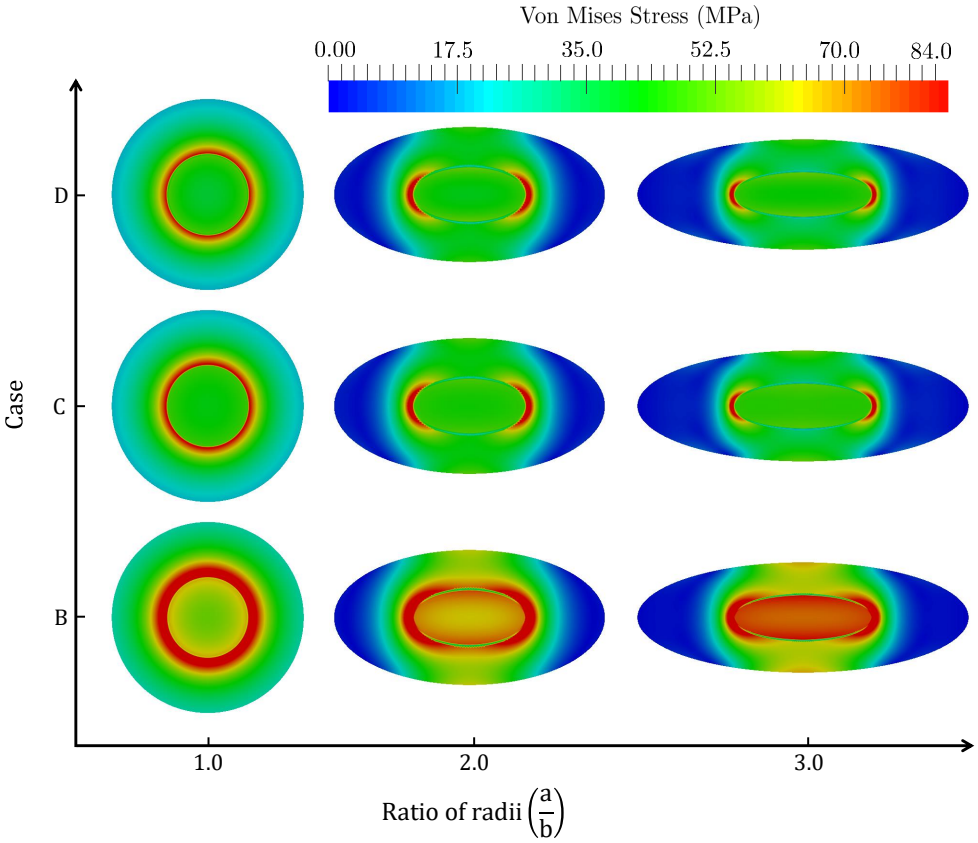

Figure 5.57: Variation of von-mises stress at the end of discharge (C-rate: 51.2) in both electrode and electrolyte.

5.5.3 Effect of electrode particle shape - 3D

Following the 2D example, the 3D effects of particle shape and topology, and damage evolution on the electrochemical performance of the battery are analyzed using the 3D numerical examples. Similar to the 2D example, three different configurations for the solid state thin-film model are considered, see Figure 5.47. The volume of the electrode and the electrolyte are set as the same as the 2D model, $V_s = 0.32\mu m^3$ and $V_l = 1.50\mu m^3$. The material and geometric properties are given in Table 5.1 and 5.7. For numerical modeling, one-eighth of the design domain is discretized with 1225, 1572, and 1695 hexahedron elements for cases $a/b = 1.0$, $a/b = 2.0$, and $a/b = 3.0$, respectively. The particle radius in the third direction is set to $c = b$. To avoid stress oscillations, quadratic interpolation polynomials have been used for the displacement field, while linear interpolations have been used for other solution fields. Similar to the 2D example, four different scenarios have been considered for each configuration. The model is discharged at C-rate of 51.2. The results are presented in terms of variation of battery's parameters in time and space.

The electrode and electrolyte concentration profiles at the end of discharge and for different aspect ratio are given in Figures 5.58 and 5.59. A comparison of the electrode concentration in x and y directions shows that the electrode concentration profiles remain the same for both directions. Although, they vary substantially as the aspect ratio changes, large aspect ratio results in higher capacity. Similar trend can be observed in the electrolyte concentration profiles. Comparison of the 2D and 3D concentration profiles reveals the 3D influence in the battery model, the comparison shows that there is great difference between concentration profiles in both electrode and electrolyte layers. This indicates that concluding 2D results for 3D purpose may not be adequate depending on the intended application. The influence of the damage on the electrochemical performance of the battery can be seen in the concentration profiles and battery discharge curves, found in Figures 5.58, 5.59, 5.60, and 5.65. For damaged materials, the results show that there is significant influence from the damage evolution on the electrochemical performance and capacity fade of the battery. However, this trend is decreasing with increasing the aspect ratio. Compared to the 2D discharge

curves, capacity fade in the 3D results is more pronounced than the 2D one, this is related to the 3D influence in the battery model.

The results of 3D stress distribution are shown in Figures 5.61 - 5.66. Similar to the 2D results, higher concentration happens at the interface, however, at the same discharge time the amount of stress is smaller than the one observed in the 2D cases.

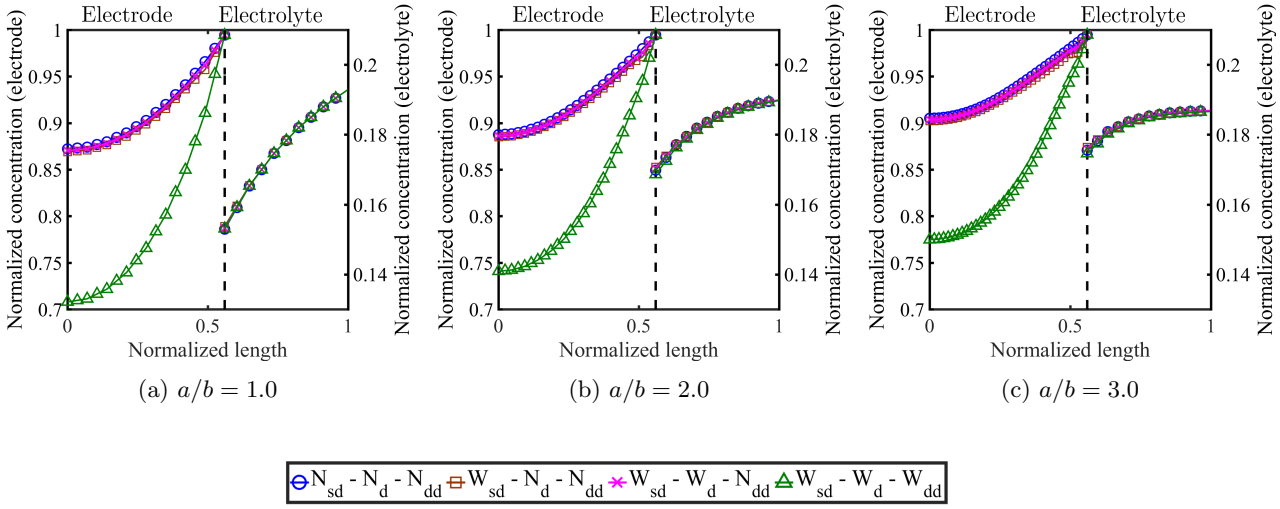

(a) $a/b = 1.0$ (b) $a/b = 2.0$ (c) $a/b = 3.0$

Figure 5.58: The normalized concentrations at the end of discharge, along x direction and for different aspect ratio (N_{sd}: without stress-diffusion coupling, W_{sd}: with stress-diffusion coupling, N_d: without damage, W_d: with damage, N_{dd}: without damage-diffusion coupling, W_{sd}: with damage-diffusion coupling).

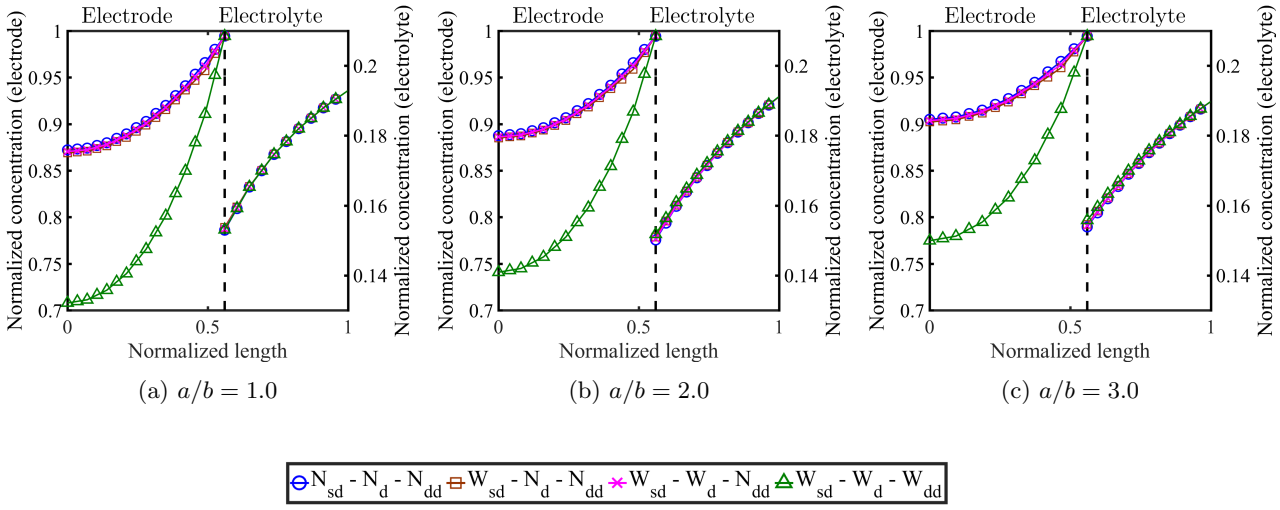

(a) $a/b = 1.0$ (b) $a/b = 2.0$ (c) $a/b = 3.0$

Figure 5.59: The normalized concentrations at the end of discharge, along y and z directions and for different aspect ratio.

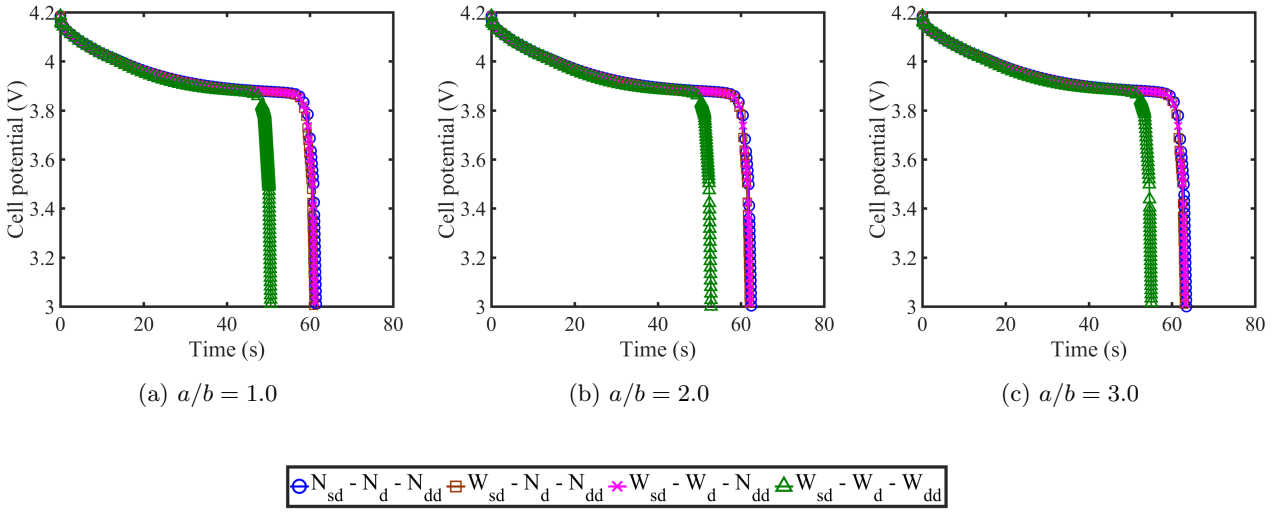

(a) $a/b = 1.0$ (b) $a/b = 2.0$ (c) $a/b = 3.0$

Figure 5.60: Variation of cell potential as a function of discharge time for different ratio of radii.

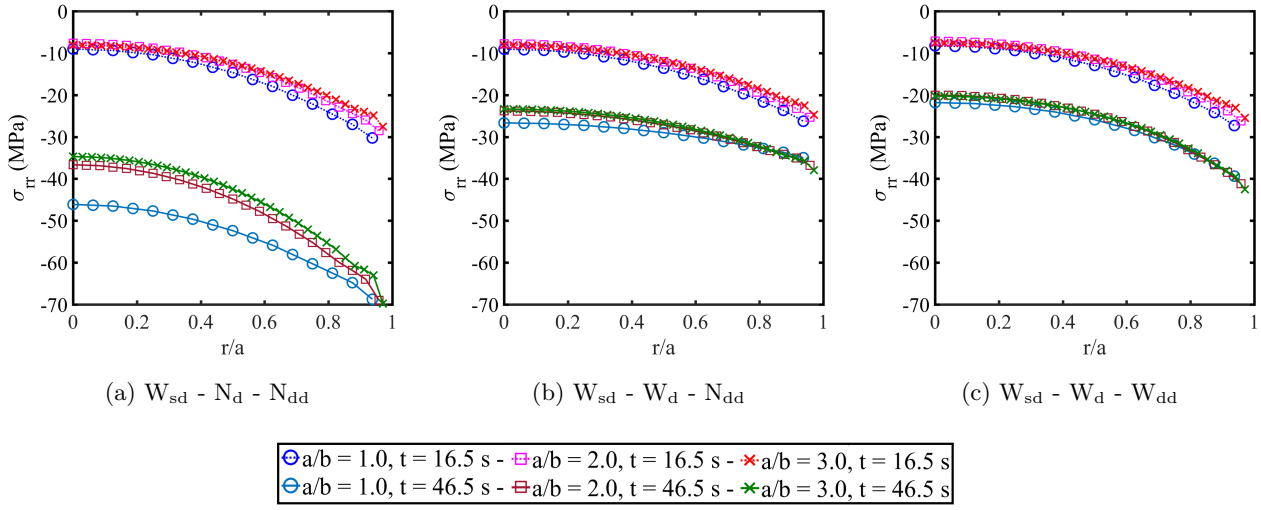

(a) W_{sd} - N_d - N_{dd} (b) W_{sd} - W_d - N_{dd} (c) W_{sd} - W_d - W_{dd}

Figure 5.61: Variation of radial stress for different discharge time and aspect ratio, along x direction.

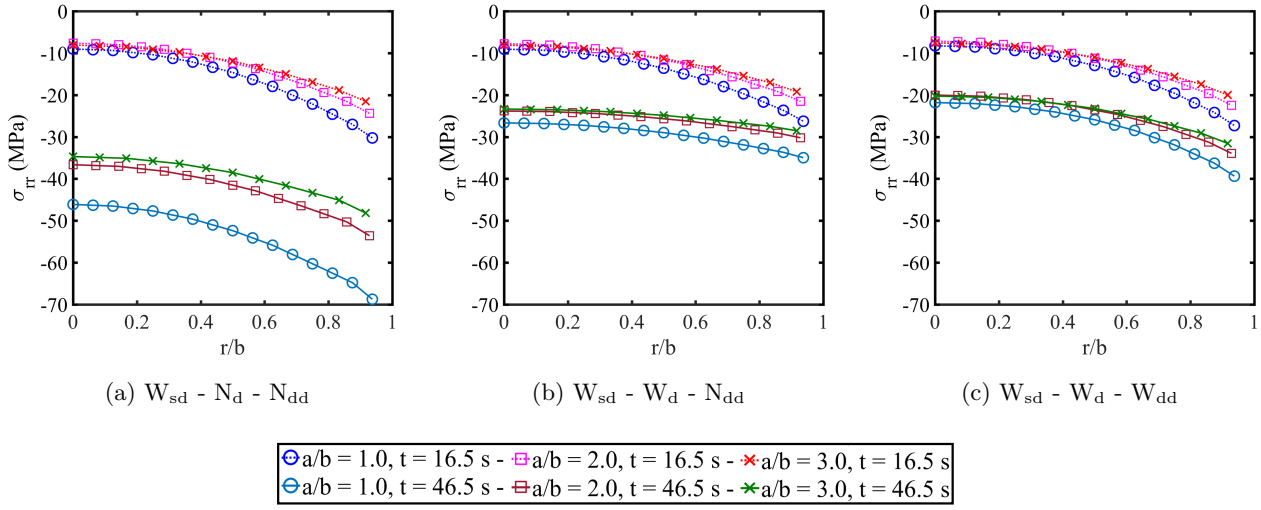

(a) W_{sd} - N_d - N_{dd} (b) W_{sd} - W_d - N_{dd} (c) W_{sd} - W_d - W_{dd}

Figure 5.62: Variation of radial stress for different discharge time and aspect ratio, along y and z directions.

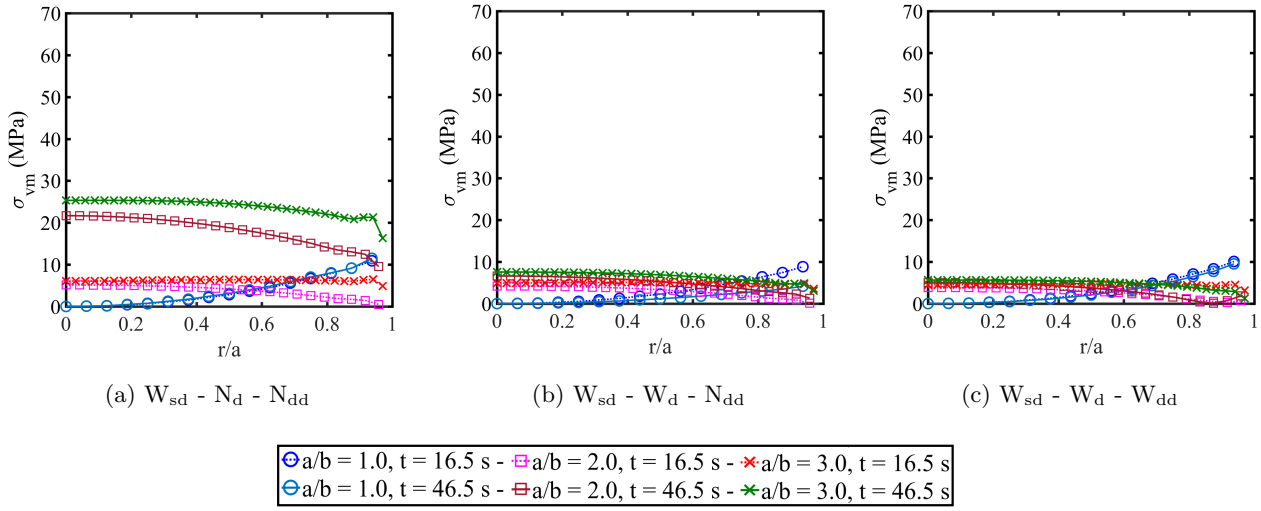

(a) W_{sd} - N_d - N_{dd} (b) W_{sd} - W_d - N_{dd} (c) W_{sd} - W_d - W_{dd}

Figure 5.63: Variation of von mises stress for different discharge time and aspect ratio, along x direction.

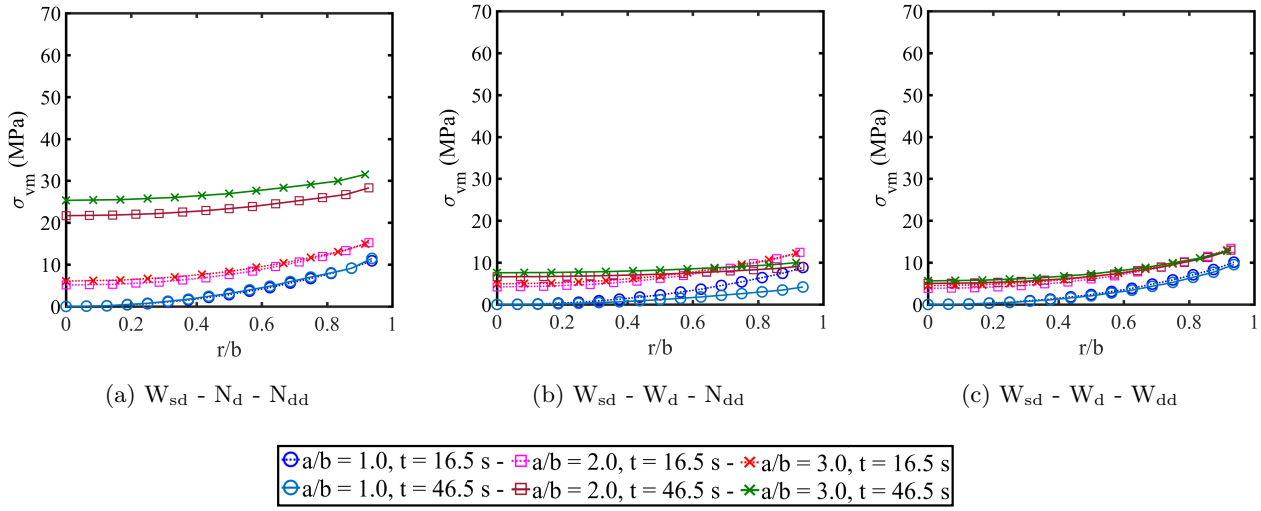

(a) W_{sd} - N_d - N_{dd} (b) W_{sd} - W_d - N_{dd} (c) W_{sd} - W_d - W_{dd}

Figure 5.64: Variation of von mises stress for different discharge time and aspect ratio, along y and z directions.

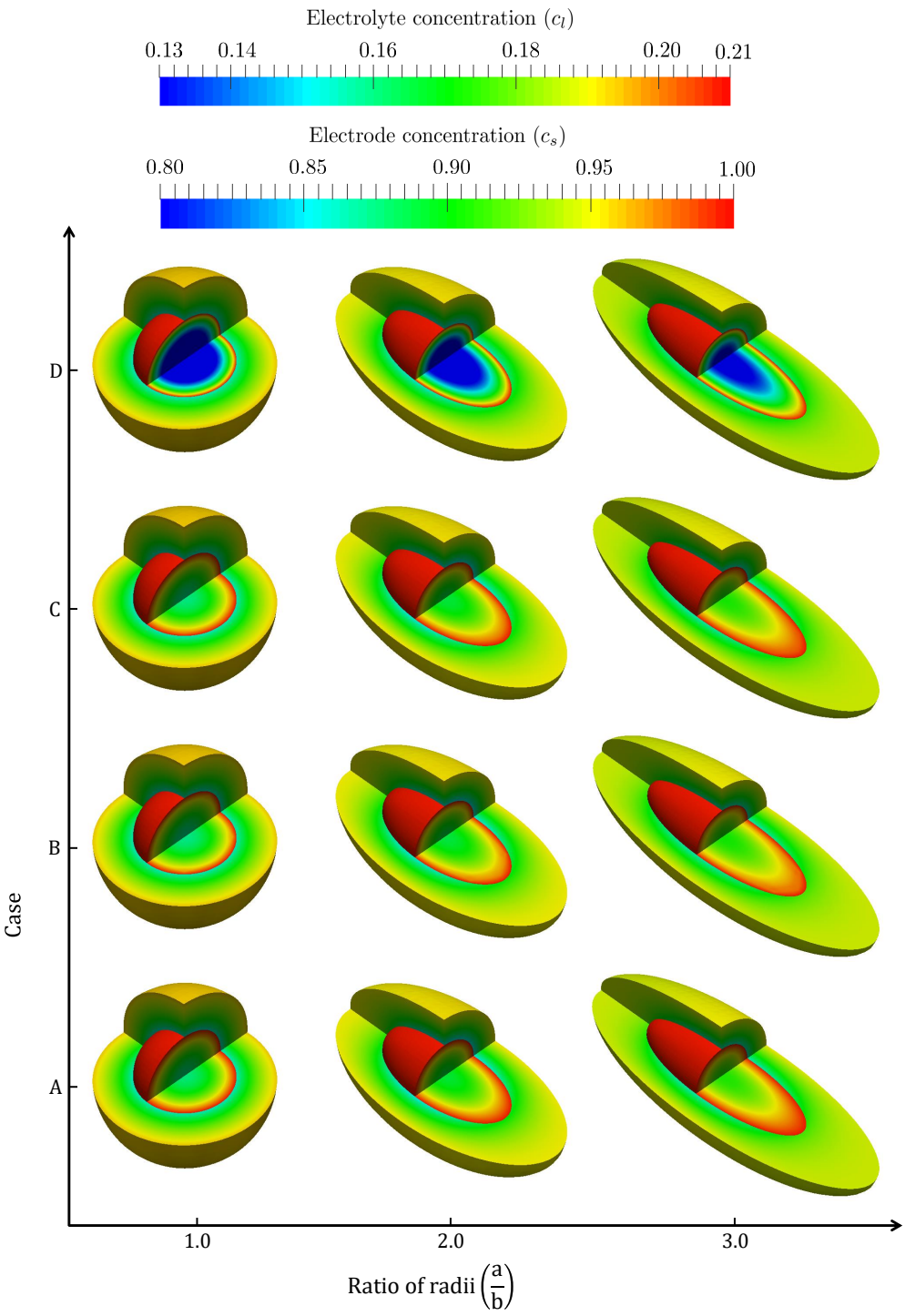

Figure 5.65: Variation of electrode and electrolyte concentrations at the end of discharge for C-rate: 51.2 (A: without stress-diffusion coupling, without damage, without damage-diffusion coupling, B: with stress-diffusion coupling, without damage, without damage-diffusion coupling, C: with stress-diffusion coupling, with damage, without damage-diffusion coupling, D: with stress-diffusion coupling, with damage, with damage-diffusion coupling).

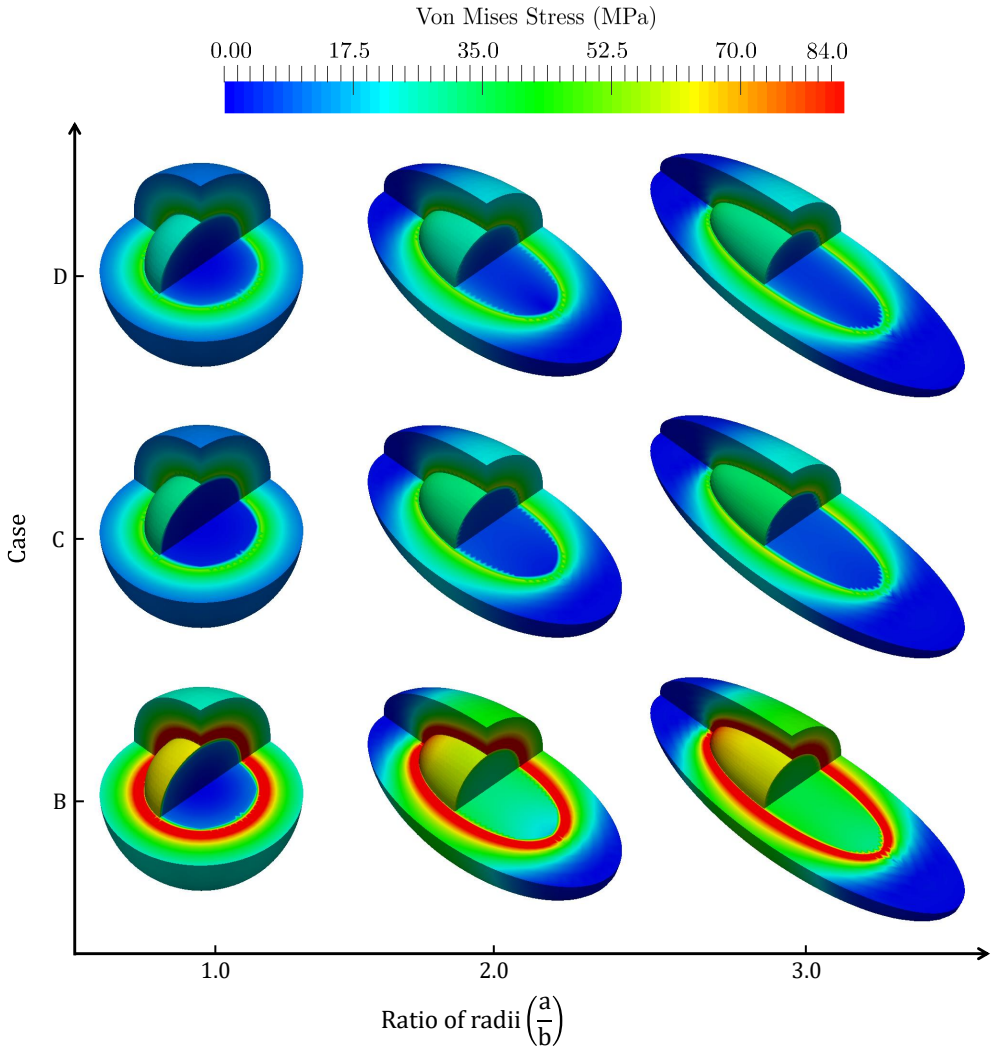

Figure 5.66: Variation of von-mises stress at the end of discharge (C-rate: 51.2) in both electrode and electrolyte.

5.5.4 Effect of cyclic charge-discharge

In this example we wish to examine the influence of coupled damage accumulation and cyclic charge-discharge process on the electrochemical performance of the battery cell. In particular, we wish to examine the evolution of both electrochemical and mechanical properties under cyclic charge-discharge process. To this end, a 2D SSLIB model with an island of electrode materials surrounded by the electrolyte is considered. Both stress-diffusion and damage-diffusion coupling effects are considered in this model. The exponential form of damage evolution law is considered in the model as shown in Figure 2.2. The material and geometric properties are adopted from the thin-film model given in Table 5.1, while, the damage parameters are set in Table 5.8. The schematic of the electrode island model is given in Figure 5.67. For numerical modeling, the design domain is discretized with 1168 quadrilateral elements. Similar to other 2D battery's examples and to avoid stress oscillations, quadratic interpolation polynomials have been used for the displacement field, while linear interpolations have been used for concentrations, electric potentials, hydrostatic stress, and non-local strain fields. The forward analysis is solved with a 2D plane strain condition.

The influence of cyclic charge-discharge process on the electrochemical performance of the battery are given in Figures 5.68 - 5.70 . Comparison of discharge curves at different discharge cycle shows that, initially the damage contribution on the electrochemical properties of the battery is negligible, however, with an increasing number of discharge cycle the damage accumulation increases such that the diffusivity of the electrode is diminished gradually. This process result in degradation in the electrode active material, capacity fade and reduction in the discharge time in the entire battery cell as shown in Figure 5.68. Similarly, the electrode concentration distribution shows that initially higher concentration occupies the entire electrode island, while, with an increasing number of discharge cycle the electrode concentration gradient is increasing which result in reduction in the electrochemical performance of the battery cell. This phenomenon can be observed by comparing the concentration distribution in discharge cycles No. 1 and No. 61 given in Figures 5.69 and 5.70, respectively.

The impacts of coupled damage and cyclic charge-discharge process on the mechanical properties of the SSLIB island model are given in terms of variation of Von-mises stress at different measurement locations shown in Figure 5.67. The results are presented in terms of variation of the stress with discharge time and discharge cycles, see Figure 5.71 and 5.72. The results show that, for all measurement points, initially higher stress evolves at the end of each cycle. However, with an increasing number of discharge cycles the damage evolution is dominant which results in reduction in the material strength and eventually the magnitude of von-mises stress.

Table 5.8: Damage parameters in the 2D SSLIB island model.

Description	Symbol	Value	Unit
damage initiation threshold	κ_0	9.0×10^{-4}	-
damage sharpness parameter	β	10	-
damage gradient parameter	c	1.0×10^{-5}	m^2
applied external current	$\mathbf{I}_{\text{ext}}$	10.24	A/m^2

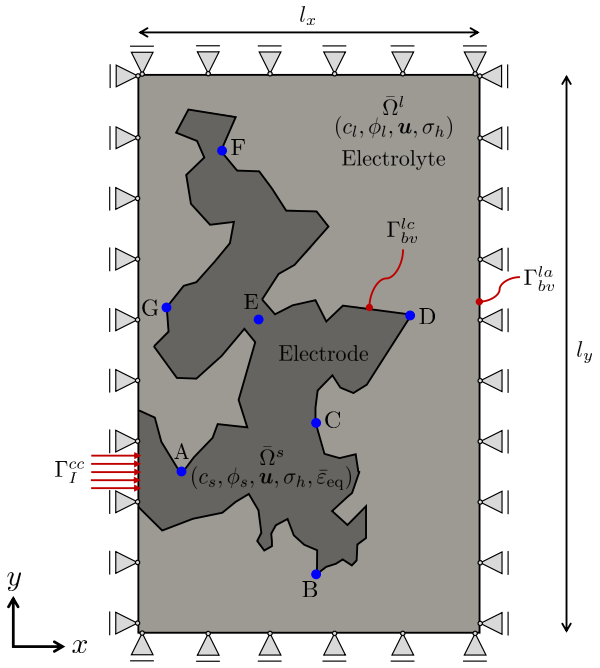

Figure 5.67: Schematic of a solid-state battery model for cyclic study.

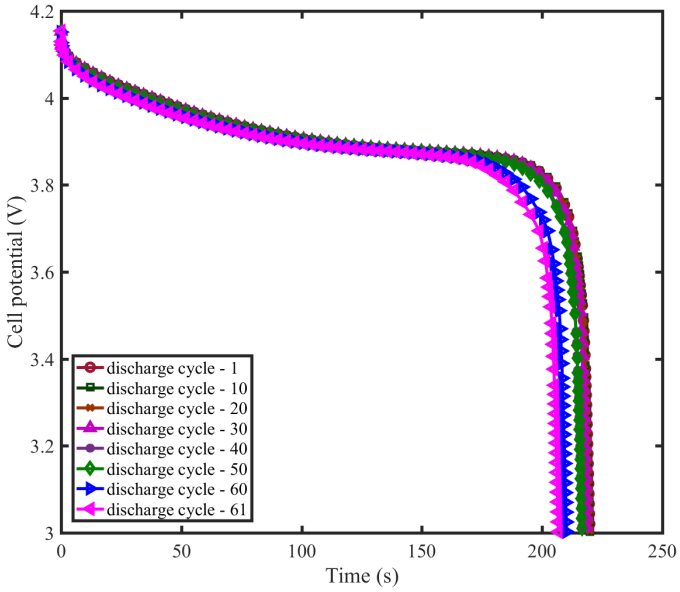

Figure 5.68: Variation of cell potential for different discharge cycle.

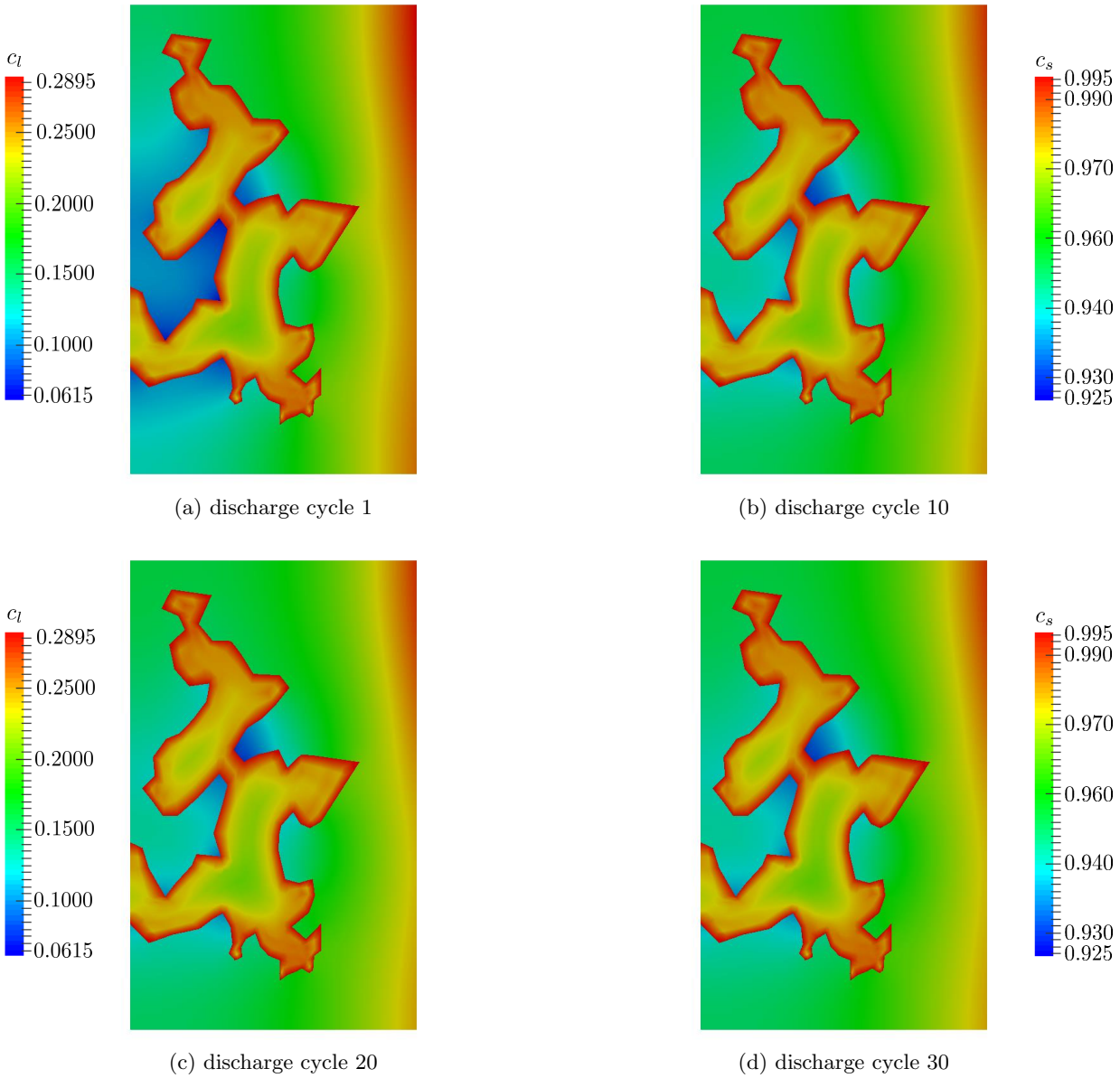

(a) discharge cycle 1

(b) discharge cycle 10

(c) discharge cycle 20

(d) discharge cycle 30

Figure 5.69: Variation of electrode and electrolyte concentrations at the end of discharge and for different discharge cycles.

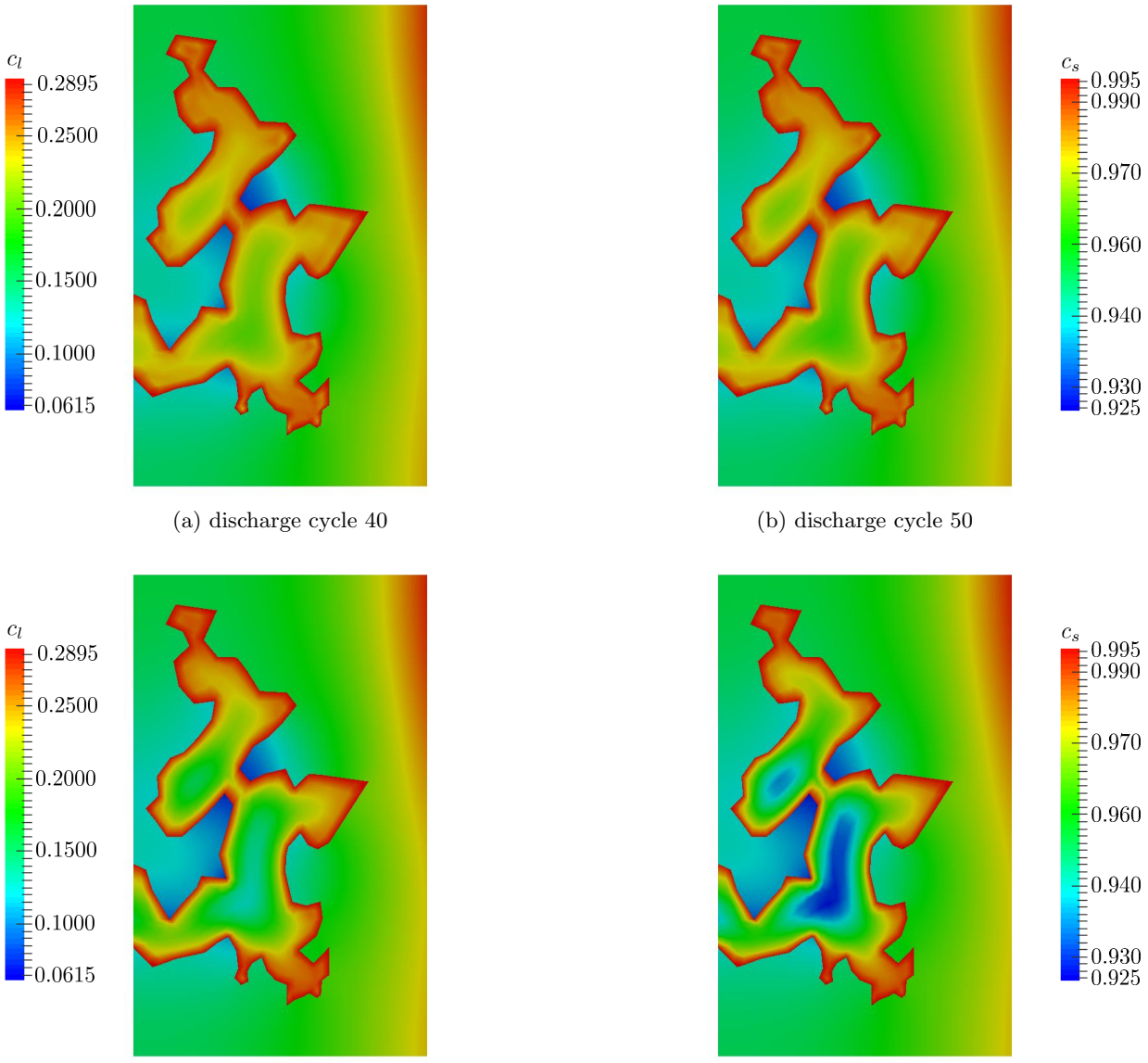

(a) discharge cycle 40

(b) discharge cycle 50

(c) discharge cycle 60

(d) discharge cycle 61

Figure 5.70: Variation of electrode and electrolyte concentrations at the end of discharge and for different discharge cycles.

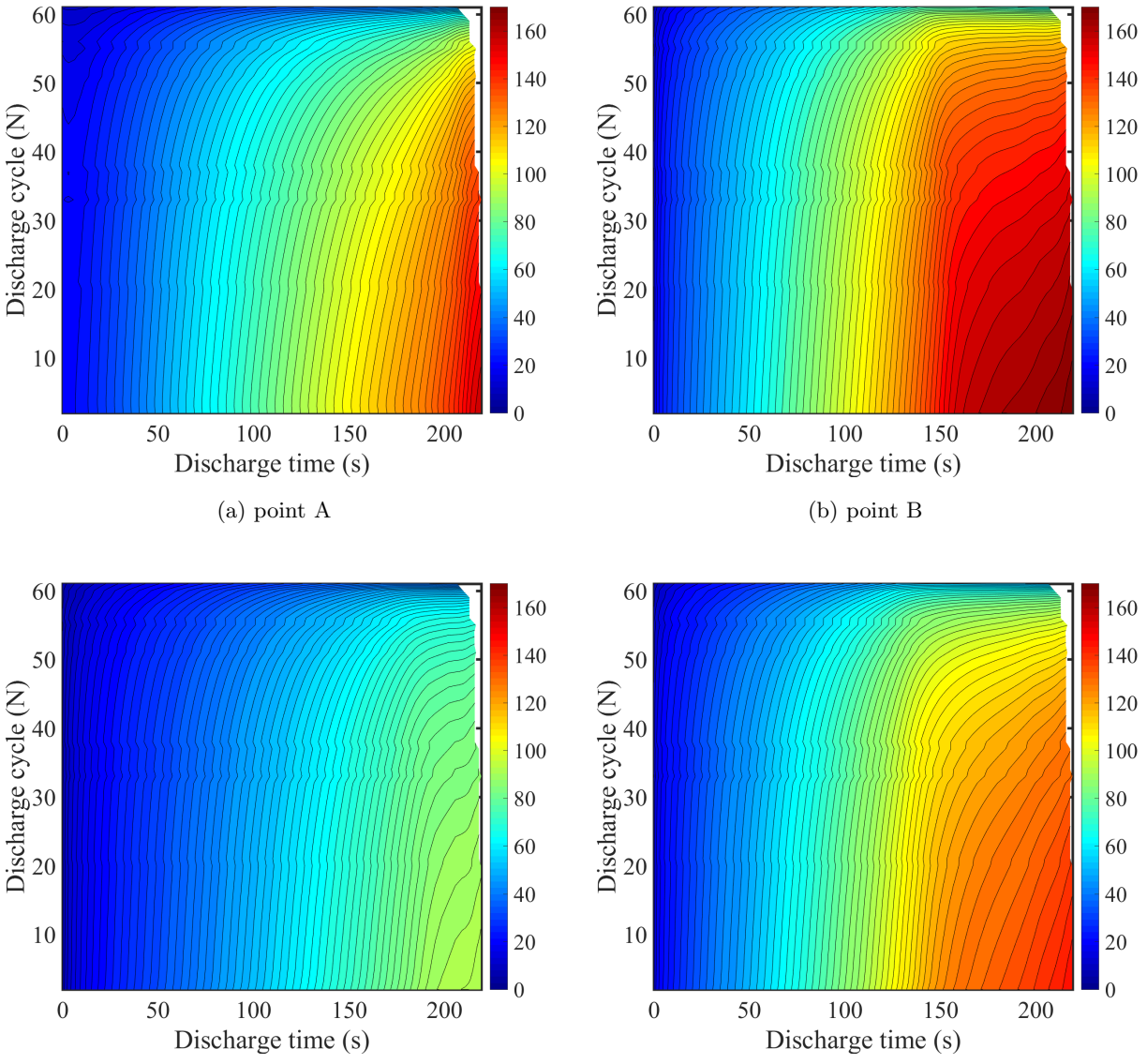

(a) point A

(b) point B

(c) point C

(d) point D

Figure 5.71: Variation of von mises stress with discharge time and discharge cycle at different measurement point (stress unit in MPa).

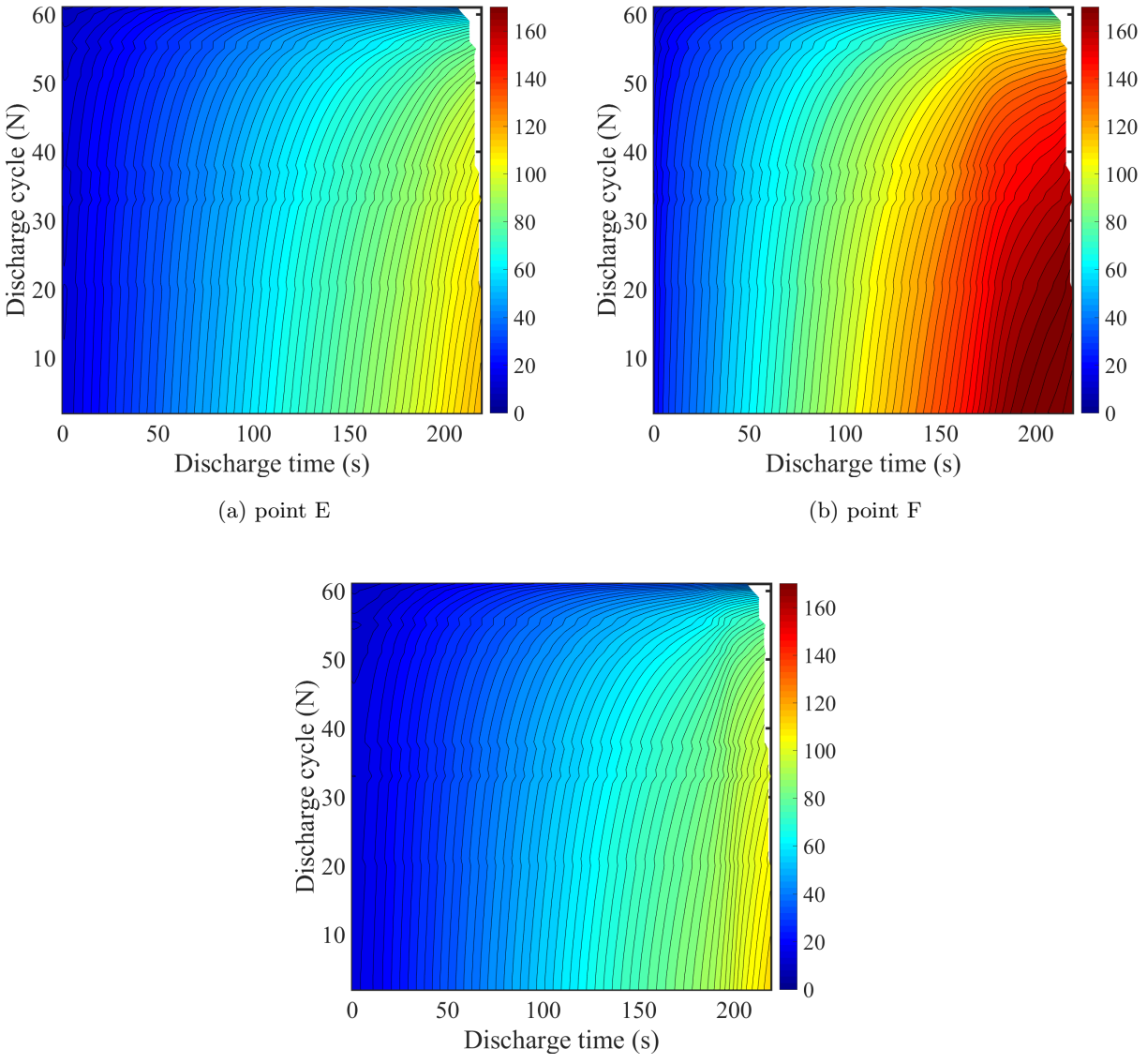

(a) point E

(b) point F

(c) point G

Figure 5.72: Variation of von mises stress with discharge time and discharge cycle at different measurement point (stress unit in MPa).

5.6 Numerical examples for the cohesive zone model

In this section, we first verify the accuracy of the implemented cohesive zone model for different modes of delamination through comparison against analytical reference solutions. To gain insight into the effectiveness and robustness of the cohesive zone model in our battery modeling framework, numerical examples for battery models with cohesive interface are considered. We studied the influences of cohesive interface parameters and the magnitude of the applied load through optimization problems. The results of this study present in Appendix E.

5.6.1 Verification of cohesive zone model for mode I of delamination

The accuracy of the XFEM formulation of the cohesive zone model discussed above is validated through comparison against the analytical solution for mode I of delamination. For this purpose, a double cantilever beam (DCB) is studied. The schematic of the DCB geometry is illustrated in Figure 5.73. Using linear elastic beam theory [5], the analytical solution for the crack length can be described as a function of cohesive fracture energy. The crack length is given by [129] as:

$$a = \sqrt[4]{\frac{3EH^3\Delta^2}{4G_c}} \ , \tag{5.45}$$

where E is the Young's modulus, Δ is the separation at the end, H is the beam height, and G_c is the cohesive fracture energy. We adapted the model parameters and problem configuration given by [129], provided in Table 5.9. For numerical modeling, the beam is discretized with 330×33 bilinear quadrilateral elements and the forward analysis is solved with a 2D plane strain condition. The measured crack length, a, is plotted as a function of end displacement, Δ, and compared to the analytical solution in Figure 5.74. The inset snapshots depict the initial and final deformed configuration of the DCB, with an expanded view of the mesh used. For visualization purposes, intersected elements are decomposed into triangles. Despite the influence of the fixed edge boundary condition, the measured relative error between two solutions is approximately 1%. This error is caused by unstable crack growth near the fixed edge of the beam, similarly observed by [5, 129].

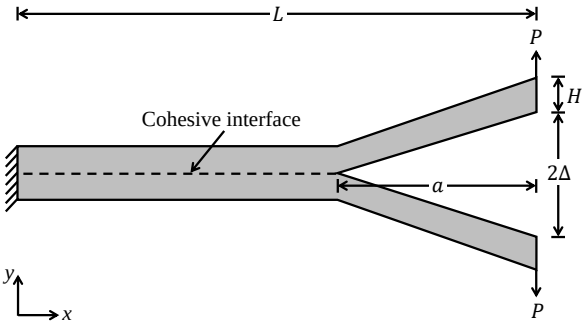

Figure 5.73: Schematic of the double cantilever beam.

Table 5.9: Model parameters for the double cantilever beam.

Description	Parameter	Value	Units
beam length	L	200	mm
beam height	H	10	mm
Young's modulus	E	14.2	GPa
Poisson's ratio	ν	0.35	
fraction energy	G_c	344	J/m^2
material strength	$\sigma_{\max}$	3.56	MPa
penalty factor	γ	20	

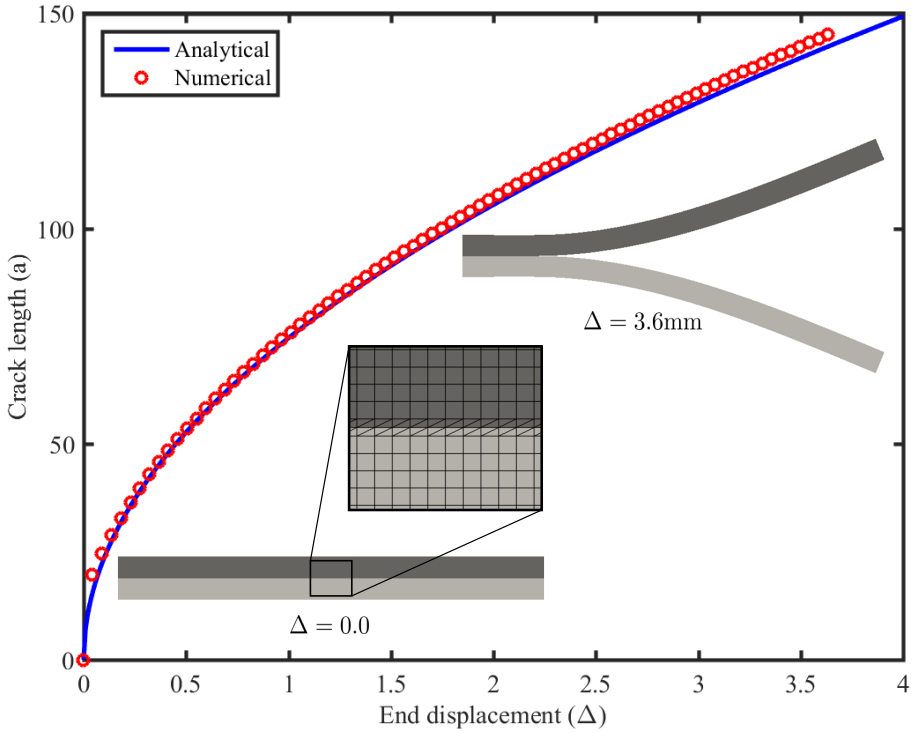

Figure 5.74: Comparison between analytical and numerical solutions for the double cantilever beam. For visualization purpose, the displacement in the deformed configuration is shown with a scaling factor 10.

5.6.2 Verification of cohesive zone model for mixed mode of delamination

In addition to mode I verification, the structural response during mixed mode uniform delamination is verified by an analytical solution. A rectangular block with a horizontal cohesive

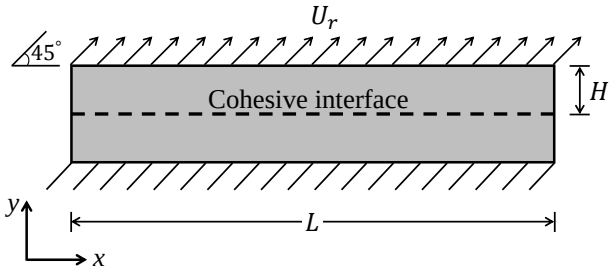

Figure 5.75: Loading and boundary conditions for the laminated structure with cohesive interface.

interface is fixed along the bottom edge and subjected to a uniform displacement along the top edge. The schematic of the problem and the boundary conditions are shown in Figure 5.75. The material and cohesive zone model parameters for the mixed mode delamination model are given in Table 5.10. For any given uniform surface separation value, the analytical solution for the total

Table 5.10: Material and cohesive zone parameters for the mixed mode model.

Description	Parameter	Value	Units
beam length	L	10	mm
beam height	H	0.1	mm
beam thickness	t	0.1	mm
applied displacement	U_r	0.15	mm
Young's modulus	E	2.0	GPa
Poisson's ratio	ν	0.3	
maximum normal traction	$\sigma_{\max}$	1.0	MPa
maximum tangential traction	$\tau_{\max}$	3.0	MPa
ultimate normal separation	δ_{f}^{n}	0.06	mm
ultimate tangential separation	δ_{f}^{t}	0.033	mm
critical normal separation	δ_{c}^{n}	0.006	mm
critical tangential separation	δ_{c}^{t}	0.0033	mm
penalty factor	γ	20	

delamination force is:

$$f = \int_{\Gamma_c} \left(T_n^2 + T_t^2\right)^{1/2} \mathrm{d}\Gamma \;\approx\; \left(T_n^2 + T_t^2\right)^{1/2} \times H \times t \;, \tag{5.46}$$

where f is the total force for uniform delamination along the cohesive interface Γ_c. For numerical modeling, the domain is discretized with 100×1 elements and the simulation is performed for 2D plane strain conditions. Since only the response at the interface is of interest, a single layer of

elements in thickness direction is sufficient. A uniform displacement is applied with a magnitude of 0.15 mm in sequence of load increments. Figure 5.76 compares numerical and analytical results for the total delamination force as a function of the magnitude of separation between the surfaces. The inset snapshots illustrate the mechanical response of a segment of the laminated structure at specific loading stages, with the intersected elements decomposed into triangles for visualization purposes. The measured relative error in the uniform mixed mode example problem is 2.25×10^{-7} %.

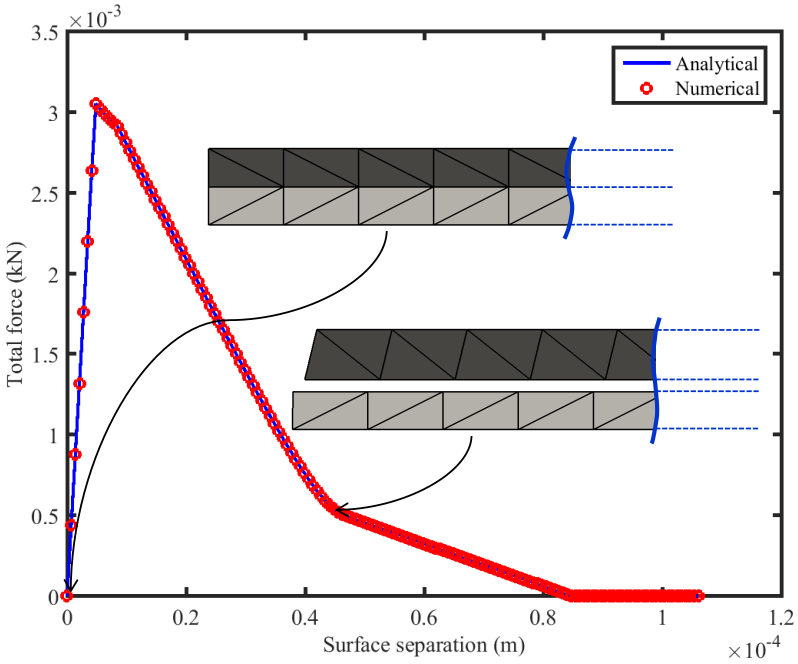

Figure 5.76: Force-separation curves for the analytical and numerical solutions in the laminated structure.

5.6.3 Influence of interfacial debonding on the electrochemical performance of the battery

In this example we wish to study the influence of debonding and delamination at the electrode and electrolyte interface on capacity fade and electrochemical performance of the battery. To this end, we used the thin-film solid state battery model presented in Section 5.1.1. The displacement

boundary condition is shown in Table 5.11. The influence of separation at the interface on the

Table 5.11: Thin-film solid-state battery displacement boundary condition.

Face	u_x	u_y	u_z
x_{min}	fixed	-	-
x_{max}	fixed	-	-
z_{min}	-	-	fixed
z_{max}	-	-	fixed
y_{min}	-	fixed	-
y_{max}	-	-	-

electrochemical performance of the battery is considered through the BV equation. In particular, for the interface in the debonded zone (see Figure 2.4) the BV contribution is neglected. Neglecting the BV contribution results in decreasing the electrochemical influence of the interface during discharge process. The interface properties for the cohesive zone model is shown in Table 5.12.

Table 5.12: Cohesive zone parameters for the thin-film solid-state battery model.

Description	Parameter	Value	Units
maximum normal traction	$\sigma_{\max}$	56.0	MPa
maximum tangential traction	$\tau_{\max}$	56.0	MPa
ultimate normal separation	δ_{f}^{n}	1.0×10^{-8}	m
ultimate tangential separation	δ_{f}^{t}	1.0×10^{-8}	m
critical normal separation	δ_{c}^{n}	5.0×10^{-9}	m
critical tangential separation	δ_{c}^{t}	5.0×10^{-9}	m
penalty factor	γ	20	

The model is discharged with different discharge rates and the results are presented in terms of variation of cell potential with discharge time. The results of the model with cohesive interface are compared with model with fully bonded interface based on Nitsche formulation (Figure 5.77). The results show that there is significant capacity fade in the battery with interfacial debonding. This indicates the influence of poor mechanical connections at the electrode/electrolyte interface on the electrochemical performance of all SSLIBs. This phenomenon needs to be studies experimentally for both thin and bulk solid-state batteries application.

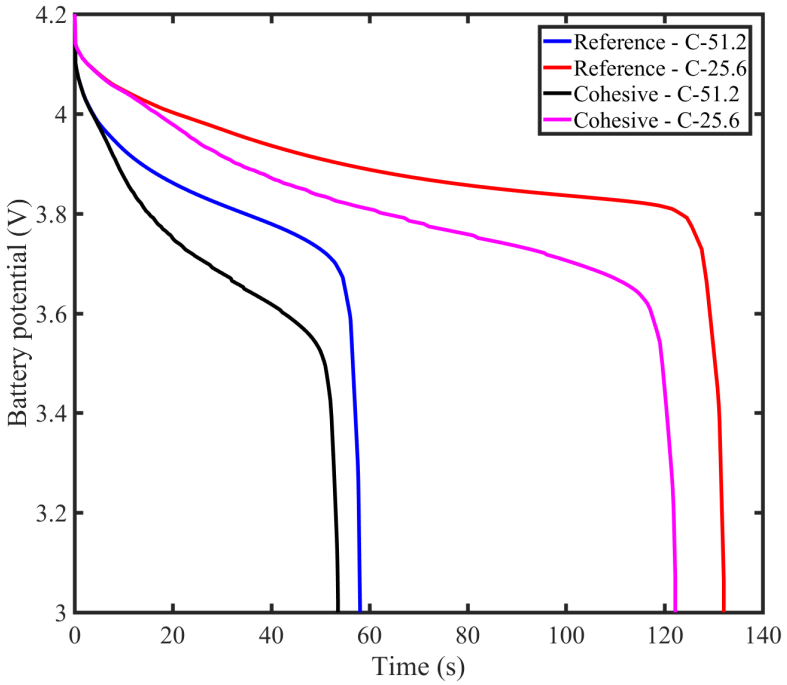

Figure 5.77: Comparison of the discharge curves for the thin-film model with cohesive interface.

Chapter 6

Conclusions

This thesis presents a comprehensive modeling framework for numerical simulation of coupled multi-physical responses in all SSLIBs. In particular, the research focuses on study and understanding the influence of damage evolution in the electrode active materials on capacity fade and life-time performance of SSLIBs, the influence of debonding and delamination at the electrode and electrolyte interface on the electrochemical performance of the battery, and the influence of material and model parameters on predicting the life-time performance of all SSLIBs. To this end, we build a full resolution modeling framework based on the FEM and XFEM approaches which enables us to study, evaluate and predict multi-physics responses of all bulk SSLIBs under the influences of electrochemical and mechanical interactions. The developed framework accounts for the electrochemical and mechanical interactions, the involved coupled physical phenomena includes mechanical deformation, diffusion-migration processes, stress-diffusion coupling, damage evolution, interfacial debunding and electrochemical surface reactions. The developed framework provides a higher-level of understanding and accuracy in evaluating the life-cycle performance and reliability of SSLIBs. To provide a predictive numerical tool for optimizing the performance of SSLIBs, an optimization algorithm is augmented into our finite element model. The optimization framework provides unique opportunities for parametric study and identifying key design parameters in life-time performance of SSLIBs.

The functionality of the developed full resolution framework is tested with comprehensive numerical benchmark examples. The numerical studies describe the accuracy, stability and conver-

gence performance of the developed framework for all SSLIB application. To compare the model prediction with experimental observations a comprehensive calibration experimental studies have been performed. The calibration examples illustrate the performance of the numerical model in capturing the experimental observations for bulk SSLIBs. However, during calibration studies some discrepancies were observed between the numerical results and experimental observations. In order to minimize these discrepancies, we developed a comprehensive parameters identification framework to study and minimize the discrepancies and mismatch between numerical and experimental results. The results showed the stability and performance of our parameters identification framework in minimizing the discrepancies, however, small discrepancies remain between the solutions which could be related to some physical phenomena (e.g. phase change, side reaction, thermal effects) that we are not including in our full resolution model. The performance of SSLIBs model under damage evolution effects were evaluated through numerical examples. In particular, we studied the influence of particle shape and cyclic charge-discharge process on the damage evolution and overall performance of SSLIBs. The impact of damage evolution on the discharge behavior and life-time performance of the battery was assessed by coupling the damage parameter with the diffusivity of the electrode particle. The results of our studies show that there is a significant contribution of the damage evolution on the electrochemical and life-time performance of the battery. The influence of delamination and debonding at the electrode and electrolyte interface has been studied through introducing cohesive zone model at the interface of the electrode and electrolyte. We coupled the delamination effects with the BV equation. The results showed that there is a great influence of separation at the interface on capacity fade and electrochemical performance of the battery.

Chapter 7

Future work

In order to improve the predictive capability of the model, the following studies should involve in the future work:

- Effects of phase change, formation of solid electrolyte interface, and side reaction through numerical modeling of SSLIBs;
- Effects of temperature and thermal diffusion on the life-time performance of the SSLIB.
- Topology optimization in the SSLIB.
- Effect of coupled delamination and damage evolution on the electrochemical performance of the SSLIB.

Bibliography

[1] S Abada, Guy Marlair, A Lecocq, M Petit, Valérie Sauvant-Moynot, and François Huet. Safety focused modeling of lithium-ion batteries: A review. Journal of Power Sources, 306:178–192, 2016.

[2] S Abada, Guy Marlair, A Lecocq, M Petit, Valérie Sauvant-Moynot, and François Huet. Safety focused modeling of lithium-ion batteries: A review. Journal of Power Sources, 306:178–192, 2016.

[3] Grégoire Allaire, François Jouve, and Anca-Maria Toader. Structural optimization using sensitivity analysis and a level-set method. Journal of computational physics, 194(1):363–393, 2004.

[4] Yonghao An, Brandon C Wood, Jianchao Ye, Yet-Ming Chiang, Y Morris Wang, Ming Tang, and Hanqing Jiang. Mitigating mechanical failure of crystalline silicon electrodes for lithium batteries by morphological design. Physical Chemistry Chemical Physics, 17(27):17718–17728, 2015.

[5] Ted L Anderson and TL Anderson. Fracture mechanics: fundamentals and applications. CRC press, 2005.

[6] Pankaj Arora, Ralph E White, and Marc Doyle. Capacity fade mechanisms and side reactions in lithium-ion batteries. Journal of the Electrochemical Society, 145(10):3647–3667, 1998.

[7] Pankaj Arora, Ralph E White, and Marc Doyle. Capacity fade mechanisms and side reactions in lithium-ion batteries. Journal of the Electrochemical Society, 145(10):3647–3667, 1998.

[8] Todd M Bandhauer, Srinivas Garimella, and Thomas F Fuller. A critical review of thermal issues in lithium-ion batteries. Journal of the Electrochemical Society, 158(3):R1–R25, 2011.

[9] Pallab Barai and Partha P Mukherjee. Stochastic analysis of diffusion induced damage in lithium-ion battery electrodes. Journal of The Electrochemical Society, 160(6):A955–A967, 2013.

[10] Zdenek P Bazant and MT Kazemi. Determination of fracture energy, process zone longth and brittleness number from size effect, with application to rock and conerete. International Journal of Fracture, 44(2):111–131, 1990.

[11] Zdenek P Bazant and Gilles Pijaudier-Cabot. Measurement of characteristic length of non-local continuum. Journal of Engineering Mechanics, 115(4):755–767, 1989.

[12] Katharina Becker-Steinberger, Stefan Funken, Manuel Landstorfer, and Karsten Urban. A mathematical model for all solid-state lithium-ion batteries. ECS Transactions, 25(36):285–296, 2010.

[13] Dick Bedeaux and Signe Kjelstrup Ratkje. The dissipated energy of electrode surfaces: Temperature jumps from coupled transport processes. Journal of the Electrochemical Society, 143(3):767–779, 1996.

[14] T Belytschko, D Organ, and C Gerlach. Element-free galerkin methods for dynamic fracture in concrete. Computer Methods in Applied Mechanics and Engineering, 187(3):385–399, 2000.

[15] Ted Belytschko, Jacob Fish, and Bruce E Engelmann. A finite element with embedded localization zones. Computer methods in applied mechanics and engineering, 70(1):59–89, 1988.

[16] M. P. Bendsøe and O. Sigmund. Topology Optimization: Theory, Methods and Applications. Springer, 2003.

[17] Martin P Bendsøe. Optimal shape design as a material distribution problem. Structural optimization, 1(4):193–202, 1989.

[18] D Bernardi, E Pawlikowski, and John Newman. A general energy balance for battery systems. Journal of the electrochemical society, 132(1):5–12, 1985.

[19] Tanmay K Bhandakkar and Huajian Gao. Cohesive modeling of crack nucleation under diffusion induced stresses in a thin strip: Implications on the critical size for flaw tolerant battery electrodes. International Journal of Solids and Structures, 47(10):1424–1434, 2010.

[20] Gerardine G Botte, Venkat R Subramanian, and Ralph E White. Mathematical modeling of secondary lithium batteries. Electrochim. Acta, 45:2595–2609, 2000.

[21] AF Bower and PR Guduru. A simple finite element model of diffusion, finite deformation, plasticity and fracture in lithium ion insertion electrode materials. Modelling and Simulation in Materials Science and Engineering, 20(4):045004, 2012.

[22] Allan F Bower, Pradeep R Guduru, and Vijay A Sethuraman. A finite strain model of stress, diffusion, plastic flow, and electrochemical reactions in a lithium-ion half-cell. Journal of the Mechanics and Physics of Solids, 59(4):804–828, 2011.

[23] M Broussely, Ph Biensan, F Bonhomme, Ph Blanchard, S Herreyre, K Nechev, and RJ Staniewicz. Main aging mechanisms in li ion batteries. Journal of power sources, 146(1):90–96, 2005.

[24] Godofredo T Camacho and M Ortiz. Computational modelling of impact damage in brittle materials. International Journal of solids and structures, 33(20):2899–2938, 1996.

[25] Candace K Chan, Hailin Peng, Gao Liu, Kevin McIlwrath, Xiao Feng Zhang, Robert A Huggins, and Yi Cui. High-performance lithium battery anodes using silicon nanowires. Nat. Nanotechnol., 3:31–35, 2008.

[26] Chien-Fan Chen, Pallab Barai, and Partha P Mukherjee. Diffusion induced damage and impedance response in lithium-ion battery electrodes. Journal of The Electrochemical Society, 161(14):A2138–A2152, 2014.

[27] Chien-Fan Chen, Pallab Barai, Kandler Smith, and Partha P Mukherjee. Scaling relations for intercalation induced damage in electrodes. Electrochimica Acta, 2016.

[28] Xin-Bing Cheng, Rui Zhang, Chen-Zi Zhao, Fei Wei, Ji-Guang Zhang, and Qiang Zhang. A review of solid electrolyte interphases on lithium metal anode. Advanced Science, 2015.

[29] Yang-Tse Cheng and Mark W Verbrugge. The influence of surface mechanics on diffusion induced stresses within spherical nanoparticles. Journal of Applied Physics, 104(8):083521, 2008.

[30] Yang-Tse Cheng and Mark W Verbrugge. Evolution of stress within a spherical insertion electrode particle under potentiostatic and galvanostatic operation. Journal of Power Sources, 190(2):453–460, 2009.

[31] John Christensen and John Newman. A mathematical model of stress generation and fracture in lithium manganese oxide. Journal of The Electrochemical Society, 153(6):A1019–A1030, 2006.

[32] John Christensen and John Newman. A mathematical model of stress generation and fracture in lithium manganese oxide. Journal of The Electrochemical Society, 153(6):A1019–A1030, 2006.

[33] John Christensen and John Newman. Stress generation and fracture in lithium insertion materials. Journal of Solid State Electrochemistry, 10(5):293–319, 2006.

[34] Peter Coffin and Kurt Maute. A level-set method for steady-state and transient natural convection problems. Structural and Multidisciplinary Optimization, 53(5):1047–1067, 2016.

[35] Bernard D Coleman and Walter Noll. The thermodynamics of elastic materials with heat conduction and viscosity. Archive for Rational Mechanics and Analysis, 13(1):167–178, 1963.

[36] Yongli Cui, Mingzhen Wang, Jiali Wang, and Quanchao Zhuang. Effect of temperature on the electronic/ionic transport properties of porous lini 0.5 mn 1.5 o 4 with high voltage for lithium ion batteries. Materials Chemistry and Physics, 2016.

[37] Yiling Dai, Long Cai, and Ralph E White. Capacity fade model for spinel limn2o4 electrode. Journal of The Electrochemical Society, 160(1):A182–A190, 2013.

[38] D Danilov, RAH Niessen, and PHL Notten. Modeling all-solid-state li-ion batteries. Journal of the Electrochemical Society, 158(3):A215–A222, 2011.

[39] Joshua D Deaton and Ramana V Grandhi. A survey of structural and multidisciplinary continuum topology optimization: post 2000. Structural and Multidisciplinary Optimization, 49(1):1–38, 2014.

[40] Christopher M DeLuca, Kurt Maute, and Martin L Dunn. Effects of electrode particle morphology on stress generation in silicon during lithium insertion. Journal of Power Sources, 196(22):9672–9681, 2011.

[41] Rutooj Deshpande, Yang-Tse Cheng, and Mark W Verbrugge. Modeling diffusion-induced stress in nanowire electrode structures. Journal of Power Sources, 195(15):5081–5088, 2010.

[42] Rutooj Deshpande, Mark Verbrugge, Yang-Tse Cheng, John Wang, and Ping Liu. Battery cycle life prediction with coupled chemical degradation and fatigue mechanics. Journal of The Electrochemical Society, 159(10):A1730–A1738, 2012.

[43] Marc Doyle, Thomas F Fuller, and John Newman. Modeling of galvanostatic charge and discharge of the lithium/polymer/insertion cell. J. Electrochem. Soc., 140:1526–1533, 1993.

[44] Marc Doyle, John Newman, Antoni S Gozdz, Caroline N Schmutz, and Jean-Marie Tarascon. Comparison of modeling predictions with experimental data from plastic lithium ion cells. J. Electrochem. Soc., 143:1890–1903, 1996.

[45] DS Dugdale. Yielding of steel sheets containing slits. Journal of the Mechanics and Physics of Solids, 8(2):100–104, 1960.

[46] ML Dunn and H Ledbetter. Elastic moduli of composites reinforced by multiphase particles. Journal of applied mechanics, 62(4):1023–1028, 1995.

[47] M Elices, GV Guinea, J Gomez, and J Planas. The cohesive zone model: advantages, limitations and challenges. Engineering fracture mechanics, 69(2):137–163, 2002.

[48] Ahmadreza Eshghinejad and Jiangyu Li. The coupled lithium ion diffusion and stress in battery electrodes. Mechanics of Materials, 91:343–350, 2015.

[49] HD Espinosa, S Dwivedi, and H-C Lu. Modeling impact induced delamination of woven fiber reinforced composites with contact/cohesive laws. Computer Methods in Applied Mechanics and Engineering, 183(3):259–290, 2000.

[50] Steve D Fabre, Delphine Guy-Bouyssou, Pierre Bouillon, Frédéric Le Cras, and Charles Delacourt. Charge/discharge simulation of an all-solid-state thin-film battery using a one-dimensional model. Journal of The Electrochemical Society, 159(2):A104–A115, 2011.

[51] Jeffrey W Fergus. Ceramic and polymeric solid electrolytes for lithium-ion batteries. Journal of Power Sources, 195(15):4554–4569, 2010.

[52] Alejandro A Franco. Multiscale modelling and numerical simulation of rechargeable lithium ion batteries: concepts, methods and challenges. RSC Advances, 3:13027–13058, 2013.

[53] Thomas-Peter Fries and Ted Belytschko. The intrinsic XFEM: a method for arbitrary discontinuities without additional unknowns. International journal for numerical methods in engineering, 68(13):1358–1385, 2006.

[54] T.P. Fries and T. Belytschko. The extended/generalized finite element method: an overview of the method and its applications. International Journal for Numerical Methods in Engineering, 84(3):253–304, 2010.

[55] Keita Funayama, Takashi Nakamura, Naoaki Kuwata, Junichi Kawamura, Tatsuya Kawada, and Koji Amezawa. Effect of mechanical stress on lithium chemical potential in positive electrodes and solid electrolytes for lithium ion batteries. Electrochemistry, 83(10):894–897, 2015.

[56] C William Gear. Numerical initial value problems in ordinary differential equations. Prentice Hall PTR, 1971.

[57] Philippe H Geubelle and Jeffrey S Baylor. Impact-induced delamination of composites: a 2d simulation. Composites Part B: Engineering, 29(5):589–602, 1998.

[58] Stephanie Golmon, Kurt Maute, and Martin L Dunn. Numerical modeling of electrochemical–mechanical interactions in lithium polymer batteries. Comput. Struct., 87:1567–1579, 2009.

[59] Stephanie Golmon, Kurt Maute, and Martin L Dunn. Multiscale design optimization of lithium ion batteries using adjoint sensitivity analysis. International Journal for Numerical Methods in Engineering, 92(5):475–494, 2012.

[60] Stephanie Golmon, Kurt Maute, and Martin L Dunn. A design optimization methodology for li+ batteries. Journal of Power Sources, 253:239–250, 2014.

[61] Parthasarathy M Gomadam, John W Weidner, Roger A Dougal, and Ralph E White. Mathematical modeling of lithium-ion and nickel battery systems. J. Power Sources, 110:267–284, 2002.

[62] John B Goodenough and Youngsik Kim. Challenges for rechargeable li batteries. Chem. Mater., 22:587–603, 2009.

[63] Rassin Grantab and Vivek B Shenoy. Location-and orientation-dependent progressive crack propagation in cylindrical graphite electrode particles. Journal of The Electrochemical Society, 158(8):A948–A954, 2011.

[64] Arne S Gullerud, Xiaosheng Gao, Robert H Dodds, and R Haj-Ali. Simulation of ductile crack growth using computational cells: numerical aspects. Engineering Fracture Mechanics, 66(1):65–92, 2000.

[65] Guifang Guo, Bo Long, Bo Cheng, Shiqiong Zhou, Peng Xu, and Binggang Cao. Three-dimensional thermal finite element modeling of lithium-ion battery in thermal abuse application. Journal of Power Sources, 195(8):2393–2398, 2010.

[66] Zhansheng Guo, Tao Zhang, Hongjiu Hu, Yicheng Song, and Junqian Zhang. Effects of hydrostatic stress and concentration-dependent elastic modulus on diffusion-induced stresses in cylindrical li-ion batteries. Journal of Applied Mechanics, 81(3):031013, 2014.

[67] Morton E Gurtin, Eliot Fried, and Lallit Anand. The mechanics and thermodynamics of continua. Cambridge University Press, 2010.

[68] Mohammad Hadigol, Kurt Maute, and Alireza Doostan. On uncertainty quantification of lithium-ion batteries: Application to an LiC6/LiCoO2 cell. Journal of Power Sources, 300:507–524, 2015.

[69] Gerhard A Holzapfel. Nonlinear solid mechanics, volume 24. Wiley Chichester, 2000.

[70] Muneo Hori and Sia Nemat-Nasser. Double-inclusion model and overall moduli of multi-phase composites. Mechanics of Materials, 14(3):189–206, 1993.

[71] Thomas JR Hughes. The finite element method: linear static and dynamic finite element analysis. Courier Corporation, 2012.

[72] Milan Jirásek. Comparative study on finite elements with embedded discontinuities. Computer methods in applied mechanics and engineering, 188(1):307–330, 2000.

[73] Keiichi Kanehori, Kazunobu Matsumoto, Katsuki Miyauchi, and Tetsuichi Kudo. Thin film solid electrolyte and its application to secondary lithium cell. Solid State Ionics, 9:1445–1448, 1983.

[74] Ali Ghorbani Kashkooli, Siamak Farhad, Dong Un Lee, Kun Feng, Shawn Litster, Siddharth Komini Babu, Likun Zhu, and Zhongwei Chen. Multiscale modeling of lithium-ion battery electrodes based on nano-scale x-ray computed tomography. Journal of Power Sources, 307:496–509, 2016.

[75] A. R. Khoei. Extended finite element method: Theory and applications. Wiley, 2015.

[76] Gi-Heon Kim, Ahmad Pesaran, and Robert Spotnitz. A three-dimensional thermal abuse model for lithium-ion cells. Journal of Power Sources, 170(2):476–489, 2007.

[77] Gi-Heon Kim, Kandler Smith, Kyu-Jin Lee, Shriram Santhanagopalan, and Ahmad Pesaran. Multi-domain modeling of lithium-ion batteries encompassing multi-physics in varied length scales. Journal of The Electrochemical Society, 158(8):A955–A969, 2011.

[78] Philippe Knauth. Inorganic solid li ion conductors: An overview. Solid State Ionics, 180(14):911–916, 2009.

[79] Sebastian Kreissl and Kurt Maute. Levelset based fluid topology optimization using the extended finite element method. Structural and Multidisciplinary Optimization, pages 1–16, 2012.

[80] Izaro Laresgoiti, Stefan Käbitz, Madeleine Ecker, and Dirk Uwe Sauer. Modeling mechanical degradation in lithium ion batteries during cycling: Solid electrolyte interphase fracture. Journal of Power Sources, 300:112–122, 2015.

[81] Seungjun Lee, Jun Yang, and Wei Lu. Debonding at the interface between active particles and pvdf binder in li-ion batteries. Extreme Mechanics Letters, 6:37–44, 2016.

[82] Feng Leng, Cher Ming Tan, and Michael Pecht. Effect of temperature on the aging rate of li ion battery operating above room temperature. Scientific reports, 5, 2015.

[83] James Chen-Min Li. Physical chemistry of some microstructural phenomena. Metallurgical Transactions A, 9(10):1353–1380, 1978.

[84] S Li and S Ghosh. Modeling interfacial debonding and matrix cracking in fiber reinforced composites by the extended voronoi cell fem. Finite elements in analysis and design, 43(5):397–410, 2007.

[85] Xianke Lin, Jonghyun Park, Lin Liu, Yoonkoo Lee, AM Sastry, and Wei Lu. A comprehensive capacity fade model and analysis for li-ion batteries. Journal of The Electrochemical Society, 160(10):A1701–A1710, 2013.

[86] Wei-Ren Liu, Zheng-Zao Guo, Wen-Shiue Young, Deng-Tswen Shieh, Hung-Chun Wu, Mo-Hua Yang, and Nae-Lih Wu. Effect of electrode structure on performance of si anode in li-ion batteries: Si particle size and conductive additive. Journal of Power Sources, 140(1):139–144, 2005.

[87] Yingjie Liu, Pengyu Lv, Jun Ma, Ruobing Bai, and Hui Ling Duan. Stress fields in hollow core–shell spherical electrodes of lithium ion batteries. In Proceedings of the Royal Society of London A: Mathematical, Physical and Engineering Sciences, volume 470, page 20140299. The Royal Society, 2014.

[88] Pin Lu, YW Leong, PK Pallathadka, and CB He. Effective moduli of nanoparticle reinforced composites considering interphase effect by extended double-inclusion model–theory and explicit expressions. International Journal of Engineering Science, 73:33–55, 2013.

[89] Zhen Luo, Liyong Tong, Michael Yu Wang, and Shengyin Wang. Shape and topology optimization of compliant mechanisms using a parameterization level set method. Journal of Computational Physics, 227(1):680–705, 2007.

[90] Yanping Ma, Marc Doyle, Thomas F Fuller, Marca M Doeff, Lutgard C De Jonghe, and John Newman. The measurement of a complete set of transport properties for a concentrated solid polymer electrolyte solution. Journal of The Electrochemical Society, 142(6):1859–1868, 1995.

[91] D. Makhija and K. Maute. Numerical instabilities in level set topology optimization with the extended finite element method. Structural and Multidisciplinary Optimization, 49(2):185–197, 2014.

[92] Jacky Mazars. Application de la mécanique de l'endommagement au comportement non linéaire et à la rupture du béton de structure. PhD thesis, 1984.

[93] C Miehe, H Dal, L-M Schänzel, and A Raina. A phase-field model for chemo-mechanical induced fracture in lithium-ion battery electrode particles. International Journal for Numerical Methods in Engineering, 2015.

[94] N. Moës, J. Dolbow, and T. Belytschko. A finite element method for crack growth without remeshing. International Journal for Numerical Methods in Engineering, 46, 1999.

[95] Nicolas Moës and Ted Belytschko. Extended finite element method for cohesive crack growth. Engineering fracture mechanics, 69(7):813–833, 2002.

[96] Tanaka Mori and K Tanaka. Average stress in matrix and average elastic energy of materials with misfitting inclusions. Acta metallurgica, 21(5):571–574, 1973.

[97] COMSOL Multiphysics. version 4.3 b. COMSOL Inc, 2013.

[98] Motohiro Nagao, Akitoshi Hayashi, and Masahiro Tatsumisago. High-capacity li 2 s–nanocarbon composite electrode for all-solid-state rechargeable lithium batteries. Journal of Materials Chemistry, 22(19):10015–10020, 2012.

[99] A Needleman. A continuum model for void nucleation by inclusion debonding. Journal of applied mechanics, 54(3):525–531, 1987.

[100] John Newman and Karen E Thomas-Alyea. Electrochemical systems. John Wiley and Sons, 2012.

[101] John Newman and William Tiedemann. Porous-electrode theory with battery applications. AIChE Journal, 21(1):25–41, 1975.

[102] Peter HL Notten. 3d-integrated all-solid-state batteries. Europhysics News, 42(3):24–29, 2011.

[103] Jos FM Oudenhoven, Loïc Baggetto, and Peter HL Notten. All-solid-state lithium-ion microbatteries: A review of various three-dimensional concepts. Advanced Energy Materials, 1(1):10–33, 2011.

[104] Siladitya Pal, Sameer S Damle, Prashant N Kumta, and Spandan Maiti. Modeling of lithium segregation induced delamination of a-si thin film anode in li-ion batteries. Computational Materials Science, 79:877–887, 2013.

[105] Siladitya Pal, Sameer S Damle, Siddharth H Patel, Moni K Datta, Prashant N Kumta, and Spandan Maiti. Modeling the delamination of amorphous-silicon thin film anode for lithium-ion battery. Journal of Power Sources, 246:149–159, 2014.

[106] Carolyn R Pals and John Newman. Thermal modeling of the lithium/polymer battery i. discharge behavior of a single cell. J. Electrochem. Soc., 142:3274–3281, 1995.

[107] Jonghyun Park, Wei Lu, and Ann Marie Sastry. Numerical simulation of stress evolution in lithium manganese dioxide particles due to coupled phase transition and intercalation. Journal of The Electrochemical Society, 158(2):A201–A206, 2011.

[108] Kyoungsoo Park and Glaucio H Paulino. Cohesive zone models: a critical review of traction-separation relationships across fracture surfaces. Applied Mechanics Reviews, 64(6):060802, 2011.

[109] Kyoungsoo Park, Glaucio H Paulino, and Jeffery R Roesler. Determination of the kink point in the bilinear softening model for concrete. Engineering Fracture Mechanics, 75(13):3806–3818, 2008.

[110] Georg Pingen, Matthias Waidmann, Anton Evgrafov, and Kurt Maute. A parametric level-set approach for topology optimization of flow domains. Structural and Multidisciplinary Optimization, 41(1):117–131, 2010.

[111] Matthew B Pinson and Martin Z Bazant. Theory of SEI formation in rechargeable batteries: capacity fade, accelerated aging and lifetime prediction. Journal of the Electrochemical Society, 160(2):A243–A250, 2013.

[112] S Prussin. Generation and distribution of dislocations by solute diffusion. Journal of Applied Physics, 32(10):1876–1881, 1961.

[113] Eliana Quartarone and Piercarlo Mustarelli. Electrolytes for solid-state lithium rechargeable batteries: recent advances and perspectives. Chemical Society Reviews, 40(5):2525–2540, 2011.

[114] Lin Rao and John Newman. Heat-generation rate and general energy balance for insertion battery systems. Journal of the Electrochemical Society, 144(8):2697–2704, 1997.

[115] Sindhuja Renganathan, Godfrey Sikha, Shriram Santhanagopalan, and Ralph E White. Theoretical analysis of stresses in a lithium ion cell. Journal of The Electrochemical Society, 157(2):A155–A163, 2010.

[116] W.A.M. Brekelmans R.H.J. Peerlings, R. de Borst and J.H.P. de Vree. Gradient enhanced damage for quasi-brittle materials. International Journal for numerical methods in engineering, 39:3391–3403, 1996.

[117] Jeffrey Roesler, Glaucio H Paulino, Kyoungsoo Park, and Cristian Gaedicke. Concrete fracture prediction using bilinear softening. Cement and Concrete Composites, 29(4):300–312, 2007.

[118] G.I.N. Rozvany, M. Zhou, and T. Birker. Generalized shape optimization without homogenization. Structural and Multidisciplinary Optimization, 4(3):250–252, 1992.

[119] M Safari, M Morcrette, A Teyssot, and C Delacourt. Life-prediction methods for lithium-ion batteries derived from a fatigue approach i. introduction: capacity-loss prediction based on damage accumulation. Journal of The Electrochemical Society, 157(6):A713–A720, 2010.

[120] A Salvadori, E Bosco, and D Grazioli. A computational homogenization approach for li-ion battery cells: Part 1–formulation. J. Mech. Phys. Solids, 65:114–137, 2014.

[121] A Salvadori, D Grazioli, and MGD Geers. Governing equations for a two-scale analysis of li-ion battery cells. In. J. Solids and Struc., 59:90–109, 2015.

[122] A Salvadori, D Grazioli, MGD Geers, D Danilov, and PHL Notten. A multiscale-compatible approach in modeling ionic transport in the electrolyte of (lithium ion) batteries. J. Power Sources, 293:892–911, 2015.

[123] Bruno Scrosati and Jürgen Garche. Lithium batteries: Status, prospects and future. J. Power Sources, 195:2419–2430, 2010.

[124] Joongpyo Shim, Robert Kostecki, Thomas Richardson, Xiangyun Song, and Kathryn A Striebel. Electrochemical analysis for cycle performance and capacity fading of a lithium-ion battery cycled at elevated temperature. Journal of Power Sources, 112(1):222–230, 2002.

[125] Ole Sigmund and Kurt Maute. Topology optimization approaches: A comparative review. Structural and Multidisciplinary Optimization, 48(6):1031–1055, 2013.

[126] Godfrey Sikha, Branko N Popov, and Ralph E White. Effect of porosity on the capacity fade of a lithium-ion battery theory. Journal of The Electrochemical Society, 151(7):A1104–A1114, 2004.

[127] Li Song and James W Evans. Electrochemical-thermal model of lithium polymer batteries. J. Electrochem. Soc., 147:2086–2095, 2000.

[128] Seong Hyeok Song, Glaucio H Paulino, and William G Buttlar. A bilinear cohesive zone model tailored for fracture of asphalt concrete considering viscoelastic bulk material. Engineering Fracture Mechanics, 73(18):2829–2848, 2006.

[129] Seong Hyeok Song, Glaucio H Paulino, and William G Buttlar. Simulation of crack propagation in asphalt concrete using an intrinsic cohesive zone model. Journal of Engineering Mechanics, 132(11):1215–1223, 2006.

[130] S Stramare, V Thangadurai, and W Weppner. Lithium lanthanum titanates: a review. Chemistry of materials, 15(21):3974–3990, 2003.

[131] Kenjiro Terada, Mitsuteru Asai, and Michihiro Yamagishi. Finite cover method for linear and non-linear analyses of heterogeneous solids. International journal for numerical methods in engineering, 58(9):1321–1346, 2003.

[132] Karen E Thomas and John Newman. Thermal modeling of porous insertion electrodes. Journal of the Electrochemical Society, 150(2):A176–A192, 2003.

[133] Martin GA Tijssens, Bert LJ Sluys, and Erik van der Giessen. Numerical simulation of quasi-brittle fracture using damaging cohesive surfaces. European Journal of Mechanics-A/Solids, 19(5):761–779, 2000.

[134] A. B. Tran, J. Yvonnet, Q-C. He, C. Toulemonde, and J. Sanahuja. A multiple level set approach to prevent numerical artefacts in complex microstructures with nearby inclusions within XFEM. International Journal for Numerical Methods in Engineering, 85(11):1436–1459, 2011.

[135] James E Trevey, Conrad R Stoldt, and Se-Hee Lee. High power nanocomposite tis2 cathodes for all-solid-state lithium batteries. Journal of The Electrochemical Society, 158(12):A1282–A1289, 2011.

[136] Viggo Tvergaard. Effect of fibre debonding in a whisker-reinforced metal. Materials science and engineering: A, 125(2):203–213, 1990.

[137] Viggo Tvergaard and John W Hutchinson. The relation between crack growth resistance and fracture process parameters in elastic-plastic solids. Journal of the Mechanics and Physics of Solids, 40(6):1377–1397, 1992.

[138] Anthony J Vaccaro, T Palanisamy, RL Kerr, and JT Maloy. Electrochemical determination of the lithium ion diffusion coefficient in tis 2. Solid State Ionics, 2(4):337–340, 1981.

[139] MJ Van den Bosch, PJG Schreurs, and MGD Geers. An improved description of the exponential xu and needleman cohesive zone law for mixed-mode decohesion. Engineering Fracture Mechanics, 73(9):1220–1234, 2006.

[140] Anton Van der Ven, John C Thomas, Qingchuan Xu, Benjamin Swoboda, and Dane Morgan. Nondilute diffusion from first principles: Li diffusion in li x tis 2. Physical Review B, 78(10):104306, 2008.

[141] Nico P van Dijk, K Maute, M Langelaar, and F Van Keulen. Level-set methods for structural topology optimization: a review. Structural and Multidisciplinary Optimization, 48(3):437–472, 2013.

[142] Laurent Van Miegroet and Pierre Duysinx. Stress concentration minimization of 2D filets using X-FEM and level set description. Structural and Multidisciplinary Optimization, 33(4-5):425–438, 2007.

[143] Mark W Verbrugge and Yang-Tse Cheng. Stress and strain-energy distributions within diffusion-controlled insertion-electrode particles subjected to periodic potential excitations. Journal of the Electrochemical Society, 156(11):A927–A937, 2009.

[144] J Vetter, P Novák, MR Wagner, C Veit, K-C Möller, JO Besenhard, M Winter, M Wohlfahrt-Mehrens, C Vogler, and A Hammouche. Ageing mechanisms in lithium-ion batteries. Journal of power sources, 147(1):269–281, 2005.

[145] C. H. Villanueva and K. Maute. Density and level set-XFEM schemes for topology optimization of 3-D structures. Computational Mechanics, 54(1):133–150, 2014.

[146] Thomas Waldmann, Marcel Wilka, Michael Kasper, Meike Fleischhammer, and Margret Wohlfahrt-Mehrens. Temperature dependent ageing mechanisms in lithium-ion batteries– a post-mortem study. Journal of Power Sources, 262:129–135, 2014.

[147] CY Wang and Venkat Srinivasan. Computational battery dynamics (CBD)electrochemical/thermal coupled modeling and multi-scale modeling. Journal of power sources, 110(2):364–376, 2002.

[148] Michael Yu Wang and Shengyin Wang. Parametric shape and topology optimization with radial basis functions. In IUTAM symposium on topological design optimization of structures, machines and materials, pages 13–22. Springer, 2006.

[149] Qingsong Wang, Ping Ping, Xuejuan Zhao, Guanquan Chu, Jinhua Sun, and Chunhua Chen. Thermal runaway caused fire and explosion of lithium ion battery. Journal of power sources, 208:210–224, 2012.

[150] S. Wang and M.Y. Wang. Radial basis functions and level set method for structural topology optimization. International journal for numerical methods in engineering, 65(12):2060–2090, 2006.

[151] C John Wen, BA Boukamp, RA Huggins, and W Weppner. Thermodynamic and mass transport properties of lial. Journal of The Electrochemical Society, 126(12):2258–2266, 1979.

[152] M Stanley Whittingham. Electrical energy storage and intercalation chemistry. Science, 192(4244):1126–1127, 1976.

[153] Hui Wu, Gerentt Chan, Jang Wook Choi, Yan Yao, Matthew T McDowell, Seok Woo Lee, Ariel Jackson, Yuan Yang, Liangbing Hu, and Yi Cui. Stable cycling of double-walled silicon nanotube battery anodes through solid-electrolyte interphase control. Nature nanotechnology, 7(5):310–315, 2012.

[154] Hui Wu and Yi Cui. Designing nanostructured si anodes for high energy lithium ion batteries. Nano Today, 7(5):414–429, 2012.

[155] Yuanyuan Xie, Jianyang Li, and Chris Yuan. Multiphysics modeling of lithium ion battery capacity fading process with solid-electrolyte interphase growth by elementary reaction kinetics. Journal of Power Sources, 248:172–179, 2014.

[156] Jiagang Xu, Rutooj D Deshpande, Jie Pan, Yang-Tse Cheng, and Vincent S Battaglia. Electrode side reactions, capacity loss and mechanical degradation in lithium-ion batteries. Journal of The Electrochemical Society, 162(10):A2026–A2035, 2015.

[157] X-P Xu and A Needleman. Void nucleation by inclusion debonding in a crystal matrix. Modelling and Simulation in Materials Science and Engineering, 1(2):111, 1993.

[158] X-P Xu and Alan Needleman. Numerical simulations of fast crack growth in brittle solids. Journal of the Mechanics and Physics of Solids, 42(9):1397–1434, 1994.

[159] Naoaki Yabuuchi and Tsutomu Ohzuku. Novel lithium insertion material of lico 1/3 ni 1/3 mn 1/3 o 2 for advanced lithium-ion batteries. Journal of Power Sources, 119:171–174, 2003.

[160] Jian Yan, Jian Zhang, Yu-Chang Su, Xi-Gui Zhang, and Bao-Jia Xia. A novel perspective on the formation of the solid electrolyte interphase on the graphite electrode for lithium-ion batteries. Electrochimica Acta, 55(5):1785–1794, 2010.

[161] B Yang and K Ravi-Chandar. A single-domain dual-boundary-element formulation incorporating a cohesive zone model for elastostatic cracks. International Journal of Fracture, 93(1-4):115–144, 1998.

[162] Thomas A Yersak, Yanfa Yan, Conrad Stoldt, and Se-Hee Lee. Ambient temperature and pressure mechanochemical preparation of nano-litis2. ECS Electrochemistry Letters, 1(1):A21–A23, 2012.

[163] Xiangchun Zhang, Ann Marie Sastry, and Wei Shyy. Intercalation-induced stress and heat generation within single lithium-ion battery cathode particles. Journal of The Electrochemical Society, 155(7):A542–A552, 2008.

[164] Xiangchun Zhang, Wei Shyy, and Ann Marie Sastry. Numerical simulation of intercalation-induced stress in li-ion battery electrode particles. Journal of the Electrochemical Society, 154(10):A910–A916, 2007.

[165] Zhengyu Jenny Zhang and Glaucio H Paulino. Cohesive zone modeling of dynamic failure in homogeneous and functionally graded materials. International journal of plasticity, 21(6):1195–1254, 2005.

[166] Kejie Zhao, Matt Pharr, Joost J Vlassak, and Zhigang Suo. Fracture of electrodes in lithium-ion batteries caused by fast charging. Journal of Applied Physics, 108(7):073517, 2010.

[167] Kejie Zhao, Matt Pharr, Joost J Vlassak, and Zhigang Suo. Inelastic hosts as electrodes for high-capacity lithium-ion batteries. Journal of Applied Physics, 109(1):016110, 2011.

[168] Liwei Zhao, Izumi Watanabe, Takayuki Doi, Shigeto Okada, and Jun-ichi Yamaki. Tg-ms analysis of solid electrolyte interphase (sei) on graphite negative-electrode in lithium-ion batteries. Journal of power sources, 161(2):1275–1280, 2006.

[169] Ting Zhu. Mechanics of high-capacity electrodes in lithium-ion batteries. Chinese Physics B, 25(1):014601, 2015.

Appendix A

Weak form and derivatives of governing equations in full resolution model

A.1 Weak form and derivatives of the electrolyte balance of mass

The residual form of the diffusion and migration of Li^+ in the electrolyte is described by:

$$\mathbf{R}_{c_l}: \int_{\bar{\Omega}^l} w_{c_l} \frac{\partial c_l}{\partial t} dv - \int_{\bar{\Omega}^l} \nabla w_{c_l} \cdot \mathbf{J}_l dv - \int_{\bar{\Omega}^l} w_{c_l} \cdot h_r dv + \int_{\Gamma^l} w_{c_l} \mathbf{J}_l \cdot \boldsymbol{n}^l ds = 0. \tag{A.1}$$

In Finite Element context

$$\begin{aligned} \mathbf{R}_{c_l}: (\hat{w}^e_{c_l})^T \Bigg(& \frac{1}{\Delta t} \int_{\bar{\Omega}^l} (\boldsymbol{N}^{e,c_l})^T \boldsymbol{N}^{e,c_l} ((\hat{\boldsymbol{c}}^e_l)^{n+1} - (\hat{\boldsymbol{c}}^e_l)^n) dv \\ & - \int_{\bar{\Omega}^l} (\boldsymbol{B}^{e,c_l})^T \mathbf{J}_l dv - \int_{\bar{\Omega}^l} (\boldsymbol{N}^{e,c_l})^T h_r dv + \int_{\Gamma^l} (\boldsymbol{N}^{e,c_l})^T \mathbf{J}_l \cdot \boldsymbol{n}^l ds \Bigg) = 0, \end{aligned} \tag{A.2}$$

where Δt is the time step size, the derivations of $\mathbf{R}_{c_l}$ with respect to independent state variables is described as follows:

$$\frac{\partial \mathbf{R}_{c_l}}{\partial (\hat{\boldsymbol{c}}^e_l)^{n+1}} = \frac{1}{\Delta t} \int_{\bar{\Omega}^l} (\boldsymbol{N}^{e,c_l})^T \boldsymbol{N}^{e,c_l} dv - \int_{\bar{\Omega}^l} (\boldsymbol{B}^{e,c_l})^T \frac{\partial \mathbf{J}_l}{\partial (\hat{\boldsymbol{c}}^e_l)^{n+1}} dv - \int_{\bar{\Omega}^l} (\boldsymbol{N}^{e,c_l})^T \frac{\partial h_r}{\partial (\hat{\boldsymbol{c}}^e_l)^{n+1}} dv, \tag{A.3}$$

where

$$\mathbf{J}_l = D_{\text{eff}} \left(\boldsymbol{B}^{e,c_l} (\hat{\boldsymbol{c}}^e_l)^{n+1} - \frac{\Omega_l \boldsymbol{N}^{e,c_l} (\hat{\boldsymbol{c}}^e_l)^{n+1}}{RT} \boldsymbol{B}^{e,\sigma_h} (\hat{\boldsymbol{\sigma}}^e_h)^{n+1} \right), \tag{A.4}$$

$$\frac{\partial \mathbf{J}_l}{\partial (\hat{\boldsymbol{c}}^e_l)^{n+1}} = D_{\text{eff}} \left(\boldsymbol{B}^{e,c_l} - \frac{\Omega_l}{RT} \boldsymbol{B}^{e,\sigma_h} (\hat{\boldsymbol{\sigma}}^e_h)^{n+1} \boldsymbol{N}^{e,c_l} \right), \tag{A.5}$$

and

$$h_r = k_d (c_{l_{max}} - \boldsymbol{N}^{e,c_l} (\hat{\boldsymbol{c}}^e_l)^{n+1}) - k_r (\boldsymbol{N}^{e,c_l} (\hat{\boldsymbol{c}}^e_l)^{n+1})^2, \tag{A.6}$$

$$\frac{\partial h_r}{\partial(\hat{\boldsymbol{c}}_l^e)^{n+1}} = -k_d \boldsymbol{N}^{e,c_l} - 2k_r(\boldsymbol{N}^{e,c_l}(\hat{\boldsymbol{c}}_l^e)^{n+1})\boldsymbol{N}^{e,c_l}, \tag{A.7}$$

$$\frac{\partial \mathbf{R}_{c_l}}{\partial(\hat{\boldsymbol{\sigma}}_h^e)^{n+1}} = -\int_{\bar{\Omega}^l} (\boldsymbol{B}^{e,c_l})^T \frac{\partial \mathbf{J}_l}{\partial(\hat{\boldsymbol{\sigma}}_h^e)^{n+1}} dv, \tag{A.8}$$

where

$$\frac{\partial \mathbf{J}_l}{\partial(\hat{\boldsymbol{\sigma}}_h^e)^{n+1}} = -D_{\text{eff}} \frac{\Omega_l \boldsymbol{N}^{e,c_l}(\hat{\boldsymbol{c}}_l^e)^{n+1}}{RT} \boldsymbol{B}^{e,\sigma_h}. \tag{A.9}$$

The derivatives of $\mathbf{R}_{c_l}$ with respect to the rest of independent variables are zero.

A.2 Weak form and derivatives of the electrolyte electric potential

The electrolyte electric potential is governed by Ohm's law and the residual form is given by:

$$\mathbf{R}_{\phi_l}: \ -\int_{\bar{\Omega}^l} \nabla w_{\phi_l} \cdot \mathbf{i}_l dv + \int_{\Gamma^l} w_{\phi_l} \mathbf{i}_l \cdot \boldsymbol{n}^l ds = 0. \tag{A.10}$$

In Finite Element context

$$\mathbf{R}_{\phi_l}: (\hat{w}_{\phi_l}^e)^T \left(-\int_{\bar{\Omega}^l} (\boldsymbol{B}^{e,\phi_l})^T \mathbf{i}_l dv + \int_{\Gamma^l} (\boldsymbol{N}^{e,\phi_l})^T \mathbf{i}_l \cdot \boldsymbol{n}^l ds \right) = 0. \tag{A.11}$$

The derivations of $\mathbf{R}_{\phi_l}$ with respect to independent state variables are described as follows:

$$\frac{\partial \mathbf{R}_{\phi_l}}{\partial(\hat{\boldsymbol{c}}_l^e)^{n+1}} = -\int_{\bar{\Omega}^l} (\boldsymbol{B}^{e,\phi_l})^T \frac{\partial \mathbf{i}_l}{\partial(\hat{\boldsymbol{c}}_l^e)^{n+1}} dv, \tag{A.12}$$

where

$$\mathbf{i}_l = -F(z_+ D_+ + z_- D_-)\boldsymbol{B}^{e,c_l}(\hat{\boldsymbol{c}}_l^e)^{n+1} - z_+ \frac{F^2 \boldsymbol{N}^{e,c_l}(\hat{\boldsymbol{c}}_l^e)^{n+1}}{RT}(z_+ D_+ - z_- D_-)\boldsymbol{B}^{e,\phi_l}(\hat{\boldsymbol{\phi}}_l^e)^{n+1}, \tag{A.13}$$

$$\frac{\partial \mathbf{i}_l}{\partial(\hat{\boldsymbol{c}}_l^e)^{n+1}} = -F(z_+ D_+ + z_- D_-)\boldsymbol{B}^{e,c_l} - z_+ \frac{F^2 \boldsymbol{N}^{e,c_l}}{RT}(z_+ D_+ - z_- D_-)\boldsymbol{B}^{e,\phi_l}(\hat{\boldsymbol{\phi}}_l^e)^{n+1}, \tag{A.14}$$

$$\frac{\partial \mathbf{R}_{\phi_l}}{\partial(\hat{\boldsymbol{\phi}}_l^e)^{n+1}} = -\int_{\bar{\Omega}^l} (\boldsymbol{B}^{e,\phi_l})^T \frac{\partial \mathbf{i}_l}{\partial(\hat{\boldsymbol{\phi}}_l^e)^{n+1}} dv, \tag{A.15}$$

where

$$\frac{\partial \mathbf{i}_l}{\partial (\hat{\boldsymbol{\phi}}_l^e)^{n+1}} = -z_+ \frac{F^2 \boldsymbol{N}^{e,\phi_l} (\hat{\boldsymbol{c}}_l^e)^{n+1}}{RT} (z_+ D_+ - z_- D_-) \boldsymbol{B}^{e,\phi_l}. \tag{A.16}$$

The derivatives of $\mathbf{R}_{\phi_l}$ with respect to the rest of independent variables are zero.

A.3 Weak form and derivatives of the electrolyte balance of linear momentum

The residual equation for the balance of linear momentum in the electrolyte is defined as:

$$\mathbf{R}_u : \int_{\bar{\Omega}^l} \nabla \boldsymbol{w}_u \cdot \boldsymbol{\sigma}_l dv - \int_{\bar{\Omega}^l} \boldsymbol{w}_u \cdot \boldsymbol{b}_l dv - \int_{\Gamma^l} \boldsymbol{w}_u \boldsymbol{\sigma}_l \cdot \boldsymbol{n}^l ds = 0. \tag{A.17}$$

In Finite element context

$$\mathbf{R}_u : (\hat{\boldsymbol{w}}_u^e)^T \left(\int_{\bar{\Omega}^l} (\boldsymbol{B}^{e,u})^T \boldsymbol{\sigma}_l dv - \int_{\bar{\Omega}^l} (\boldsymbol{N}^{e,u})^T \boldsymbol{b}_l dv - \int_{\Gamma^l} (\boldsymbol{N}^{e,u})^T \boldsymbol{\sigma}_l \cdot \boldsymbol{n}^l ds \right) = 0, \tag{A.18}$$

where

$$\boldsymbol{\sigma}_l = \mathbb{C}_l \left(\boldsymbol{B}^{e,u} (\hat{\boldsymbol{u}}^e)^{n+1} - \frac{1}{3} \Omega_l \boldsymbol{N}^{e,c_l} \left((\hat{\boldsymbol{c}}_l^e)^{n+1} - (\hat{\boldsymbol{c}}_l^e)^0 \right) \boldsymbol{I}. \right) \tag{A.19}$$

The derivations of $\mathbf{R}_u$ with respect to independent state variables are described as follows:

$$\frac{\partial \mathbf{R}_u}{\partial (\hat{\boldsymbol{c}}_l^e)^{n+1}} = \int_\Omega (\boldsymbol{B}^{e,u})^T \frac{\partial \boldsymbol{\sigma}_l}{\partial (\hat{\boldsymbol{c}}_l^e)^{n+1}} dv, \tag{A.20}$$

where

$$\frac{\partial \boldsymbol{\sigma}_l}{\partial (\hat{\boldsymbol{c}}_l^e)^{n+1}} = -\frac{1}{3} \mathbb{C}_l \Omega_l \boldsymbol{N}^{e,c_l} \boldsymbol{I}, \tag{A.21}$$

$$\frac{\partial \mathbf{R}_u}{\partial (\hat{\boldsymbol{u}}^e)^{n+1}} = \int_\Omega (\boldsymbol{B}^{e,u})^T \frac{\partial \boldsymbol{\sigma}_l}{\partial (\hat{\boldsymbol{u}}^e)^{n+1}} dv, \tag{A.22}$$

where

$$\frac{\partial \boldsymbol{\sigma}_l}{\partial (\hat{\boldsymbol{u}}^e)^{n+1}} = \mathbb{C}_l \boldsymbol{B}^{e,u}. \tag{A.23}$$

The derivatives of $\mathbf{R}_u$ with respect to the rest of independent variables are zero.

A.4 Weak form and derivatives of the electrolyte hydrostatic stress

The residual form of hydrostatic stress in the electrolyte is described by:

$$\mathbf{R}_{\sigma_h}\colon \int_{\bar{\Omega}^l} w_{\sigma_h}\sigma_h dv - \int_{\bar{\Omega}^l} \frac{1}{3} w_{\sigma_h}\mathrm{tr}(\boldsymbol{\sigma}_l)dv = 0. \tag{A.24}$$

In Finite Element context

$$\mathbf{R}_{\sigma_h}\colon (\hat{w}^e_{\sigma_h})^T\left(\int_{\bar{\Omega}^l}(\boldsymbol{N}^{e,\sigma_h})^T\boldsymbol{N}^{e,\sigma_h}(\hat{\boldsymbol{\sigma}}^e_h)^{n+1}dv - \int_{\bar{\Omega}^l}\frac{1}{3}(\boldsymbol{N}^{e,\sigma_h})^T\mathrm{tr}(\boldsymbol{\sigma}_l)dv\right) = 0. \tag{A.25}$$

The derivations of $\mathbf{R}_{\sigma_h}$ with respect to independent state variables are described as follows:

$$\frac{\partial \mathbf{R}_{\sigma_h}}{\partial(\hat{\boldsymbol{c}}^e_l)^{n+1}} = -\int_{\bar{\Omega}^l}\frac{1}{3}(\boldsymbol{N}^{e,\sigma_h})^T\frac{\partial(\mathrm{tr}(\boldsymbol{\sigma}_l))}{\partial(\hat{\boldsymbol{c}}^e_l)^{n+1}}dv, \tag{A.26}$$

where

$$\begin{aligned}\mathrm{tr}(\boldsymbol{\sigma}_l) &= \Big(3\lambda+2\mu\Big)\boldsymbol{I}\boldsymbol{\varepsilon}_l - 3K\Omega_l\Delta c_l \\ &= \Big(3\lambda+2\mu\Big)\boldsymbol{I}\boldsymbol{B}^{e,u}(\hat{\boldsymbol{u}}^e)^{n+1} - 3K\Omega_l\boldsymbol{N}^{e,c_l}\Big((\hat{\boldsymbol{c}}^e_l)^{n+1} - (\hat{\boldsymbol{c}}^e_l)^0\Big),\end{aligned} \tag{A.27}$$

$$\frac{\partial(\mathrm{tr}(\boldsymbol{\sigma}_l))}{\partial(\hat{\boldsymbol{c}}^e_l)^{n+1}} = -3K\Omega_l\boldsymbol{N}^{e,c_l}, \tag{A.28}$$

$$\frac{\partial \mathbf{R}_{\sigma_h}}{\partial(\hat{\boldsymbol{u}}^e)^{n+1}} = -\int_{\bar{\Omega}^l}\frac{1}{3}(\boldsymbol{N}^{e,\sigma_h})^T\frac{\partial(\mathrm{tr}(\boldsymbol{\sigma}_l))}{\partial(\hat{\boldsymbol{u}}^e)^{n+1}}dv, \tag{A.29}$$

where

$$\frac{\partial(\mathrm{tr}(\boldsymbol{\sigma}_l))}{\partial(\hat{\boldsymbol{u}}^e)^{n+1}} = \Big(3\lambda+2\mu\Big)\boldsymbol{I}\boldsymbol{B}^{e,u}, \tag{A.30}$$

$$\frac{\partial \mathbf{R}_{\sigma_h}}{\partial(\hat{\boldsymbol{\sigma}}^e_h)^{n+1}} = \int_{\bar{\Omega}^l}(\boldsymbol{N}^{e,\sigma_h})^T\boldsymbol{N}^{e,\sigma_h}dv, \tag{A.31}$$

where K is the bulk modulus, λ and μ are the Lame parameters. The derivatives of $\mathbf{R}_{\sigma_h}$ with respect to the rest of independent variables are zero.

A.5 Weak form and derivatives of the electrode balance of mass

Similar to the balance of mass for the electrolyte, the residual form of diffusion of Li^+ in the electrode is described by:

$$\mathbf{R}_{c_s}: \int_{\bar{\Omega}^s} w_{c_s} \frac{\partial c_s}{\partial t} dv - \int_{\bar{\Omega}^s} \nabla w_{c_s} \cdot \mathbf{J}_s dv + \int_{\Gamma^s} w_{c_s} \mathbf{J}_s \cdot \boldsymbol{n}^s ds = 0. \tag{A.32}$$

In Finite Element context

$$\begin{aligned} \mathbf{R}_{c_s}: (\hat{w}^e_{c_s})^T \Bigg(& \frac{1}{\Delta t} \int_{\bar{\Omega}^s} (\boldsymbol{N}^{e,c_s})^T \boldsymbol{N}^{e,c_s} ((\hat{\boldsymbol{c}}^e_s)^{n+1} - (\hat{\boldsymbol{c}}^e_s)^n) dv \\ & - \int_{\bar{\Omega}^s} (\boldsymbol{B}^{e,c_s})^T \mathbf{J}_s dv + \int_{\Gamma^s} (\boldsymbol{N}^{e,c_s})^T \mathbf{J}_s \cdot \boldsymbol{n}^s ds \Bigg) = 0, \end{aligned} \tag{A.33}$$

where Δt is the time step size, the derivations of $\mathbf{R}_{c_s}$ with respect to independent state variables is described as follows:

$$\frac{\partial \mathbf{R}_{c_s}}{\partial (\hat{\boldsymbol{c}}^e_s)^{n+1}} = \frac{1}{\Delta t} \int_{\bar{\Omega}^s} (\boldsymbol{N}^{e,c_s})^T \boldsymbol{N}^{e,c_s} dv - \int_{\bar{\Omega}^s} (\boldsymbol{B}^{e,c_s})^T \frac{\partial \mathbf{J}_s}{\partial (\hat{\boldsymbol{c}}^e_s)^{n+1}} dv, \tag{A.34}$$

where

$$\mathbf{J}_s = -D_s \left(\boldsymbol{B}^{e,c_s} (\hat{\boldsymbol{c}}^e_s)^{n+1} - \frac{\Omega_s \boldsymbol{N}^{e,c_s} (\hat{\boldsymbol{c}}^e_s)^{n+1}}{RT} \boldsymbol{B}^{e,\sigma_h} (\hat{\boldsymbol{\sigma}}^e_h)^{n+1} \right), \tag{A.35}$$

$$\frac{\partial \mathbf{J}_s}{\partial (\hat{\boldsymbol{c}}^e_s)^{n+1}} = -D_s \left(\boldsymbol{B}^{e,c_s} - \frac{\Omega_s}{RT} \boldsymbol{B}^{e,\sigma_h} (\hat{\boldsymbol{\sigma}}^e_h)^{n+1} \boldsymbol{N}^{e,c_s} \right), \tag{A.36}$$

and

$$\frac{\partial \mathbf{R}_{c_s}}{\partial (\hat{\boldsymbol{\sigma}}^e_h)^{n+1}} = - \int_{\bar{\Omega}^s} (\boldsymbol{B}^{e,c_s})^T \frac{\partial \mathbf{J}_s}{\partial (\hat{\boldsymbol{\sigma}}^e_h)^{n+1}} dv, \tag{A.37}$$

where

$$\frac{\partial \mathbf{J}_s}{\partial (\hat{\boldsymbol{\sigma}}^e_h)^{n+1}} = D_s \frac{\Omega_s \boldsymbol{N}^{e,c_s} (\hat{\boldsymbol{c}}^e_s)^{n+1}}{RT} \boldsymbol{B}^{e,\sigma_h}. \tag{A.38}$$

The derivatives of $\mathbf{R}_{c_s}$ with respect to the rest of independent variables are zero.

A.6 Weak form and derivatives of the electrode hydrostatic stress

The residual form of hydrostatic stress in the electrode is described by:

$$\mathbf{R}_{\sigma_h}: \int_{\bar{\Omega}^s} w_{\sigma_h} \sigma_h dv - \int_{\bar{\Omega}^s} \frac{1}{3} w_{\sigma_h} \mathrm{tr}(\boldsymbol{\sigma}_s) dv = 0. \tag{A.39}$$

In Finite Element context

$$\mathbf{R}_{\sigma_h}: (\hat{w}^e_{\sigma_h})^T \left(\int_{\bar{\Omega}^s} (\boldsymbol{N}^{e,\sigma_h})^T \boldsymbol{N}^{e,\sigma_h} (\hat{\boldsymbol{\sigma}}^e_h)^{n+1} dv - \int_{\bar{\Omega}^s} \frac{1}{3} (\boldsymbol{N}^{e,\sigma_h})^T \mathrm{tr}(\boldsymbol{\sigma}_s) dv \right) = 0. \tag{A.40}$$

The derivations of $\mathbf{R}_{\sigma_h}$ with respect to independent state variables are described as follows:

$$\frac{\partial \mathbf{R}_{\sigma_h}}{\partial (\hat{\boldsymbol{c}}^e_s)^{n+1}} = - \int_{\bar{\Omega}^s} \frac{1}{3} (\boldsymbol{N}^{e,\sigma_h})^T \frac{\partial (\mathrm{tr}(\boldsymbol{\sigma}_s))}{\partial (\hat{\boldsymbol{c}}^e_s)^{n+1}} dv, \tag{A.41}$$

where

$$\begin{aligned} \mathrm{tr}(\boldsymbol{\sigma}_s) &= \Big(3\lambda + 2\mu\Big) \boldsymbol{I} \boldsymbol{\varepsilon}_s - 3K\Omega_s \Delta c_s \\ &= \Big(3\lambda + 2\mu\Big) \boldsymbol{I} \boldsymbol{B}^{e,u} (\hat{\boldsymbol{u}}^e)^{n+1} - 3K\Omega_s \boldsymbol{N}^{e,c_s} \Big((\hat{\boldsymbol{c}}^e_s)^{n+1} - (\hat{\boldsymbol{c}}^e_s)^0 \Big), \end{aligned} \tag{A.42}$$

$$\frac{\partial (\mathrm{tr}(\boldsymbol{\sigma}_s))}{\partial (\hat{\boldsymbol{c}}^e_s)^{n+1}} = -3K\Omega_s \boldsymbol{N}^{e,c_s}, \tag{A.43}$$

$$\frac{\partial \mathbf{R}_{\sigma_h}}{\partial (\hat{\boldsymbol{u}}^e)^{n+1}} = - \int_{\bar{\Omega}^s} \frac{1}{3} (\boldsymbol{N}^{e,\sigma_h})^T \frac{\partial (\mathrm{tr}(\boldsymbol{\sigma}_s))}{\partial (\hat{\boldsymbol{u}}^e)^{n+1}} dv, \tag{A.44}$$

where

$$\frac{\partial (\mathrm{tr}(\boldsymbol{\sigma}_s))}{\partial (\hat{\boldsymbol{u}}^e)^{n+1}} = \Big(3\lambda + 2\mu\Big) \boldsymbol{I} \boldsymbol{B}^{e,u}, \tag{A.45}$$

$$\frac{\partial \mathbf{R}_{\sigma_h}}{\partial (\hat{\boldsymbol{\sigma}}^e_h)^{n+1}} = \int_{\bar{\Omega}^s} (\boldsymbol{N}^{e,\sigma_h})^T \boldsymbol{N}^{e,\sigma_h} dv. \tag{A.46}$$

The derivatives of $\mathbf{R}_{\sigma_h}$ with respect to the rest of independent variables are zero.

A.7 Weak form and derivatives of the electrode electric potential

The electrode electric potential is governed by the Ohm's law:

$$\mathbf{R}_{\phi_s}: \; - \int_{\bar{\Omega}^s} \nabla w_{\phi_s} \cdot \mathbf{i}_s dv + \int_{\Gamma^s} w_{\phi_s} \mathbf{i}_s \cdot \boldsymbol{n}^s ds = 0. \tag{A.47}$$

In Finite Element context

$$\mathbf{R}_{\phi_s}: (\hat{w}^e_{\phi_s})^T \left(- \int_{\bar{\Omega}^s} (\boldsymbol{B}^{e,\phi_s})^T \mathbf{i}_s dv + \int_{\Gamma^s} (\boldsymbol{N}^{e,\phi_s})^T \mathbf{i}_s \cdot \boldsymbol{n}^s ds \right) = 0. \tag{A.48}$$

The derivations of $\mathbf{R}_{\phi_s}$ with respect to independent state variables are described as follows:

$$\frac{\partial \mathbf{R}_{\phi_s}}{\partial (\hat{\boldsymbol{\phi}}_s^e)^{n+1}} = -\int_{\bar{\Omega}^s} (\boldsymbol{B}^{e,\phi_s})^T \frac{\partial \mathbf{i}_s}{\partial (\hat{\boldsymbol{\phi}}_s^e)^{n+1}} dv, \tag{A.49}$$

where

$$\mathbf{i}_s = -\lambda_s \boldsymbol{B}^{e,\phi_s} (\hat{\boldsymbol{\phi}}_s^e)^{n+1}, \tag{A.50}$$

$$\frac{\partial \mathbf{i}_s}{\partial (\hat{\boldsymbol{\phi}}_s^e)^{n+1}} = -\lambda_s \boldsymbol{B}^{e,\phi_s}. \tag{A.51}$$

The derivatives of $\mathbf{R}_{\phi_s}$ with respect to the rest of independent variables are zero.

A.8 Weak form and derivatives of the electrode balance of linear momentum

For the electrode the residual equation for the balance of linear momentum is described as:

$$\mathbf{R}_u \colon \int_{\bar{\Omega}^s} \nabla \boldsymbol{w}_u \cdot \boldsymbol{\sigma}_s dv - \int_{\bar{\Omega}^s} \boldsymbol{w}_u \cdot \boldsymbol{b}_s dv - \int_{\Gamma^s} \boldsymbol{w}_u \boldsymbol{\sigma}_s \cdot \boldsymbol{n}^s ds = 0. \tag{A.52}$$

In Finite element context

$$\mathbf{R}_u \colon (\hat{\boldsymbol{w}}_u^e)^T \left(\int_{\bar{\Omega}^s} (\boldsymbol{B}^{e,u})^T \boldsymbol{\sigma}_s dv - \int_{\bar{\Omega}^s} (\boldsymbol{N}^{e,u})^T \boldsymbol{b}_s dv - \int_{\Gamma^s} (\boldsymbol{N}^{e,u})^T \boldsymbol{\sigma}_s \cdot \boldsymbol{n}^s ds \right) = 0, \tag{A.53}$$

where

$$\boldsymbol{\sigma}_s = \mathbb{C}_s \left(\boldsymbol{B}^{e,u} (\hat{\boldsymbol{u}}^e)^{n+1} - \frac{1}{3} \Omega_s \boldsymbol{N}^{e,c_s} \left((\hat{\boldsymbol{c}}_s^e)^{n+1} - (\hat{\boldsymbol{c}}_s^e)^0 \right) \boldsymbol{I} \right). \tag{A.54}$$

The derivations of $\mathbf{R}_u$ with respect to independent state variables are described as follows:

$$\frac{\partial \mathbf{R}_u}{\partial (\hat{\boldsymbol{c}}_s^e)^{n+1}} = \int_{\Omega} (\boldsymbol{B}^{e,u})^T \frac{\partial \boldsymbol{\sigma}_s}{\partial (\hat{\boldsymbol{c}}_s^e)^{n+1}} dv, \tag{A.55}$$

where

$$\frac{\partial \boldsymbol{\sigma}_s}{\partial (\hat{\boldsymbol{c}}_s^e)^{n+1}} = -\frac{1}{3} \mathbb{C}_s \Omega_s \boldsymbol{N}^{e,c_s} \boldsymbol{I}, \tag{A.56}$$

$$\frac{\partial \mathbf{R}_u}{\partial (\hat{\boldsymbol{u}}^e)^{n+1}} = \int_{\Omega} (\boldsymbol{B}^{e,u})^T \frac{\partial \boldsymbol{\sigma}_s}{\partial (\hat{\boldsymbol{u}}^e)^{n+1}} dv, \tag{A.57}$$

where

$$\frac{\partial \boldsymbol{\sigma}_s}{\partial (\hat{\boldsymbol{u}}^e)^{n+1}} = \mathbb{C}_s \boldsymbol{B}^{e,u}. \tag{A.58}$$

The derivatives of $\mathbf{R}_u$ with respect to the rest of independent variables are zero.

A.9 Weak form and derivatives of the Helmholtz-type differential equation

The weak form of the Helmholtz-type differential equation is described as:

$$\mathbf{R}_{\bar{\boldsymbol{\varepsilon}}_{\mathrm{eq}}} : \int_{\bar{\Omega}^s} w_{\bar{\boldsymbol{\varepsilon}}_{\mathrm{eq}}} \cdot \bar{\boldsymbol{\varepsilon}}_{\mathrm{eq}} + \int_{\bar{\Omega}^s} \nabla w_{\bar{\boldsymbol{\varepsilon}}_{\mathrm{eq}}} \cdot c \nabla \bar{\boldsymbol{\varepsilon}}_{\mathrm{eq}} dv - \int_{\bar{\Omega}^s} w_{\bar{\boldsymbol{\varepsilon}}_{\mathrm{eq}}} \cdot \boldsymbol{\varepsilon}_{\mathrm{eq}} dv = 0. \tag{A.59}$$

In Finite element context

$$\begin{aligned} \mathbf{R}_{\bar{\boldsymbol{\varepsilon}}_{\mathrm{eq}}} : (\hat{w}^e_{\bar{\boldsymbol{\varepsilon}}_{\mathrm{eq}}})^T \Bigg(& \int_{\bar{\Omega}^s} (\boldsymbol{N}^{e,\bar{\boldsymbol{\varepsilon}}_{\mathrm{eq}}})^T \boldsymbol{N}^{e,\bar{\boldsymbol{\varepsilon}}_{\mathrm{eq}}} (\hat{\bar{\boldsymbol{\varepsilon}}}_{\mathrm{eq}})^{n+1} dv \\ + \int_{\bar{\Omega}^s} c \cdot (\boldsymbol{B}^{e,\bar{\boldsymbol{\varepsilon}}_{\mathrm{eq}}})^T \boldsymbol{B}^{e,\bar{\boldsymbol{\varepsilon}}_{\mathrm{eq}}} (\hat{\bar{\boldsymbol{\varepsilon}}}_{\mathrm{eq}})^{n+1} dv & - \int_{\bar{\Omega}^s} (\boldsymbol{N}^{e,\bar{\boldsymbol{\varepsilon}}_{\mathrm{eq}}})^T \boldsymbol{\varepsilon}^{n+1}_{\mathrm{eq}} dv \Bigg) = 0. \end{aligned} \tag{A.60}$$

Assuming the following relationship for the local equivalent strain:

$$\boldsymbol{\varepsilon}^{n+1}_{\mathrm{eq}} = \sqrt{\frac{\boldsymbol{\varepsilon}^{n+1}_s : \mathbb{C}_s : \boldsymbol{\varepsilon}^{n+1}_s}{E}} \tag{A.61}$$

The derivations of $\mathbf{R}_{\bar{\boldsymbol{\varepsilon}}_{\mathrm{eq}}}$ with respect to independent state variables are described as follows:

$$\frac{\partial \mathbf{R}_{\bar{\boldsymbol{\varepsilon}}_{\mathrm{eq}}}}{\partial (\hat{\boldsymbol{u}}^e)^{n+1}} = - \int_{\bar{\Omega}^s} (\boldsymbol{N}^{e,\bar{\boldsymbol{\varepsilon}}_{\mathrm{eq}}})^T \frac{\partial \boldsymbol{\varepsilon}^{n+1}_{\mathrm{eq}}}{\partial (\hat{\boldsymbol{u}}^e)^{n+1}} dv, \tag{A.62}$$

where

$$\frac{\partial \boldsymbol{\varepsilon}^{n+1}_{\mathrm{eq}}}{\partial (\hat{\boldsymbol{u}}^e)^{n+1}} = \frac{\boldsymbol{\sigma}_s}{E \boldsymbol{\varepsilon}^{n+1}_{\mathrm{eq}}} \boldsymbol{B}^{e,u}, \tag{A.63}$$

and

$$\frac{\partial \mathbf{R}_{\bar{\boldsymbol{\varepsilon}}_{\mathrm{eq}}}}{\partial (\hat{\bar{\boldsymbol{\varepsilon}}}_{\mathrm{eq}})^{n+1}} = \int_{\bar{\Omega}^s} (\boldsymbol{N}^{e,\bar{\boldsymbol{\varepsilon}}_{\mathrm{eq}}})^T \boldsymbol{N}^{e,\bar{\boldsymbol{\varepsilon}}_{\mathrm{eq}}} dv + \int_{\bar{\Omega}^s} c \cdot (\boldsymbol{B}^{e,\bar{\boldsymbol{\varepsilon}}_{\mathrm{eq}}})^T \boldsymbol{B}^{e,\bar{\boldsymbol{\varepsilon}}_{\mathrm{eq}}} dv. \tag{A.64}$$

The derivatives of $\mathbf{R}_{\bar{\boldsymbol{\varepsilon}}_{\mathrm{eq}}}$ with respect to the rest of independent variables are zero.

Appendix B

The effective elasticity tensor

B.1 General effective moduli of inclusion with interface

Consider a composite domain composed of finite volumes of matrix, particle, and inter-layer phases defined by V_m, V_p and V_i, respectively [88]. The volume fractions implies that $V_m + V_p + V_i = 1$. The elasticity tensors in the phases are denoted by $\mathbf{C}^m, \mathbf{C}^p$ and $\mathbf{C}^i$ respectively. Assume the domain is subjected to displacement displacement boundary conditions that is compatible with constant strain $\mathbf{e}^0$, then, the effective elasticity tensor, $\bar{\mathbf{C}}$, for this composite domain is defined by

$$\bar{\boldsymbol{\sigma}} = \bar{\mathbf{C}}\ \bar{\mathbf{e}} = \bar{\mathbf{C}}\ \mathbf{e}^0 \tag{B.1}$$

where $\bar{\boldsymbol{\sigma}}$ and $\bar{\mathbf{e}}$ are the volume average stress and strain in the composite domain defined by

$$\bar{\boldsymbol{\sigma}} = V_m \bar{\boldsymbol{\sigma}}^m + V_p \bar{\boldsymbol{\sigma}}^p + V_i \bar{\boldsymbol{\sigma}}^i \tag{B.2}$$

$$\bar{\mathbf{e}} = V_m \bar{\mathbf{e}}^m + V_p \bar{\mathbf{e}}^p + V_i \bar{\mathbf{e}}^i \tag{B.3}$$

and the average stress and strain in the matrix, inclusion and interlayer phases implies that

$$\bar{\boldsymbol{\sigma}}^m = \mathbf{C}^m\ \bar{\mathbf{e}}^m, \qquad \bar{\boldsymbol{\sigma}}^p = \mathbf{C}^p\ \bar{\mathbf{e}}^p, \qquad \bar{\boldsymbol{\sigma}}^i = \mathbf{C}^i\ \bar{\mathbf{e}}^i \tag{B.4}$$

Technically, the average strain in the matrix is not equal to constant strain $\mathbf{e}^0$. Lets introduce an averaged perturbed strain, $\tilde{\mathbf{e}}^m$, from $\mathbf{e}^0$. This perturbed strain is introduced due to the presence of inclusions. The average perturbed stress is related to the average perturbed strain through

elasticity tensor for the matrix by $\bar{\boldsymbol{\sigma}}^m = \mathbf{C}^m\tilde{\mathbf{e}}^m$. The principle of linear superposition implies that the total stress in the matrix after the perturbation is

$$\bar{\boldsymbol{\sigma}}^t = \bar{\boldsymbol{\sigma}} + \tilde{\boldsymbol{\sigma}}^m = \mathbf{C}^m(\mathbf{e}^0 + \tilde{\mathbf{e}}^m) \tag{B.5}$$

Lets also define $\tilde{\mathbf{e}}^i$ and $\tilde{\mathbf{e}}^p$ as average perturbed strain in the interphase and particle with respect to the matrix, respectively. The Eshelbys equivalent principle implies that the total stress in the interphase and the particle may be written as

$$\begin{aligned} \bar{\boldsymbol{\sigma}}^t &= \bar{\boldsymbol{\sigma}} + \tilde{\boldsymbol{\sigma}}^m + \tilde{\boldsymbol{\sigma}}^i \\ &= \mathbf{C}^i(\mathbf{e}^0 + \tilde{\mathbf{e}}^m + \tilde{\mathbf{e}} \\ &= \mathbf{C}^m(\mathbf{e}^0 + \tilde{\mathbf{e}}^m + \tilde{\mathbf{e}}^i - \tilde{\mathbf{e}}^{*i}) \end{aligned} \tag{B.6}$$

From Equation (B.6)

$$(\mathbf{C}^i - \mathbf{C}^m)(\mathbf{e}^0 + \tilde{\mathbf{e}}^m + \tilde{\mathbf{e}}^i) + \mathbf{C}^m\tilde{\mathbf{e}}^{*i} = 0 \tag{B.7}$$

In the same manner for particle

$$\begin{aligned} \bar{\boldsymbol{\sigma}}^t &= \bar{\boldsymbol{\sigma}} + \tilde{\boldsymbol{\sigma}}^m + \tilde{\boldsymbol{\sigma}}^p \\ &= \mathbf{C}^p(\mathbf{e}^0 + \tilde{\mathbf{e}}^m + \tilde{\mathbf{e}}^p) \\ &= \mathbf{C}^m(\mathbf{e}^0 + \tilde{\mathbf{e}}^m + \tilde{\mathbf{e}}^p - \tilde{\mathbf{e}}^{*p}) \end{aligned} \tag{B.8}$$

From Equation B.8

$$(\mathbf{C}^p - \mathbf{C}^m)(\mathbf{e}^0 + \tilde{\mathbf{e}}^m + \tilde{\mathbf{e}}^p) + \mathbf{C}^m\tilde{\mathbf{e}}^{*p} = 0 \tag{B.9}$$

where $\tilde{\mathbf{e}}^{*i}$ and $\tilde{\mathbf{e}}^{*p}$ are the average equivalent transformation strains of the interphase and the particle, respectively. For the double-inclusion model, the Eshelbys solutions for the average perturbed strains $\tilde{\mathbf{e}}^i$ and $\tilde{\mathbf{e}}^p$ are given by Hori and Nemat-Nasser [70].

$$\tilde{\mathbf{e}}^i = \mathbf{S}^i\tilde{\mathbf{e}}^{*i} + \frac{V_p}{V_i}\Delta\mathbf{S}(\tilde{\mathbf{e}}^{*p} - \tilde{\mathbf{e}}^{*i}) \tag{B.10}$$

$$\tilde{\mathbf{e}}^p = \mathbf{S}^p\tilde{\mathbf{e}}^{*p} + \Delta\mathbf{S}\tilde{\mathbf{e}}^{*i} \tag{B.11}$$

where $\mathbf{S}^i$ and $\mathbf{S}^p$ are Eshelbys tensors for the domain of interphase with particle and the particle region, respectively, and $\Delta\mathbf{S} = \mathbf{S}^i - \mathbf{S}^p$. By substituting Equations (B.10) and (B.11) into Equations (B.7) and (B.9)

$$(\mathbf{C}^i - \mathbf{C}^m)\left[\mathbf{e}^0 + \tilde{\mathbf{e}}^m + \mathbf{S}^i\tilde{\mathbf{e}}^{*i} + \frac{V_p}{V_i}\Delta\mathbf{S}(\tilde{\mathbf{e}}^{*p} - \tilde{\mathbf{e}}^{*i})\right] + \mathbf{C}^m\tilde{\mathbf{e}}^{*i} = 0 \tag{B.12}$$

$$(\mathbf{C}^p - \mathbf{C}^m)(\mathbf{e}^0 + \tilde{\mathbf{e}}^m + \mathbf{S}^p\tilde{\mathbf{e}}^{*p} + \Delta\mathbf{S}\tilde{\mathbf{e}}^{*i}) + \mathbf{C}^m\tilde{\mathbf{e}}^{*p} = 0 \tag{B.13}$$

In the above equations the eigenstrains $\tilde{\mathbf{e}}^{*i}$ and $\tilde{\mathbf{e}}^{*p}$ can be solved in term of $\mathbf{e}^0 + \tilde{\mathbf{e}}^m$. Solving the above equations for eigenstrains gives

$$\tilde{\mathbf{e}}^{*i} = \mathbf{\Phi}^i(\mathbf{e}^0 + \tilde{\mathbf{e}}^m) \tag{B.14}$$

$$\tilde{\mathbf{e}}^{*p} = \mathbf{\Phi}^p(\mathbf{e}^0 + \tilde{\mathbf{e}}^m) \tag{B.15}$$

where the fourth-order tensors $\mathbf{\Phi}^i$ and $\mathbf{\Phi}^p$ are

$$\mathbf{\Phi}^i = -\left[\Delta\mathbf{S} + (\mathbf{S}^p + \mathbf{E}^p)\left(\mathbf{S}^p - \frac{V_p}{V_i}\Delta\mathbf{S} + \mathbf{E}^p\right)^{-1}\left(\mathbf{S}^p - \frac{V_p}{V_i}\Delta\mathbf{S} + \mathbf{E}^i\right)\right]^{-1} \tag{B.16}$$

$$\mathbf{\Phi}^p = -\left[(\mathbf{S}^p + \mathbf{E}^p) + \Delta\mathbf{S}\left(\mathbf{S}^p - \frac{V_p}{V_i}\Delta\mathbf{S} + \mathbf{E}^i\right)^{-1}\left(\mathbf{S}^p - \frac{V_p}{V_i}\Delta\mathbf{S} + \mathbf{E}^p\right)\right]^{-1} \tag{B.17}$$

with

$$\mathbf{E}^i = (\mathbf{C}^i - \mathbf{C}^m)^{-1}\mathbf{C}^m \tag{B.18}$$

$$\mathbf{E}^p = (\mathbf{C}^p - \mathbf{C}^m)^{-1}\mathbf{C}^m \tag{B.19}$$

Moreover, by substituting Equations (B.14) and (B.15) into Equations (B.10) and (B.11), the average perturbed strains $\tilde{\mathbf{e}}^i$ and $\tilde{\mathbf{e}}^p$ can be expressed in term of $\mathbf{e}^0 + \tilde{\mathbf{e}}^m$ as

$$\tilde{\mathbf{e}}^i = \left[\mathbf{S}^i\mathbf{\Phi}^i + \frac{V_p}{V_i}\Delta\mathbf{S}(\mathbf{\Phi}^p - \mathbf{\Phi}^i)\right](\mathbf{e}^0 + \tilde{\mathbf{e}}^m) \tag{B.20}$$

$$\tilde{\mathbf{e}}^p = \left[\mathbf{S}^p\mathbf{\Phi}^p + \Delta\mathbf{S}\mathbf{\Phi}^i\right](\mathbf{e}^0 + \tilde{\mathbf{e}}^m) \tag{B.21}$$

From Equations (B.5-B.8) one can write the average strains in the matrix, interphase and particle as

$$\bar{\mathbf{e}}^m = \mathbf{e}^0 + \tilde{\mathbf{e}}^m \tag{B.22}$$

$$\bar{\mathbf{e}}^i = \mathbf{e}^0 + \tilde{\mathbf{e}}^m + \tilde{\mathbf{e}}^i \tag{B.23}$$

$$\bar{\mathbf{e}}^p = \mathbf{e}^0 + \tilde{\mathbf{e}}^m + \tilde{\mathbf{e}}^p \tag{B.24}$$

By substituting Equations (B.16) and (B.17) into Equations (B.22 - B.24), we obtain the following relations

$$\bar{\mathbf{e}}^i = \mathbf{A}^i_{di}\bar{\mathbf{e}}^m \tag{B.25}$$

$$\bar{\mathbf{e}}^p = \mathbf{A}^p_{di}\bar{\mathbf{e}}^m \tag{B.26}$$

where

$$\mathbf{A}^i_{di} = \mathbf{I} + \mathbf{S}^i\mathbf{\Phi}^i + \frac{V_p}{V_i}\Delta\mathbf{S}(\mathbf{\Phi}^p - \mathbf{\Phi}^i) \tag{B.27}$$

$$\mathbf{A}^p_{di} = \mathbf{I} + \mathbf{S}^p\mathbf{\Phi}^p + \Delta\mathbf{S}\mathbf{\Phi}^i \tag{B.28}$$

Equations (B.27) and (B.28) are dilute or local concentration tensors for the double-inclusion model [70]. In the derivations of Dunn et al., the dilute concentration tensors B.27 and B.28 should be known in advance ([46]). Using these relations, the effective properties of the three phase materials with finite matrix volume can be predicted as follow. Form Equation (B.3) and (B.25) and (B.26)

$$\bar{\mathbf{e}} = \left(V_m\mathbf{I} + V_i\mathbf{A}^i_{di} + V_p\mathbf{A}^p_{di}\right)\bar{\mathbf{e}}^m \tag{B.29}$$

In addition, form Equations (B.2) and (B.4) and (B.25) and (B.26)

$$\bar{\boldsymbol{\sigma}} = \left(V_m \mathbf{C}^m + V_i \mathbf{C}^i \mathbf{A}^i_{di} + V_p \mathbf{C}^p \mathbf{A}^p_{di}\right) \bar{\mathbf{e}}^m \tag{B.30}$$

Finally the effective elasticity tensor can be given as

$$\bar{\mathbf{C}} = \left(V_m \mathbf{C}^m + V_i \mathbf{C}^i \mathbf{A}^i_{di} + V_p \mathbf{C}^p \mathbf{A}^p_{di}\right) \left(V_m \mathbf{I} + V_i \mathbf{A}^i_{di} + V_p \mathbf{A}^p_{di}\right)^{-1}$$

$$= \mathbf{C}^m + \left[V_i (\mathbf{C}^i - \mathbf{C}^m)\mathbf{A}^i_{di} + V_p (\mathbf{C}^p - \mathbf{C}^m)\mathbf{A}^p_{di}\right] \left(V_m \mathbf{I} + V_i \mathbf{A}^i_{di} + V_p \mathbf{A}^p_{di}\right)^{-1} \tag{B.31}$$

Define

$$\mathbf{A}^i_g = \mathbf{A}^i_{di} \left(V_m \mathbf{I} + V_i \mathbf{A}^i_{di} + V_p \mathbf{A}^p_{di}\right)^{-1} \tag{B.32}$$

$$\mathbf{A}^p_g = \mathbf{A}^p_{di} \left(V_m \mathbf{I} + V_i \mathbf{A}^i_{di} + V_p \mathbf{A}^p_{di}\right)^{-1} \tag{B.33}$$

Finally the effective elasticity tensor (Equation B.31) can be written in a compact form as

$$\bar{\mathbf{C}} = \mathbf{C}^m + \left[V_i (\mathbf{C}^i - \mathbf{C}^m)\mathbf{A}^i_g + V_p (\mathbf{C}^p - \mathbf{C}^m)\mathbf{A}^p_g\right] \tag{B.34}$$

B.2 Effective moduli for inclusion model without interphase

For inclusion without interlayer phase, the Eshelby tensor can be written as $\mathbf{S}^p = \mathbf{S}$, therefore total stress in matrix is

$$\boldsymbol{\sigma}^t = \bar{\boldsymbol{\sigma}} + \tilde{\boldsymbol{\sigma}}^m$$

$$= \mathbf{C}^m (\mathbf{e}^0 + \tilde{\mathbf{e}}^m) \tag{B.35}$$

and in the inclusion

$$\boldsymbol{\sigma}^t = \bar{\boldsymbol{\sigma}} + \tilde{\boldsymbol{\sigma}}^m + \tilde{\boldsymbol{\sigma}}^p$$

$$= \mathbf{C}^p (\mathbf{e}^0 + \tilde{\mathbf{e}}^m + \tilde{\mathbf{e}}^p)$$

$$= \mathbf{C}^m(\mathbf{e}^0 + \tilde{\mathbf{e}}^m + \tilde{\mathbf{e}}^p - \tilde{\mathbf{e}}^{*p}) \tag{B.36}$$

From Equations (B.35) and (B.36)

$$(\mathbf{C}^p - \mathbf{C}^m)(\mathbf{e}^0 + \tilde{\mathbf{e}}^m + \tilde{\mathbf{e}}^p) + \mathbf{C}^m\tilde{\mathbf{e}}^{*p} = 0 \tag{B.37}$$

where

$$\tilde{\mathbf{e}}^p = \mathbf{S}\tilde{\mathbf{e}}^{*p} \tag{B.38}$$

by replacing Equation (B.38) into (B.37)

$$(\mathbf{C}^p - \mathbf{C}^m)(\mathbf{e}^0 + \tilde{\mathbf{e}}^m + \mathbf{S}\tilde{\mathbf{e}}^{*p}) + \mathbf{C}^m\tilde{\mathbf{e}}^{*p} = 0 \tag{B.39}$$

by more simplification the eigenstrain will be

$$\tilde{\mathbf{e}}^{*p} = -\left[(\mathbf{C}^p - \mathbf{C}^m)\mathbf{S} + \mathbf{C}^m\right]^{-1}(\mathbf{C}^p - \mathbf{C}^m)\ \bar{\mathbf{e}}^m$$

$$= -\left\{(\mathbf{C}^p - \mathbf{C}^m)^{-1}\left[(\mathbf{C}^p - \mathbf{C}^m)\mathbf{S} + \mathbf{C}^m\right]\right\}^{-1}\ \bar{\mathbf{e}}^m$$

$$= -\left[\mathbf{S} + (\mathbf{C}^p - \mathbf{C}^m)^{-1}\mathbf{C}^m\right]^{-1}\ \bar{\mathbf{e}}^m \tag{B.40}$$

Based on Equations (B.22)- B.24)

$$\begin{aligned}
\bar{\mathbf{e}}^p &= \mathbf{e}^0 + \tilde{\mathbf{e}}^m + \tilde{\mathbf{e}}^p \\
&= \mathbf{e}^0 + \tilde{\mathbf{e}}^m + \mathbf{S}\tilde{\mathbf{e}}^{*p} \\
&= \bar{\mathbf{e}}^m + \mathbf{S}\tilde{\mathbf{e}}^{*p} \\
&= \left(\mathbf{I} - \mathbf{S}\left[\mathbf{S} + (\mathbf{C}^p - \mathbf{C}^m)^{-1}\mathbf{C}^m\right]^{-1}\right)\ \bar{\mathbf{e}}^m \\
&= \left(\mathbf{I} - \mathbf{S}\left[\mathbf{S} + (\mathbf{C}^p - \mathbf{C}^m)^{-1}\mathbf{C}^m\right]^{-1}\right)\ \bar{\mathbf{e}}^m \\
&= \left(\left[\mathbf{S} + (\mathbf{C}^p - \mathbf{C}^m)^{-1}\mathbf{C}^m - \mathbf{S}\right]\left[\mathbf{S} + (\mathbf{C}^p - \mathbf{C}^m)^{-1}\mathbf{C}^m\right]^{-1}\right)\ \bar{\mathbf{e}}^m \\
&= \left((\mathbf{C}^p - \mathbf{C}^m)^{-1}\mathbf{C}^m\left[\mathbf{S} + (\mathbf{C}^p - \mathbf{C}^m)^{-1}\mathbf{C}^m\right]^{-1}\right)\ \bar{\mathbf{e}}^m \\
&= \left(\left[\mathbf{S} + (\mathbf{C}^p - \mathbf{C}^m)^{-1}\mathbf{C}^m\right](\mathbf{C}^m)^{-1}(\mathbf{C}^p - \mathbf{C}^m)\right)^{-1}\ \bar{\mathbf{e}}^m \\
&= \left[\mathbf{I} + \mathbf{S}(\mathbf{C}^m)^{-1}(\mathbf{C}^p - \mathbf{C}^m)\right]^{-1}\ \bar{\mathbf{e}}^m
\end{aligned} \tag{B.41}$$

Define

$$\mathbf{A}_D = \left[\mathbf{I} + \mathbf{S}(\mathbf{C}^m)^{-1}(\mathbf{C}^p - \mathbf{C}^m)\right]^{-1} \tag{B.42}$$

so

$$\bar{\mathbf{e}}^p = \mathbf{A}_D \ \bar{\mathbf{e}}^m \tag{B.43}$$

The effective strain would be

$$\bar{\mathbf{e}} = (V_m\mathbf{I} + V_p\mathbf{A}_D) \ \bar{\mathbf{e}}^m \tag{B.44}$$

and the effective stress

$$\begin{aligned}
\bar{\boldsymbol{\sigma}} &= V_m\boldsymbol{\sigma}^m + V_p\boldsymbol{\sigma}^p \\
&= V_m \ \mathbf{C}^m \ \bar{\mathbf{e}}^m + V_p \ \mathbf{C}^p \ \bar{\mathbf{e}}^p \\
&= \left[V_m\mathbf{C}^m + V_p\mathbf{C}^p\mathbf{A}_D\right] \ \bar{\mathbf{e}}^m \\
&= \left[V_m\mathbf{C}^m + V_p\mathbf{C}^p\mathbf{A}_D\right]\left[V_m\mathbf{I} + V_p\mathbf{A}_D\right]^{-1} \ \bar{\mathbf{e}} \\
&= \left[V_m\mathbf{C}^m + V_p\mathbf{C}^m\mathbf{A}_D - V_p\mathbf{C}^m\mathbf{A}_D + V_p\mathbf{C}^p\mathbf{A}_D\right]\left[V_m\mathbf{I} + V_p\mathbf{A}_D\right]^{-1} \ \bar{\mathbf{e}} \\
&= \left[\mathbf{C}^m(V_m\mathbf{I} + V_p\mathbf{A}_D) + V_p(\mathbf{C}^p - \mathbf{C}^m)\mathbf{A}_D\right]\left[V_m\mathbf{I} + V_p\mathbf{A}_D\right]^{-1} \ \bar{\mathbf{e}} \\
&= \left\{\mathbf{C}^m + V_p(\mathbf{C}^p - \mathbf{C}^m)\mathbf{A}_D\left[V_m\mathbf{I} + V_p\mathbf{A}_D\right]^{-1}\right\} \ \bar{\mathbf{e}}
\end{aligned} \tag{B.45}$$

Define

$$\mathbf{A}_S = \mathbf{A}_D\left[V_m\mathbf{I} + V_p\mathbf{A}_D\right]^{-1} \tag{B.46}$$

Finally the effective elasticity tensor will be

$$\bar{\mathbf{C}} = \mathbf{C}^m + V_p(\mathbf{C}^p - \mathbf{C}^m)\mathbf{A}_S \tag{B.47}$$

B.3 Eshelby tensor for isotropic material with different shape of inclusion

B.3.1 Ellipsoidal inclusion

For an ellipsoid inclusion ($a_1 > a_2 > a_3$) some nonzero components of the fourth-order Eshelby tensor can be expressed in matrix form as

$$\mathbf{S}_{1111} = \frac{3}{8\pi(1-\nu)}a_1^2 \ \mathbf{I}_{11} + \frac{1-2\nu}{8\pi(1-\nu)} \ \mathbf{I}_1 \tag{B.48}$$

$$\mathbf{S}_{1122} = \frac{1}{8\pi(1-\nu)} a_2^2 \, \mathbf{I}_{12} + \frac{1-2\nu}{8\pi(1-\nu)} \, \mathbf{I}_1 \tag{B.49}$$

$$\mathbf{S}_{1133} = \frac{1}{8\pi(1-\nu)} a_3^2 \, \mathbf{I}_{13} + \frac{1-2\nu}{8\pi(1-\nu)} \, \mathbf{I}_1 \tag{B.50}$$

$$\mathbf{S}_{1212} = \frac{a_1^2 + a_2^2}{16\pi(1-\nu)} \, \mathbf{I}_{12} + \frac{1-2\nu}{16\pi(1-\nu)} \, (\mathbf{I}_1 + \mathbf{I}_2) \tag{B.51}$$

In the above equations, the constants $\mathbf{I}_1, \mathbf{I}_2, \mathbf{I}_{11}, \mathbf{I}_{12}, \mathbf{I}_{13}$ are defined as follow

$$\mathbf{I}_1 = \frac{4\pi a_1 a_2 a_3}{(a_1^2 - a_2^2)(a_1^2 - a_3^2)^{1/2}} \left\{ F(\theta, k) - E(\theta, k) \right\} \tag{B.52}$$

$$\mathbf{I}_3 = \frac{4\pi a_1 a_2 a_3}{(a_2^2 - a_3^2)(a_1^2 - a_3^2)^{1/2}} \left\{ \frac{a_2 (a_1^2 - a_3^2)^{1/2}}{a_1 a_3} - E(\theta, k) \right\} \tag{B.53}$$

where the elliptical integrals are defined by

$$F(\theta, k) = \int_0^\theta \frac{dw}{(1 - k^2 \sin^2 w)^{1/2}} dw \tag{B.54}$$

$$E(\theta, k) = \int_0^\theta (1 - k^2 \sin^2 w)^{1/2} dw \tag{B.55}$$

where

$$\theta = \sin^{-1}(1 - a_3^2/a_1^2)^{1/2}, \qquad k = \left\{ (a_1^2 - a_2^2)/(a_1^2 - a_3^2) \right\}^{1/2} \tag{B.56}$$

Moreover

$$\mathbf{I}_1 + \mathbf{I}_2 + \mathbf{I}_3 = 4\pi \tag{B.57}$$

$$3\mathbf{I}_{11} + \mathbf{I}_{12} + \mathbf{I}_{13} = 4\pi/a_1^2 \tag{B.58}$$

$$3a_1^2 \mathbf{I}_{11} + a_2^2 \mathbf{I}_{12} + a_3^2 \mathbf{I}_{13} = 3\mathbf{I}_1 \tag{B.59}$$

$$\mathbf{I}_{12} = (\mathbf{I}_2 - \mathbf{I}_1)/(a_1^2 - a_2^2) \tag{B.60}$$

The remaining components of $\mathbf{S}_{ijkl}$ can be calculated by cyclic permutations of (1,2,3). Any components that cannot be obtained from these formulas are zero: thus $\mathbf{S}_{1112} = \mathbf{S}_{1223} = \mathbf{S}_{1232} = 0$ etc. Note that $\mathbf{S}_{ijkl}$ has many of the symmetries of the elastic compliance tensor (e.g. $\mathbf{S}_{ijkl} = \mathbf{S}_{jikl}$), but does not have major symmetry $\mathbf{S}_{ijkl} = \mathbf{S}_{klij}$. Additional terms follow from the symmetry conditions $\mathbf{S}_{ijkl} = \mathbf{S}_{jikl} = \mathbf{S}_{ijlk} = \mathbf{S}_{jilk}$.

B.3.2 Prolate spheroidal inclusion

For a prolate spheroidal inclusion ($a_2 = a_3 < a_1$), the Eshelby matrix is reduced to

$$\mathbf{S} = \begin{bmatrix} \mathbf{S}_{1111} & \mathbf{S}_{1122} & \mathbf{S}_{1133} & \mathbf{0} & \mathbf{0} & \mathbf{0} \\ \mathbf{S}_{2211} & \mathbf{S}_{2222} & \mathbf{S}_{2233} & \mathbf{0} & \mathbf{0} & \mathbf{0} \\ \mathbf{S}_{3311} & \mathbf{S}_{3322} & \mathbf{S}_{3333} & \mathbf{0} & \mathbf{0} & \mathbf{0} \\ \mathbf{0} & \mathbf{0} & \mathbf{0} & \mathbf{S}_{2323} & \mathbf{0} & \mathbf{0} \\ \mathbf{0} & \mathbf{0} & \mathbf{0} & \mathbf{0} & \mathbf{S}_{3131} & \mathbf{0} \\ \mathbf{0} & \mathbf{0} & \mathbf{0} & \mathbf{0} & \mathbf{0} & \mathbf{S}_{1212} \end{bmatrix} \tag{B.61}$$

where

$$\mathbf{S}_{1111} = \mathbf{S}_{2222} = \frac{3}{8(1-\nu)}\frac{\alpha^2}{(\alpha^2-1)} + \frac{1}{4(1-\nu)}\left\{1 - 2\nu - \frac{9}{4(\alpha^2-1)}\right\} g \tag{B.62}$$

$$\mathbf{S}_{3333} = \frac{1}{2(1-\nu)}\left[1 - 2\nu + \frac{3\alpha^2-1}{\alpha^2-1} - \left\{1 - 2\nu + \frac{3\alpha^2}{(\alpha^2-1)}\right\} g\right] \tag{B.63}$$

$$\mathbf{S}_{1122} = \mathbf{S}_{2211} = \frac{1}{4(1-\nu)}\left[\frac{\alpha^2}{2(\alpha^2-1)} - \left\{1 - 2\nu + \frac{3}{4(\alpha^2-1)}\right\} g\right] \tag{B.64}$$

$$\mathbf{S}_{1133} = \mathbf{S}_{2233} = -\frac{1}{2(1-\nu)}\frac{\alpha^2}{(\alpha^2-1)} + \frac{1}{4(1-\nu)}\left\{\frac{3\alpha^2}{(\alpha^2-1)} - (1-2\nu)\right\} g \tag{B.65}$$

$$\mathbf{S}_{3311} = \mathbf{S}_{3322} = -\frac{1}{2(1-\nu)}\left\{1 - 2\nu + \frac{1}{\alpha^2-1}\right\} + \frac{1}{2(1-\nu)}\left\{1 - 2\nu + \frac{3}{2(\alpha^2-1)}\right\} g \tag{B.66}$$

$$\mathbf{S}_{1212} = \frac{1}{8(1-\nu)}\frac{\alpha^2}{(\alpha^2-1)} + \frac{1}{4(1-\nu)}\left\{1 - 2\nu - \frac{3}{4(\alpha^2-1)}\right\} g \tag{B.67}$$

$$\mathbf{S}_{2323} = \mathbf{S}_{1313} = \frac{1}{4(1-\nu)}\left\{1 - 2\nu - \frac{\alpha^2+1}{\alpha^2-1}\right\} - \frac{1}{8(1-\nu)}\left\{1 - 2\nu - \frac{3(\alpha^2+1)}{(\alpha^2-1)}\right\} g \tag{B.68}$$

where where ν is the Poisson ratio of the matrix, α is the aspect ratio of the inclusion ($\alpha = a_1/a_3$), and is given by

$$g = \frac{\alpha}{(\alpha^2-1)^{3/2}}\left\{\alpha(\alpha^2-1)^{1/2} - \cosh^{-1}\alpha\right\} \tag{B.69}$$

B.3.3 Oblate spheroidal inclusion

For a oblate spheroidal inclusion ($a_2 = a_3 > a_1$), the Eshelby matrix components is

$$\mathbf{S}_{1111} = \mathbf{S}_{2222} = -\frac{3}{8(1-\nu)}\frac{\alpha^2}{(1-\alpha^2)} + \frac{1}{4(1-\nu)}\left\{1 - 2\nu + \frac{9}{4(1-\alpha^2)}\right\} g \tag{B.70}$$

$$\mathbf{S}_{3333} = \frac{1}{2(1-\nu)}\left\{4 - 2\nu - \frac{2}{1-\alpha^2}\right\} + \frac{1}{2(1-\nu)}\left\{-4 + 2\nu + \frac{3}{(1-\alpha^2)}\right\} g \tag{B.71}$$

$$\mathbf{S}_{1122} = \mathbf{S}_{2211} = \frac{1}{8(1-\nu)}\left\{1 - \frac{1}{(1-\alpha^2)}\right\} + \frac{1}{16(1-\nu)}\left\{-4(1-2\nu) + \frac{3}{(1-\alpha^2)}\right\} g \tag{B.72}$$

$$\mathbf{S}_{1133} = \mathbf{S}_{2233} = -\frac{1}{2(1-\nu)}\frac{\alpha^2}{(1-\alpha^2)} - \frac{1}{4(1-\nu)}\left\{1 - 2\nu + \frac{3\alpha^2}{(1-\alpha^2)}\right\} g \tag{B.73}$$

$$\mathbf{S}_{3311} = \mathbf{S}_{3322} = \frac{1}{2(1-\nu)}\left\{-(1-2\nu) + \frac{1}{1-\alpha^2}\right\} + \frac{1}{4(1-\nu)}\left\{2(1-2\nu) - \frac{3}{(1-\alpha^2)}\right\} g \tag{B.74}$$

$$\mathbf{S}_{1212} = -\frac{1}{8(1-\nu)}\frac{\alpha^2}{(1-\alpha^2)} + \frac{1}{16(1-\nu)}\left\{4(1-2\nu) + \frac{3}{(1-\alpha^2)}\right\} g \tag{B.75}$$

$$\mathbf{S}_{2323} = \mathbf{S}_{1313} = \frac{1}{4(1-\nu)}\left\{1 - 2\nu + \frac{1+\alpha^2}{1-\alpha^2}\right\} - \frac{1}{8(1-\nu)}\left\{1 - 2\nu + \frac{3(1+\alpha^2)}{(1-\alpha^2)}\right\} g \tag{B.76}$$

where

$$g = \frac{\alpha}{(1-\alpha^2)^{3/2}} \left\{ \cos^{-1}\alpha - \alpha(1-\alpha^2)^{1/2} \right\} \tag{B.77}$$

B.3.4 Spheroidal inclusion

For a spheroidal inclusion ($a_1 = a_2 = a_3$), the Eshelby matrix components is

$$\mathbf{S}_{1111} = \mathbf{S}_{2222} = \mathbf{S}_{3333} = \frac{7-5\nu}{15(1-\nu)} \tag{B.78}$$

$$\mathbf{S}_{1122} = \mathbf{S}_{2233} = \mathbf{S}_{3311} = \mathbf{S}_{1133} = \mathbf{S}_{2211} = \mathbf{S}_{3322} = \frac{5\nu-1}{15(1-\nu)} \tag{B.79}$$

$$\mathbf{S}_{1212} = \mathbf{S}_{2323} = \mathbf{S}_{3131} = \frac{4-5\nu}{15(1-\nu)} \tag{B.80}$$

Appendix C

Stabilized Lagrange Multiplier for elastic problem with stress-diffusion coupling

C.1 Stabilized Lagrange multiplier

In linear elasticity the strong form of governing equation and boundary condition for two-phase material can be expressed in the following settings:

$$\begin{cases} \nabla \cdot \boldsymbol{\sigma}_p + \boldsymbol{b}_p = 0 & \text{in} \quad \bar{\Omega}^p \\ \boldsymbol{\sigma}_p = \mathbb{C}_p \colon \left(\boldsymbol{\varepsilon}_p - \frac{1}{3}\Omega_p \Delta c_p \boldsymbol{I}\right) & \text{with} \quad \boldsymbol{\varepsilon}_p = \frac{1}{2}\left(\nabla \boldsymbol{u} + \nabla \boldsymbol{u}^T\right), \\ \boldsymbol{u}_l = \boldsymbol{u}_s & \text{on} \quad \Gamma^{ls} \end{cases} \tag{C.1}$$

where p represents either of phases. Applying weak form on the strong format of governing equation and performing integration by parts leads the following relation:

$$\int_{\bar{\Omega}^l} \boldsymbol{w}_{u_l}(\nabla \cdot \boldsymbol{\sigma}_l + \boldsymbol{b}_l)dv + \int_{\bar{\Omega}^s} \boldsymbol{w}_{u_s}(\nabla \cdot \boldsymbol{\sigma}_s + \boldsymbol{b}_s)dv = 0, \tag{C.2}$$

where $\boldsymbol{w}_{u_l}$ and $\boldsymbol{w}_{u_s}$ are test functions. By applying Divergence Theorem on Equation (C.2)

$$\begin{aligned} &\int_{\Gamma^{ls}} \boldsymbol{w}_{u_l} \cdot \boldsymbol{\sigma}_l \cdot \boldsymbol{n}_l ds - \int_{\bar{\Omega}^l} \nabla \boldsymbol{w}_{u_l} \cdot \boldsymbol{\sigma}_l dv + \int_{\bar{\Omega}^l} \boldsymbol{w}_{u_l} \cdot \boldsymbol{b}_l dv \\ &+ \int_{\Gamma^{ls}} \boldsymbol{w}_{u_s} \cdot \boldsymbol{\sigma}_s \cdot \boldsymbol{n}_s ds - \int_{\bar{\Omega}^s} \nabla \boldsymbol{w}_{u_s} \cdot \boldsymbol{\sigma}_s dv + \int_{\bar{\Omega}^s} \boldsymbol{w}_{u_s} \cdot \boldsymbol{b}_s dv = 0, \end{aligned} \tag{C.3}$$

where $\boldsymbol{n}_s = -\boldsymbol{n}_l = \boldsymbol{n}$. The simplified format of Equation (C.3) can be written as

$$\begin{aligned} &\int_{\bar{\Omega}^l} \nabla \boldsymbol{w}_{u_l} \cdot \boldsymbol{\sigma}_l dv + \int_{\bar{\Omega}^s} \nabla \boldsymbol{w}_{u_s} \cdot \boldsymbol{\sigma}_s dv \\ &+ \int_{\Gamma^{ls}} \boldsymbol{w}_{u_l} \cdot \boldsymbol{\sigma}_l \cdot \boldsymbol{n}_s ds - \int_{\Gamma^{ls}} \boldsymbol{w}_{u_s} \cdot \boldsymbol{\sigma}_s \cdot \boldsymbol{n}_s ds \\ &= \int_{\bar{\Omega}^l} \boldsymbol{w}_{u_l} \cdot \boldsymbol{b}_l dv + \int_{\bar{\Omega}^s} \boldsymbol{w}_{u_s} \cdot \boldsymbol{b}_s dv, \end{aligned} \tag{C.4}$$

where the boundary term is expressed as:

$$\int_{\Gamma^{ls}} \boldsymbol{w}_{u_l} \cdot \boldsymbol{\sigma}_l \cdot \boldsymbol{n}_s ds - \int_{\Gamma^{ls}} \boldsymbol{w}_{u_s} \cdot \boldsymbol{\sigma}_s \cdot \boldsymbol{n}_s ds. \tag{C.5}$$

Introducing

$$\lambda = \boldsymbol{\sigma}_l \cdot \boldsymbol{n} = \boldsymbol{\sigma}_s \cdot \boldsymbol{n}. \tag{C.6}$$

By inserting Dirichlet boundary condition, Equation (C.6) can be written in the following compact format:

$$-\int_{\Gamma^{ls}} \|\boldsymbol{w}\| \cdot \lambda ds \mp \int_{\Gamma^{ls}} \mu \cdot \|\boldsymbol{u}\| \, ds, \tag{C.7}$$

where μ is the Lagrange multiplier test function and the jump in the displacement and test function can be described as follow:

$$\|\boldsymbol{w}\| = \boldsymbol{w}_{u_l} - \boldsymbol{w}_{u_s}; \qquad \|\boldsymbol{u}\| = \boldsymbol{u}_l - \boldsymbol{u}_s. \tag{C.8}$$

In the case of stabilized Lagrange multiplier, the Lagrange multiplier parameter can be defined as follow:

$$\lambda = \frac{1}{2} \left(\boldsymbol{\sigma}_l + \boldsymbol{\sigma}_s \right) \cdot \boldsymbol{n} = \bar{\boldsymbol{\sigma}} \cdot \boldsymbol{n}. \tag{C.9}$$

Using the stabilized Lagrange multiplier approach and satisfying the weak form of compatibility of the stresses, one can compute the Lagrange multiplier as follow:

$$\underbrace{\int_{\Gamma^{ls}} \mu \left(\lambda - \bar{\boldsymbol{\sigma}} \cdot \boldsymbol{n} \right) ds}_{\text{consistency}} - \gamma \underbrace{\int_{\Gamma^{ls}} \mu \cdot \|\boldsymbol{u}\| \, ds}_{\text{constraint}} = 0. \tag{C.10}$$

In this case the residual contribution of the interface based on the stabilized Lagrange multiplier can be constructed in the following settings. Using Equation (C.10):

$$\mathbf{R}_{\Gamma^{ls}} = \underbrace{\int_{\Gamma^{ls}} \|\delta \boldsymbol{u}\| \cdot \lambda ds}_{\mathbf{R}^{u}_{\Gamma^{ls}}} + \underbrace{\int_{\Gamma^{ls}} \mu \left(\lambda - \bar{\boldsymbol{\sigma}} \cdot \boldsymbol{n} - \gamma \|\boldsymbol{u}\| \right) ds}_{\mathbf{R}^{\lambda}_{\Gamma^{ls}}}. \tag{C.11}$$

Since the test function is the same for the both parts of the Lagrange multiplier residual equation, thus it can be factored out from the equation.

$$\mathbf{R}^{\lambda}_{\Gamma^{ls}} = \mu \left[\int_{\Gamma^{ls}} \left(\lambda - \bar{\boldsymbol{\sigma}} \cdot \boldsymbol{n} - \gamma \|\boldsymbol{u}\| \right) ds \right]. \tag{C.12}$$

At the time step $(n+1)$ the stabilized Lagrange multiplier contribution of the total residual can be written as follow:

$$(\mathbf{R}^{\lambda}_{\Gamma^{ls}})^{n+1}_i = \mu \int_{\Gamma^{ls}} \delta_{ij} \hat{\lambda}^{n+1}_j ds - \mu \int_{\Gamma^{ls}} \bar{\sigma}^{n+1}_{ij} \cdot n_j ds - \gamma\mu \int_{\Gamma^{ls}} \|u_i\|^{n+1} ds. \tag{C.13}$$

In the Finite element context:

$$\begin{aligned}(\mathbf{R}^{\lambda}_{\Gamma^{ls}})^{n+1}_i &= \underbrace{\mu \int_{\Gamma^{ls}} \delta_{ij} ds}_{\mathbf{K}_\lambda} \left\{ \hat{\lambda}^{n+1}_j \right\} \\ &\underbrace{- \mu \int_{\Gamma^{ls}} \bar{\sigma}^{n+1}_{ij} \cdot n_j ds - \gamma\mu \int_{\Gamma^{ls}} \|u_i\|^{n+1} ds}_{\mathbf{f}}.\end{aligned} \tag{C.14}$$

By solving for $\hat{\lambda}^{n+1}$, the stabilized Lagrange multiplier parameter can be condensed out at elemental level:

$$[\mathbf{K}_\lambda] \left[\hat{\lambda}^{n+1} \right] = [\mathbf{f}] \Rightarrow \left[\hat{\lambda}^{n+1} \right] = [\mathbf{K}_\lambda]^{-1} [\mathbf{f}]. \tag{C.15}$$

By substituting the computed stabilized Lagrange multiplier parameter into the displacement contribution of the residual

$$(\mathbf{R}^{u}_{\Gamma^{ls}})^{n+1}_i = \int_{\Gamma^{ls}} \|\delta u_i\|^{n+1} \cdot \hat{\lambda}^{n+1} ds. \tag{C.16}$$

C.2 Cohesive zone model with stabilized Lagrange multiplier

Since we augmented the stabilized Lagrange multiplier formulation into our bilinear cohesive zone model, we are interested in the normal component of pressure at the interface. For a coupled cohesive-stabilized Lagrange multiplier formulation, one can define the stabilized Lagrange multiplier formulation as follow:

$$(\mathbf{R}^{\lambda}_{\Gamma^{ls}})^{n+1}_k = \mu \int_{\Gamma^{ls}} \delta_{kj} \hat{\lambda}^{n+1}_j ds - \mu \int_{\Gamma^{ls}} \bar{P}^{n+1} \cdot n_k ds - \gamma\mu \int_{\Gamma^{ls}} \tilde{g} \cdot n_k ds, \tag{C.17}$$

where

$$\begin{aligned}\bar{P}^{n+1} &= \bar{\sigma}^{n+1}_{ij} n_i n_j, \\ \tilde{g} &= ((u_l)_i - (u_s)_i) n_i,\end{aligned} \tag{C.18}$$

The derivatives of $(\mathbf{R}^{\lambda}_{\Gamma^{ls}})^{n+1}_{k}$ with respect to independent state variables($(\hat{\boldsymbol{c}}^{e}_{l})^{n+1}$, $(\hat{\boldsymbol{c}}^{e}_{s})^{n+1}$, $(\hat{\boldsymbol{u}}^{e}_{l})^{n+1}$, $(\hat{\boldsymbol{u}}^{e}_{s})^{n+1}$) are described as

$$\frac{\partial \mathbf{R}^{\lambda}_{\Gamma^{ls}}}{\partial (\hat{\boldsymbol{c}}^{e}_{l})^{n+1}} = -\mu \int_{\Gamma^{ls}} \frac{\partial \bar{P}^{n+1}}{\partial (\hat{\boldsymbol{c}}^{e}_{l})^{n+1}} \cdot \boldsymbol{n} ds, \tag{C.19}$$

where

$$\boldsymbol{\sigma}_{l} = \mathbb{C}_{l}\left(\boldsymbol{B}^{e,u}(\hat{\boldsymbol{u}}^{e}_{l})^{n+1} - \frac{1}{3}\Omega_{l}\boldsymbol{N}^{e,c_{l}}\Big((\hat{\boldsymbol{c}}^{e}_{l})^{n+1} - (\hat{\boldsymbol{c}}^{e}_{l})^{0}\Big)\boldsymbol{I}. \right), \tag{C.20}$$

$$\frac{\partial \boldsymbol{\sigma}_{l}}{\partial (\hat{\boldsymbol{c}}^{e}_{l})^{n+1}} = -\frac{1}{3}\mathbb{C}_{l}\Omega_{l}\boldsymbol{N}^{e,c_{l}}\boldsymbol{I}, \tag{C.21}$$

$$\frac{\partial \bar{P}^{n+1}}{\partial (\hat{\boldsymbol{c}}^{e}_{l})^{n+1}} = \frac{1}{2}\frac{\partial \boldsymbol{\sigma}_{l}}{\partial (\hat{\boldsymbol{c}}^{e}_{l})^{n+1}}\boldsymbol{n}^{T}\boldsymbol{n} \tag{C.22}$$

$$\frac{\partial \mathbf{R}^{\lambda}_{\Gamma^{ls}}}{\partial (\hat{\boldsymbol{c}}^{e}_{s})^{n+1}} = -\mu \int_{\Gamma^{ls}} \frac{\partial \bar{P}^{n+1}}{\partial (\hat{\boldsymbol{c}}^{e}_{s})^{n+1}} \cdot \boldsymbol{n} ds \tag{C.23}$$

where

$$\boldsymbol{\sigma}_{s} = \mathbb{C}_{s}\left(\boldsymbol{B}^{e,u}(\hat{\boldsymbol{u}}^{e}_{s})^{n+1} - \frac{1}{3}\Omega_{s}\boldsymbol{N}^{e,c_{s}}\Big((\hat{\boldsymbol{c}}^{e}_{s})^{n+1} - (\hat{\boldsymbol{c}}^{e}_{s})^{0}\Big)\boldsymbol{I} \right), \tag{C.24}$$

$$\frac{\partial \boldsymbol{\sigma}_{s}}{\partial (\hat{\boldsymbol{c}}^{e}_{s})^{n+1}} = -\frac{1}{3}\mathbb{C}_{s}\Omega_{s}\boldsymbol{N}^{e,c_{s}}\boldsymbol{I}, \tag{C.25}$$

$$\frac{\partial \bar{P}^{n+1}}{\partial (\hat{\boldsymbol{c}}^{e}_{s})^{n+1}} = \frac{1}{2}\frac{\partial \boldsymbol{\sigma}_{l}}{\partial (\hat{\boldsymbol{c}}^{e}_{s})^{n+1}}\boldsymbol{n}^{T}\boldsymbol{n}, \tag{C.26}$$

$$\frac{\partial \mathbf{R}^{\lambda}_{\Gamma^{ls}}}{\partial (\hat{\boldsymbol{u}}^{e}_{l})^{n+1}} = -\mu \int_{\Gamma^{ls}} \frac{\partial \bar{P}^{n+1}}{\partial (\hat{\boldsymbol{u}}^{e}_{l})^{n+1}} \cdot \boldsymbol{n} ds - \gamma\mu \int_{\Gamma^{ls}} \frac{\partial \tilde{g}}{\partial (\hat{\boldsymbol{u}}^{e}_{l})^{n+1}} \cdot \boldsymbol{n} ds, \tag{C.27}$$

$$\frac{\partial \boldsymbol{\sigma}_{l}}{\partial (\hat{\boldsymbol{u}}^{e}_{l})^{n+1}} = \mathbb{C}_{l}\boldsymbol{B}^{e,u}, \tag{C.28}$$

$$\frac{\partial \bar{P}^{n+1}}{\partial (\hat{\boldsymbol{u}}^{e}_{l})^{n+1}} = \frac{1}{2}\frac{\partial \boldsymbol{\sigma}_{l}}{\partial (\hat{\boldsymbol{u}}^{e}_{l})^{n+1}}\boldsymbol{n}^{T}\boldsymbol{n}, \tag{C.29}$$

$$\tilde{g} = \left(\boldsymbol{N}_l^{e,u} (\hat{\boldsymbol{u}}_l^e)^{n+1} - \boldsymbol{N}_s^{e,u} (\hat{\boldsymbol{u}}_s^e)^{n+1} \right) \cdot \boldsymbol{n}, \tag{C.30}$$

$$\frac{\partial \tilde{g}}{\partial (\hat{\boldsymbol{u}}_l^e)^{n+1}} = \boldsymbol{N}_l^{e,u} \cdot \boldsymbol{n}, \tag{C.31}$$

$$\frac{\partial \mathbf{R}_{\Gamma^{ls}}^{\lambda}}{\partial (\hat{\boldsymbol{u}}_s^e)^{n+1}} = -\mu \int_{\Gamma^{ls}} \frac{\partial \bar{P}^{n+1}}{\partial (\hat{\boldsymbol{u}}_s^e)^{n+1}} \cdot \boldsymbol{n} ds - \gamma\mu \int_{\Gamma^{ls}} \frac{\partial \tilde{g}}{\partial (\hat{\boldsymbol{u}}_s^e)^{n+1}} \cdot \boldsymbol{n} ds, \tag{C.32}$$

$$\frac{\partial \boldsymbol{\sigma}_s}{\partial (\hat{\boldsymbol{u}}_s^e)^{n+1}} = \mathbb{C}_s \boldsymbol{B}^{e,u}, \tag{C.33}$$

$$\frac{\partial \bar{P}^{n+1}}{\partial (\hat{\boldsymbol{u}}_s^e)^{n+1}} = \frac{1}{2} \frac{\partial \boldsymbol{\sigma}_s}{\partial (\hat{\boldsymbol{u}}_s^e)^{n+1}} \boldsymbol{n}^T \boldsymbol{n}, \tag{C.34}$$

$$\tilde{g} = \left(\boldsymbol{N}_l^{e,u} (\hat{\boldsymbol{u}}_l^e)^{n+1} - \boldsymbol{N}_s^{e,u} (\hat{\boldsymbol{u}}_s^e)^{n+1} \right) \cdot \boldsymbol{n}, \tag{C.35}$$

$$\frac{\partial \tilde{g}}{\partial (\hat{\boldsymbol{u}}_s^e)^{n+1}} = -\boldsymbol{N}_s^{e,u} \cdot \boldsymbol{n}. \tag{C.36}$$

Appendix D

Derivation of non-dimensionalization in SSLIBs model

D.1 Electrolyte phase

D.1.1 Electrolyte diffusion coefficients

For electrolyte diffusion coefficients:

$$\begin{aligned} D_{+/-} &= \left(\frac{\mathrm{m}^2}{\mathrm{s}}\right)\tilde{D}_{+/-} \\ &= \left(\frac{\frac{\mathrm{mol}}{\mathrm{m}^3}}{\frac{\mathrm{mol}}{\mathrm{m}^3}}\frac{\mathrm{m}^2}{\mathrm{s}}\right)\tilde{D}_{+/-} \\ &= \frac{c_{s_{\mathrm{ref}}}D_{\mathrm{ref}}}{c_{l_{\mathrm{ref}}}}\tilde{D}_{+/-} \end{aligned} \tag{D.1}$$

therefore

$$D_{+/-} = \frac{c_{s_{\mathrm{ref}}}D_{\mathrm{ref}}}{c_{l_{\mathrm{ref}}}}\tilde{D}_{+/-} \quad \Rightarrow \tilde{D}_{+/-} = \frac{c_{l_{\mathrm{ref}}}}{c_{s_{\mathrm{ref}}}D_{\mathrm{ref}}}D_{+/-} \tag{D.2}$$

D.1.2 Electrolyte flux

For flux in the electrolyte ($z_+ = -z_- = 1$):

$$\begin{aligned} \mathbf{J}_l &= -\frac{2D_+D_-}{D_+ + D_-}\nabla c_l \\ &= -\frac{2\left(\frac{c_{s_{\mathrm{ref}}}D_{\mathrm{ref}}}{c_{l_{\mathrm{ref}}}}\tilde{D}_+\right)\left(\frac{c_{s_{\mathrm{ref}}}D_{\mathrm{ref}}}{c_{l_{\mathrm{ref}}}}\tilde{D}_-\right)}{\left(\frac{c_{s_{\mathrm{ref}}}D_{\mathrm{ref}}}{c_{l_{\mathrm{ref}}}}\tilde{D}_+\right)+\left(\frac{c_{s_{\mathrm{ref}}}D_{\mathrm{ref}}}{c_{l_{\mathrm{ref}}}}\tilde{D}_-\right)}\frac{1}{L_{\mathrm{ref}}}\tilde{\nabla}\left(\tilde{c}_l c_{l_{\mathrm{ref}}}\right) \\ &= -\frac{c_{s_{\mathrm{ref}}}D_{\mathrm{ref}}}{L_{\mathrm{ref}}}\frac{2\tilde{D}_+\tilde{D}_-}{\tilde{D}_+ + \tilde{D}_-}\tilde{\nabla}\tilde{c}_l \end{aligned} \tag{D.3}$$

so

$$\mathbf{J}_l = \mathbf{J}_{l_{\mathrm{ref}}}\tilde{\mathbf{J}}_l; \qquad \mathbf{J}_{l_{\mathrm{ref}}} = \frac{c_{s_{\mathrm{ref}}}D_{\mathrm{ref}}}{L_{\mathrm{ref}}}, \qquad \tilde{\mathbf{J}}_l = -\frac{2\tilde{D}_+\tilde{D}_-}{\tilde{D}_+ + \tilde{D}_-}\tilde{\nabla}\tilde{c}_l \tag{D.4}$$

D.1.3 Recombination rate constant

$$\begin{aligned} k_r &= \frac{\mathrm{m}^3}{\mathrm{mol}\cdot\mathrm{s}}\tilde{k}_r \\ &= \frac{1}{\frac{\mathrm{mol}}{\mathrm{m}^3}\cdot\mathrm{s}}\tilde{k}_r \\ &= \frac{D_{\mathrm{ref}}}{L_{\mathrm{ref}}^2 c_{l_{\mathrm{ref}}}}\tilde{k}_r \end{aligned} \tag{D.5}$$

so

$$k_r = \frac{D_{\mathrm{ref}}}{L_{\mathrm{ref}}^2 c_{l_{\mathrm{ref}}}}\tilde{k}_r \quad \Rightarrow \tilde{k}_r = \frac{L_{\mathrm{ref}}^2 c_{l_{\mathrm{ref}}}}{D_{\mathrm{ref}}} k_r \tag{D.6}$$

D.1.4 Dissociation rate constant

$$\begin{aligned} k_d &= \frac{\mathrm{m}^3}{\mathrm{mol}\cdot\mathrm{s}}\frac{\mathrm{mol}}{\mathrm{m}^3}\tilde{k}_d \\ &= \frac{1}{\mathrm{s}}\tilde{k}_d \\ &= \frac{D_{\mathrm{ref}}}{L_{\mathrm{ref}}^2}\tilde{k}_d \end{aligned} \tag{D.7}$$

so

$$k_d = \frac{D_{\mathrm{ref}}}{L_{\mathrm{ref}}^2}\tilde{k}_d \quad \Rightarrow \tilde{k}_d = \frac{L_{\mathrm{ref}}^2}{D_{\mathrm{ref}}} k_d \tag{D.8}$$

This rate constant is also function of k_r:

$$\begin{aligned} k_d &= k_r \; c_{l_{\max}} \frac{\xi_{c_l}^2}{1-\xi_{c_l}} \\ &= \frac{D_{\mathrm{ref}}}{L_{\mathrm{ref}}^2 c_{l_{\mathrm{ref}}}}\tilde{k}_r \; \tilde{c}_{l_{\max}} c_{l_{\mathrm{ref}}} \frac{\xi_{c_l}^2}{1-\xi_{c_l}} \\ &= \frac{D_{\mathrm{ref}}}{L_{\mathrm{ref}}^2}\tilde{k}_r \; \tilde{c}_{l_{\max}} \frac{\xi_{c_l}^2}{1-\xi_{c_l}} \end{aligned} \tag{D.9}$$

so

$$k_d = k_{d_{\mathrm{ref}}}\tilde{k}_d; \qquad k_{d_{\mathrm{ref}}} = \frac{D_{\mathrm{ref}}}{L_{\mathrm{ref}}^2}, \qquad \tilde{k}_d = \tilde{k}_r \tilde{c}_{l_{\max}} \frac{\xi_{c_l}^2}{1-\xi_{c_l}} \tag{D.10}$$

D.1.5 Generation/recombination reaction

For the generation/recombination reaction:

$$h_r = k_d(c_{l_{max}} - c_l) - k_r c_l^2 \tag{D.11}$$

By substituting parameters

$$\begin{aligned} h_r &= \frac{D_{\text{ref}}}{L_{\text{ref}}^2}\tilde{k}_d(\tilde{c}_{l_{max}}c_{l_{\text{ref}}} - \tilde{c}_l c_{l_{\text{ref}}}) - \frac{D_{\text{ref}}}{L_{\text{ref}}^2 c_{l_{\text{ref}}}}\tilde{k}_r(\tilde{c}_l c_{l_{\text{ref}}})^2 \\ &= \frac{D_{\text{ref}}c_{l_{\text{ref}}}}{L_{\text{ref}}^2}\tilde{k}_d(\tilde{c}_{l_{max}} - \tilde{c}_l) - \frac{D_{\text{ref}}c_{l_{\text{ref}}}}{L_{\text{ref}}^2}\tilde{k}_r(\tilde{c}_l)^2 \\ &= \frac{D_{\text{ref}}c_{l_{\text{ref}}}}{L_{\text{ref}}^2}\left(\tilde{k}_d(\tilde{c}_{l_{max}} - \tilde{c}_l) - \tilde{k}_r(\tilde{c}_l)^2\right) \end{aligned} \tag{D.12}$$

so

$$h_r = h_{r_{\text{ref}}}\tilde{h}_r; \qquad h_{r_{\text{ref}}} = \frac{D_{\text{ref}}c_{l_{\text{ref}}}}{L_{\text{ref}}^2}, \qquad \tilde{h}_r = \tilde{k}_d(\tilde{c}_{l_{max}} - \tilde{c}_l) - \tilde{k}_r\tilde{c}_l^2 \tag{D.13}$$

D.1.6 Electrolyte diffusion

$$\frac{\partial c_l}{\partial t} + \nabla.\mathbf{J}_l = 0 \tag{D.14}$$

By substituting all parameters

$$\frac{\partial(\tilde{c}_l\ c_{l_{\text{ref}}})}{\partial\left(\tilde{t}\frac{L_{\text{ref}}^2}{D_{\text{ref}}}\right)} + \frac{1}{L_{\text{ref}}}\tilde{\nabla}\cdot(\mathbf{J}_{l_{\text{ref}}}\tilde{\mathbf{J}}_l) = 0 \tag{D.15}$$

By simplifying

$$\frac{D_{\text{ref}}c_{l_{\text{ref}}}}{L_{\text{ref}}^2}\frac{\partial\tilde{c}_l}{\partial\tilde{t}} + \frac{D_{\text{ref}}c_{s_{\text{ref}}}}{L_{\text{ref}}^2}\tilde{\nabla}.\tilde{\mathbf{J}}_l = 0 \tag{D.16}$$

Finally

$$\gamma\frac{\partial\tilde{c}_l}{\partial\tilde{t}} + \tilde{\nabla}.\tilde{\mathbf{J}}_l = 0; \qquad \gamma = \frac{c_{l_{\text{ref}}}}{c_{s_{\text{ref}}}} \tag{D.17}$$

In the presence of generation/recombination reaction

$$\frac{\partial c_l}{\partial t} + \nabla.\mathbf{J}_l - h_r = 0 \tag{D.18}$$

$$\frac{\partial(\tilde{c}_l\ c_{l_{\text{ref}}})}{\partial\left(\tilde{t}\frac{L_{\text{ref}}^2}{D_{\text{ref}}}\right)} + \frac{1}{L_{\text{ref}}}\tilde{\nabla}\cdot(\mathbf{J}_{l_{\text{ref}}}\tilde{\mathbf{J}}_l) - h_{r_{\text{ref}}}\tilde{h}_r = 0 \tag{D.19}$$

then

$$\frac{D_{\text{ref}}c_{l_{\text{ref}}}}{L_{\text{ref}}^2}\frac{\partial \tilde{c}_l}{\partial \tilde{t}} + \frac{D_{\text{ref}}c_{s_{\text{ref}}}}{L_{\text{ref}}^2}\tilde{\nabla}.\tilde{\mathbf{J}}_l - \frac{D_{\text{ref}}c_{l_{\text{ref}}}}{L_{\text{ref}}^2}\tilde{h}_r = 0 \tag{D.20}$$

$$\gamma\frac{\partial \tilde{c}_l}{\partial \tilde{t}} + \tilde{\nabla}.\tilde{\mathbf{J}}_l - \gamma\tilde{h}_r = 0; \qquad \gamma = \frac{c_{l_{\text{ref}}}}{c_{s_{\text{ref}}}} \tag{D.21}$$

Finally

$$\gamma\frac{\partial \tilde{c}_l}{\partial \tilde{t}} + \tilde{\nabla}.\tilde{\mathbf{J}}_l - \gamma\tilde{h}_r = 0; \qquad \gamma = \frac{c_{l_{\text{ref}}}}{c_{s_{\text{ref}}}} \tag{D.22}$$

D.1.7 Electric potential in the electrolyte

For potential in the electrolyte:

$$\begin{aligned} \phi_l &= \frac{\text{N.m}}{\text{C}}\tilde{\phi}_l \\ &= \frac{\frac{\text{N.m}}{\text{K.mol}}\cdot \text{K}}{\frac{\text{C}}{\text{mol}}}\tilde{\phi}_l \\ &= \frac{R_{g_{\text{ref}}}T_{\text{ref}}}{F_{\text{ref}}}\tilde{\phi}_l \end{aligned} \tag{D.23}$$

so

$$\phi_l = \phi_{\text{ref}}\tilde{\phi}_l; \qquad \phi_{\text{ref}} = \frac{R_{g_{\text{ref}}}T_{\text{ref}}}{F_{\text{ref}}} \tag{D.24}$$

D.1.8 Current in the electrolyte

The current in the electrolyte:

$$\mathbf{i}_l = -F(D_+ - D_-)\nabla c_l - \frac{F^2 c_l}{R_g T}(D_+ + D_-)\nabla\phi_l \tag{D.25}$$

$$
\begin{aligned}
\mathbf{i}_l &= -\tilde{F} F_{\text{ref}} \frac{c_{s_{\text{ref}}} D_{\text{ref}}}{c_{l_{\text{ref}}}} (\tilde{D}_+ \\
-\tilde{D}_-) \frac{1}{L_{\text{ref}}} \tilde{\nabla}(\tilde{c}_l c_{l_{\text{ref}}}) - \frac{\tilde{F}^2 F_{\text{ref}}^2 \tilde{c}_l c_{l_{\text{ref}}}}{\tilde{R}_g R_{g_{\text{ref}}} \tilde{T} T_{\text{ref}}} \frac{c_{s_{\text{ref}}} D_{\text{ref}}}{c_{l_{\text{ref}}}} (\tilde{D}_+ + \tilde{D}_-) \frac{1}{L_{\text{ref}}} \tilde{\nabla}(\tilde{\phi}_l \phi_{\text{ref}}) \\
&= -F_{\text{ref}} \frac{c_{s_{\text{ref}}} D_{\text{ref}}}{c_{l_{\text{ref}}}} \frac{1}{L_{\text{ref}}} c_{l_{\text{ref}}} \tilde{F} (\tilde{D}_+ - \tilde{D}_-) \tilde{\nabla} \tilde{c}_l - \\
&\quad \frac{F_{\text{ref}}^2 c_{l_{\text{ref}}}}{R_{g_{\text{ref}}} T_{\text{ref}}} \frac{c_{s_{\text{ref}}} D_{\text{ref}}}{c_{l_{\text{ref}}}} \frac{\phi_{\text{ref}}}{L_{\text{ref}}} \left(\frac{\tilde{F}^2 \tilde{c}_l}{\tilde{R}_g \tilde{T}} (\tilde{D}_+ + \tilde{D}_-) \tilde{\nabla} \tilde{\phi}_l \right) \\
&= \frac{F_{\text{ref}} c_{s_{\text{ref}}} D_{\text{ref}}}{L_{\text{ref}}} \left(-\tilde{F} (\tilde{D}_+ - \tilde{D}_-) \tilde{\nabla} \tilde{c}_l - \frac{\tilde{F}^2 \tilde{c}_l}{\tilde{R}_g \tilde{T}} (\tilde{D}_+ + \tilde{D}_-) \tilde{\nabla} \tilde{\phi}_l \right)
\end{aligned}
\tag{D.26}
$$

so

$$
\begin{aligned}
\mathbf{i}_l &= \mathbf{i}_{l_{\text{ref}}} \tilde{\mathbf{i}}_l; \qquad \mathbf{i}_{l_{\text{ref}}} = \frac{F_{\text{ref}} c_{s_{\text{ref}}} D_{\text{ref}}}{L_{\text{ref}}}, \\
\tilde{\mathbf{i}}_2 &= -\tilde{F} (\tilde{D}_+ - \tilde{D}_-) \tilde{\nabla} \tilde{c}_l - \frac{\tilde{F}^2 \tilde{c}_l}{\tilde{R}_g \tilde{T}} (\tilde{D}_+ + \tilde{D}_-) \tilde{\nabla} \tilde{\phi}_l
\end{aligned}
\tag{D.27}
$$

D.1.9 Electric potential equation in the electrolyte

The electric potential in the electrolyte:

$$
\nabla \cdot \mathbf{i}_l = 0 \tag{D.28}
$$

By substituting

$$
\frac{1}{L_{\text{ref}}} \tilde{\nabla} \cdot \mathbf{i}_l = 0 \tag{D.29}
$$

$$
\tilde{\nabla} \cdot \mathbf{i}_{l_{\text{ref}}} \tilde{\mathbf{i}}_l = 0 \tag{D.30}
$$

so

$$
\tilde{\nabla} \cdot \tilde{\mathbf{i}}_l = 0 \tag{D.31}
$$

D.1.10 Electrode diffusion coefficient

For electrode diffusion coefficient

$$
\begin{aligned}
D_s &= \left(\frac{\text{m}^2}{\text{s}} \right) \tilde{D}_s \\
&= D_{\text{ref}} \tilde{D}_s
\end{aligned}
\tag{D.32}
$$

so

$$D_s = D_{\text{ref}}\tilde{D}_s \quad \Rightarrow \tilde{D}_s = \frac{D_s}{D_{\text{ref}}} \tag{D.33}$$

D.1.11 Electrode flux

$$\begin{aligned} \mathbf{J}_s &= -D_s \nabla c_s \\ &= -\tilde{D}_s D_{\text{ref}} \frac{1}{L_{\text{ref}}} \tilde{\nabla} \left(\tilde{c}_s c_{s_{\text{ref}}}\right) \\ &= \frac{c_{s_{\text{ref}}} D_{\text{ref}}}{L_{\text{ref}}} \left(-\tilde{D}_s \tilde{\nabla} \tilde{c}_s\right) \end{aligned} \tag{D.34}$$

so

$$\mathbf{J}_s = \mathbf{J}_{s_{\text{ref}}} \tilde{\mathbf{J}}_s; \qquad \mathbf{J}_{s_{\text{ref}}} = \frac{c_{s_{\text{ref}}} D_{\text{ref}}}{L_{\text{ref}}}, \qquad \tilde{\mathbf{J}}_s = -\tilde{D}_s \tilde{\nabla} \tilde{c}_s \tag{D.35}$$

D.1.12 Diffusion in the electrode

$$\frac{\partial c_s}{\partial t} + \nabla . \mathbf{J}_s = 0 \tag{D.36}$$

$$\frac{c_{s_{\text{ref}}} D_{\text{ref}}}{L_{\text{ref}}^2} \frac{\partial \tilde{c}_s}{\partial \tilde{t}} + \frac{c_{s_{\text{ref}}} D_{\text{ref}}}{L_{\text{ref}}^2} \tilde{\nabla} . \tilde{\mathbf{J}}_s = 0 \tag{D.37}$$

Finally

$$\frac{\partial \tilde{c}_s}{\partial \tilde{t}} + \tilde{\nabla} . \tilde{\mathbf{J}}_s = 0 \tag{D.38}$$

D.1.13 Electrode electric potential

The potential in the electrode:

$$\begin{aligned} \phi_s &= \frac{\text{N.m}}{\text{C}} \tilde{\phi}_s \\ &= \frac{\frac{\text{N.m}}{\text{K.mol}} \cdot \text{K}}{\frac{\text{C}}{\text{mol}}} \tilde{\phi}_s \\ &= \frac{R_{g_{\text{ref}}} T_{\text{ref}}}{F_{\text{ref}}} \tilde{\phi}_s \end{aligned} \tag{D.39}$$

so

$$\phi_s = \phi_{\text{ref}} \tilde{\phi}_s; \qquad \phi_{\text{ref}} = \frac{R_{g_{\text{ref}}} T_{\text{ref}}}{F_{\text{ref}}} \tag{D.40}$$

D.1.14 Electrode electronic conductivity

$$
\begin{aligned}
\lambda &= \frac{\mathrm{S}}{\mathrm{m}}\tilde{\lambda} \\
&= \frac{\mathrm{C}^2}{\mathrm{N.m^2.s}}\tilde{\lambda} \\
&= \frac{\mathrm{C}}{\frac{\mathrm{N\cdot m}}{\mathrm{C}}\cdot \mathrm{m}\cdot \mathrm{s}}\tilde{\lambda} \\
&= \frac{\frac{\mathrm{C}}{\mathrm{mol}}\frac{\mathrm{mol}}{\mathrm{m^3}}\mathrm{m}^3}{\frac{\mathrm{N\cdot m}}{\mathrm{C}}\cdot \mathrm{m}\cdot \mathrm{s}}\tilde{\lambda} \\
&= \frac{\frac{\mathrm{C}}{\mathrm{mol}}\frac{\mathrm{mol}}{\mathrm{m^3}}\frac{\mathrm{m^2}}{\mathrm{s}}}{\frac{\mathrm{N\cdot m}}{\mathrm{C}}}\tilde{\lambda} \\
&= \frac{\frac{\mathrm{C}}{\mathrm{mol}}\frac{\mathrm{mol}}{\mathrm{m^3}}\frac{\mathrm{m^2}}{\mathrm{s}}}{\frac{\mathrm{N\cdot m}}{\mathrm{C}}}\tilde{\lambda} \\
&= \frac{D_{\mathrm{ref}}c_{s_{\mathrm{ref}}}F_{\mathrm{ref}}}{\phi_{\mathrm{ref}}}\tilde{\lambda}
\end{aligned}
\tag{D.41}
$$

so

$$
\lambda = \frac{D_{\mathrm{ref}}c_{s_{\mathrm{ref}}}F_{\mathrm{ref}}}{\phi_{\mathrm{ref}}}\tilde{\lambda} \quad \Rightarrow \tilde{\lambda} = \frac{\phi_{\mathrm{ref}}}{D_{\mathrm{ref}}c_{s_{\mathrm{ref}}}F_{\mathrm{ref}}}\lambda \tag{D.42}
$$

D.1.15 Current in the electrode

The current in the electrode:

$$
\begin{aligned}
\mathbf{i}_s &= -\lambda\nabla\phi_s \\
&= -\frac{D_{\mathrm{ref}}c_{s_{\mathrm{ref}}}F_{\mathrm{ref}}}{\phi_{\mathrm{ref}}}\tilde{\lambda}\frac{1}{L_{\mathrm{ref}}}\tilde{\nabla}(\tilde{\phi}_s\phi_{\mathrm{ref}}) \\
&= -\frac{D_{\mathrm{ref}}c_{s_{\mathrm{ref}}}F_{\mathrm{ref}}}{L_{\mathrm{ref}}}\tilde{\lambda}\tilde{\nabla}\tilde{\phi}_s
\end{aligned}
\tag{D.43}
$$

so

$$
\mathbf{i}_s = \mathbf{i}_{s_{\mathrm{ref}}}\tilde{\mathbf{i}}_1; \qquad \mathbf{i}_{1_{\mathrm{ref}}} = \frac{F_{\mathrm{ref}}c_{s_{\mathrm{ref}}}D_{\mathrm{ref}}}{L_{\mathrm{ref}}}, \qquad \tilde{\mathbf{i}}_s = -\tilde{\lambda}\tilde{\nabla}\tilde{\phi}_s \tag{D.44}
$$

D.1.16 Electric potential in the electrode

The electric potential in the electrode:

$$
\nabla\cdot\mathbf{i}_s = 0 \tag{D.45}
$$

By substituting

$$\frac{1}{L_{\text{ref}}}\tilde{\nabla}\cdot\mathbf{i}_s = 0 \tag{D.46}$$

$$\tilde{\nabla}\cdot\mathbf{i}_{s_{\text{ref}}}\tilde{\mathbf{i}}_s = 0 \tag{D.47}$$

So

$$\tilde{\nabla}\cdot\tilde{\mathbf{i}}_s = 0 \tag{D.48}$$

Appendix E

Paper: Level set topology optimization of structural problems with interface cohesion

INTERNATIONAL JOURNAL FOR NUMERICAL METHODS IN ENGINEERING
Int. J. Numer. Meth. Engng 2016; **00**:204–227
Published online in Wiley InterScience (www.interscience.wiley.com). DOI: 10.1002/nme

Level set topology optimization of structural problems with interface cohesion

Reza Behrou[1], Matthew Lawry[2] and Kurt Maute[2*†]

[1]*Department of Civil, Environmental and Architectural Engineering, University of Colorado Boulder, Boulder, CO 80309-0428, USA*
[2]*Department of Aerospace Engineering, University of Colorado Boulder, Boulder, CO 80309-0429, USA*

SUMMARY

This paper presents a finite element topology optimization framework for the design of two-phase structural systems considering contact and cohesion phenomena along the interface. The geometry of the material interface is described by an explicit Level Set Method (LSM) and the structural response is predicted by the eXtended Finite Element Method (XFEM). In the present work the interface condition is described by a bilinear cohesive zone model based on the traction-separation constitutive relation. The non-penetration condition in the presence of compressive interface forces is enforced by a stabilized Lagrange multiplier method. The mechanical model assumes a linear elastic isotropic material, infinitesimal strain theory, and a quasi-static response. The optimization problem is solved by a nonlinear programming method and the design sensitivities are computed by the adjoint method. The performance of the presented method is evaluated by 2D and 3D numerical examples. The results obtained from topology optimization reveal distinct design characteristics for the various interface phenomena considered. In addition, three-dimensional examples demonstrate optimal geometries that cannot be fully captured by reduced dimensionality. The optimization framework presented is limited to two-phase structural systems where the material interface is coincident in the undeformed configuration, and to structural responses that remain valid considering small strain kinematics. Copyright © 2016 John Wiley & Sons, Ltd.

Received . . .

KEY WORDS: topology optimization, level set method, extended finite element method, cohesive zone model, nonlinear interface, contact model, adaptive dynamic relaxation

1. INTRODUCTION

The performance of structures composed of multiple components such as anchors, fasteners, laminated composites, and snap-fit designs is afforded in part by mechanical interface phenomena such as frictionless contact and material cohesion. From a design perspective, interfacial properties must be carefully considered for intended applications whose functionality relies on structural component interactions. However, accurate mechanical response prediction and design optimization of such systems proves challenging, given the interface response is surface orientation-dependent and often highly nonlinear. This paper presents a topology optimization method for structural problems involving frictionless contact and bilateral cohesive interface phenomena in both two and three dimensions.

Design optimization methods can be classified by the geometric changes that are allowable during the optimization process. Optimization methods in which geometry variation is restricted to

*Correspondence to: Kurt Maute, Department of Aerospace Engineering and Sciences, University of Colorado Boulder, CB 429, Boulder, CO 80301-0429, USA.
†Email: kurt.maute@colorado.edu

affecting the shape of the material interface is known as shape optimization. Optimization methods in which geometry variation affords changes in both shape and number of design components is known as topology optimization. To provide a high level of design freedom, a topology optimization framework is used in this paper.

The interface conditions considered in this study are inherently nonlinear. For frictionless contact, interfacial forces act to prevent the penetration of bodies but vanish during separation. Material cohesion provides resistance to shear and normal separation of joined materials, but can result in rapid delamination when the cohesive limit is surpassed. Due to their complex behavior, problems with contact phenomena have only been considered in a few two dimensional topology optimization studies. This paper presents a novel topology optimization method for two and three dimensional problems involving interface cohesion and delamination.

Density methods, such as the Solid Isotropic Material with Penalization (SIMP) approach, are the most common method of describing the geometry in topology optimization. The SIMP approach was originally developed by [1, 2] and describes the geometry of a body by defining the material distribution in the design domain as a function of design variables. A fictitious porous material with density, $0 \leq \rho \leq 1$, defines a continuous transition between two or more materials. For more information and an overview of recent developments, the reader is referred to [3–5]. By representing topology as a continuous transition between materials, density methods effectively smear the interface geometry. This loss of precise interface geometry proves challenging when modeling design dependent surface loads. To recover the interface behavior, a common approach is to convert surface loads into a volumetric body force; see for example [6], [7], and [8]. This approach is ill-suited for modeling surface orientation-dependent contact behavior, as the interface geometry is not explicitly defined. A second approach introduced by [9] approximates surface geometry by iso-volumetric density curves. This method introduces approximation error in surface position and orientation, which is ill suited for problems whose mechanical response is highly sensitive to surface geometry. The density method has been used to optimize the material distribution surrounding surface geometries defined by body-fitted meshes, as is the case for [10] and [11]. In these works, the contact interface is mesh conforming and excluded from the geometry variation in the optimization process.

The LSM is a promising alternative approach for defining the geometry of the interface in topology optimization problems. In the LSM, the boundary between materials is explicitly defined by an iso-contour of the Level Set Function (LSF), ϕ, at a particular value; commonly $\phi = 0$ at the interface. For more information and a review of recent developments of LSMs, the reader is referred to [12]. For geometries defined through the LSM, the mechanical model can be constructed by either a body fitted mesh, an Ersatz material approach, or immersed boundary techniques.

In this study, we combine the LSM with the XFEM, a finite element method for immersed boundaries. The XFEM retains the sharp definition of surface geometry afforded by the LSM and provides a reliable mechanical response throughout the evolution of the design domain. The reader is referred to [13] and [14] for an introduction and general overview of the XFEM. Previously [15] applied the XFEM-LSM to topology optimization of structural problems with bilateral, frictionless sliding contact. Initially applied to two dimensional frictionless contact problems, it was subsequently extended to interface cohesion problems [16]. Liu et al. [17] recently leveraged the XFEM-LSM framework to minimize the compliance of multi-material structures with interface cohesion. Using adjoint sensitivities and the Hamilton-Jacobi equation to advance the structural boundary, optimal solutions were achieved for two dimensional problems. The presented method builds on the work of [16], extending it to the treatment of interface cohesion between two materials in three dimensions.

Material cohesion represents a progressive nonlinear behavior along the interface. This phenomenon, which relates separation along the interface to surface traction, is also called the cohesive zone model. The cohesive zone model is frequently used to describe material failure and interfacial debonding in engineering structures. It was initially introduced by Dugdale [18] to analyze the damage evolution and material failure within a localized region surrounding the tip of a crack. During separation, the traction along the interface grows to a maximum value, then

diminishes to zero. Numerical modeling of structural problems with cohesive zone models have received considerable attention, seminally introduced by Needleman [19]. Normal and tangential traction at the interface can be represented as either independent or coupled functions of normal and tangential separation. The constitutive relation between traction and separation has been described by exponential, bilinear, and polynomial forms of cohesive zone laws [20–23]. The standard bilinear cohesive zone model is used often for the simulation of interfacial debonding, matrix cracking, delamination of fiber reinforced composites [24, 25], and failure in functionally graded materials [26]. This work considers an uncoupled, bilinear representation of the cohesive zone models. For more information about cohesive zone models, the reader is referred to [27].

Numerical simulation of interface phenomena may be carried out through different approaches, such as: the boundary element formulation [28], the element free Galerkin method [29], and the finite element formulation [30]. In standard finite element methods, a common approach is to introduce an interface element between volume elements. Remeshing may or may not be necessary depending on the magnitude of surface geometry changes in the mechanical deformation and design optimization processes [31–34]. The XFEM has been developed to model arbitrary discontinuities in the finite element model without remeshing. This method leverages the partition of unity concept with appropriate enrichment functions to accurately resolve displacement fields along the interface [35,36]. A variety of contact modeling methods have been explored in the XFEM. A penalty method has been employed to model small strain frictional contact problem using XFEM, for example, by [37–39]. The XFEM framework has been used to investigate interface cohesion effects on the mechanical performance of nano-structures [40]. A Lagrange multiplier formulation has been used in a few approaches, see [41] and [42]. A mixed Lagrange multiplier formulation has been applied for contact problems by [43] and mortar methods have been studied by [44], respectively. Finite deformations have been considered in a few contact problems, for example, by [45–49].

Many cohesive zone laws rely on a penalty method to prevent surface penetration during compression. To mitigate ill-conditioning and accuracy issues often caused by penalty formulations, in this work a stabilized Lagrange method is adopted for the enforcement of non-penetration. During the process of delamination, the mechanical model can experience instabilities. To mitigate this issue, a dynamic relaxation method is employed for the evaluation of the structural response. The interface geometry between two distinct material phases is described by an explicit LSM. Unlike an implicit LSM, which typically describes the evolution of the level set field in the optimization process by the Hamilton-Jacobi equation (e.g. [50]), explicit LSMs define the discretized level set field as explicit functions of the optimization variables [51–53]. To retain a sharp definition of the interface, we adopt the XFEM for predicting the mechanical response. The particular framework for integrating the explicit LSM and the generalized formulation of the XFEM used in this study are described in detail in [54] and [55].

The remainder of this paper is organized as follows: in Section 2, we outline the formulation of the optimization problems considered in this study. In Section 3, we discuss the geometry model used to describe the phase boundaries. In Section 4, the mechanical model of problems with cohesive interfaces is described. The XFEM formulation is summarized in Section 5. The numerical implementation is described in Section 6. In Section 7, we study the main characteristics of the proposed XFEM-LSM method with numerical examples. Insight gained from the numerical studies and areas for future research are summarized in Section 8.

2. OPTIMIZATION PROBLEM

In this study, we consider the interactions between two phases, A and B, in two and three dimensions. A representative configuration of the optimization problems relevant to this paper is shown in Figure 1. The design domain Ω^D consists of two non-overlapping subdomains Ω^A and Ω^B, such that $\Omega^D = \Omega^A \cup \Omega^B$ and $\Gamma^{AB} = \Omega^A \cap \Omega^B$ is the interface between both subdomains. Frictionless sliding or a cohesive interface behavior is modeled at the material interface Γ^{AB}. Displacements are prescribed at the boundary Γ_U^B while material A is fixed at the boundary Γ_U^A. In the optimization examples presented in Section 7 we seek to maximize the reaction force at Γ_U^A.

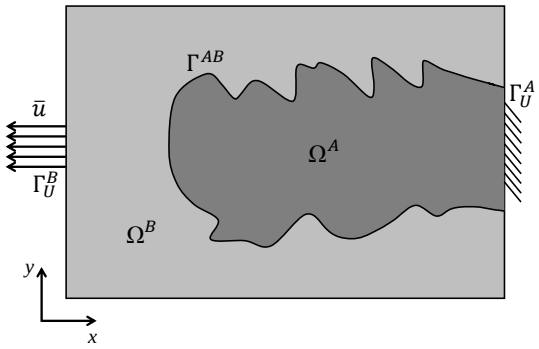

Figure 1. Representative configuration of an optimization problem.

To discourage the emergence of oscillatory shapes mimicking a rough surface, we introduce a perimeter penalty term into the formulation of the objective function. This penalty term measures the interface between domains Ω^A and Ω^B and is computed as follows:

$$P = \int_{\Gamma^{AB}} \mathrm{d}\Gamma \, . \tag{1}$$

While a perimeter penalty does not allow explicit control of the local shape and the size of geometric features, it has been reported effective in regularizing structural optimization problems [12]. For additional reading on the use of perimeter measures for regularization, the reader is referred to [15, 56, 57]. Geometric features that approach the length scale of element size can result in poor mechanical response predictions. To suppress the formation of such features, a gradient measure penalty is used and will be further discussed in Section 3. Finally, we constrain the ratio of volumes occupied by either solid, V^A and V^B, to exclude trivial solutions.

The optimization problem is defined by the following nonlinear program:

$$\begin{aligned} &\min_{\mathbf{s}} \left(\frac{c_u}{z_0} z(\mathbf{u}(\mathbf{s})) + \frac{c_p}{P_0} P(\mathbf{s}) + \frac{c_g}{G_0} G(\mathbf{s}) \right) \\ &\text{s.t. } V^A(\mathbf{s}) - c_v \, V^B(\mathbf{s}) \leq 0 \\ &\quad \mathbf{s} \in \mathbf{S} = \left\{ \mathbb{R}^{N_s} | s_{min} \leq s_i \leq s_{max}, \; i = 1....N_s \right\} \, , \end{aligned} \tag{2}$$

where z denotes the contribution of the mechanical response to the objective, c_u is the associated weighting factor, z_0 is the initial mechanical response in objective, c_p is the weight of the material interface penalty, P_0 is the initial measure of the material interface, c_g is the weight of gradient measure penalty, G_0 is the initial gradient measure, and c_v controls the desired volume ratio between the two solids, respectively. The number of optimization variables is N_s; the lower and upper bounds on the optimization variables are denoted by s_{min} and s_{max}, respectively. The structural response, $z(\mathbf{u}(\mathbf{s}))$, depends on the discretized state variables, $\mathbf{u}$, which are implicitly dependent on design variables, $\mathbf{s}$. While the proposed optimization framework allows considering other objectives and constraints, such as strain energy, displacement and stress measures, the formulations of the optimization problem used here are well suited to illustrate the influence of mechanical interface conditions on optimized designs. The optimization problem (2) is solved by a nonlinear programming method, and the design sensitivities are calculated by the adjoint method.

3. GEOMETRY MODEL

The geometry of the structure is defined by the LSF, $\phi(\mathbf{x})$, where $\mathbf{x}$ is the vector of spatial coordinates. For a two-phase problem, the LSF describes the spatial distribution of both phases

as follows:

$$\begin{cases} \phi(\mathbf{x}) > 0 & \forall\, \mathbf{x} \in \Omega^A \\ \phi(\mathbf{x}) < 0 & \forall\, \mathbf{x} \in \Omega^B \\ \phi(\mathbf{x}) = 0 & \forall\, \mathbf{x} \in \Gamma^{AB} \end{cases} , \tag{3}$$

where Ω^A is the volume occupied by phase A, Ω^B is the volume occupied by phase B, and Γ^{AB} is the interface between two phases. The parameters of the discretized LSF are defined by explicit functions of the optimization variables. The level set field can be parameterized to describe any particular geometry such as circles or rectangles. The location and geometry of these primitives are defined by the optimization variables. This approach has proven to be effective in optimization studies of stress and strain energy minimization [58, 59]. Following to the approach of [60], to increase design freedom, the domain is discretized by finite elements and one optimization variable is associated with each finite element node, i.e. $N_s = N_n$, where N_n is the number of nodes. The level set value at the i^{th} node is defined by the following linear filter:

$$\phi_i = \left(\sum_{j=1}^{N_n} w_{ij} \right)^{-1} \sum_{j=1}^{N_n} w_{ij} s_j \ , \qquad \text{with} \qquad w_{ij} = max\left(0, (r - |\mathbf{x}_i - \mathbf{x}_j|)\right) \ , \tag{4}$$

where r is the filter radius, and $\mathbf{x}_j$ the position of the j^{th} node. The level set filter (4) enhances the convergence of the optimization process by widening the zone of influence of the optimization variables on the level set field [60].

In this paper, the LSF is discretized by quad-4 and hex-8 elements for 2D and 3D design domains, respectively. This choice of discretization limits the complexity of interface geometry within an element, but can still result in sub-element features. These features can cause poor structural response predictions, as well as optimization convergence issues if they are found to be advantageous to the design [61]. To mitigate these issues, we adopt the approach of [62] that suppresses sub-element features by introducing a constraint on the norm of the spatial gradient of the LSF in the vicinity of the material interface along with setting the lower and upper limits of the optimization variables to values that depend on the element size.

A constraint is imposed on the integral measure, G, that is evaluated over the design domain as follows:

$$G = \int_{\Omega^D} e^{-\alpha^2} \left(|\nabla \phi| - 1 \right)^2 \mathrm{d}\Omega \qquad \text{with} \qquad \alpha = e_p \frac{\phi}{\Delta\phi} \ , \quad \Delta\phi = \phi_{max} - \phi_{min} \ , \tag{5}$$

where e_p is the penalization parameter, and $\Delta\phi$ is the range of allowable level-set values within the design domain, with ϕ_{max} and ϕ_{min} denoting the upper and lower limits of the level set value, respectively. The first term in (5) vanishes away from the zero level set isosurfaces, but is unity in its vicinity. The second term encourages a signed distance-like level set field, i.e. $|\nabla\phi| = 1$. The combination of these two terms identifies level set gradients that do not match the desired value of 1 near the material interface. The use of the integral measure G for regularization is only successful in discouraging sub-element features with appropriate upper and lower bounds of the level set values, ideally $\phi_{max} = h/2$ and $\phi_{min} = -h/2$ where h corresponds to the element size. This approach was used successfully towards the optimization of convective heat dissipation problems [62, 63], where it was observed that the lower and upper bounds can be relaxed to $\mp h$ to improve the convergence of the optimization process.

4. PHYSICAL MODEL

Static equilibrium in the design domain is defined by the balance of linear momentum

$$\nabla \cdot \boldsymbol{\sigma} + \mathbf{b} = \mathbf{0} \quad \text{in} \quad \Omega^D \ , \tag{6}$$

with the following Dirichlet boundary conditions:

$$\mathbf{u} = \bar{\mathbf{u}} \quad \text{on} \quad \Gamma_U \ , \tag{7}$$

where $\boldsymbol{\sigma}$ is the Cauchy stress tensor, $\mathbf{b}$ is the body force vector, and $\bar{\mathbf{u}}$ is the prescribed displacement at the surface Γ_U, respectively. By assuming small strain behavior, the constitutive and linear kinematic relations for both materials are defined as follows:

$$\boldsymbol{\sigma}(\mathbf{u}) = \mathbb{C} \cdot \boldsymbol{\varepsilon}(\mathbf{u}) \ , \tag{8}$$

$$\boldsymbol{\varepsilon}(\mathbf{u}) = \frac{1}{2}\left(\nabla \mathbf{u} + (\nabla \mathbf{u})^T\right) \ , \tag{9}$$

where $\mathbb{C}$ is the fourth order elasticity tensor, and $\boldsymbol{\varepsilon}$ is the infinitesimal strain tensor.

To describe the mechanical response at the interface between Ω^A and Ω^B, Figure 2 illustrates contact relations pertinent to the interface phenomena considered in this paper. Here we introduce superscript p to represent either of phases A and B. Surface quantities $\mathbf{T}^p$, $\mathbf{n}^p$, and $\mathbf{t}^p$ are the traction, normal vector, and tangential vector for phase p, respectively. We define $\mathbf{u}^{BA}$ as the displacement jump across the interface. The mechanical response at the interface depends on the traction and relative displacement across the interface. For any given point on the interface, the normal and tangential traction and separations are defined as:

$$\begin{aligned} \Delta_n = \mathbf{u}^{BA} \cdot \mathbf{n}^A, \qquad \Delta_t = \mathbf{u}^{BA} \cdot \mathbf{t}^A, \qquad \mathbf{n}^A = -\mathbf{n}^B, \qquad \mathbf{t}^A = -\mathbf{t}^B \ , \\ \tilde{T}_n = \mathbf{T}^A \cdot \mathbf{n}^A = -\mathbf{T}^B \cdot \mathbf{n}^A, \qquad \tilde{T}_t = \mathbf{T}^A \cdot \mathbf{t}^A = -\mathbf{T}^B \cdot \mathbf{t}^A \ , \end{aligned} \tag{10}$$

where Δ_n is the normal separation, Δ_t is the tangential separation, $\tilde{T}_n$ is the magnitude of normal traction, and $\tilde{T}_t$ is the magnitude of tangential traction. The relationship between surface traction and relative displacement are illustrated in Figure 3. The variables δ_c^n, δ_c^t, δ_f^n, and δ_f^t represent the critical normal separation, the critical tangential separation, the normal separation at which the normal traction vanishes, and the tangential separation at which the tangential traction vanishes, respectively. In our uncoupled bilinear cohesive zone law three distinct regions are defined. The bonded zone refers to the linear elastic region where $\Delta_n \leq \delta_c^n$ and $\Delta_t \leq \delta_c^t$. The reduced zone is defined as the region where $\delta_c^n \leq \Delta_n \leq \delta_f^n$ and $\delta_c^t \leq \Delta_t \leq \delta_f^t$. Finally, the debonded zone refers to the region in which cohesion has vanished, i.e. $\Delta_n \geq \delta_f^n$ and $\Delta_t \geq \delta_f^t$.

Departing from the frequently used penalty method to prevent surface penetration, the compressive region depicted in the lower left quadrant of Figure 3(a) is handled separately by a stabilized Lagrange formulation. This mitigates ill-conditioning and accuracy issues that can arise

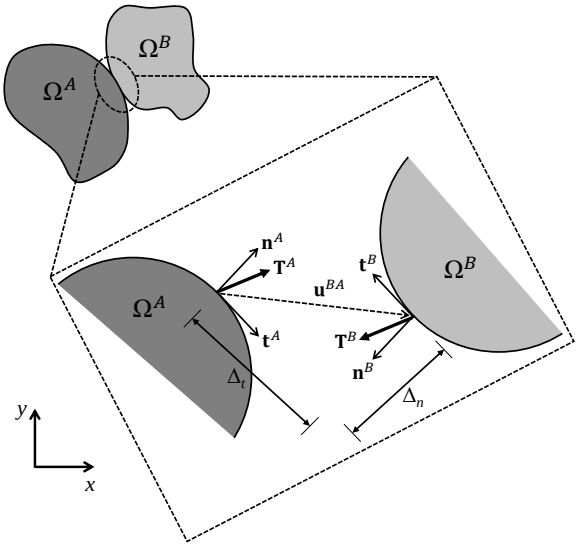

Figure 2. Schematic of two bodies in contact with cohesive interface.

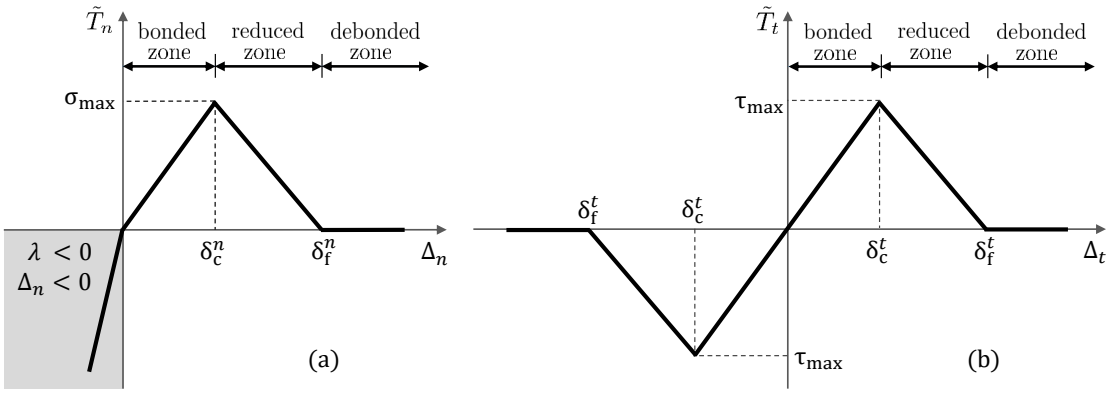

Figure 3. Uncoupled bilinear cohesive zone law, (a) normal response, (b) tangential response.

with the use of penalty methods. During separation, the magnitude of normal and shear traction at the interface increases linearly to a prescribed maximum value, then falls to zero when separation has surpassed the cohesion limit. The governing equations for bilinear cohesion are defined as follows:

$$\tilde{T}_n(\Delta_n,\lambda) = \begin{cases} \lambda & \text{if } \lambda \le 0 \\ \frac{\sigma_{max}}{\delta_c^n}\Delta_n & \text{if } 0 \le \Delta_n \le \delta_c^n \\ \frac{\sigma_{max}(\delta_f^n - \Delta_n)}{\delta_f^n - \delta_c^n} & \text{if } \delta_c^n < \Delta_n \le \delta_f^n \\ 0 & \text{if } \Delta_n > \delta_f^n \end{cases}, \tag{11}$$

and

$$\tilde{T}_t(\Delta_t) = \begin{cases} \frac{\tau_{max}}{\delta_c^t}\Delta_t & \text{if } -\delta_c^t \le \Delta_t \le \delta_c^t \\ \frac{\tau_{max}(\delta_f^t - \Delta_t)}{\delta_f^t - \delta_c^t} & \text{if } \delta_c^t < \Delta_t \le \delta_f^t \\ -\frac{\tau_{max}(\delta_f^t - \Delta_t)}{\delta_f^t - \delta_c^t} & \text{if } -\delta_f^t \le \Delta_t < -\delta_c^t \\ 0 & \text{if } |\Delta_t| > \delta_f^t \end{cases}, \tag{12}$$

where σ_{max} is the value of normal traction at the critical normal separation, δ_c^n; τ_{max} is the tangential traction at the critical tangential separation, δ_c^t; λ is the Lagrange multiplier associated with the non-penetration condition. The constraint equation associated with the stabilized Lagrange multiplier is evaluated as follows:

$$\lambda - \bar{\mathbf{T}} \cdot \mathbf{n}^A - \gamma\Delta_n = 0\,, \tag{13}$$

with

$$\bar{\mathbf{T}} = \bar{\boldsymbol{\sigma}} \cdot \mathbf{n}^A, \qquad \bar{\boldsymbol{\sigma}} = \omega^A \boldsymbol{\sigma}^A + \omega^B \boldsymbol{\sigma}^B\,, \tag{14}$$

where γ is a penalty factor. The penalty factor discourages penetration during the early stages of convergence but becomes insignificant as equilibrium is achieved and the relative normal separation goes to zero, i.e. $\Delta_n \approx 0$. The weighting factors, ω^p, are such that $\omega^A + \omega^B = 1$; in this work we assume that $\omega^A = \omega^B = 0.5$.

5. XFEM DISCRETIZATION

The weak form of the governing equations are discretized with the XFEM: for additional information about the weak form of the governing equations involving cohesive zone model and frictionless contact, the reader is referred to [36] and [64]. For problems involving sliding contact and separation, the solution field at material boundaries are discontinuous. Therefore, a Heaviside enrichment strategy is used exclusively for this work. For more information regarding different

enrichment strategies, the reader is referred to [65]. The displacements, u_i, throughout the design domain are defined as follows:

$$u_i(\mathbf{x}) = \sum_{m=1}^{M} \left(H(-\phi(\mathbf{x})) \sum_{k=1}^{N_e} N_k(\mathbf{x})\ \delta_{mp}^{A,k}\ u_{i,k}^{A,m} + H(\phi(\mathbf{x})) \sum_{k=1}^{N_e} N_k(\mathbf{x})\ \delta_{mq}^{B,k}\ u_{i,k}^{B,m} \right) , \tag{15}$$

where the Heaviside step function is:

$$H(\phi) = \begin{cases} 1 & \text{if } \phi > 0, \\ 0 & \text{if } \phi \leq 0\ . \end{cases} \tag{16}$$

The shape functions are denoted as $N_i(\mathbf{x})$, M is the number of enrichment levels, N_e is the number of elemental node, $u_{i,k}^{p,m}$ is the degree of freedom of enrichment level m at node k corresponding to the displacement u_i in phase $p \in \{A,B\}$, and δ is the Kronecker delta. The Heaviside function turns on/off the interpolation functions associated with each material. For each material, multiple enrichment functions may be necessary to interpolate the solution to multiple, disconnected regions to prevent fictitious coupling or load transferring. The Kronecker delta, $\delta_{mq}^{p,k}$, applies the active enrichment level q for node k such that the displacements at point $\mathbf{x}$ are interpolated by only one set of degrees of freedom defined at node k, satisfying the partition of unity principle. To maintain the continuity of the displacement field across the elemental boundaries, an appropriate enrichment level is chosen. The approach used in this study is adapted from [54], for more description the reader is referred to [54, 66, 67]. The XFEM allows the integration of the weak form of governing equations in an intersected element by decomposing into triangles (2D) and tetrahedrons (3D) while in non-intersected elements the displacement field is approximated by the standard finite element interpolation.

In this paper, the displacements are approximated by quad-4 and hex-8 elements in 2D and 3D, respectively. The stabilized Lagrange multiplier for the contact non-penetration condition described in Equation (13) is approximated as being element-wise constant. The Lagrange multipliers are condensed out locally to determine the structural response. To cure the ill-conditioning of the XFEM formulation associated with small intersections, the geometric preconditioning scheme detailed by [68] is employed.

6. IMPLEMENTATION

The discretized model yields a non-linear system of equations, which is solved in a quasi-static manner using a Newton-Raphson iterative procedure. Convergence difficulties often arise in Newton-Raphson based solvers when the solution approaches a strong material or geometric nonlinearity. To mitigate these convergence issues, we use dynamic relaxation. This method uses an artificial damping term which mitigates oscillations in the system response and increases the stability and convergence toward the steady state solution. The damping parameter is updated during the iterative solve based on convergence criteria, and vanishes as convergence is achieved. Dynamic relaxation has been successfully used for solving variety of nonlinear problems such as elasto-plasticity, wrinkling, large deflection analysis, simulation of atomic structures and materials [69–71].

In this paper, we adopt a Levenberg-Marquardt similar method [72] for dynamic relaxation. Originally developed to solve non-linear least square problems, the Levenberg-Marquardt algorithm has shown to be useful in density method topology optimization; specifically by reducing analysis instabilities caused by element distortion in large strain compliant mechanisms [73]. In this paper we follow a similar approach by modifying the Jacobian matrix as follows:

$$\tilde{\mathbf{J}} = \mathbf{J} + \tilde{\beta}\ \text{diag},(\mathbf{J})\ , \tag{17}$$

where $\mathbf{J}$ is the original Jacobian of the system, $\tilde{\beta}$ is the damping parameter, and $\tilde{\mathbf{J}}$ is the modified Jacobian of the system, respectively. The basic algorithm and convergence criteria for computing the structural response using an adaptive dynamic relaxation method are presented in Algorithm 1.

Algorithm 1: A basic algorithm for computing the structural response using the adaptive dynamic relaxation method.

Input: damping parameter $\tilde{\beta}_{\text{int}}$

for $n \leftarrow 1$ **to** *maximum time iterations* **do**

  Restart damping parameter: $\tilde{\beta}^n = \tilde{\beta}_{\text{int}}$

  for $k \leftarrow 1$ **to** *maximum Newton's iteration* **do**

    for $m \leftarrow 1$ **to** *maximum dynamic relaxation iteration* **do**

      1) Compute new damping parameter for relaxation iteration

$$\tilde{\beta}^{n+1}_{(k+1)_m} = \begin{cases} 10\tilde{\beta}^n & \text{if} \quad \left|\mathbf{R}^{n+1}_{(k+1)_m}\right| > \left|\mathbf{R}^n_k\right| \\ \tilde{\beta}^n/10 & \text{if} \quad \left|\mathbf{R}^{n+1}_{(k+1)_m}\right| \leq \left|\mathbf{R}^n_k\right| \end{cases}$$

      2) Update the Jacobian matrix

$$\tilde{\mathbf{J}}^{n+1}_{(k+1)_m} = \mathbf{J}^{n+1}_{(k+1)_m} + \tilde{\beta}^{n+1}_{(k+1)_m}\ \text{diag}(\mathbf{J}^{n+1}_{(k+1)_m})$$

      3) Solve for current relaxation iteration

$$\Delta\mathbf{u}^{n+1}_{(k+1)_m} = -(\tilde{\mathbf{J}}^{n+1}_{(k+1)_m})^{-1}\mathbf{R}^{n+1}_{(k+1)_m}$$
$$\hat{\mathbf{u}}^{n+1}_{(k+1)_m} = \mathbf{u}^n_k + \Delta\mathbf{u}^{n+1}_{(k+1)_m}$$

      4) Check the convergence of dynamic relaxation

      if $\left(\left|\mathbf{R}^{n+1}_{(k+1)_m}\right| < \left|\mathbf{R}^{n+1}_k\right|\right)$ *or* $\left(\left|\Delta\mathbf{u}^{n+1}_{(k+1)_m}\right| < \left|\Delta\mathbf{u}^{n+1}_k\right|\right)$ **then**

        accept current solution: $\mathbf{u}^{n+1}_{k+1} = \hat{\mathbf{u}}^{n+1}_{(k+1)_m}$

        go to next Newton's iteration: $k = k+1$

        break

For each Newton step k, the physical response solver applies m dynamic relaxation iterations. Damping parameter $\tilde{\beta}$ is either increased or decreased depending on whether or not the norm of the residual, $|\mathbf{R}|$, has reduced from the previous iteration. If the norm of the residual or the solution increment, $|\Delta\mathbf{u}|$, has decreased from the previous Newton iteration, the solution increment is accepted. However, if these convergence criteria are not met, the solution increment is rejected and dynamic relaxation continues to the next iteration. The reliable convergence behavior afforded by dynamic relaxation is offset by additional computational expense; for the numerical experiments presented, the computational time required for response prediction often doubled.

7. NUMERICAL EXAMPLES

In this section, we first verify the accuracy of the implemented cohesive zone model for different modes of delamination through comparison against analytical reference solutions. To gain insight into the effectiveness and robustness of the optimization framework, both 2D and 3D optimization problems are considered. We study the influence of cohesive interface parameters on the optimized design through numerical examples. The effect of the gradient measure penalty on optimal

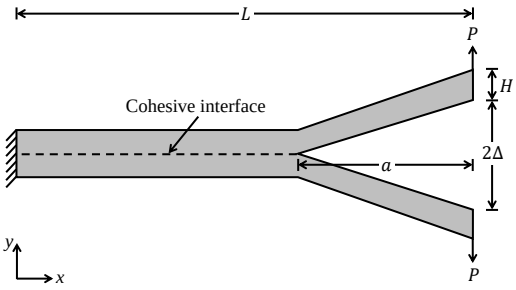

Figure 4. Schematic of the double cantilever beam.

Table I. Model parameters for the double cantilever beam.

Description	Parameter	Value	Units
beam length	L	200	mm
beam height	H	10	mm
Young's modulus	E	14.2	GPa
Poisson's ratio	ν	0.35	
fraction energy	G_c	344	J/m^2
material strength	$\sigma_{\max}$	3.56	MPa
penalty factor	γ	20	

performance is evaluated, and the impact of surface debonding on the optimized geometry is assessed by varying the magnitude of the applied loads.

The optimization problems are solved by the Globally Convergent Method of Moving Asymptotes (GCMMA) [74]. The parameters controlling the adaptation of the lower and upper asymptotes are set to 0.5, 0.7, and 1.2, respectively. The relative step size, Δs, is provided for each example. The GCMMA constraint penalty is set to 50. For all optimization examples provided in this paper, the upper and lower limits for the optimization variables are set to $s_{max} = h$ and $s_{min} = -h$, where h represents the length of the elements. For the sensitivity analysis we adopt a discrete formulation similar to that used by [63, 75], which can be readily evaluated from the governing equations of the design problem. The partial derivatives of the objection function, the constraint, and the element residual with respect to the design variables are evaluated by a finite difference method. The linearized sub-problems within the Newton iterations and the adjoint sensitivity analysis are solved using the UMFPACK direct solver [76] for the 2D examples and a Generalized Minimal RESidual (GMRES) iterative solver with incomplete LU factorization [77] for the 3D examples.

7.1. Verification of cohesive zone model

The accuracy of the XFEM formulation of the cohesive zone model discussed above is validated through comparison against the analytical solution for mode I of delamination. For this purpose, a double cantilever beam (DCB) is studied. The schematic of the DCB geometry is illustrated in Figure 4. Using linear elastic beam theory [78], the analytical solution for the crack length can be described as a function of cohesive fracture energy. The crack length is given by [79] as:

$$a = \sqrt[4]{\frac{3EH^3\Delta^2}{4G_c}}\,, \tag{18}$$

where E is the Young's modulus, Δ is the separation at the end, H is the beam height, and G_c is the cohesive fracture energy. We adapted the model parameters and problem configuration given by [79], provided in Table I. For numerical modeling, the beam is discretized with 330×33 bilinear quadrilateral elements and the forward analysis is solved with a 2D plane strain condition. The measured crack length, a, is plotted as a function of end displacement, Δ, and compared to the analytical solution in Figure 5. The inset snapshots depict the initial and final deformed configuration of the DCB, with an expanded view of the mesh used. For visualization purposes, intersected elements are decomposed into triangles. Despite the influence of the fixed edge boundary condition, the measured relative error between two solutions is approximately 1%. This error is caused by unstable crack growth near the fixed edge of the beam, similarly observed by [78, 79].

In addition to mode I verification, the structural response during mixed mode uniform delamination is verified by an analytical solution. A rectangular block with a horizontal cohesive interface is fixed along the bottom edge and subjected to a uniform displacement along the top edge. The schematic of the problem and the boundary conditions are shown in Figure 6. The material and cohesive zone model parameters for the mixed mode delamination model are given in Table II. For any given uniform surface separation value, the analytical solution for the total delamination force

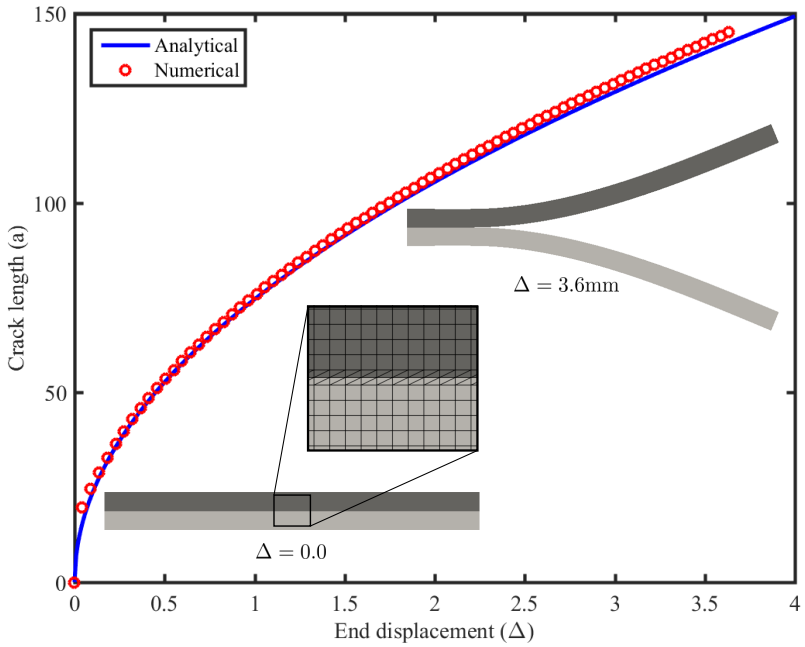

Figure 5. Comparison between analytical and numerical solutions for the double cantilever beam. For visualization purpose, the displacement in the deformed configuration is shown with a scaling factor 10.

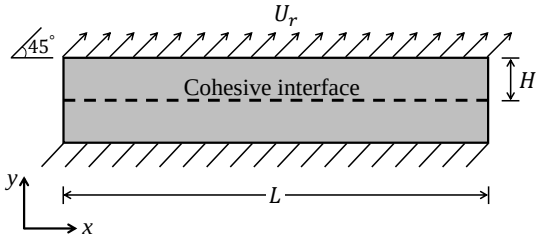

Figure 6. Loading and boundary conditions for the laminated structure with cohesive interface.

Table II. Material and cohesive zone parameters for the mixed mode model.

Description	Parameter	Value	Units
beam length	L	10	mm
beam height	H	0.1	mm
beam thickness	t	0.1	mm
applied displacement	U_r	0.15	mm
Young's modulus	E	2.0	GPa
Poisson's ratio	ν	0.3	
maximum normal traction	$\sigma_{\max}$	1.0	MPa
maximum tangential traction	$\tau_{\max}$	3.0	MPa
ultimate normal separation	δ_{f}^{n}	0.06	mm
ultimate tangential separation	δ_{f}^{t}	0.033	mm
critical normal separation	δ_{c}^{n}	0.006	mm
critical tangential separation	δ_{c}^{t}	0.0033	mm
penalty factor	γ	20	

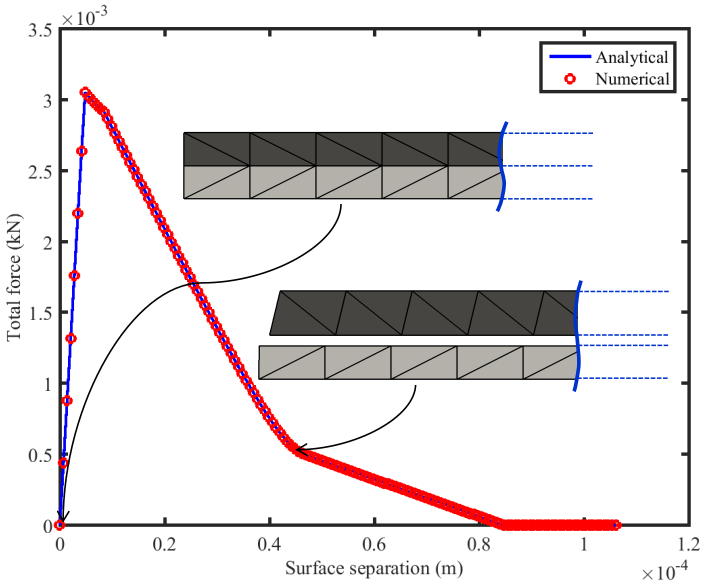

Figure 7. Force-separation curves for the analytical and numerical solutions in the laminated structure.

is:

$$f = \int_{\Gamma_c} \left(T_n^2 + T_t^2\right)^{1/2} \mathrm{d}\Gamma \;\approx\; \left(T_n^2 + T_t^2\right)^{1/2} \times H \times t \;, \tag{19}$$

where f is the total force for uniform delamination along the cohesive interface Γ_c. For numerical modeling, the domain is discretized with 100×1 elements and the simulation is performed for 2D plane strain conditions. Since only the response at the interface is of interest, a single layer of elements in thickness direction is sufficient. A uniform displacement is applied with a magnitude of 0.15 mm in sequence of load increments. Figure 7 compares numerical and analytical results for the total delamination force as a function of the magnitude of separation between the surfaces. The inset snapshots illustrate the mechanical response of a segment of the laminated structure at specific loading stages, with the intersected elements decomposed into triangles for visualization purposes. The measured relative error in the uniform mixed mode example problem is 2.25×10^{-7} %.

7.2. Material anchor - 2D

To explore the characteristics of the proposed optimization method, we first introduce the 2D material anchor design problem shown in Figure 8. A structural anchor (represented by phase A) is embedded in a host material (designated as phase B) with frictionless and cohesive interface conditions, imposed at the boundary between both phases. In this problem, we wish to determine the optimal geometry such that the holding force of the anchor is maximized. Originally studied for frictionless contact by [15], this problem is extended to account for cohesion at the interface.

The anchor is fixed along the boundary Γ_1, and a prescribed displacement, U_x^B, is applied to the host material along Γ_{2-4}. Displacements in the y direction are constrained to zero along Γ_{2-4}. To exclude the trivial case in which the anchor material directly connects boundary Γ_1 to boundaries Γ_{2-4}, these boundaries are excluded from the design domain. Considering the symmetric nature of the problem, only one half of the design domain is analyzed.

The response dependent contribution to the objective function in Equation (2) is defined through the holding force of the anchor in the x direction along Γ_1. The holding force is measured by integrating the normal stress σ_{xx} along Γ_1. This contribution to the objective function is defined as follows:

$$z = -\int_{\Gamma_1} \sigma_{xx}\, d\Gamma \;. \tag{20}$$

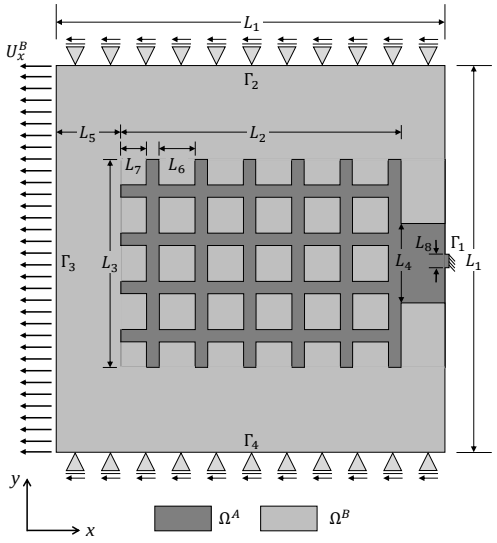

Figure 8. Initial design of the material anchor problem.

Table III. Nominal parameters for the material anchor design problem.

Description	Parameter
length of domain	$L_1 = 1.0$ m
length of anchor head	$L_2 = 0.715$ m
length of anchor width	$L_3 = 0.523$ m
anchor base width	$L_4 = 0.20$ m
anchor distance from end	$L_5 = 0.175$ m
inclusion width	$L_6 = 0.0833$ m
inclusion width	$L_7 = 0.0667$ m
fixed section width	$L_8 = 0.0333$ m
thickness	$t = 1/13$ m
applied displacement	$U_x^B = \text{var.}$
Young's modulus	$E^A = 10^4 \text{N/m}^2$
Young's modulus	$E^B = 10^4 \text{N/m}^2$
Poisson's ratio	$\nu^A = 0.3$
Poisson's ratio	$\nu^B = 0.3$
spring stiffness	$K = 2.0 \times 10^3 \text{N/m}^2$
response weight	$c_u = 5.0 \times E^A$
perimeter weight	$c_p = 0.25$
volume constraint weight	$c_v = 0.5$
gradient measure weight	$c_g = \text{var.}$
penalization parameter	$e_p = 1.0$
desired level set gradient	$\text{d}\phi_p = 1.0$
penalty factor	$\gamma = 20$
initial damping parameter	$\tilde{\beta}_{\text{int}} = 0.01$
GCMMA step size	$\Delta s = 3.0 \times 10^{-5}$

The optimization problem is regularized by applying a perimeter penalty and the level set gradient measure penalty along the interface. In order to ensure that the anchor material geometry does not occupy the entire design domain geometry, a volume constraint of 50% is imposed.

Half of the design domain is discretized with 120×60 elements and the physical response is predicted assuming plane strain conditions. To mitigate mechanical response convergence issues due to material inclusions undergoing rigid body rotations, the host material is grounded elastically by a distributed system of weak linear springs with stiffness K. The LSF is discretized by the XFEM mesh and the nodal level set values are defined as the optimization variables. The LSF is initialized by an array of cuboids as shown in Figure 8. The smoothing radius of the linear filter in (4) is 0.0375m.

The effect of the perimeter penalty on optimized designs for frictionless contact was studied in [15]. In this work, we study the effectiveness of constraining the level set gradient measure to regularize the optimization problem and consider different values of the weighting factor c_g in Equation (2). The influence of the interface conditions and the cohesive zone parameters on the optimized design are studied by varying the normal and tangential interface resistance. An example designed to initially exhibit total debonding is optimized to recover interface cohesion. Finally, the influences of the applied load are investigated through the variation of the applied displacement magnitude.

7.2.1. Nominal design We first illustrate the geometry evolution and convergence behavior of the nominal design. Design parameters are consistent with those given in Table III, and we exclude the influence of the level set gradient measure by setting $c_g = 0.0$. The nominal model assumes frictionless sliding contact, excluding material cohesion, and the applied displacement is set to $U_x^B = 0.025$m. The evolution of the nominal design is shown in Figure 9. During the optimization

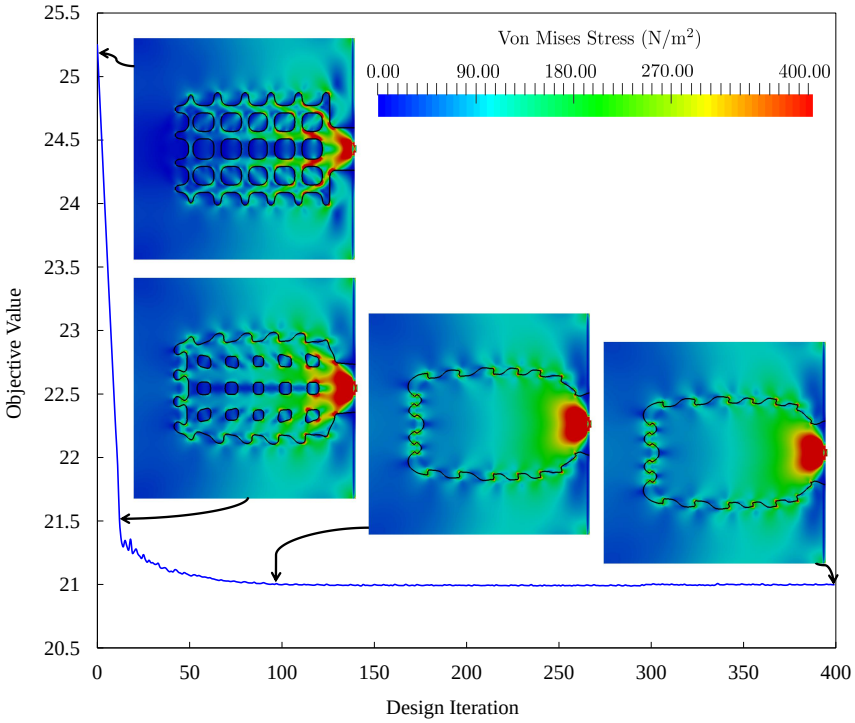

Figure 9. Objective evolution and convergence behavior of the nominal design.

Table IV. Holding force and interface length in the initial and optimized stages of the nominal design.

Design iteration	Holding force (N)	Interface length (m)
Initial	1.1432	3.86387
Optimized	1.8835	1.36123

process, the anchor material coalesces into a unified body. Interlocking tabs at the anchor head and barbs along the sides afford resistance to separation. The initial and optimized values for the holding force and the interface length are given in Table IV. While the general design traits are similar to that of [15], the increase of prescribed displacements in this study produce interlocking tabs at the head of the anchor.

7.2.2. Influence of gradient measure penalty Optimization problems involving sliding contact can lead to the formation of extremely sharp protrusions or periodic surface oscillations to maximize the resistance to surface separation. These small features can lead to poor mechanical response predictions when they approach the length scale of an element. Additionally, small features can be problematic for manufacturing. The level set gradient measure penalty helps to regularize the problem by discouraging small features. However, this form of regularization may lessen the formation of barbs along the side and separation resistant features if it is overemphasized in the objective function. To explore the impact of gradient measure regularization, the nominal design is solved for different values of the gradient measure penalty weight, c_g. The applied load is increased to $U_x^B = 0.05$m to amplify optimized geometry features, while all other model parameters and boundary conditions are the same as defined for the nominal design.

With an initial penalty weight of $c_g = 0.0$, the optimized geometry and subsequent holding force provide a reference value free of gradient measure regularization. The penalty weight is then increased incrementally to $c_g = 1.0$, and the percentage of the reduction in holding force is evaluated

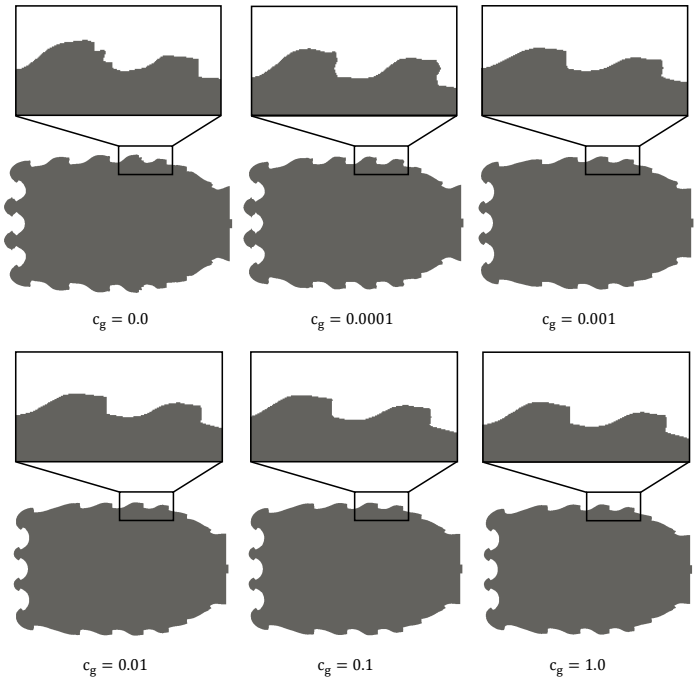

Figure 10. Effect of gradient measure penalty on the optimized design.

Table V. Holding force, reduction in holding force and the interface length of the optimized design for different gradient measure penalty weights, c_g.

Gradient measure penalty c_g	Holding force (N)	Reduction in holding force (%)	Interface length (m)
0.0	4.0827	0.0	1.3885
0.0001	4.0830	0.009	1.4244
0.001	4.0728	0.242	1.2857
0.01	4.0739	0.216	1.2861
0.1	4.0806	0.052	1.2859
1.0	4.0805	0.053	1.4553

by comparison to the optimized design with no gradient measure penalty. The optimization results are given in Figure 10 and Table V. The gradient measure regularization reduces the prevalence of small features at a minimal cost to the resulting holding force. For the remaining 2D examples provided in this paper, a gradient measure penalty of $c_g = 0.01$ is used.

7.2.3. Influence of interface conditions While optimized geometries for frictionless contact are somewhat intuitive, additional interface phenomena, such as cohesion and debonding, complicate design considerations. The optimized anchor design in the presence of cohesive interface conditions is investigated by varying the normal and tangential resistance at the interface. While the critical and final separation cohesion parameters are kept constant, $\delta_c^n = \delta_c^t = 0.007\text{m}, \delta_f^n = \delta_f^t = 0.2\text{m}$, the optimization problem is solved for different values of maximum normal and tangential traction, σ_{max} and τ_{max}. To provide an intuitive metric for the normal and tangential resistance experienced at the interface, we define the effective normal and shear cohesion modulus as follows:

$$E^N = \frac{\sigma_{max}}{\delta_c^n}, \qquad E^T = \frac{\tau_{max}}{\delta_c^t}, \tag{21}$$

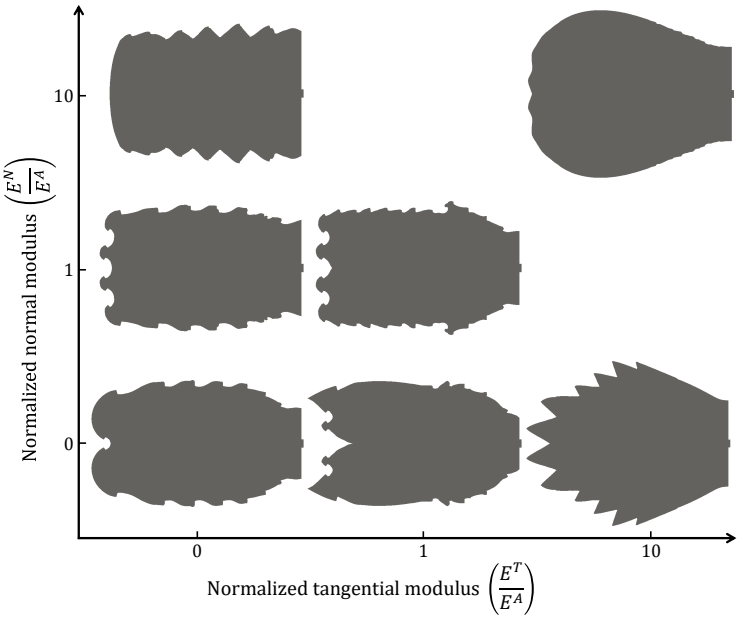

Figure 11. Influence of interface conditions on the optimized design, $U_x^B = 0.025$m.

where E^N is the effective normal cohesion modulus and E^T is the effective shear cohesion modulus. Figure 11 illustrates optimized geometries for various normal and shear cohesion moduli values normalized by the anchor material Young's modulus (E^A). As the tangential cohesion modulus is increased, the contact interface aligns with the direction of the applied displacement to maximize resistance. In the case of a large normal cohesion modulus, the trailing edges of barbs or tines flatten out to provide resistance to normal separation. For a design involving large shear and normal cohesion, analogous to perfect bonding at the interface, a reduction of surface features and consolidated anchor mass are observed. This design trend has also been observed by [15] for the case of perfect bonding and separable interface. For all examples with cohesion presented in Figure 11, interface cohesion remains in the bonded zone; see Figure 3.

7.2.4. Optimization of problems experiencing debonding In the numerical studies above, the initial anchor geometry provides significant interface resistance. During the evolution of the anchor geometry, features quickly emerged to further increase the surface traction. This section considers the case where the optimization process is initialized with a design that experiences complete delamination. To this end, the optimized geometry for the highest pure tangential cohesion case, $E^N/E^A = 0.0$ and $E^T/E^A = 10.0$ from Figure 11, is chosen as the initial configuration. The final separation parameters are set to $\delta_{\mathrm{f}}^n = \delta_{\mathrm{f}}^t = 0.014$m, the maximum tangential traction parameter to $\tau_{max} = 140\mathrm{N/m}^2$ and the applied displacement to $U_x^B = 0.1$m. All other material parameters remain the same as the nominal design.

The objective history during optimization, supported by snapshots of the physical response and force-displacement curves for select iterations, are shown in Figure 12. During the initial stages of design evolution, full debonding occurs when the applied displacement surpasses 0.05m. This behavior is evident by the sudden drop in holding force at the applied displacement of $U_x^B \approx 0.05$m, shown in the inset of Figure 12. Within the first ten design iterations total debonding is mitigated. After optimization, the entirety of the material interface remains in the bonded zone of cohesion at the maximum applied displacement, as demonstrated by the linear force-displacement curve. Similar to the frictionless nominal design, the geometry produces barbs along the sides that provide resistance to the separation. This example also demonstrates that dynamic relaxation provides a

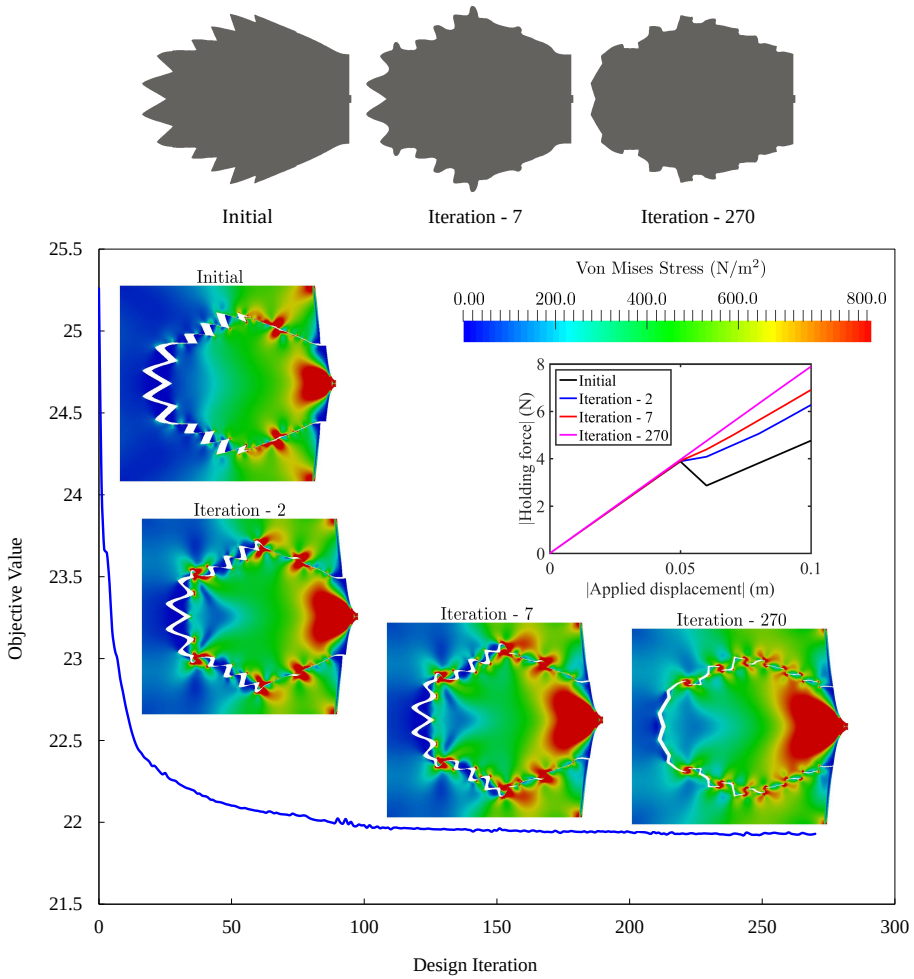

Figure 12. Evolution of design and load-displacement curve during optimization.

reliable evaluation of the mechanical response experiencing rapid delamination, throughout design iterations.

7.2.5. Influence of applied load In the previous example, complete debonding of the initial design was induced by selecting the initial geometry, load conditions, and interface properties favorable to such a response. To further investigate design traits associated with reduced cohesion, in this study we focus our attention on the influence of the magnitude of the applied displacement on the optimized geometry. Beginning with the optimized design and model parameters for the tangential resistance case $E^N/E^A = 0.0$ and $E^T/E^A = 1.0$ shown in Figure 11, the applied displacement is incrementally raised to match the final separation cohesion parameter, i.e. $U_x^B = \delta_f^t = 0.2m$. The optimization problem is solved at each load level using the initial design shown in Figure 8. The evolution of the optimized design as the applied displacement increases is shown in Figure 13.

For small displacements, the optimized design exhibits an interface that is predominantly aligned with the direction of applied load to afford cohesive resistance to separation. As the applied displacement increases, cohesion diminishes gradually in localized regions. The physical response in these regions is dominated by sliding contact interactions. At the highest loading case of $U_x^B = 0.2$m, the majority of interfacial separation is greater than the critical separation value. With a

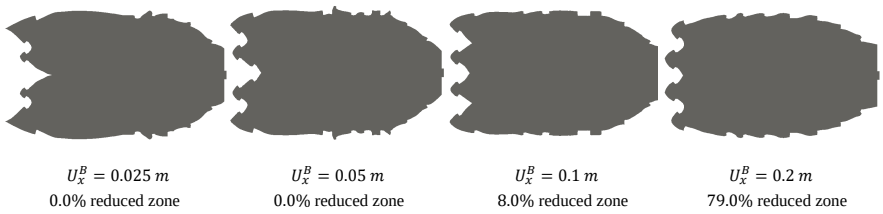

Figure 13. Influence of applied load on the optimized design, $E^T/E^A = 1.0$.

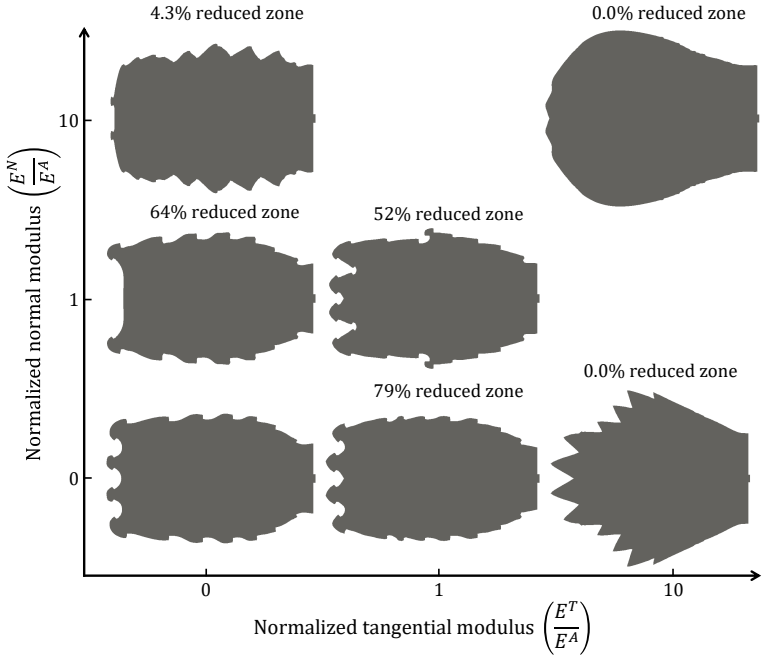

Figure 14. Influence of extreme loading condition on the optimized design, $U_x^B = 0.2$m.

reduced influence of cohesion, the optimized design for the maximum load scenario shows a close resemblance to the nominal design without cohesion.

The highest loading level, i.e. $U_x^B = 0.2m$, is applied to the material interface configurations studied in Section 7.2.3, and the resulting optimized geometries are illustrated in Figure 14. The percentage of the interface which resides in the reduced zone of cohesion is provided above each case. Comparison between Figures 11 and 14 shows that under the maximum loading condition, there is a general trend towards the development of barbs or interlocking features to prevent separation. For this load case scenario, the benefit of such features outweighs the cost of the interface measure penalty. However, design problems in which the entire interface remains in the bonded zone of cohesion (Figure 3) remain relatively unchanged.

The studies performed on the 2D material anchor design problem demonstrate that the proposed optimization framework is sufficient to solve a broad range of problems, including those exhibiting complete debonding. Interfacial properties have shown to be a dominant design consideration for material anchors. The study on varying the magnitude of the applied load showed that design characteristics can be tailored in localized regions where either cohesion or frictionless contact are prevalent.

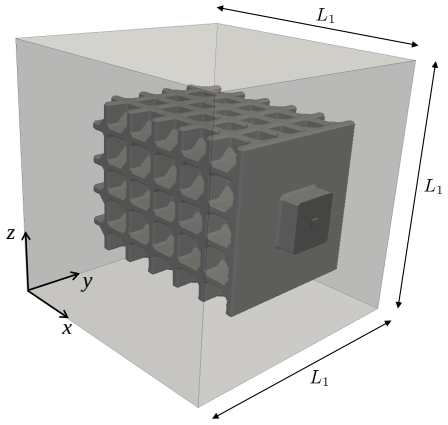

Figure 15. Schematic of the initial design in the 3D anchor problem.

7.3. Material anchor - 3D

The following examples extend the design domain to study three dimensional problems. The design domain of the 2D example in Figure 8 is repeated in the out-of-plane direction. The schematic of the 3D model initial configuration is shown in Figure 15. All material parameters and interface conditions are adopted from 2D example; see Table III.

Similar to the 2D example, the objective is to maximize the holding force of the anchor. Line boundary Γ_1 is extended to a surface boundary where the 3D anchor exits the design domain. Line boundaries Γ_2 and Γ_4 are extended to the $x-y$ and $x-z$ planes at the design domain boundaries. Finally, line boundary Γ_3 is extended to a surface boundary at the $x=0$ plane. Considering the symmetric nature of the problem, only one fourth of the domain is analyzed with $60\times30\times30$ elements. The optimization step size is set to $\Delta s = 0.001$. Similar to the 2D example, the response dependent contribution to the objective function in Equation (2) is defined through the holding force of the anchor in the x direction along Γ_1. The holding force is measured by integrating the normal stress σ_{xx} along Γ_1 (20). The optimization problem is regularized by applying a perimeter penalty and gradient measure penalty for the level set field along the interface. The response, perimeter, and volume constraint weights are the same as provided in Table III, whereas the gradient measure weight is kept consistent with the 2D analog for each study. Specifically, the gradient measure weight is set to $c_g = 0.0$ for the nominal design and $c_g = 0.01$ for the remaining 3D examples.

We first illustrate the geometric evolution and convergence behavior of the nominal design. In all 3D examples, the applied displacement is set to $U_x^B = 0.007$m; higher loads resulted in numerical instabilities from complex geometric features. The evolution of the nominal design is shown in Figure 16. Similar to the 2D problem, the anchor material evolves into a unified body. Ridges or spines along the outer face of the anchor provide resistance to separation.

7.3.1. Influence of interface conditions The 3D effects of interface cohesion on the optimized design are investigated for different levels of normal and tangential cohesive resistance. All cases of interfacial properties investigated in Section 7.2.3 are studied here for the three dimensional configuration. The resulting geometries for these sets of interface parameters are shown in Figure 17. For comparison, a cutaway view is provided in Figure 18.

Although 2D and 3D examples show design trend similarities, the 3D optimized geometries exhibit traits that cannot be fully represented in two dimensions. The relative size and placement of barbs in the x direction along the outer surface varies radially, which cannot be deduced from 2D examples. The non-uniform radial profile is likely a result of the square shaped design domain. The plain strain assumption used in 2D examples determines the physical response appropriate for an extruded 3D domain. Due to the cylindrical nature of the optimized geometry in 3D examples, the relative size of barbs is not directly comparable. For all 3D examples presented, the entirety of

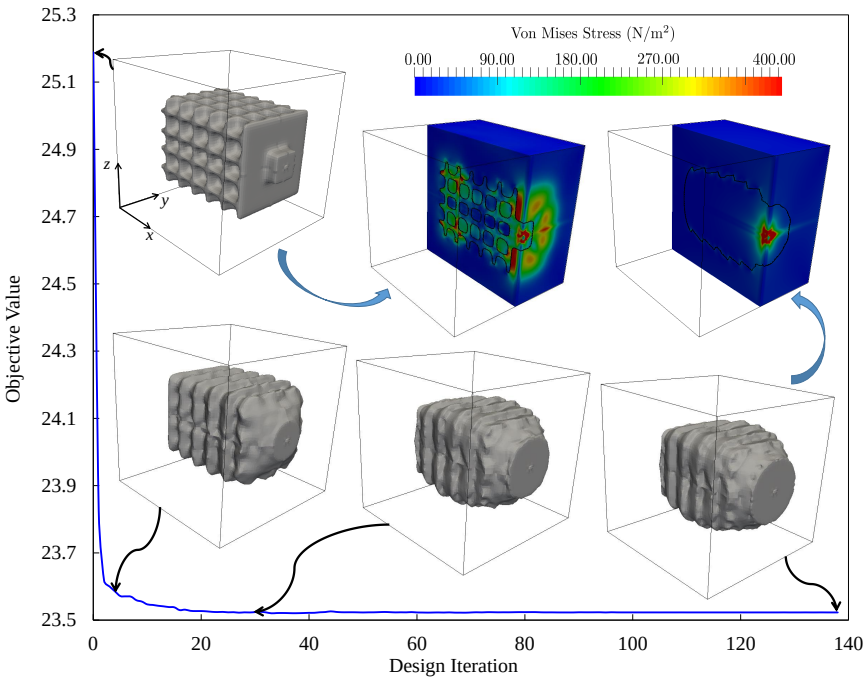

Figure 16. Objective evolution for the 3D nominal design.

the interface remained in the bonded zone of cohesion. Note that the reduction of barbs size in the 3D examples when compared to 2D cases could be a result of the reduced applied load. However, these examples demonstrate that concluding 3D geometries from a 2D analysis may not be adequate depending on the intended application.

8. CONCLUSIONS

This paper presented a topology optimization framework for two-phase materials with cohesive interface phenomena. The interface condition is described by a bilinear cohesive zone model. To prevent surface penetration and to provide more accurate solution of the finite element analysis, the constitutive cohesive zone model is augmented by a stabilized Lagrange multiplier formulation. The material behavior of the mechanical model is described by linear elastic isotropic material and infinitesimal strains are assumed for the mechanical deformation. The XFEM is used to discretize and integrate the governing equations. To remedy the convergence difficulties for large separation and post delamination, an adaptive dynamic relaxation method is adopted for computing the static response.

An explicit LSM is used to describe the interface geometry between two distinct material phases. The LSF is defined by explicit functions of the optimization variables. The optimization problem is solved with a nonlinear programming method. The optimization problems studied in this paper consider the mechanical response and penalty terms on the material interface surface area and a level set gradient measure to suppress sub-element geometric features. A constraint on the volume ratio of the material phase is imposed. The design sensitivities are evaluated by the adjoint method.

The presented optimization framework proved reliable for a variety of 2D and 3D examples, optimizing the topology of a material anchor by maximizing the holding force. Gradient measure regularization was shown to be successful at removing small features that are problematic for accurate response prediction and for manufacturing considerations at a minimal cost to design performance. The interface conditions were shown to have a strong influence on optimized geometry, as various levels of normal and tangential resistance yielded drastically different designs.

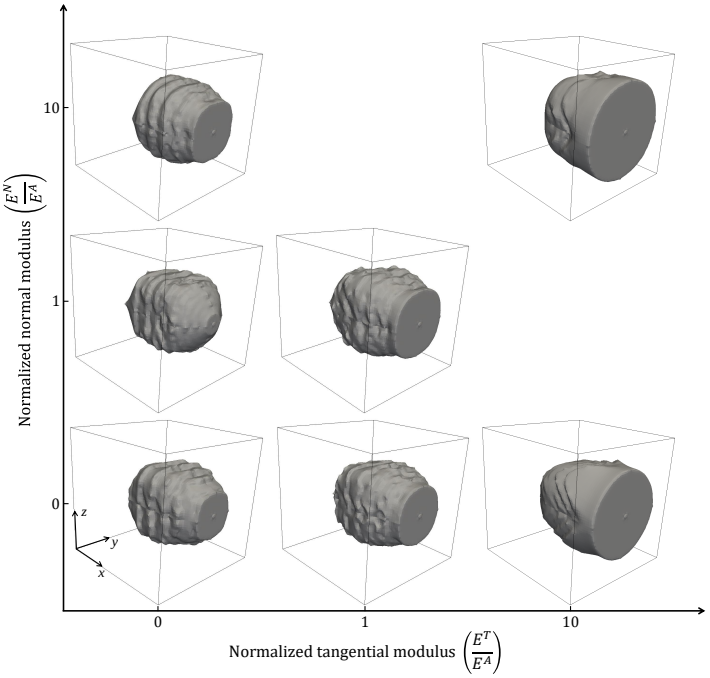

Figure 17. 3D view of the influence of interface conditions on the optimized design, $U_x^B = 0.007$m.

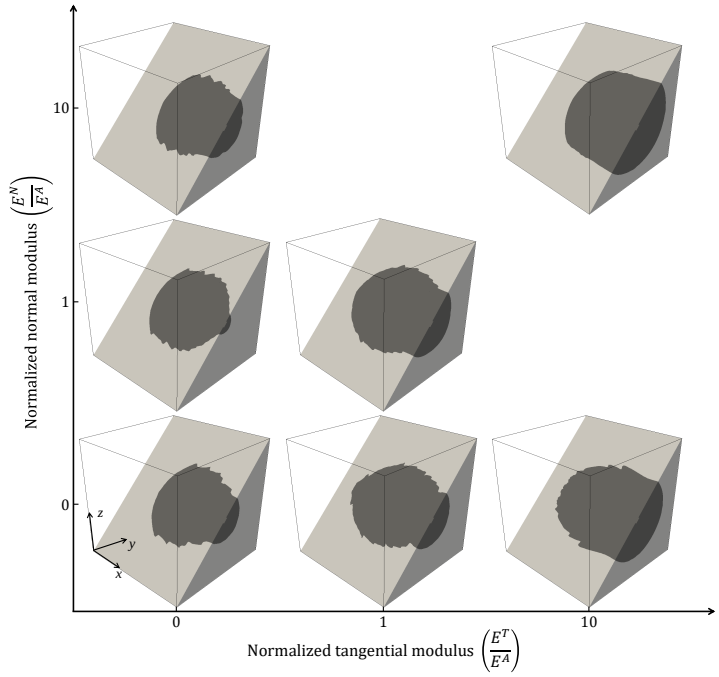

Figure 18. Inclined cross section view of the influence of interface conditions on the optimized design, $U_x^B = 0.007$m.

An initial design experiencing total debonding was optimized to recover interface cohesion and a monotonic resistance to separation. The applied load study demonstrated that geometry can be tailored to localized regions where either cohesion or delamination are present. A three dimensional

example revealed design traits that could not deduced from 2D studies, such as circumferential barb size and placement.

While only bilinear cohesion and frictionless contact were considered in this study, the developed method allows for the convenient extension of the framework for different interface constitutive relations. The applied load in three dimensional studies was reduced, as convergence difficulties in the mechanical model were encountered at higher loads. Additional solution techniques, such as the arc length method, should be explored to improve the stability of the physical response prediction. The proposed method is currently limited to two-phase material problems in the small strain regime. For future studies, this method needs to be extended to multi-phase material problems in the finite strain regime.

ACKNOWLEDGMENTS

The first and third authors gratefully acknowledge the support of the National Science Foundation under grant CMMI-1231048. The second and third authors acknowledge the support of the National Science Foundation under grant CMMI-1235532 and support through Sandia National Laboratories under Contract Agreement 1396470. The third author acknowledges the support of Air Force Office of Scientific Research under Contract No. FA9550-13-1-0088. The opinions and conclusions presented in this paper are those the authors and do not necessarily reflect the views of the sponsoring organizations.

REFERENCES

1. Bendsøe MP. Optimal shape design as a material distribution problem. *Structural optimization* 1989; **1**(4):193–202.
2. Rozvany G, Zhou M, Birker T. Generalized shape optimization without homogenization. *Structural and Multidisciplinary Optimization* 1992; **4**(3):250–252.
3. Bendsøe MP, Sigmund O. *Topology Optimization: Theory, Methods and Applications*. Springer, 2003.
4. Sigmund O, Maute K. Topology optimization approaches: A comparative review. *Structural and Multidisciplinary Optimization* 2013; **48**(6):1031–1055.
5. Deaton JD, Grandhi RV. A survey of structural and multidisciplinary continuum topology optimization: post 2000. *Structural and Multidisciplinary Optimization* 2014; **49**(1):1–38.
6. Kikuchi N, Chen BC. Topology optimization with design-dependent loads. *Finite Elements in Analysis and Design* 2001; **37**(1):57–70.
7. Sigmund O, Clausen PM. Topology optimization using a mixed formulation: an alternative way to solve pressure load problems. *Computer Methods in Applied Mechanics and Engineering* 2007; **196**(13):1874–1889.
8. Yoon GH. Topology optimization for stationary fluid–structure interaction problems using a new monolithic formulation. *International journal for numerical methods in engineering* 2010; **82**(5):591–616.
9. Hammer V, Olhoff N. Topology optimization of continuum structures subjected to pressure loading. *Struct. Multidisc. Optim.* 2000; **19**:85–92.
10. Strömberg N. The influence of sliding friction in optimal topologies. *Recent Advances in Contact Mechanics*, vol. 56, Stravroulakis GE (ed.), 5th Contact Mechanics International Symposium (CMIS2009), Springer, 2009; 327–336.
11. Andrade-Campos A, Ramos A, Simões J. A model of bone adaptation as a topology optimization process with contact. *Journal of Biomedical Science and Engineering* 2012; **5**:229–244.
12. van Dijk NP, Maute K, Langelaar M, Van Keulen F. Level-set methods for structural topology optimization: a review. *Structural and Multidisciplinary Optimization* 2013; **48**(3):437–472.
13. Fries TP, Belytschko T. The intrinsic XFEM: a method for arbitrary discontinuities without additional unknowns. *International journal for numerical methods in engineering* 2006; **68**(13):1358–1385.
14. Khoei AR. *Extended finite element method: Theory and applications*. Wiley, 2015.
15. Lawry M, Maute K. Level set topology optimization of problems with sliding contact interfaces. *Structural and Multidisciplinary Optimization* 2015; **52**(6):1107–1119.
16. Lawry M, Behrou R, Maute K. On the influence of interface models on the optimum layout of multi-component structures and material systems. *11th World Congress on Structural and Multidisciplinary Optimisation*, Sydney Austrailia, 2015.
17. Liu P, Luo Y, Kang Z. Multi-material topology optimization considering interface behavior via XFEM and level set method. *Computer Methods in Applied Mechanics and Engineering* 2016; .
18. Dugdale D. Yielding of steel sheets containing slits. *Journal of the Mechanics and Physics of Solids* 1960; **8**(2):100–104.
19. Needleman A. A continuum model for void nucleation by inclusion debonding. *Journal of applied mechanics* 1987; **54**(3):525–531.
20. Camacho GT, Ortiz M. Computational modelling of impact damage in brittle materials. *International Journal of solids and structures* 1996; **33**(20):2899–2938.

21. Tvergaard V. Effect of fibre debonding in a whisker-reinforced metal. *Materials science and engineering: A* 1990; **125**(2):203–213.
22. Tvergaard V, Hutchinson JW. The relation between crack growth resistance and fracture process parameters in elastic-plastic solids. *Journal of the Mechanics and Physics of Solids* 1992; **40**(6):1377–1397.
23. Xu XP, Needleman A. Void nucleation by inclusion debonding in a crystal matrix. *Modelling and Simulation in Materials Science and Engineering* 1993; **1**(2):111.
24. Espinosa H, Dwivedi S, Lu HC. Modeling impact induced delamination of woven fiber reinforced composites with contact/cohesive laws. *Computer Methods in Applied Mechanics and Engineering* 2000; **183**(3):259–290.
25. Li S, Ghosh S. Modeling interfacial debonding and matrix cracking in fiber reinforced composites by the extended voronoi cell fem. *Finite elements in analysis and design* 2007; **43**(5):397–410.
26. Zhang ZJ, Paulino GH. Cohesive zone modeling of dynamic failure in homogeneous and functionally graded materials. *International journal of plasticity* 2005; **21**(6):1195–1254.
27. Park K, Paulino GH. Cohesive zone models: a critical review of traction-separation relationships across fracture surfaces. *Applied Mechanics Reviews* 2011; **64**(6):060 802.
28. Yang B, Ravi-Chandar K. A single-domain dual-boundary-element formulation incorporating a cohesive zone model for elastostatic cracks. *International Journal of Fracture* 1998; **93**(1-4):115–144.
29. Belytschko T, Organ D, Gerlach C. Element-free galerkin methods for dynamic fracture in concrete. *Computer Methods in Applied Mechanics and Engineering* 2000; **187**(3):385–399.
30. Xu XP, Needleman A. Numerical simulations of fast crack growth in brittle solids. *Journal of the Mechanics and Physics of Solids* 1994; **42**(9):1397–1434.
31. Gullerud AS, Gao X, Dodds RH, Haj-Ali R. Simulation of ductile crack growth using computational cells: numerical aspects. *Engineering Fracture Mechanics* 2000; **66**(1):65–92.
32. Tijssens MG, Sluys BL, van der Giessen E. Numerical simulation of quasi-brittle fracture using damaging cohesive surfaces. *European Journal of Mechanics-A/Solids* 2000; **19**(5):761–779.
33. Belytschko T, Fish J, Engelmann BE. A finite element with embedded localization zones. *Computer methods in applied mechanics and engineering* 1988; **70**(1):59–89.
34. Jirásek M. Comparative study on finite elements with embedded discontinuities. *Computer methods in applied mechanics and engineering* 2000; **188**(1):307–330.
35. Moës N, Dolbow J, Belytschko T. A finite element method for crack growth without remeshing. *International Journal for Numerical Methods in Engineering* 1999; **46**.
36. Moës N, Belytschko T. Extended finite element method for cohesive crack growth. *Engineering fracture mechanics* 2002; **69**(7):813–833.
37. Liu F, Borja R. A contact algorithm for frictional crack propagation with the extended finite element method. *International Journal For Numerical Methods In Engineering* 2008; **76**:1489–1512.
38. Mueller-Hoeppe DS, Wriggers P, Loehnert S. Crack face contact for hexahedral-based XFEM formulation. *Computational Mechanics* 2012; **49**:725–734.
39. Khoei A, Nikbakht M. An enriched finite element algorithm for numerical computation of contact friction problems. *International Journal of Mechanical Sciences* 2007; **49**(2):183–199.
40. Farsad M, Vernerey FJ, Park HS. An extended finite element/level set method to study surface effects on the mechanical behavior and properties of nanomaterials. *International Journal for Numerical Methods in Engineering* 2010; **84**(12):1466–1489.
41. Geniaut S, Massin P, Moës N. A stable 3D contact formulation using X-FEM. *REMN* 2007; **16**:259–275.
42. Amdouni S, Hild P, Lleras V, Moakher M, Renard Y. A stabilised lagrange multiplier method for the enriched finite-element approximation of contact problems of cracked elastic bodies. *ESAIM: Mathematical Modelling and Numerical Analysis* 2012; **46**:813–839.
43. Liu F, Borja RI. Stabilized low-order finite elements for frictional contact with the extended finite element method. *Computer Methods in Applied Mechancis and Engineering* 2010; **199**:2456–2471.
44. Giner E, Tur M, Tarancon JE, Fuenmayor FJ. Crack face contact in X-FEM using a segment-to-segment approach. *International Journal for Numercial Methods in Engineering* 2010; **82**:1424–1449.
45. Nistor I, Guiton MLE, Massin P, Moës N, Géniaut S. An X-FEM approach for large sliding contact along discontinuities. *International Journal For Numerical Methods In Engineering* 2009; **78**:1407–1435.
46. Siavelis M, Massin P, Guiton MLE, Mazet S, Moës N. Robust implementation of contact under friction and large sliding with the extended finite element method. *European Journal of Computational Mechanics* 2010; **19**:189–203.
47. Khoei A, Mousavi ST. Modeling of large deformation–large sliding contact via the penalty X-FEM technique. *Computational Materials Science* 2010; **48**(3):471–480.
48. Taheri Mousavi SMJ, Taheri Mousavi SM. Modeling large sliding frictional contact along non-smooth discontinuities in X-FEM. *International Journal of Modeling and Optimization* 2011; **1**:169–173.
49. Biotteau E, Ponthot JP. Modeling frictional contact conditions with the penalty method in the extended finite element framework. *European Congress on Computational Methods in Applied Sciences and Engineering*, 2012.
50. Allaire G, Jouve F, Toader AM. Structural optimization using sensitivity analysis and a level-set method. *Journal of computational physics* 2004; **194**(1):363–393.
51. Wang S, Wang M. Radial basis functions and level set method for structural topology optimization. *International journal for numerical methods in engineering* 2006; **65**(12):2060–2090.
52. Luo Z, Tong L, Wang MY, Wang S. Shape and topology optimization of compliant mechanisms using a parameterization level set method. *Journal of Computational Physics* 2007; **227**(1):680–705.
53. Pingen G, Waidmann M, Evgrafov A, Maute K. A parametric level-set approach for topology optimization of flow domains. *Structural and Multidisciplinary Optimization* 2010; **41**(1):117–131.
54. Makhija D, Maute K. Numerical instabilities in level set topology optimization with the extended finite element method. *Structural and Multidisciplinary Optimization* 2014; **49**(2):185–197.
55. Villanueva CH, Maute K. Density and level set-XFEM schemes for topology optimization of 3-D structures. *Computational Mechanics* 2014; **54**(1):133–150.

56. Maute K, Kreissl S, Makhija D, Yang R. Topology optimization of heat conduction in nano-composites. *9th World Congress on Structural and Multidisciplinary Optimization, Shizuoka, Japan*, 2011.
57. van Dijk N, Langelaar M, van Keulen F. Explicit level-set-based topology optimization using an exact heaviside function and consistent sensitivity analysis. *International Journal for Numerical Methods in Engineering* 2012; **91**(1):67–97.
58. Van Miegroet L, Duysinx P. Stress concentration minimization of 2D filets using X-FEM and level set description. *Structural and Multidisciplinary Optimization* 2007; **33**(4-5):425–438.
59. Wang MY, Wang S. Parametric shape and topology optimization with radial basis functions. *IUTAM symposium on topological design optimization of structures, machines and materials*, Springer, 2006; 13–22.
60. Kreissl S, Maute K. Levelset based fluid topology optimization using the extended finite element method. *Structural and Multidisciplinary Optimization* 2012; :1–16.
61. Jenkins N, Maute K. Level set topology optimization of stationary fluid-structure interaction problems. *Structural and Multidisciplinary Optimization* 2015; **52**(1):179–195.
62. Coffin P, Maute K. Level set topology optimization of cooling and heating devices using a simplified convection model. *Structural and Multidisciplinary Optimization* 2015; :1–19.
63. Coffin P, Maute K. A level-set method for steady-state and transient natural convection problems. *Structural and Multidisciplinary Optimization* 2015; :1–21.
64. Wriggers P. *Computational Contact Mechanics*. Wiley, 2002.
65. Fries T, Belytschko T. The extended/generalized finite element method: an overview of the method and its applications. *International Journal for Numerical Methods in Engineering* 2010; **84**(3):253–304.
66. Terada K, Asai M, Yamagishi M. Finite cover method for linear and non-linear analyses of heterogeneous solids. *International journal for numerical methods in engineering* 2003; **58**(9):1321–1346.
67. Tran AB, Yvonnet J, He QC, Toulemonde C, Sanahuja J. A multiple level set approach to prevent numerical artefacts in complex microstructures with nearby inclusions within XFEM. *International Journal for Numerical Methods in Engineering* 2011; **85**(11):1436–1459.
68. Lang C, Makhija D, Doostan A, Maute K. A simple and efficient preconditioning scheme for xfem with heaviside enrichments. *Computational Mechancis* 2014; **54**(5):1357–1374.
69. Zhang L, Yu T. Modified adaptive dynamic relaxation method and its application to elastic-plastic bending and wrinkling of circular plates. *Computers & structures* 1989; **33**(2):609–614.
70. Salehi M, Aghaei H. Dynamic relaxation large deflection analysis of non-axisymmetric circular viscoelastic plates. *Computers & structures* 2005; **83**(23):1878–1890.
71. Pan L, Metzger DR, Niewczas M. The meshless dynamic relaxation techniques for simulating atomic structures of materials. *ASME 2002 Pressure Vessels and Piping Conference*, American Society of Mechanical Engineers, 2002; 15–26.
72. Moré JJ. The Levenberg-Marquardt algorithm: implementation and theory. *Numerical analysis*. Springer, 1978; 105–116.
73. Kawamoto A. Stabilization of geometrically nonlinear topology optimization by the Levenberg-Marquardt method. *Struct. Multidisc. Optim.* 2009; **37**:429–433.
74. Svanberg K. A globally convergent version of MMA without linesearch. *Proceedings of the First World Congress of Structural and Multidisciplinary Optimization, 28 May - 2 June 1995*, Goslar, Germany, 1995; 9–16.
75. Kreissl S, Pingen G, Maute K. Topology optimization for unsteady flow. *International Journal for Numerical Methods in Engineering* 2011; **87**(13):1229–1253.
76. Davis TA. Algorithm 832: UMFPACK V4. 3—an unsymmetric-pattern multifrontal method. *ACM Transactions on Mathematical Software (TOMS)* 2004; **30**(2):196–199.
77. Saad Y. Ilut: A dual threshold incomplete lu factorization. *Numerical Linear Algebra with Applications* 1994; **1**(4):387–402.
78. Anderson TL, Anderson T. *Fracture mechanics: fundamentals and applications*. CRC press, 2005.
79. Song SH, Paulino GH, Buttlar WG. Simulation of crack propagation in asphalt concrete using an intrinsic cohesive zone model. *Journal of Engineering Mechanics* 2006; **132**(11):1215–1223.